Exploring Protein Conformations with Mass Spectrometry

Submitted in partial fulfilment for the degree of
Doctor of Philosophy

Hannah V. Florance

PhD by Research

The University of Edinburgh

2007

Work like you don't need the money

Love like you've never been hurt

Dance like nobody's watching

Unknown

For GG x

Declaration

This thesis is submitted in part fulfilment of the requirement for the degree of Doctor of Philosophy at the University of Edinburgh. Unless otherwise stated, the work is original and has not been previously submitted, in whole or in part, for any degree at this, or any other University.

Acknowledgements

I have so many thank you's it's hard to know where to begin. The person however, who must come top of the list is Dr Perdita Barran, without whom I wouldn't be in this situation. Little did I know that when I went to her for some careers advice that she'd end up being my mentor. Thank you Perdi!

Thanks also to Professors Malcolm Walkinshaw and Nick Turner who provided the opening for the project and welcomed me on board. Thanks also to their group members Kirk Malone, Colin Dunsmore and Kevin Bailey for supplying all those ligands, Alan Patterson and the wonderfully patient and helpful Martin Wear for my constant supply of cyclophilin.

A special thank you to Alan Taylor, not just for his wisdom and help with the LCQ, but his Am Dram entertainment too!

Thanks also to the entire Barran group and other friends in chemistry (you know who you are) who made the years so enjoyable.

Thanks to all the bellydancers of Edinburgh (and Cairo) who kept me sane – a surprising number of whom are themselves scientists. Keep shimmying!

Last but not least, one very special man and two very psychotic dogs who have provided me with unconditional emotional support – I believe Graeme, you are a better cook because of my write-up period!

Abstract

Mass spectrometry is a sensitive, dynamic, fast and versatile technique for studying biological systems. The use of *native electrospray ionisation* allows retention of secondary and tertiary structure(s) into the gas phase, where the use of mass spectrometry can yield much information on the intrinsic intra- and intermolecular noncovalent interactions.

The first part of this thesis describes the development and viability of a phase I screening system for obtaining a rank order of affinity of new ligands against the immunophilin, cyclophilin A (CypA). The naturally occurring inhibitor cyclosporin A (CsA) was used as a positive control to validate a method for calculating the dissociation constant (K_d). An HPLC autosampler and pumping system was used as a high throughput on-line ESI-MS sampling system. Optimised ESI conditions were then used to screen novel ligands from 3 combinatorial libraries and approaches for data analysis are discussed.

Hydrogen / deuterium exchange (HDX) can be used directly and indirectly as a means for studying protein conformations. Melittin, the major component of honey bee venom is taken here as a model system for studying secondary structure in solution and the gas phase. Comprising a 26 amino acid polypeptide, melittin occupies a random coil in aqueous conditions which can be transformed into an α-helix under increasingly hydrophobic conditions.

A variety of HDX techniques were utilised: i) comparing rates of deuterium (*d*-) uptake by direct infusion – ESI at different pDs and methanol concentrations; ii) PLIMSTEX (protein-ligand interactions by mass spectrometry, titration and HDX) at high and low salt concentrations with varying pDs; iii) gas phase exchange in an LCQ ion trap using He / *d*-methanol as the bath gas. Melittin was pre-incubated in a variety of methanol concentrations. Comparing results from these different approaches, α-helical retention has been shown to exist in the N-terminal half of the peptide.

All the afore-mentioned techniques developed using melittin were adapted for CypA. Comparisons of *d*-uptake in the presence and absence of CsA shows the ligand to have a stabilising affect on the protein.

Table of Contents

List of Abbreviations

CA	capsid protein
CID	collision induced dissociation
CRM	charged residue model
CsA	cyclosporin A
CypA	human cyclophilin A
CypA-CsA	cyclophilin – cyclosporin complex
D	deuterium
d-	prefix to denote deuteration
Da	Daltons
dc	direct current
DI	direct infusion
ECD	electron capture dissociation
EI	electron impact
ESI	electrospray ionisation (mass spectrometry)
EX1 / EX2	hydrogen/deuterium exchange regimes
FAB	fast atom bombardment
FIA	flow injection analysis
FT-ICR	Fourier transform –ion cyclotron resonance (mass spectrometry)
FT-MS	Fourier transform mass spectrometry
HDX	hydrogen/deuterium exchange
HHM	horse heart myoglobin
HIV	human immunodeficiency virus
HPLC	high performance liquid chromatography
ICR	ion cyclotron resonance
ICR-MS	ion cyclotron resonance mass spectrometry
IEM	ion evaporation model
IL-2	interleukin-2 (cytokine)
IMMS	ion mobility mass spectrometry
IRMPD	infra-red multiphoton dissociation

K_d	dissociation constant
LC	liquid chromatography
LCQ	ThermoElectron quadrupole ion trap mass spectrometer
MALDI	matrix assisted laser desorption ionisation
min	minute(s)
MS	mass spectrometry
MS^2	tandem mass spectrometry
m/z	mass to charge ratio
NMR	nuclear magnetic resonance
PPIase	peptidyl propyl isomerase
PLIMSTEX	protein–ligand interactions by mass spectrometry, titration and hydrogen/deuterium exchange
psi	pounds per square inch
QIT	quadrupole ion trap
Q-ToF	quadrupole - time of flight
Ref-1	regulator of fusion protein
rf	radio frequency
rpm	revolutions per minute
s or sec	second(s)
SAR	structure activity relationships
SDS-PAGE	sodium dodecylsulfate-polyacrylamide gel electrophoresis
SIM	selective ion monitoring
SUPREX	stability of unpurified proteins by rates of hydrogen/deuterium exchange
TBS	tris buffered saline
TIC	total ion current
UV	ultra violet
Vpr	viral protein R
ZMD	Micromass single quadrupole mass spectrometer

1 Introduction

In 1990 an ambitious international project to map the human genome began. This was initially co-ordinated by the US Department of Energy and the National Institutes of Health but over the intervening years another 18 partners and contributors including the UK, Japan, France, Germany and China became involved. The goal was finally achieved in 2003, two years ahead of schedule.[1] Prior to this only smaller, less evolved species such as the worm, *Caenorhabditis elegans*[2] or the fruit fly, *Drosophila melanogaster*[3] had been fully sequenced. The project was undertaken in part to release the information held in the genome (20000 – 25000 genes in humans) to further an understanding of human physiology and the genetic origin of diseases. This effort coupled with developments in soft ionisation techniques has led to the use of Mass Spectrometry based methods which seek to define the *proteome*, 'the compliment of proteins derived from the genome.'

The area of research which encompasses these post-genomic technologies is known as ***proteomics***. This thesis is concerned with two branches of this ever expanding research field:

1. ***Structural proteomics***. (high-throughput) determination of protein structures.
2. ***Interaction proteomics.*** This concerns the investigation of protein interactions on the atomic, molecular and cellular levels.

Protein structures and dynamics of these complex moieties have traditionally been studied by techniques such as X-ray crystallography,[4] circular dichroism,[5] fluorescence,[6] infrared spectroscopy[7] and NMR.[8,9] The main drawbacks encountered with these techniques are high sample consumption and low throughput, but also a limitation on molecular size. Mass spectrometry, in contrast, is sensitive, versatile, dynamic, fast and relatively low on sample consumption, lending itself well to high-throughput analyses.

There have been a number of developments in the field of mass spectrometry to meet the demand for analysis of increasingly large molecules and molecular complexes such as proteins,[10] DNA,[11,12] oligosaccharides[13] and lipids.[14] The critical criterion to this involves the detection of large intact molecules of interest which has necessitated non-invasive or gentle ionisation techniques. Mass spectrometry has an upper mass limit for detection which is currently far higher than that feasible by NMR and crystallographic methods.

The first part of this thesis (Chapters 3) develops a high throughput screening technique for the analysis of protein-ligand interactions. The aim was to develop a mass spectrometry (MS) based "proof of principle" technique. The second part of this thesis (Chapters 4-6) addresses an alternative approach to studying protein dynamics and noncovalent interactions.

Hydrogen / deuterium (H/D) exchange has become a popular method for characterising protein folding and binding over the last 30 years. A technique usually associated with NMR was first linked with gas chromatography mass spectrometry in 1976 by Blum *et al.* as a means of structure analysis in complex mixtures.[15] It has become a popular technique with nearly 90% of the 200 research articles being published during the last decade.[♣] Comparative studies involving exchange in both solution and the gas phase are utilised here to maximise understanding of protein structure in different environments.

1.1 Macromolecular Structures

Proteins, the building blocks of life, are large complicated molecules, comprised of linear chains of amino acids which fold into an active form. Mutations in the amino acid sequence and/or malfunctions in the folding process can result in impairment of the proteins physical function.

[♣] Figures generated from a literature search using ISI Web of Knowledge

Protein structure can be classified into four categories[16] (Figure 1-1):

a) *Primary structure*. The fundamental constituents of proteins. Amino acids, are linked together in a specific order by peptide bonds to form an unbranched polypeptide chain.

b) *Secondary structure*. Hydrogen bonds (Section 1.1.1.3) form between the carbonyl oxygen on –C=O**:** and the amide hydrogen of –(**H**)N- of the peptide backbone to form an α-helix (spiral structure comprising 3.6 amino acid residues per turn) or β-sheet (a flat zigzagging sheet where the sequence can run in a parallel (depicted in Figure 1-1) or antiparallel fashion. The α-helix is often amphipathic with one side of the molecule being predominantly hydrophobic and the other hydrophilic. A classic example of an α-helical peptide is melittin.[4]

c) *Tertiary structure*. The side chains of the amino acids assist the coalescence of secondary structure(s) to form features such as a β-barrels. Many cytosolic proteins, including CypA[17] possess a hydrophobic core with hydrophilic residues predominantly at the surface. Alternatively, in the case of fibrous proteins such as keratins, multiple helices intertwine to form filaments up to 10nm in diameter.[18]

d) *Quaternary structure*. Discrete domains/monomeric proteins can form multimeric noncovalent complexes. This provides the final level of protein structure. Perhaps one of the most intricately studied proteins over the last 40 years is the tetramer haemoglobin comprising 2 α- and 2 β-subunits.[19]

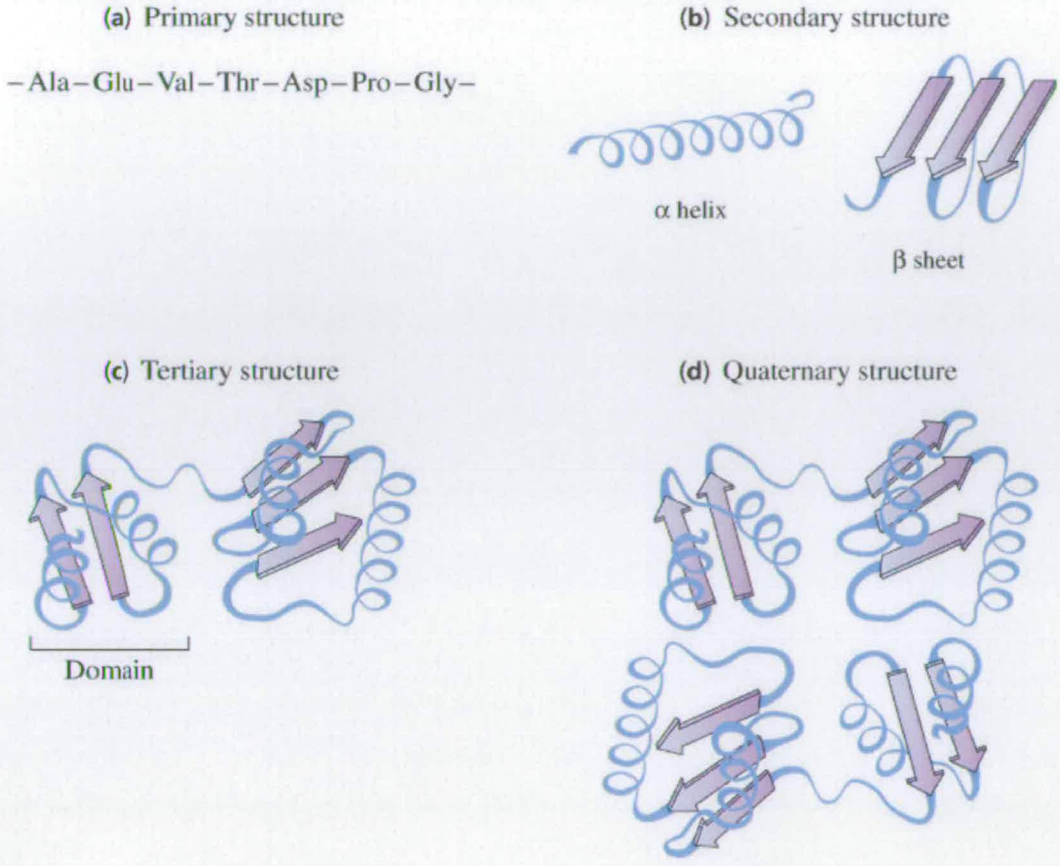

Figure 1-1 Illustrations of the different levels of protein structure♠

1.1.1 Noncovalence in Biomolecules

Noncovalent interactions in biomolecules are essential for two functions: 1) they stabilise protein structure, ensuring molecular recognition and 2) they facilitate biochemical reactions by lowering activation energies. They comprise charge-charge; dipolar; dispersion and steric inter- and intramolecular interactions at the atomic and molecular level.[20] The three types of noncovalent bond are a) electrostatic forces, b) nonpolar or hydrophobic interactions and c) hydrogen bonds.

♠ Illustration reproduced from Sally Shirran, PhD Thesis 2005

1.1.1.1 Nonbonding Electrostatic Potentials

These consist of long range (electrostatic) and medium range interactions (polar), which are both dependent on the polarisability of the solvent. The overall electrostatic potential (V_e) is dependent on Coulomb's law (Equation 1-1). Therefore if the atoms are of an opposite charge, the closer they become, the lower the energy is and the more favourable the interaction.[20]

$$V_e = \frac{Z_1 Z_2 e^2}{Dr}$$

V_e = Electrostatic potential
Z_1 and Z_2 = Unit charges
D = Dielectric constant
r = Distance between atoms
e = Charge of a proton 1.602×10^{-19} C

Equation 1-1

Molecules situated in close proximity containing atoms or functional groups of opposite signs, may form salt bridges due to electrostatic interactions.[21] These are especially significant when molecules are in a liquid.

The dielectric constant of water is 78.9 and ranges from 2 - 4 within a protein. Functional groups on individual amino acids exhibit specific dielectric constants which are influenced both by properties of the surrounding functional groups within the molecule and solvent interface.[16] For example electronegative groups such as nitrogen, oxygen and sulphur will interact favourably with a nearby proton from an amino or hydroxyl group further along the protein or in the solvent environment.

1.1.1.2 Nonpolar (Hydrophobic) Interactions

Nonpolar interactions are proportional to dipole moments (μ), and are weaker than electrostatic forces. A potential (V_{dd}) between two dipoles is calculated using Equations 1-2 as a function of distance (r); the dielectric constant (D); orientation (parallel or antiparallel) and whether they lie **a)** side by side or **b)** end to end.

a) $$V_{dd} = \frac{\pm|\mu_1|\cdot|\mu_2|}{D|r|^3}$$

(+) parallel
(-) antiparallel

b) $$V_{dd} = \frac{\pm 2\,|\mu_1|\cdot|\mu_2|}{D|r|^3}$$

(+) antiparallel
(-) parallel

Equations 1-2

Van der Waals forces originate from induced dipole moments, proportional to the number of polarisable electrons in each interacting group. For example the dipole moment of an electron dense aromatic ring will experience a fluctuating slight negative charge on one side. This may interact with the positive side of another aromatic ring and so on to achieve π stacking.

1.1.1.3 Hydrogen Bonding

H-bonds occur when two electronegative atoms compete for the same hydrogen atom. A given hydrogen atom covalently bonded to one hetero atom may have a strong affinity with another electronegative atom situated in close proximity. The dipole of the covalent bond skews the energy leaving the hydrogen with a slight positive charge and therefore able to interact with another atom bearing a slight negative charge. In strong H-bonds however, the second atom may transfer a lone pair of electrons, a phenomenon most frequently seen with oxygen. The strength of the H-bond is typically 10-40 kJ mol^{-1} and its length 2.70-2.90 Å compared to an average 463 kJ mol^{-1} and 1.03 Å in –O-H.[22,23]

Watson and Crick recognised the importance of hydrogen bonding in macromolecules when they unveiled their DNA double helix in 1953. In their structure each base pair (G-C and A-T) were joined by two H-bonds. It was Pauling however who realised the importance of H-bonds in conferring global stability on the structure when he established the presence and necessity of a third H-bond across the G-C coupling in 1956.[24]

The stability of H-bonds can be calculated using data obtained from thermodynamic reactions designed to estimate the enthalpy of bond formation. These measurements can be used to understand protein folding and protein - ligand binding for structural prediction and drug design.[25]

1.1.2 Does a Gas Phase Conformation Reflect that in Solution?

Several factors alter the importance of noncovalent interactions to protein conformation following transfer into the solvent free environment of the mass spectrometer:

1) The removal of solvent (usually water) means that internal hydrogen bonds no longer have to compete with those formed with surrounding water molecules. As a consequence H-bonds that exist between a protein and a ligand are strengthened.
2) Removal of water weakens hydrophobic interactions which are often key to the stabilisation of a given native fold. Disturbing hydrogen bonding networks, either due to weakening of some bonds or the strengthening of others (point 1 above) can result in significant conformational changes.
3) Electrostatic interactions are strengthened by a factor of up to 80, (ε_0 becomes 1) see Equation 1-1 above.
4) A final consequence of transfer into the gas phase is that if a noncovalent bond is broken in a solvent free environment, it will not generally reform.

Despite these facts, methodology employed in Chapter 3 works on the assumption that noncovalent interactions of protein-ligand complexes in the solution phase are not compromised by the ESI process. Many research groups have employed a plethora of methods to try to understand if protein structure can be perfectly preserved from solution to the gas-phase.

For example, studies by Alpin *et al.*[26] produced conflicting data whereby solution based competitive elastase bio-assays were not reproduced using ESI-MS. Non-specific interactions of substrates were found to occur during the desolvation process. However, experiments on large macromolecular protein complexes involving metal ions by Robinson and co-workers[27] show specific binding comprising electrostatic and hydrophobic interactions. They were able to infer close comparisons between these data and native solution structures.

Williams and co-workers[28] showed the retention of lysozyme conformers akin to those found in solution along with unfolding events that occur in the gas phase. Current developments in ion mobility coupled with mass spectrometry (IMMS) provide a means of separating different conformers by measuring collisional cross sections. Koerniger *et al.*[29] assigned specific charge states of ubiquitin with conformational states, assumed to be found in solution. Loo *et al.*[30] used collision activated dissociation (CAD) to demonstrate the retention of a hydrogen bond on a looped peptide. Barran *et al.*[31] went one step further using multiple gas phase MS techniques (ion-mobility, collision induced dissociation (CID), electron capture dissociation (ECD)), to successfully map the secondary structure of small biologically relevant peptide systems (gonadotropin releasing hormones and defensins). Freitas *et al.*[32] used gas phase HDX of ubiquitin to assign specific conformers to charge states and Clemmer and co-workers[33] used HDX coupled to IMMS on cytochrome C for temperature dependent studies on conformers.

1.1.3 Structure – Activity Relationships (SAR)

Small scale and / or preliminary drug design typically follows a strategy for determining structure-activity relationships (SAR) via biophysical assays. Performing such assays on a series of compounds provides a preliminary rank order of efficacy whether the method employed is, for example, high-throughput mass spectrometry (MS) screening or fluorescence bioassays. Grouping the candidate compounds together in relation to their functional groups, hydrophobicity, solubility and steric properties based on this order enables characterisation of the desirable

properties for a candidate drug.[34] Computer aided drug design and informatics are frequently employed to aid the process eliminating substructures before the first hurdle and can even predict toxicological effects and binding affinities.[35]

In this thesis the preliminary screen for single ligand binding to CypA is performed with mass spectrometry. A similar approach was adopted for multiple ligand binding to the FK506 binding protein (FKBP) using NMR by Fesik and co-workers.[36] This required cross-linking two ligands. Each potential compound required both individual and paired testing before obtaining the optimal ligand-ligand compound.

1.1.3.1 Environmental Influences

The solvent environment plays a critical role to protein-ligand interactions. Consequently, an MS based screen may not be a true representation of binding in solution phase. Electrostatic forces are increased in the gas phase due to the lack of solvent screening. For the same reason, hydrophobic interactions weaken. In the gas phase with no external polar solvent creating dipole moments, hydrophobic interactions are significantly reduced.

1.2 Protein Systems

1.2.1 Melittin

Melittin is a 26 amino acid peptide which is the major component of honey bee (*Apis Mellifera)* venom. The amphipathic properties of this peptide enable violation of cell membranes leading to cell lysis.[4,37,38] Studies have shown melittin to possess anti-viral properties against murine retroviruses,[39] tobacco mosaic virus[40] and herpes simplex.[41] There is also evidence of its ability to suppress HIV-1 replication.[40] Many studies have been performed on melittin to ascertain its structure in various environments and a summary of relevant literature can be found in Appendix B.

The ability of melittin to adopt different conformations under apolar and aqueous conditions is key to its biological behaviour. It can be manipulated to switch between

random coil and α-helical conformations simply by changing the solvent environment. This is largely due to its amphipathic nature possessing both large hydrophobic and hydrophilic regions (Figure 1-2).

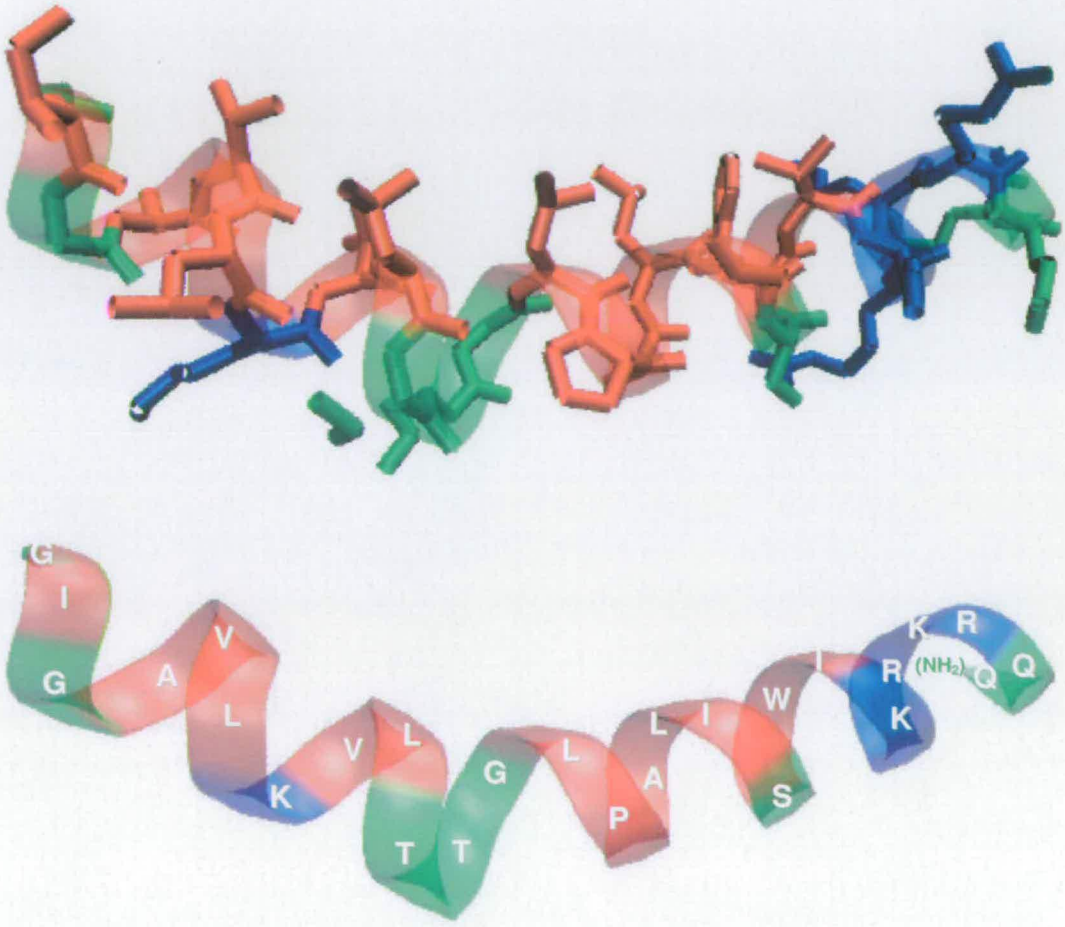

Figure 1-2 Melittin in helical formation derived from an NMR dimer structure[4] (residues: red (non-polar); green (polar); blue (basic))

Exactly how melittin penetrates a lipid-bilayer is still open to question. Studies by Bernèche *et al.*[42] found strong agreement between helical conformations found with both crystallographic[38] and NMR[43] techniques. Molecular dynamic simulations of melittin determined that residue Lys-7 located in the hydrophobic moiety of the helix forms H-bonds with the hydrophilic end of lipid chains, anchoring the chain parallel to the bilayer. Further simulations suggested the charged and polar C-terminal region

comprising Lys-23 – Arg-24 – Gln-25 exhibits a strong interaction with the polar heads of the lipids, further anchoring the peptide to the membrane. The plethora of water molecules at the membrane interface results in a disruption of the α-helix at the basic C-terminus. The relative hydrophobic character of the N-terminus is consistent with a stable helix embedded in the upper lipid layer. This is further backed up by circular dichroism (CD) studies by Vogel who postulated that as much as 72% of the membrane bound melittin is helical.[44]

Crystal studies by Terwilliger *et al.*[45] show that high salt concentrations induce the formation of two planes of dimers to form hydrophilic tetramers. They hypothesize that one layer emulates the surface of a lipid membrane and the other the interaction of the melittin dimer. In turn dimer formation due to an association of the termini, may mimic the interaction of melittin with phospholipid headgroups in a membrane. Bachar and Becker[46] and Hristova *et al.*[47] performed molecular dynamics using Terwilliger's co-ordinates and ascertained that one helix on its own is ineffectual for global perturbation of a lipid bilayer and multiple peptides were necessary and also that orientation of the peptide assembly and the depth of penetration is concentration dependent.

Fluorescence studies by Raghuraman and Chattopadhyay[48] used 7-nitrobenz-2-oxa-1,3-diazol-4-yl (NBD) labelled Gly-1 and Lys-7 to investigate the orientation of melittin in negatively charged membranes containing chloresterol, having already established that orientation and depth are dependent on peptide concentration, temperature and lipid composition (Figure 1-3). Conclusions regarding which conformation is adopted and when, is still unclear in this model.

Melittin provides a good model to understand the mechanism by which α-helical peptides cross cell membranes. Findings from the studies referred to above suggest melittin shows similarities to apolipoproteins and peptide hormones,[49,50] signal peptides[51] and the envelope glycoprotein gp41 from HIV. In the latter case there is evidence that melittin mimics the N-terminus of HIV-1 virulence factor Nef1-25.[52,53]

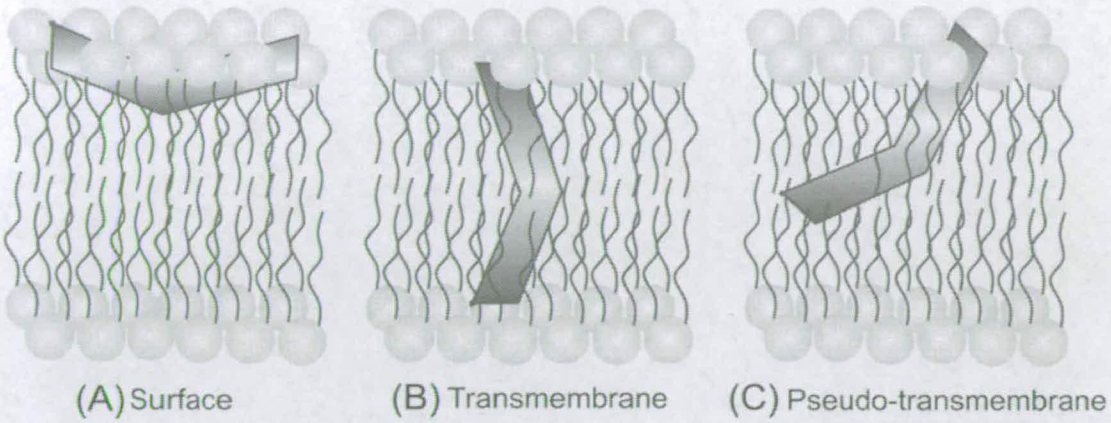

Figure 1-3 Possible melittin orientations within a membrane lipid bilayer[♣]

1.2.2 Cyclophilin A (CypA)

1.2.2.1 The Immunophilins

The T-lymphocyte antigen (Ag) activation cascade which ultimately results in the transcription of cytokines such as interleukin – 2 (IL-2) is regulated by the presence of a cytosolic peptidyl prolyl isomerase (PPIase) family, the immunophilins. The cyclophilins (Cyp), FK506 binding proteins (FKBPs) and parvulins are enzymes involved in the regulation of protein folding and transport and are often found as part of much larger proteins such as nuclear pore complexes.[54,55,56] There are four different members of the Cyp family A, B, C and D of which CypA is studied here.

Although structurally very different, Cyp proteins do have a homologous domain with FKBP. The residues of this common domain are located in several unrelated regions: Tyr-48 and Phe-53 are located in the hydrophobic core; Tyr-79 is found on the surface; and Phe-60 is linked with the active site known to bind cyclosporin A (CsA).[57] This site, commonly referred to as the CsA binding pocket, has been well characterised using x-ray crystallography and NMR[17,58,59,60] and is discussed in Section 1.2.2.4.

[♣] Figure reproduced from reference 48

The rate limiting step of protein folding is determined by the conversion of *cis*-prolines to the *trans* conformation. CypA catalyses this process, and is known as a isomerase enzyme. Arg 55 plays a major role in the peptidyl-prolyl *cis / trans* isomerase activity of CypA.[61] This PPIase activity indirectly increases the rate of protein folding by reducing the energy required for *cis-trans* isomeration of proline imidic peptide and protein bonds (Figure 1-4).[62,63,64]

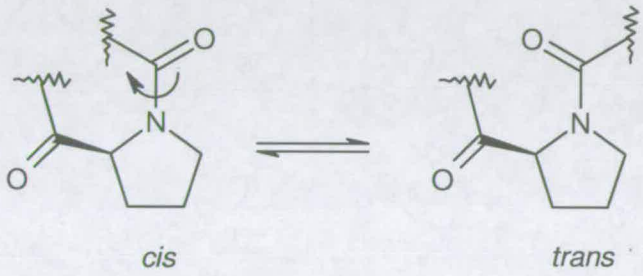

Figure 1-4 Cis/trans isomerisation of the Xaa-Pro bond, where Xaa refers to any amino acid.

Nematodes and other free living parasites express large families of cyclophilins. Research has shown these to be involved with exoskeleton / cuticle synthesis. By blocking the cyclophilin activity, misfolding of skeletal proteins can occur causing the production of mutant worms which cannot reproduce.[65]

1.2.2.2 The Immune Response Cascade

CypA has been identified as the target for cyclosporin A (CsA), a natural inhibitor produced as a metabolite by the fungus *Tolypoclodium inflatum*.[66] The resulting CypA-CsA complex, binds to the secondary target calcineurin (calcium/calmodulin dependent serine/threonine protein phosphatase (CN)) blocking its phophatase activity[54,67] (Figure 1-5). During T-cell activation calmodulin (CaM) binds to CN. The complex dephosphorylates the nuclear factor of activating T-cells (NF-AT) which then enters the nucleus and activates transcription of Interleuken 2 (IL-2). The CypA-CsA complex also binds to the CaM-CN complex, preventing dephosphorylation of NF-AT.[54]

The primary interaction in the CypA-CsA complex involves residues 9, 10, 11, 1, 2, 3 of CsA, and alters the ligand structure from that found for the free ligand in solution.[54] Of course the initial conformation of CsA will dependent on solvent composition, when incorporated as part of the CypA-CsA complex, it adopts a form resembling that found in an organic apolar solvent.[17] The remaining residues are available for secondary interaction with calcineurin via the exposed hydrophobic regions.[17] The ultimate effect of this two stage complex is phosphatase inhibition and a halt in the cytokine expression leading to immunosuppression (Figure 1-5).

Due to the biological significance of CypA, much effort has been directed into finding ligands which will act as alternatives to CsA and inhibit CypA isomerase activity without blocking the immuno-response cascade. Potential ligands being studied at the moment with these characteristics are NIM811[68] and sanglifehrin A.[69]

1.2.2.3 CypA and Viral Proliferation - HIV

The activity of CypA has clinical relevance to the replication of the viral protein R (Vpr) in human immunodeficiency virus, type 1 (HIV-1).

Recent studies have shown Vpr to be involved in the induction of G(2) host cell cycle arrest and the transport of the pre-integration complex into the cell nucleus. The N-terminus of Vpr has a highly conserved proline rich region, in which two of the four prolines, show a preference for the *cis* imidic bond conformation.[70] Interaction with a host PPIase such as CypA is imperative for *cis / trans* isomeration of the Vpr prolines. As a result, CypA binds to HIV-1 capsid protein (CA) enabling it to avoid recognition by inhibitory host factors such as Ref-1 (regulator of fusion protein), thus facilitating infection.[71]

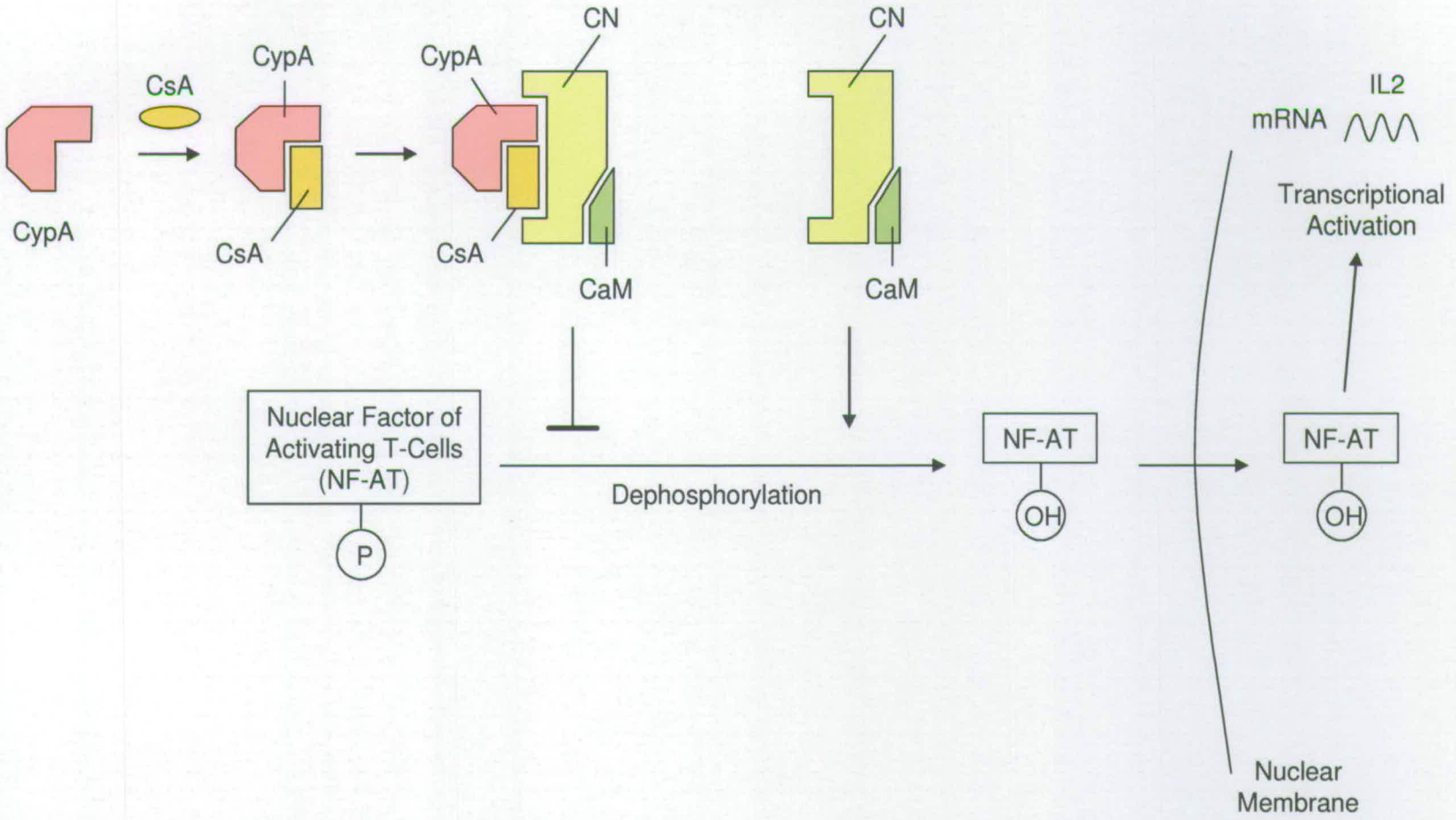

Figure 1-5 The role of CypA in the T-lymphocyte antigen cascade.

1.2.2.4 Structural Studies on CypA

NMR has been employed to map the hydrophobic core of CypA comprising 2 α-helices and 8 β-strands where numerous aromatic residues reside.[57] The CsA binding site of this isomerase is well characterised and has been studied extensively by Walkinshaw and co-workers amongst others using x-ray crystallography and NMR as complimentary techniques.[17,58,59,60] Studies by x-ray crystallography have revealed up to 5 water molecules as crucial for CypA-CsA complex formation[17,58] (shown as green spheres in Figure 1-6. More recent thermodynamic calculations performed by Li and Lizaridis[72] found evidence suggesting the presence of 4 water molecules at the CypA-CsA binding interface, no evidence for these is found in the gas phase complex.[73]

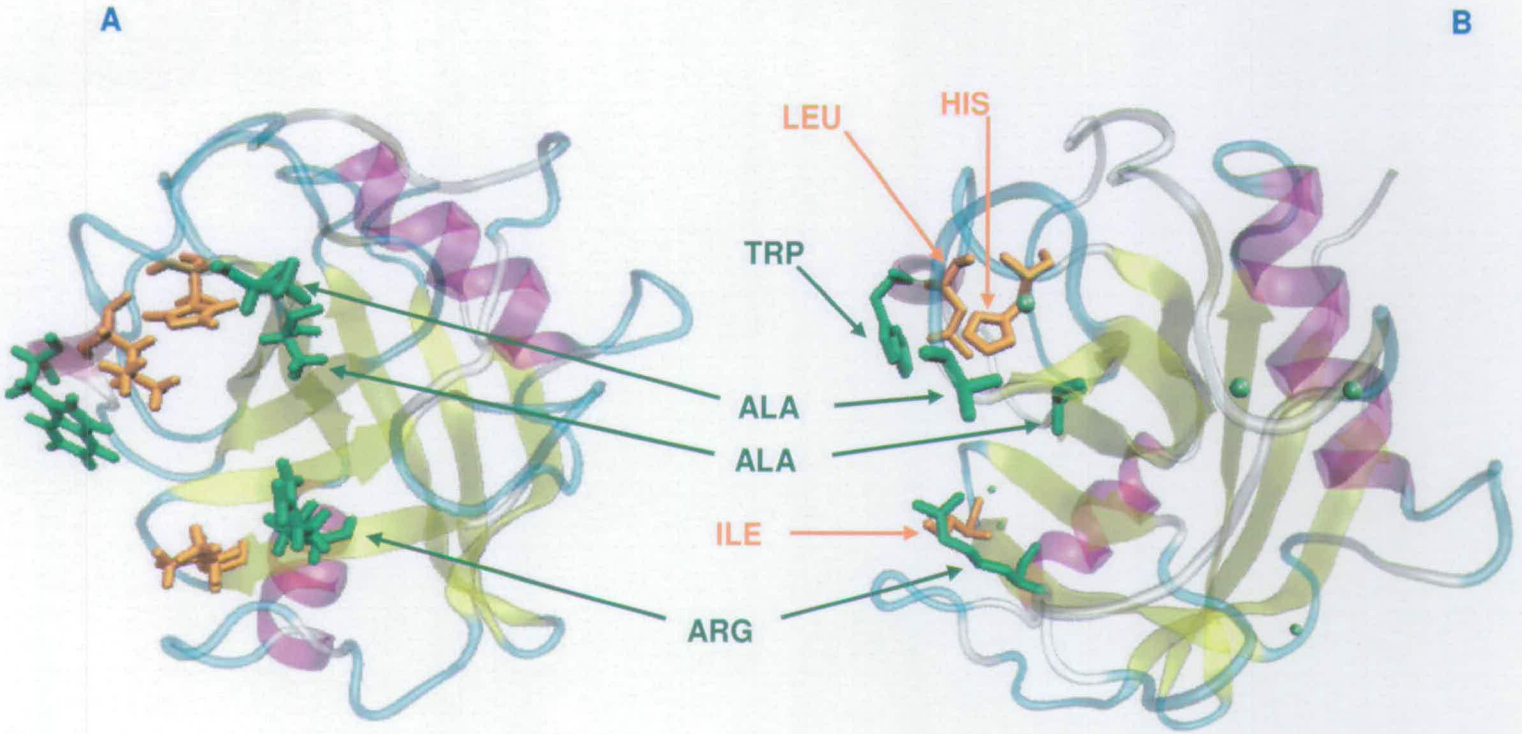

Figure 1-6 Structural conformers of CypA observed when (A) unbound[74] and (B) bound[17] to CsA (not shown) with residues initiating the docking depicted in green and residues associating with specific CsA side chains in orange (including Arg-55 and Trp-121)

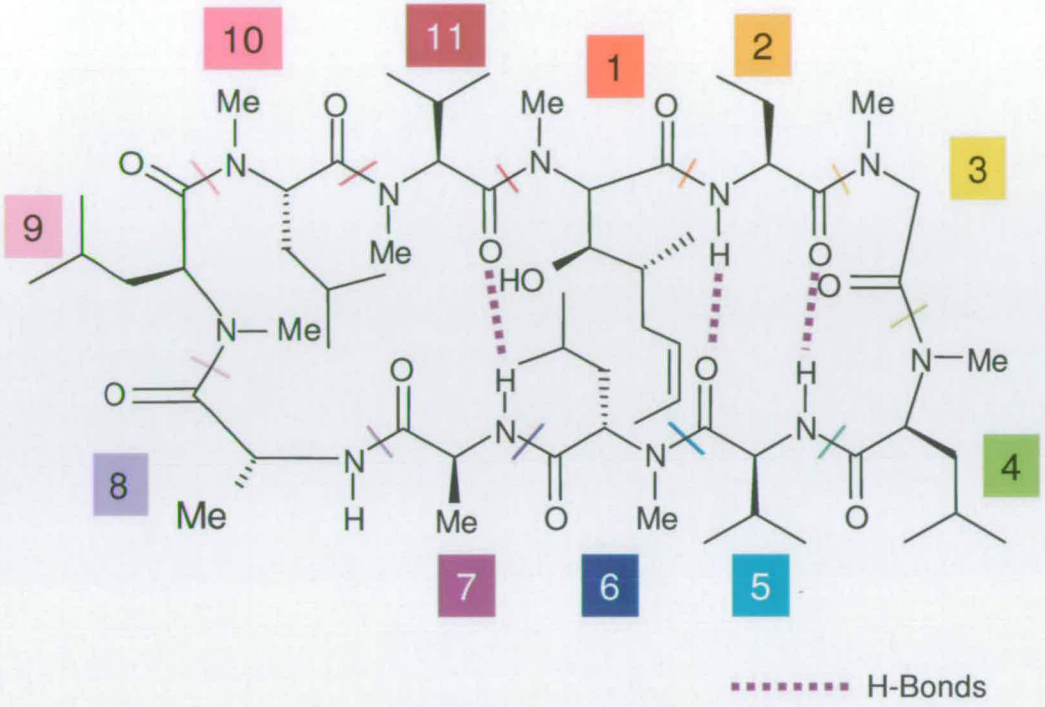

1. 4R-4[(E)-2-butenyl]-4,N-dimethyl-L-threonine (MeBmt); 2. L-α-Aminobutyric acid (Abu); 3. Sarcosine (Sar); 4. Leucine (Leu); 5. Valine (Val), 6. N-Methylleucine (MeLeu); 7. Alanine (Ala); 8. D-Ala; 9. MeLeu; 10. MeLeu; 11. N-Methylvaline (MeVal). Sequence mass 1202.68Da.

Figure 1-7 Illustration of CsA in apolar conditions which induces the structural change required for the CypA-CsA complex

Docking of CsA is initiated by interactions from the CypA residues Arg-55, Ala-101, Ala-103 and Trp-121 with subsequent interactions to CsA sidechains occurring with Arg-55, Ile-57, Leu-122 and His-126.[58]

Trp-121 was identified as a vital residue for CsA binding using fluorescence as early as 1984 by Handschumacher *et al*[77] and this was re-iterated 6 years later by Harrison and Stein.[78] NMR studies have also been utilised to establish the role of Trp-121 by Armitage and co-workers[75] and Fesik *et al.*[79] This interaction was further specified by Walkinshaw and co-workers[58] as being due to an H-bond which forms between Trp-121 and the carbonyl group of MeLeu-9 of CsA.

1.3 Macromolecular Systems - Biological Mass Spectrometry

The first mass spectrometers (known then as spectrographs) were developed by Thomson and Aston at the turn of the 20th century to establish the existence of non-radioactive isotopes. Developments over the last century, particularly in ionisation, have enabled the analysis of increasingly larger molecules, such that it is now routine to use them to analyse proteins and other biological macromolecules.

1.3.1 Components of a Mass Spectrometer

Mass spectrometers comprise of some or all of the following components[80,81] (Figure 1-8).

1. A mechanism for sample introduction which may be direct, or involve a pre-MS sample clean up separation stage e.g. HPLC, gas chromatography (GC), flow injection analysis (FIA), capillary electrophoresis (CE);
2. An ionisation source for the generation of ions into the gas phase (section 1.3.2) e.g. atmospheric pressure ionisation (API) such as electrospray (ES), or fast atom bombardment (FAB);
3. A mass analyser (section 1.3.3) i.e. quadrupole / triple quad, time of flight (TOF), ion trap, Fourier Transform – Ion Cyclotron Resonance (FT-ICR);
4. A detector (section 1.3.4) i.e. electron multiplier, photomultiplier, multiple channel plates (MCP);
5. A processing unit.

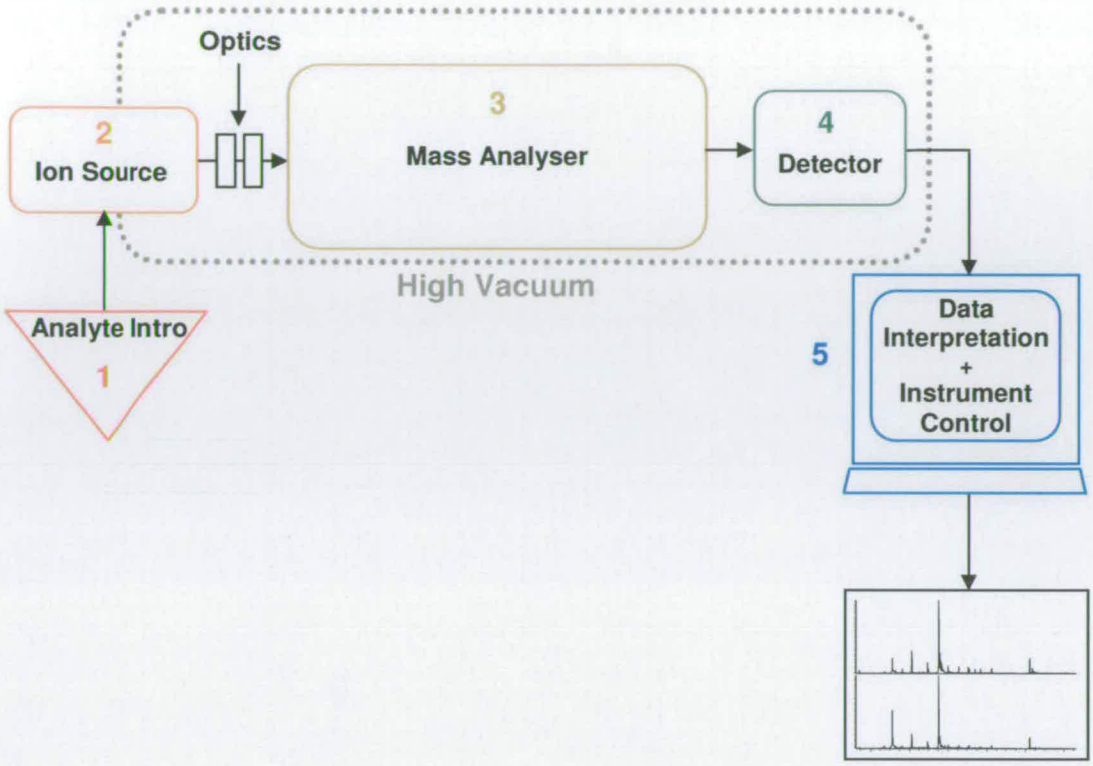

Figure 1-8 Basic components of a mass spectrometer

1.3.2 Ionisation

The most critical component in any mass spectrometer to enable successful analysis to proceed is the ionisation source. Over the last century technology has seen ionisation processes progress from techniques conducted under vacuum to solution phase and desorption approaches performed at atmosphere. The major processes are discussed briefly below:

i) *Electron Ionisation* (EI), the bombarding of volatile analyte with electrons to form radical cations. Although useful for the analysis of non polar analytes it is a high energy technique which promotes fragmentation;

ii) *Fast Atom Bombardment* (FAB) generates ions by bombarding a solid matrix / analyte mix with a fast particle beam of an inert gas such as Argon or Xenon;[82]

Two common types of ESI sources are utilised in this thesis. Ions can be generated in a direct line of sight of the z-axis of the mass spectrometer i.e. on axis (see 2 below) or off axis a so called Z-spay source.

1) The Z-spray ion source designed by Micromass (Figure 1-10) works under the same principle as an on-axis source stack. N_2 desolvation and nebulising gas is introduced co-axially to the analyte spray with a high voltage and temperature applied. A potential difference between the spray needle and the sampling cone / ion block draws the ions into the source assisted by the desolvation gas. Solvents and other contaminants of low polarity fail to be guided through the sampling cone minimising potential ion suppression.

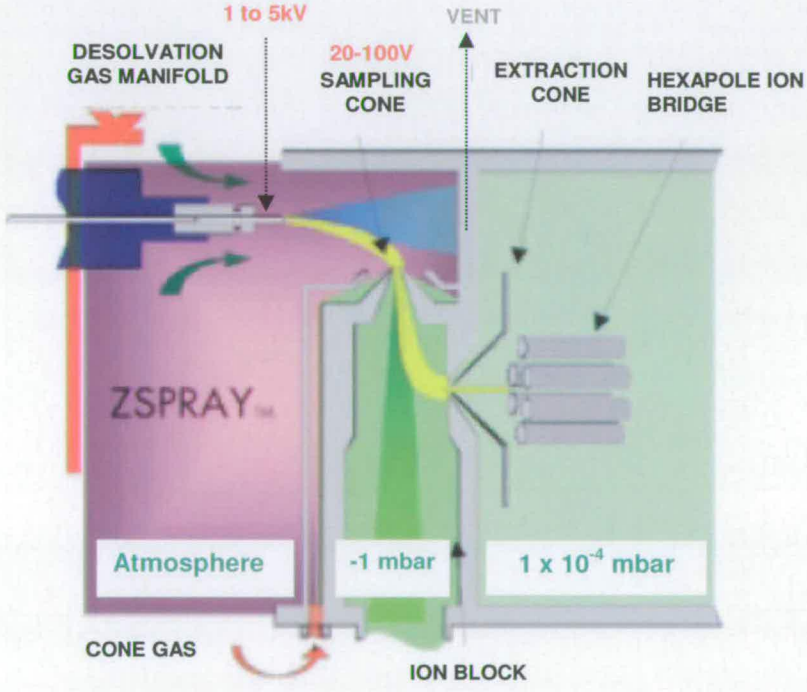

Figure 1-10 The Z-Spray ion source designed by Micromass UK as used on the QToF and ZMD Quadrupole mass spectrometer[80]

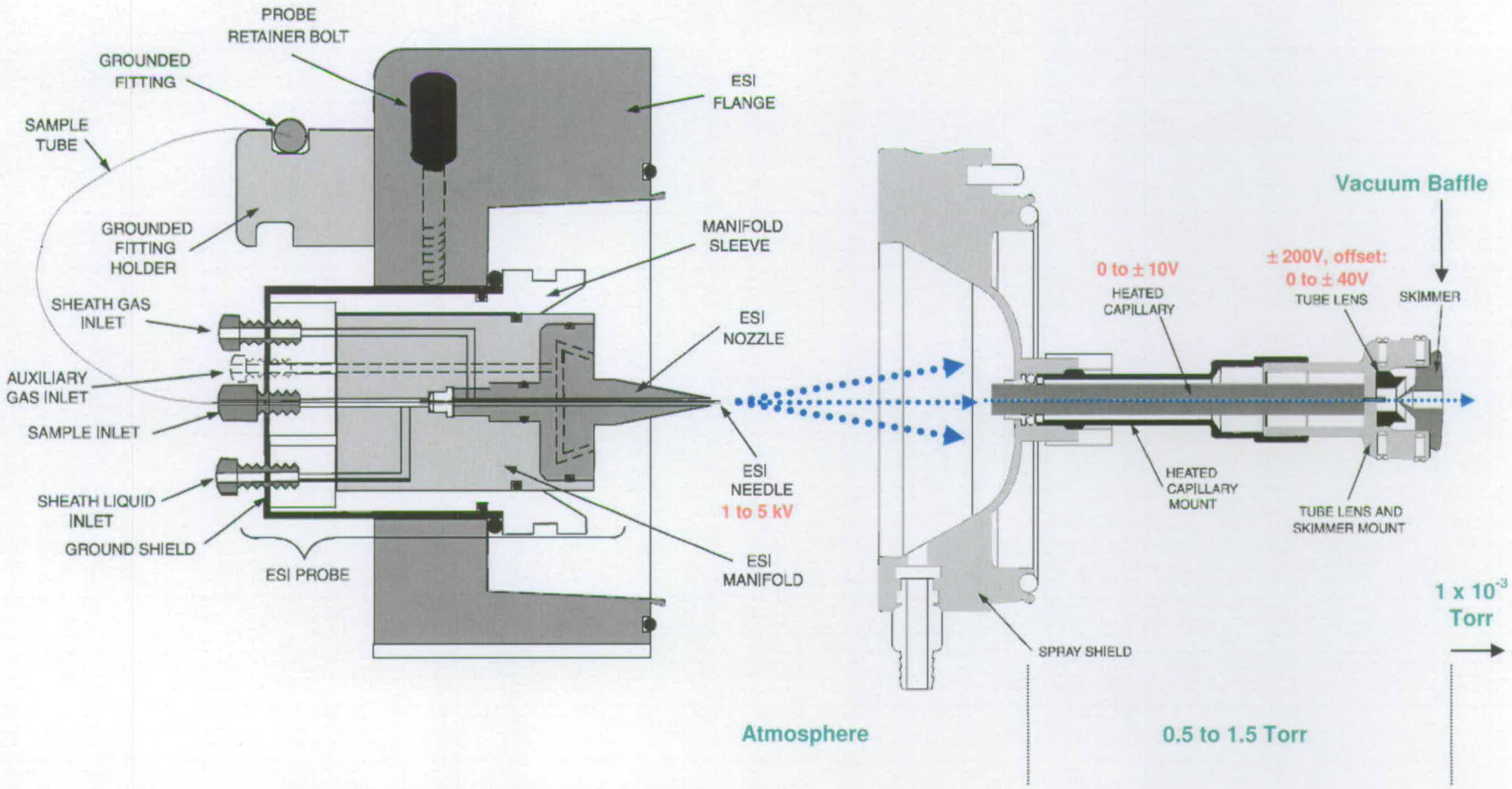

Figure 1-11 ESI stack and API source schematic of the LCQ[100]

2) Figure 1-11 illustrates the on axis ESI source of the LCQ which also has a heated capillary rather than the Z-configuration of extraction cones in the Z-spray source above. Analyte introduction is achieved via an HPLC line with coaxial desolvation using N_2 (sheath gas). A potential and pressure difference draws the droplets into the heated capillary which serves to break up any remaining clusters. The tube gate deflects incorrectly charged ions away from the opening of the skimmer which acts as a vacuum baffle into the high vacuum region.

	+ve Ion Mode	**-ve Ion Mode**
Capillary Voltage (kV)	1 to 5	-1 to -5
Principle Residues Involved	Lys; Arg	Asp; Glu
Charged Group	$-NH_3^+$	$-COO^-$
Charge State Annotation	$[M + nH]^{n+}$	$[M - nH]^{n-}$

Table 1-2 Summary of differences between +ve and –ve ion mode for molecule, M

For either type of source, typical conditions and voltages are listed in Table 1-2. Peaks detected are identified by their mass / charge ratio (*m/z*) with neighbouring peaks differing by one charge. In positive ion mode charging is achieved by the addition of *n* protons and in negative ion mode, the loss of *n* protons, where *n* denotes the charge state of the peak. The charge state and molecular mass of a macromolecule can be calculated by solving the simultaneous equations Equation 1-3Equation 1-4 below.

$$n = \frac{m' + H}{m' - m''}$$

n = charge state of m"
m' = mass of $[M + nH]^{n+}$
m" = mass of $[M + (n+1)H]^{n+1}$
m/z of m' > *m/z* of m"

Equation 1-3

$$M = n\,(m'' - H)$$

M = neutral mass of molecule

Equation 1-4

All proteins used within these studies readily protonate with the numbers of basic residues outweighing or equalling the number of acidic residues for all proteins except insulin (Table 1-3).

Protein	Basic Residues	Acidic Residues
Melittin	5	0
Insulin	2	4
Cyclophilin A	20	19
Horse Heart Myoglobin	21	21

Table 1-3 Basic and acidic residues of the proteins used within these studies

Studies by McLafferty and co-workers[32] have demonstrated the relationship between charge state and protein conformation. Figure 1-12 depicts a typical mass spectrum of horse heart myoglobin (HHM) displaying a full charge state distribution. Both holo- and apo- forms of the protein retain the heme group at lower charge states, proving that some tertiary structure is retained. As the protein unfolds, previously buried basic groups become exposed enabling further protonation. Under harsh desolvation conditions coulombic repulsion can also force the protein to open, further increasing the number of available protonation sites. The apo-protein charge states exhibit a bimodal distribution. The most abundant distribution is the high charge state envelope inferring a preference for a more unfolded form. There is also inference of a stable, partially unfolded apo- state with the second, lower charge distribution which coincides with the first detection of holo-HHM at charge state $[HHM+11H]^{11+}$.

Figure 3-3 (Chapter 3) depicts spectra obtained for CypA after incubation in ammonium acetate buffered to pHs 3.3, 6.0, 6.8 and 9.0. As the buffer becomes progressively more acidic, there is a sudden shift in the charge states from low ($[CypA + 7H]^{7+}$ to $[CypA + 9H]^{9+}$) to high ($[CypA + 10H]^{10+}$ to $[CypA + 21H]^{21+}$).

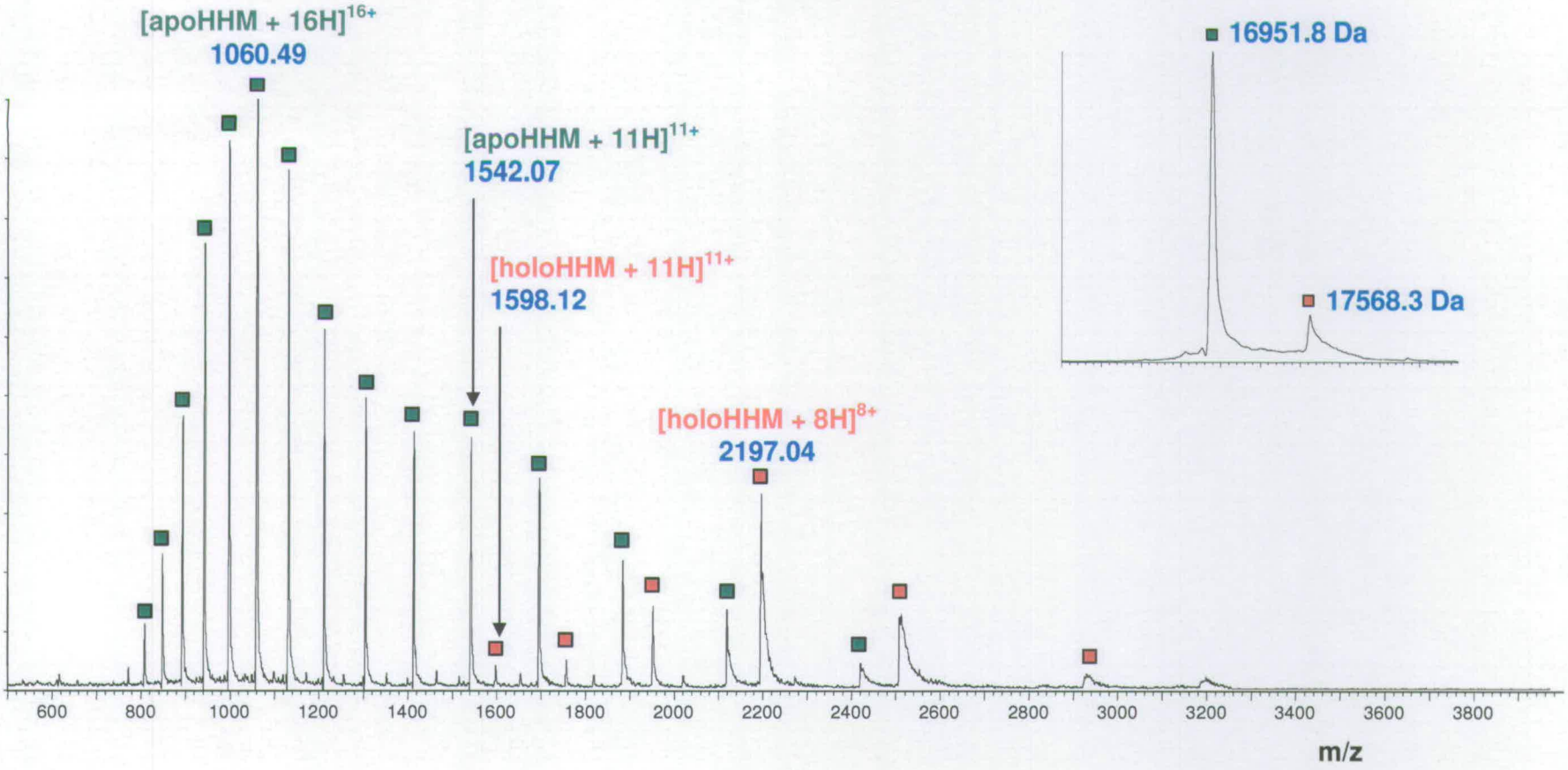

Figure 1-12 Full charge state distribution of HHM: red squares - native (holo-) HHM (+ heme); green squares – denatured (apo-) HHM (- heme); inset: deconvoluted spectrum indicating relative quantities of native (holo-) HHM and non-native (apo-) HHM

In summary under conducive conditions, noncovalent complexes can be maintained. Under these circumstances, it is assumed that there is some similarity between the solution and gas phase structures.

Nanospray (NS) ionisation utilises the same principle as electrospray. Here the flow is reduced from µl/min to nl/min. As a result the ionisation process is less destructive. The analyte is introduced via a glass needle either coated with a conductive material comprising a gold - platinum mix or uncoated with a platinum wire forming a bridge between the solution and ESI probe. Capillary action, the movement of liquid through the needle by the effects of surface tension, eliminates the need for a nebulising gas by drawing liquid out in small droplets.[101,102] The size of the initial droplets is also much smaller ensuring fewer collisions are needed to reduce the size.[103]

1.3.3 Mass Analysers

A series of lenses coupled with a potential drop focus ions from the source into the mass analyser. Several common types of mass analysers are utilised for the studies within this thesis including; single quadrupole, ion trap (LCQ), time of flight (QToF) and Fourier Transform Ion Cyclotron resonance (FT-ICR) instruments. All have differing *m/z* ranges, resolving powers and accuracies. Methods of calculating the latter two parameters are explained below.

1. Resolution (R) can be calculated in two different ways

   a) Low resolving instrumentation: *Single ion method*
      R = mass (m) / peak width at half maximum peak height (Δm)

   b) High resolving instrumentation: *Double ion method*
      R = m / difference in mass between 2 peaks with maximum 10% valley (Δmr)

2. Mass accuracy (A) can also be expressed in two different ways

   a) Low resolving instrumentation:

      A = Difference (Δm) between theroretical mass (m_{real}) and measured mass ($m_{measured}$)

   b) High resolving instrumentation:

      $A(ppm) = 10^6 \times [(m_{real} - m_{measured}) / m_{measured}]$

1.3.3.1 Quadrupole

The linear quadrupole was developed in the early 1950s by Paul and Steinwedel[104] and many instruments utilise a quadrupole for parent ion mass scanning and selection. Quadrupoles are easily coupled to an LC interface and can scan over a fairly wide m/z range (10 to 4000 A.M.U.) with good accuracy (0.1 to 0.2 A.M.U.) and resolution at high speed scanning rates (up to 5000 A.M.U. per second). They also lend themselves to rapid switching of voltages enabling the study of both positive and negative ions. Aligning 2 or more quadrupoles enables secondary ion monitoring and the ability to fragment selected ions (see tandem MS Section 1.4).

A quadrupole mass analyzer, as its name suggests, comprises 2 pairs of metal rods. An rf (radio frequency) current with a constant +/- dc (direct current) offset oscillates between two pairs of rods where one set is positive and the other negative (Figure 1-13). Equation 1-5 expresses the relationship between the dc offset voltage (V_{dc}), the zero to peak rf voltage (V) and the angular rf frequency (ω) with time (t) with the applied potential of the rods (Φ_0).

$$\Phi_0 = (V_{dc} + V \cos \omega t) \quad \text{and} \quad -\Phi_0 = -(V_{dc} + V \cos \omega t)$$

Equation 1-5

The potential at any given point between the rods ($\Phi_{x,y}$) is therefore related to the applied potential (Φ_0), the radius between the rods (r_0) (Figure 1-14) and the distances x and y from the centre of the field (Equation 1-6) (z by convention is the ion axis).

$$\Phi_{(x,y)} = \Phi_0 \frac{x^2 - y^2}{r_0^2}$$

Equation 1-6

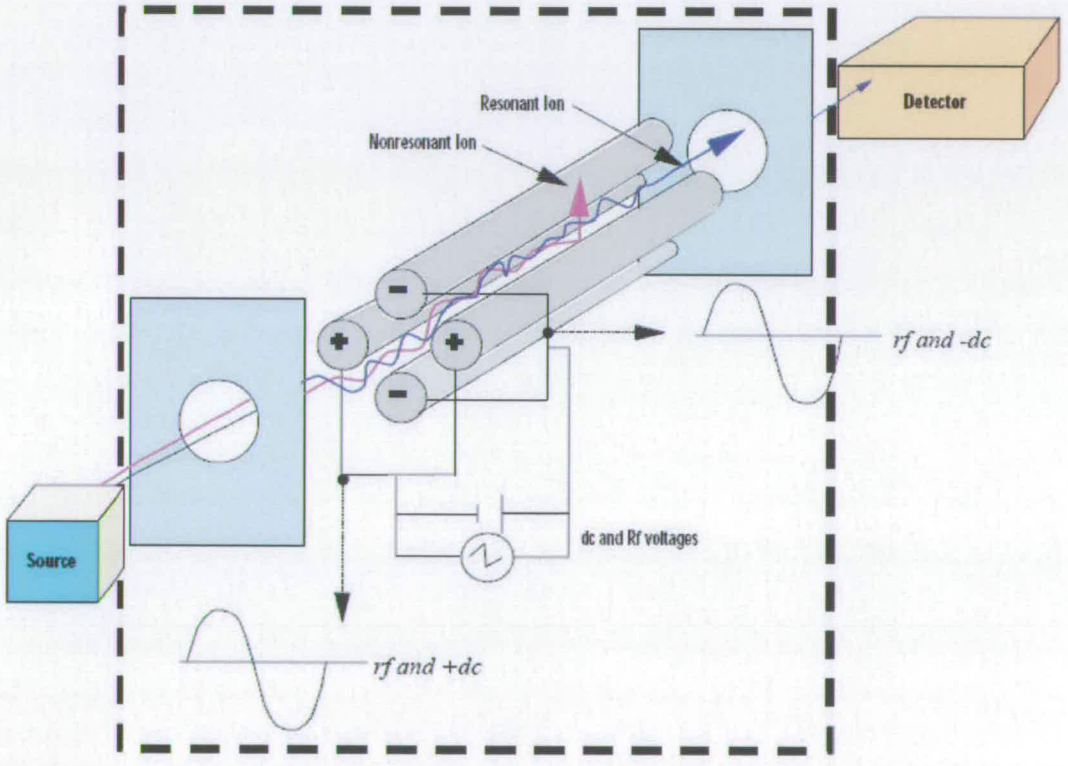

Figure 1-13 Quadrople Mass Analyzer[80]

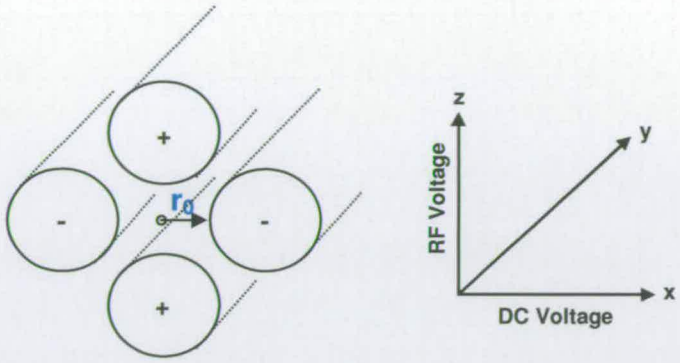

Figure 1-14 Description of axes which voltages act within a quadrupole

Ions at a given *m/z* will resonate at a specific rf / dc ratio and pass through the quadrupole. Other ions will be destabilised and hit the rods. The longer the ions spend in the quadrupole assembly, the better the ability to separate ions close in *m/z* and increase resolution. The life-time of an ion from its formation in the source to its detection is typically 50-100 μs.[80]

The current voltages can be set to enable ions of a single *m/z* value to pass through, enabling single ion monitoring (SIM) or scanning over a large mass range. SIM improves sensitivity with regards to a specific ion or fragment by increasing the time devoted to its detection. By ramping the amplitude of rf and dc voltages whilst keeping the ratio constant, a scan mode can be implemented. i.e. a low dc corresponds to scanning low mass ions and high dc, to larger ions.

Rod assemblies such as quadrupoles, hexapoles or octapoles with only rf voltages can be used as ion guides. This feature is often utilised for transfer optics between the ion source and analyser regions. For example the QToF has a single hexapole whereas the LCQ ion trap optics region comprises 2 octapoles.

1.3.3.2 The Quadrupole Ion Trap (QIT)

The quadrupole ion trap (QIT) was developed by Paul[104] in parallel with the linear quadrupole. QITs differ from quadrupoles, which accept a continuous ion beam, by requiring ions to be pulsed into the trapping region. This is because these are ion storage devices.

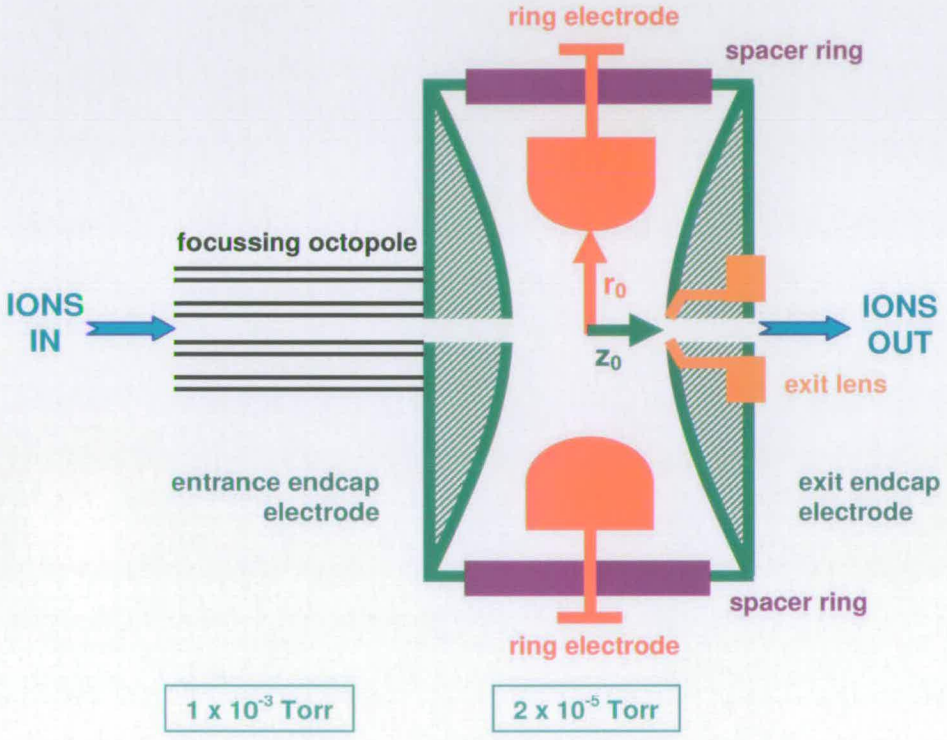

Figure 1-15 Cross section of a quadrupole ion trap

The QIT (Figure 1-15) comprises a doughnut-shaped ring electrode and two end-cap electrodes which allow ions in and out of the trap. The distances r_0 and z_0 are related in that $r_0^2 = 2z_0^2$. As with the linear quadrupole, ramping the dc (V_{dc}) and ac (rf) voltages enables ions with a broad *m/z* range to be held within the trap electrodes. Increasing the amplitude of these parameters along with the frequency of the rf signal (ω) results in ions becoming sequentially unstable. The stability axis is denoted as the dimensionless value q_z which is proportional to the rf voltage (Equation 1-7) and a_z which is directly proportional to the dc voltage (Equation 1-8). Ions are ejected in

the z direction as they reach instability levels. Ion stability levels can be predicted using the Mathieu stability diagram (Figure 1-16) where resolution depends on the a/q ratio.[104]

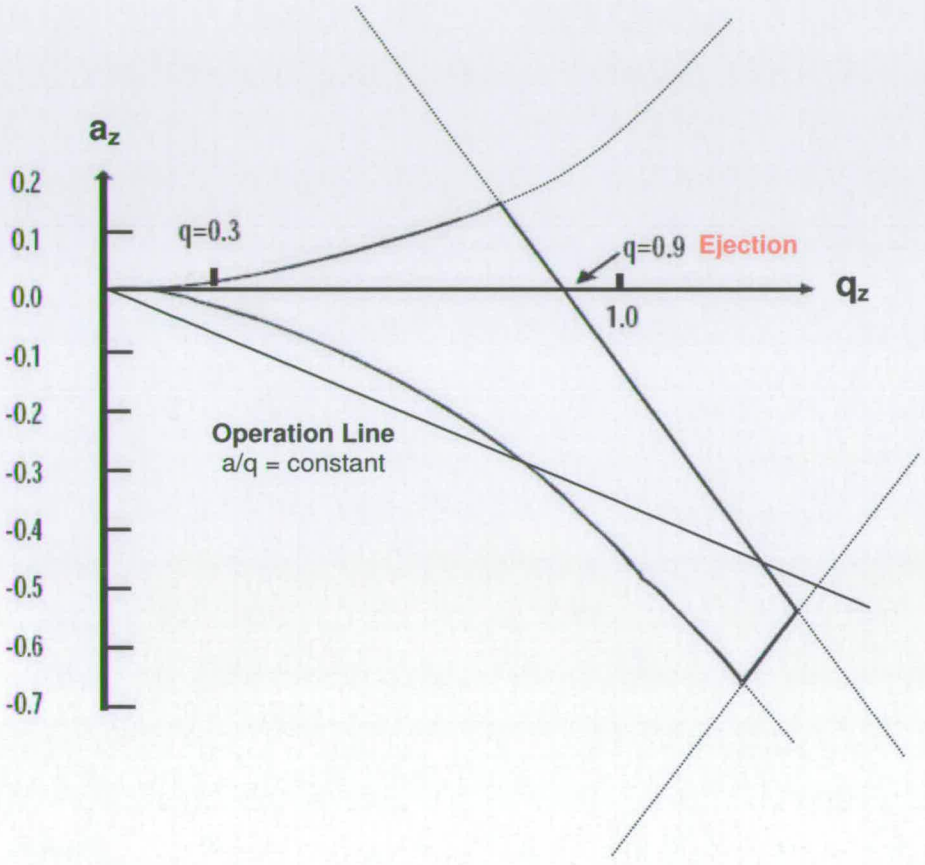

Figure 1-16 Mathieu stability diagram with the q_z axis dictating the point at which ions become unstable and subsequently ejected from the trap

$$q_z = \frac{8\,e\,RF}{m(r_0^2 + 2z_0^2)\omega^2}$$

e = charge = z
m = mass
r_0 = radius of ring electrode
z_0 = radius of end-cap electrodes
ω = rf frequency
RF = rf voltage

Equation 1-7

$$a_z = \frac{16\,e\,DC}{m(r_0^2 + 2z_0^2)\omega^2}$$

where DC = dc voltage

Equation 1-8

Ions are scanned into the trap by changing the rf voltage across the end plates. The frequency is dropped to zero allowing the ions to be propelled into the trap. To prevent the ions flying straight through or hitting the exit endcap electrode the dampening gas helium (He) acts as an energy buffer. Analyte ions collide with controlled levels of He which absorbs their excess kinetic energy, drastically reducing their velocity and focussing them into the centre of the trap.[105] Ions must be retained within the stability region which relates directly to the arbitrary q_z axis.[106] Ions are exit the QIT by the application of an rf ramp, causing the trajectories to become unstable.

1.3.3.3 Quadrapole Time of Flight (ToF)

Ions exit the source and are focussed into the quadrupole using an rf lens. The quadrupole analyser, used in scanning or SIM mode, transfers ions into another hexapole, the collision cell, where CID may take place (see Section 1.4, tandem MS) prior to being focussed into the ToF tube and detected.

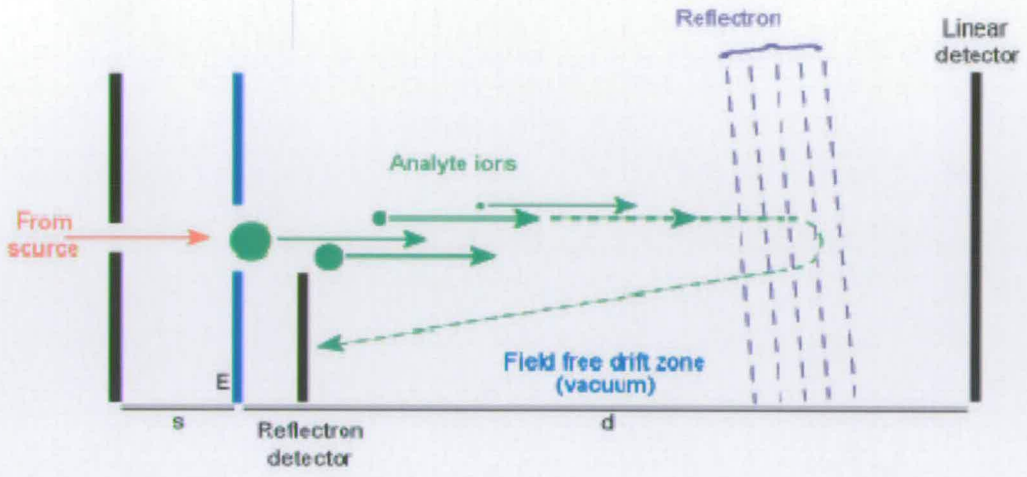

Figure 1-17 Schematic of the ToF[107]

The ToF itself (Figure 1-17) comprises a field free drift tube into which the ions are accelerated at a high voltage. They are then separable by their constant velocities in the field free region, which are inversely proportional to their *m/z* (Equation 1-9). Consequently each *m/z* has its own time of flight from source to detector (Equation 1-10).

$$v = \left(\frac{2zeV}{m}\right)^{1/2}$$

$v =$ velocity
$m =$ mass
$zeV =$ kinetic energy where
z = charge on ion
e = charge of an electron
V = accelerating potential

Equation 1-9

$$t = \frac{L}{v} = L\left(\frac{m}{2zeV}\right)^{1/2}$$

$t =$ time
$L =$ tube length

Equation 1-10

Extending the length of time ions spend in the tube and correcting any differences in kinetic energy improves resolution. In the 1970's Mamyrin[108] developed the use of an electrostatic mirror which has the effect of lengthening the flight path. Comprising a series of electrostatic lenses aligned with increasing repelling voltages, it deflects ions with given *m/z* values back towards the detector (Figure 1-17 and Figure 1-18). Typically the larger the *m/z* of the ion, the more energy it takes to reverse its route, so the longer it spends in the reflectron.

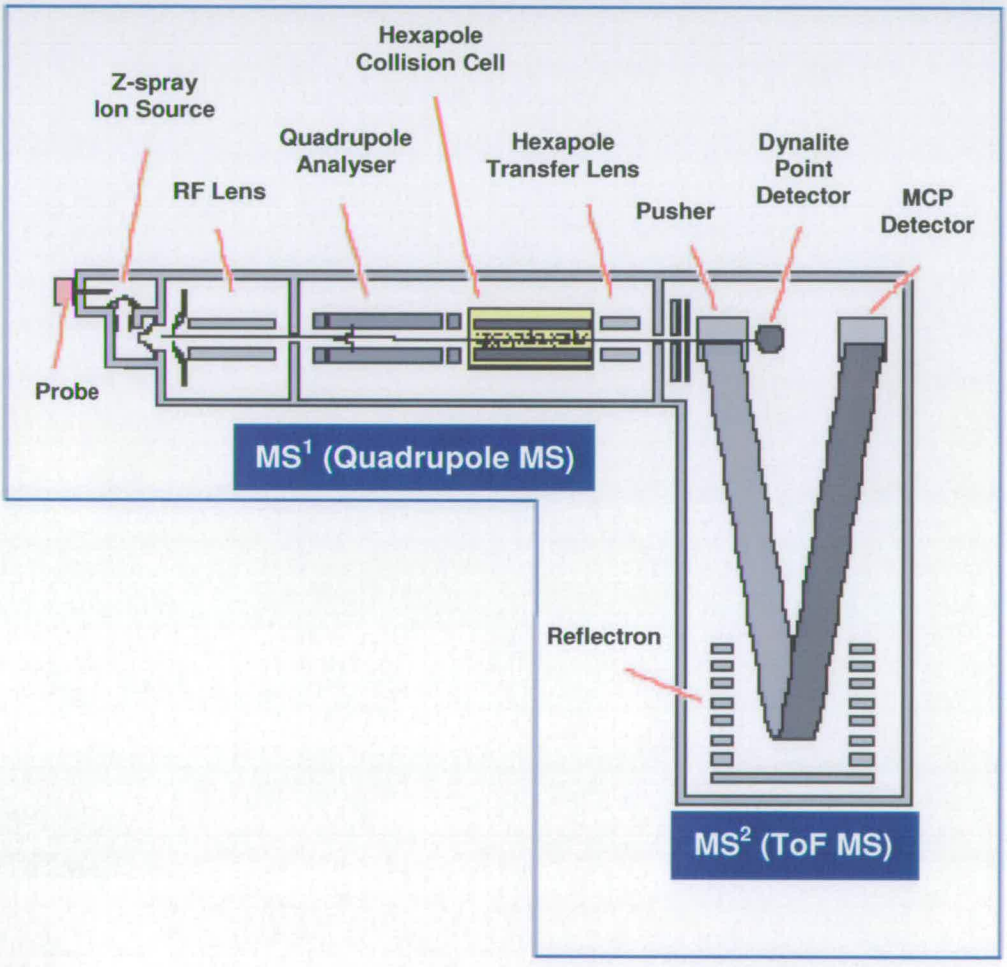

Figure 1-18 Schematic of Q-TOF mass spectrometer

A time of flight (ToF) analyser can cope with high ion transmission and acquisition rates providing a high degree of flexibility with respect to sample introduction.

1.3.3.4 Fourier Transform Ion Cyclotron Resonance (FT-ICR)

FT-ICR was developed in the early 1970s by Marshall and Comisarow[109] building on the ICR-MS technology of Hipple and co-workers in the 1950s.[110]

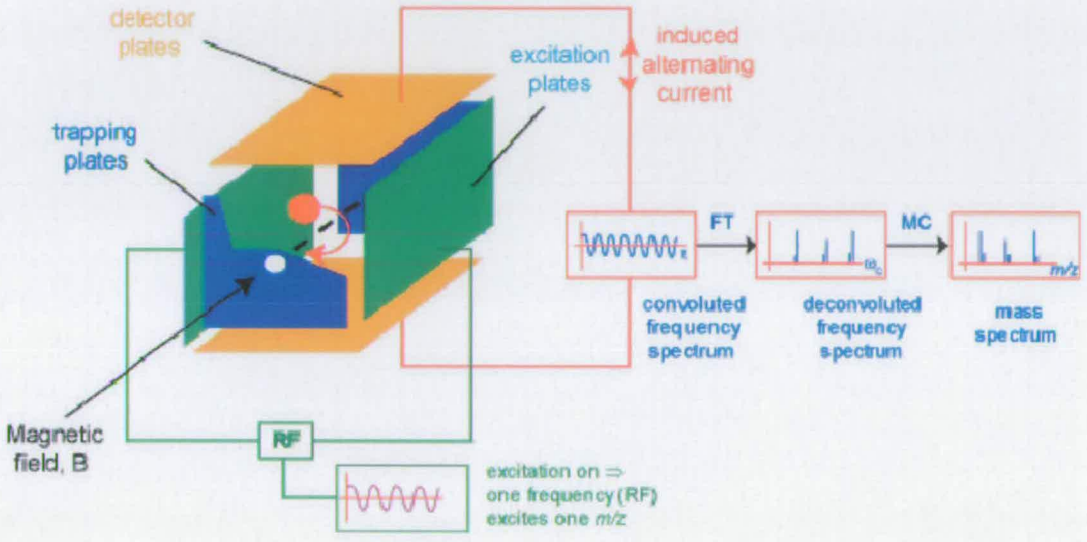

Figure 1-19 Schematic of FT-ICR-MS[107]

The benefits of high mass accuracy, resolution and long trapping times make this a useful technique for probing macromolecular structures and noncovalent complexes. For example Breuker *et al.*[111] used FTMS to monitor folding and unfolding of ubiquitin using electron capture dissociation (ECD) where as Kaltashov and Eyles[112,113] made use of the extended trapping times possible with this instrumentation to study the refolding kinetics of proteins by gaseous hydrogen / deuterium exchange (HDX).

Ions are pulsed into the ICR cell held at ultra vacuum (0.1-1 E-10 Torr) and surrounded by a magnetic field. An electric potential across the front and rear end plates trap the ions in the cell. The ions travel in a circular orbit at frequency (ω_c) defined by their *m/z* value. The time taken for a single revolution is defined in

Equations 1-11 where z is the charge of the ion; m is the mass; *v* is the ion velocity; r is the radius of the cell and B is the magnetic field strength.

$$t = \frac{2\pi r}{v} \quad \Longrightarrow \quad t = 2\pi \frac{m}{zB}$$

Equations 1-11

The resulting cyclotron frequency is defined as the number of revolutions per second (Equation 1-12).

$$\omega_0 = \frac{zB}{2\pi m}$$

Equation 1-12

To obtain mass to charge information about the trapped ions it is necessary to exite the ions to move at a larger radius and as a coherent packet. To achieve this a "broadband" excitation pulse in applied to parallel plates in the ICR cell, allowing ions with different *m/z* values possessing cyclotron frequencies falling within the applied frequency range to simultaneously absorb energy. The orbits gradually increase separating into packets ions with identical *m/z* values. These frequencies are sent as an rf signal as the ions approach the detector plates. The signal is amplified and firstly converted to a "time-domain free ion-decay" signal which is Fourier Transformed to produce a "frequency-domain signal" i.e. a transient. Resolving power can be increased by increasing the magnetic field.[114]

1.3.4 Detectors

Three detectors, which act as signal amplifiers are commonly found in commercial mass spectrometers;[100] i) the electron multiplier, ii) microchannel plates and iii) a photomultiplier. Electron multiplier detectors are commonly coupled to quadrapole or ion trap analysers, for example, a ZMD mass spectrometer. Negative and positive ions are converted into electrons and amplified by a cascade using a channeltron (a horn shaped tube) or tube comprising of a series of dynodes to produce a measurable current.

TOF mass spectrometers are generally coupled to microchannel plate (mcp) detectors. These have a quick time response and high sensitivity, typically <1 ns and a single ion signal of 50 mV respectively. Each plate contains thousands of channels enabling the detection of large numbers of ions at the same time. This is ideally suited to laser ionisation where hundreds of ions are created within nanoseconds.

1.4 Structure Elucidation

Many different approaches can be taken to use MS to provide information on whole protein structure. Some of these involve the use of dissociation techniques to break up the protein and discern structural information from the fragments produced. A catch all term for this is so called "top down" sequencing and it is best practiced with the use of FT-ICR-MS. Its high resolution and sensitivity has making it ideal for this. Jennings and McLafferty have pioneered the use of fragmentation methods to interrogate structure, demonstrating it via: nozzle skimmer dissociation;[115] electron capture dissociation (ECD);[116] collision induced dissociation (CID)[117] and infrared multiphoton dissociation (IRMPD).[118] These tactics are not employed in the work described in this study although CID was used in the study of melittin (Chapters 4 and 5).

1.4.1 Tandem Mass Spectrometry

Tandem MS or MS/MS is achieved by coupling two analysers separated by a collision cell. Precursor ions, selected using a quadrupole, are accelerated into the collision cell where they fragment. Conditions within the cell can be manipulated to increase or lessen fragmentation. The cell contains an inert gas (helium or argon) which collides with ions resulting in collision induced dissociation (CID). In a Q-ToF the pressure of the collision cell is maintained at 1 E-5 Torr with argon or in the case of an LCQ, helium. The voltage can be ramped to increase the energy within the cell, thus increasing the rate of, and amount of, energy transferred on collision. This has the adverse effect of decreasing ion transmission, so a practical compromise must be reached. Fragments obtained in the collision cell pass into either a second quadrupole, or in the case of a Q-ToF, the ToF analyser. Here fragment ions are separated and *m/z* values obtained.

Tandem MS has proved to be a powerful tool for investigating compounds and complex structures. Structural characterisation by MS has been particularly useful for analysing post translational modifications such as phosphorylation[119] or glycosylation[120] of proteins. It is now often used as the preferred method for obtaining sequence data of protein fragments and peptides rather than Edman degradation[121,122] (the traditional method for N-terminal sequencing).

1.4.1.1 Mechanisms of Fragmentation

There are 3 points at which a peptide backbone can fragment. The nomenclature of the daughter ions generated was developed by Roepstorff and Fohlmann[123] in 1984 and is shown in Figure 1-20. Collision Induced Dissociation (CID) generates b and y fragments, whereas Electron Capture Dissociation (ECD) generates c and z fragments.

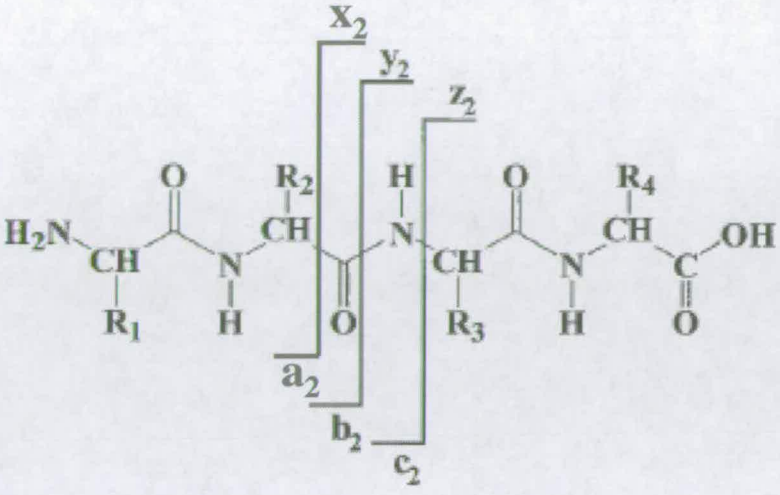

Figure 1-20 Standard nomenclature of fragments generated by mass spectrometry[123]

Mechanisms for these fragmentations have been proposed by Paizs and Suhai[124] and the resulting fragmentation patterns are dependent not only on the method of excitation and subsequent internal energy of the ion, but also the peptide / protein sequence and charge state of the parent ion.

1.4.1.2 Charge Sequestering and the 'Mobile Proton' by CID

Basic residues have been shown by Wysocki and co-workers[125] to play a crucial role in peptide cleavage. There is a strong link between basicity of the protonated amino acid and the kinetic energy of the ions that is required to achieve fragmentation. They showed that energy required for fragmentation increases when arginines were introduced into neutral peptides. The positioning of the basic residue dictates which fragments are detected.[126] If the basic residue is at the N-terminus, only b ions are obtained whereas if the basic residue was on the C-terminus, y residues are obtained. If the basic residue is in the middle of the peptide, a mixture of b and y fragments is observed. Similar observations have been made where the basic residue was a lysine or histidine.[127] Fragmentation patterns therefore, are dictated by the type and location of the base.[128]

The general cleavage pathway producing b-y fragments is shown in Figure 1-21. The basicity of residues located either side of the NH_2 group, dictates which species is generated.

Where all available protons are bound to basic residues, cleavage is likely to occur on the C-terminal side of the acidic residues.[129] If however, the number of protons exceeds the number of arginines, cleavage occurs elsewhere in a more unpredictable fashion, although cleavage on the N terminal side of proline appears to be strongly favoured.

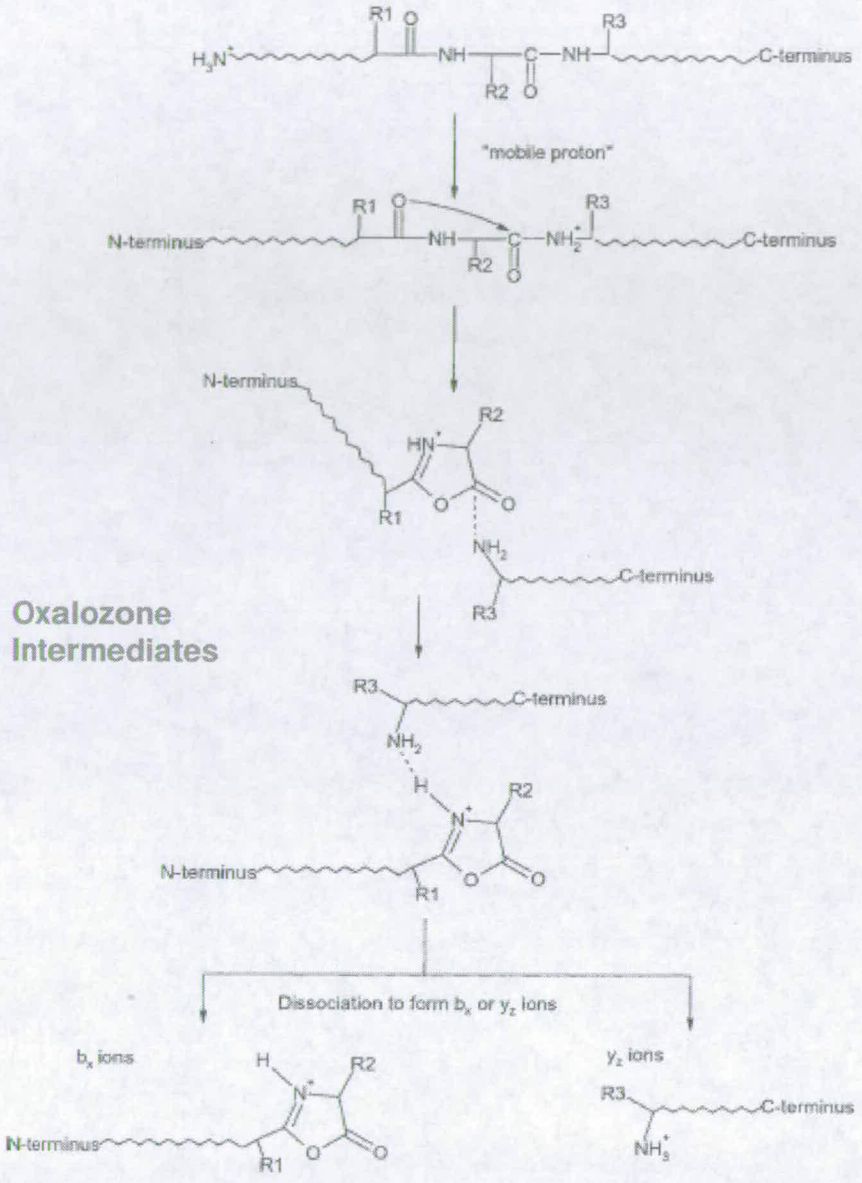

Figure 1-21 The b-y fragmentation pathway (reproduced from reference 124)

1.4.1.3 Fragmentation by ECD

Fragmentation via ECD predominantly generates c and z fragments initiated by a nucleophile attacking a backbone carbonyl group (Equation 1-13). Breuker *et al.*[130] have used ECD to characterise intramolecular noncovalence. A low energy electron is captured to produce a radical which rapidly dissociates via proton transfer to the backbone carbonyl group.

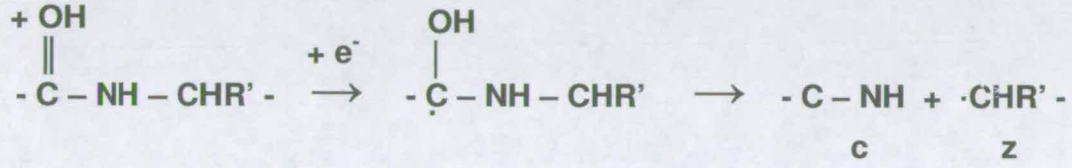

Equation 1-13

Adams *et al.*[131] have inferred that ECD possesses structural selectivity. This was further demonstrated by Barran *et al.*[31] who showed ECD was a useful diagnostic tool for distinguishing between monomeric and dimeric defensins (antimicrobial peptides). They demonstrated preferential cleavage of an exposed disulphide bond on a defensin dimer. Disulphide bonds shielded within the monomeric structure however were not susceptible to nucleophilic attack.

1.4.1.4 Proton scrambling

CID is used in this thesis to map helical retention using H/D exchange across melittin (Chapters 4 and 5). Proton scrambling can occur during CID as a result of intramolecular proton transfer[132] and specifics regarding melittin are discussed in the following chapters. Low energy and fast CID minimises proton migration along the peptide backbone.[132,133] As discussed in Section 1.4.1.1, relative gas phase basicities of amino acids[134] and the positioning of basic residues, in particular arginine,[125] dictate which fragments are detected. Proton / deuteron affinities vary between amino acids and as such the effect of scrambling is system specific.[134,135] Smith and co-workers[136] observed minimal scrambling whereas Jørgensen *et al.*[137] have observed exchange on peptides which should be *d*-free.

1.5 Hydrogen – Deuterium Exchange (HDX)

It was Linderstrøm-Lang and co-workers who, in the 1950s, made the connection that hydrogen bonding found by Pauling in α-helices and β-sheets might be analysed using hydrogen-deuterium exchange (HDX). Although their original ideas turned out to be somewhat flawed, the equations they developed for exchange dynamics are still used today.[138]

HDX is useful for studying protein folding and unfolding events and mass spectrometry is able to detect exchange rates down to 10^{-3} seconds (Figure 1-22).[139] Although much slower than the rates which can be detected by NMR, MS is still useful in providing a global overview of protein dynamics.

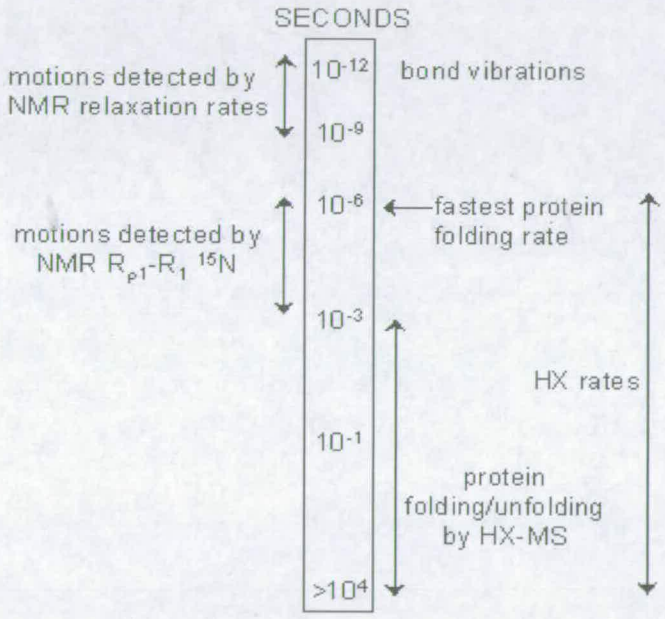

Figure 1-22 Timescales of HDX rates related to protein dynamics (reproduced from reference 139)

1.5.1 Exchange Models

Hvidt and Nielsen[140] proposed a two state kinetic model for peptide / protein HDX, based on the back exchange rates of backbone hydrogens, in 1966 (Equation 1-14). k_{op} and k_{cl} represent the opening (unfolding) and closing (refolding) rate constants. In this instance the intrinsic exchange rate, k_{int} of **ND** to **NH** is assumed to be irreversible as the buffer concentration of **NH** is at least an order of magnitude greater than **ND**. When the protein is classed as 'incompetent' or native, no exchange of the buried amide backbone hydrogens will take place until it opens to become 'competent' or non-native. If the protein remains 'competent', i.e. the conformation adopted is a stable partially or fully unfolded intermediate, back exchange may occur, otherwise it will revert back to its 'incompetent' or native form.

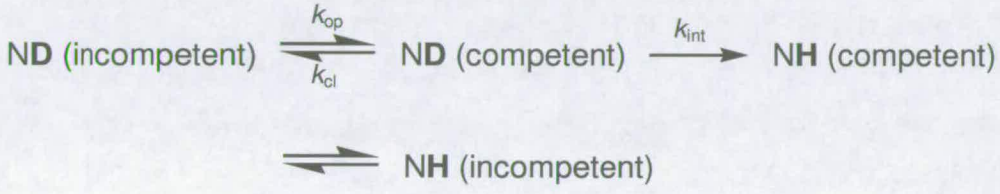

Equation 1-14

Dynamics and protein stability can be described by EX1 and EX2 regimes. The EX2 regime prevails if the intermediate state is not stable enough to remain open for exchange to take place, i.e. $k_{int} < k_{cl}$. The probability of a single opening event is show in Equation 1-15

$$k^{HDX} = k_{op} \cdot (k_{int} / k_{cl})$$

Equation 1-15

If $k_{int} >> k_{cl}$ however, exchange will occur in a single opening event and the rate of exchange is defined by the rate of unfolding (Equation 1-16). The unfolded intermediate is stable enough for exchange to occur and the protein follows an EX1 regime.

$$k^{HDX} = k_{op}$$

Equation 1-16

1.5.2 Proton Populations - Rates and Types of Exchange

Three types of hydrogen are found within peptide structures. These are illustrated in Figure 1-23.[141]

Type I : Found on the side chain functional groups these undergo rapid forward and back exchange under all conditions.

Type II : Amide backbone hydrogen exchange is very sensitive to buffer conditions. Dropping pH and temperature to reduce back exchange rates is useful for studying backbone folding and unfolding kinetics.

Type III : Carbon bound hydrogens do not exchange under these conditions and time-scales. For the purposes of the experiments in this thesis, these can be ignored.

The numbers of exchangeable hydrogens available on each neutral amino acid are listed in Appendix A.

Type I and II hydrogens are considered labile if they are exposed to solvent. Initial experiments by Katta and Chait,[142] the first report which coupled HDX with MS, demonstrated that as the protein was gradually denatured by lowering the pH, total *d*-uptake increased.

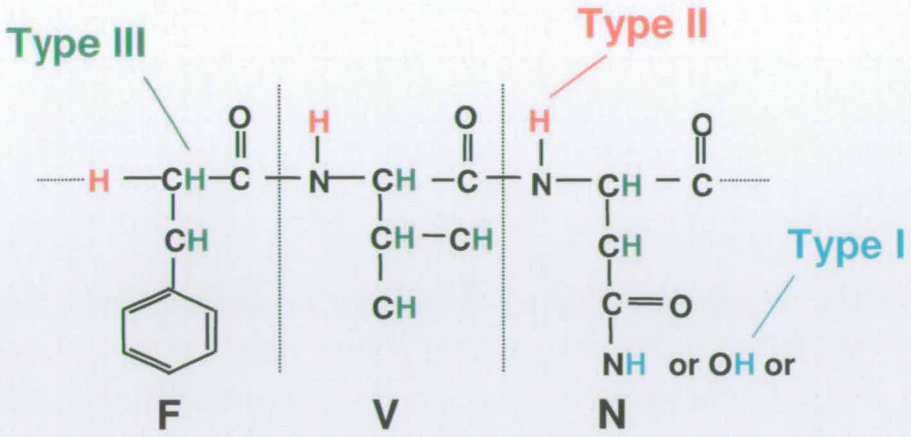

Figure 1-23 Types of hydrogens found on polypeptides

The rate of exchange is also slowed by a drop in pH (Figure 1-24)[139] lengthening the experimental time for data acquisition. Dropping the temperature also lowers the rates of exchange and when coupled with a drop in temperature, experimental time is further increased.

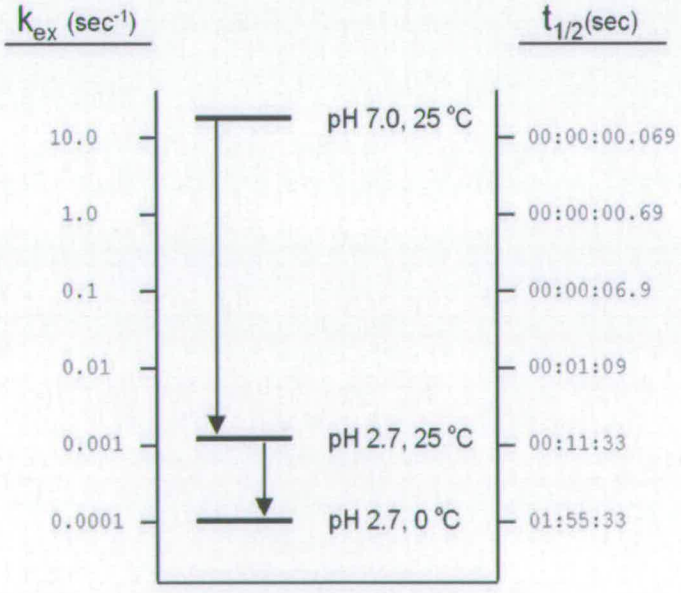

Figure 1-24 The effect of pH and temperature on the rate of exchange (reproduced from reference 139)

1.5.3 Exchange Mechanisms

1.5.3.1 Solution Phase Exchange

Intrinsic exchange rates of backbone and side chain hydrogens vary between amino acids. Average exchange rates as a function of pH are shown in Figure 1-25. At pHs greater than 2.7, base catalysed exchange occurs which shifts to acid catalysed exchange below this value.

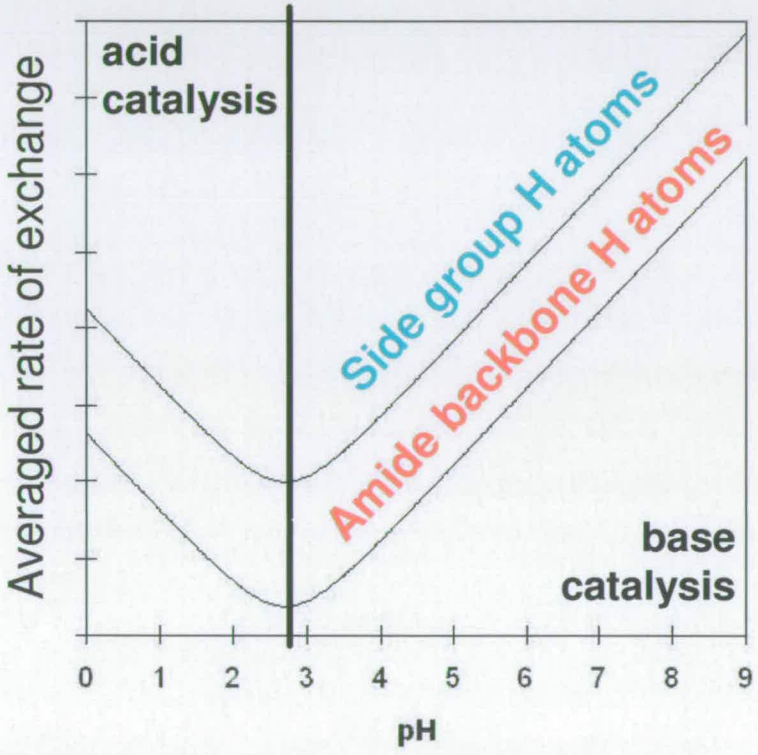

Figure 1-25 Average intrinsic exchange rates ($mins^{-1}$) of backbone and sidechain hydrogens (reproduced from reference 139)

Intrinsic exchange rates are expressed as shown in Equation 1-17.[146]

$$k_{int} = k_{acid}[H^+] + k_{base}[OH^-] + k_{water}$$

Equation 1-17

Base catalysed exchange in solution is initiated by abstraction of a proton by OD^- to give an imidate anion (Equation 1-18).[143]

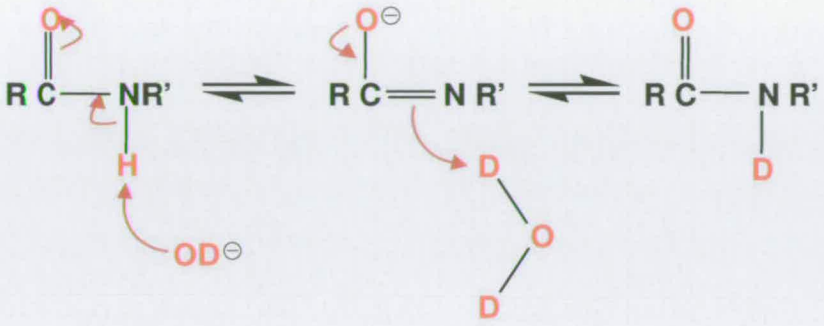

Equation 1-18

Acid catalysed exchange can be expressed in two ways (Equations 1-19):[143]

A) Reversible protonation by the amide hydrogen

B) Protonation of the amide oxygen (imidic acid mechanism)

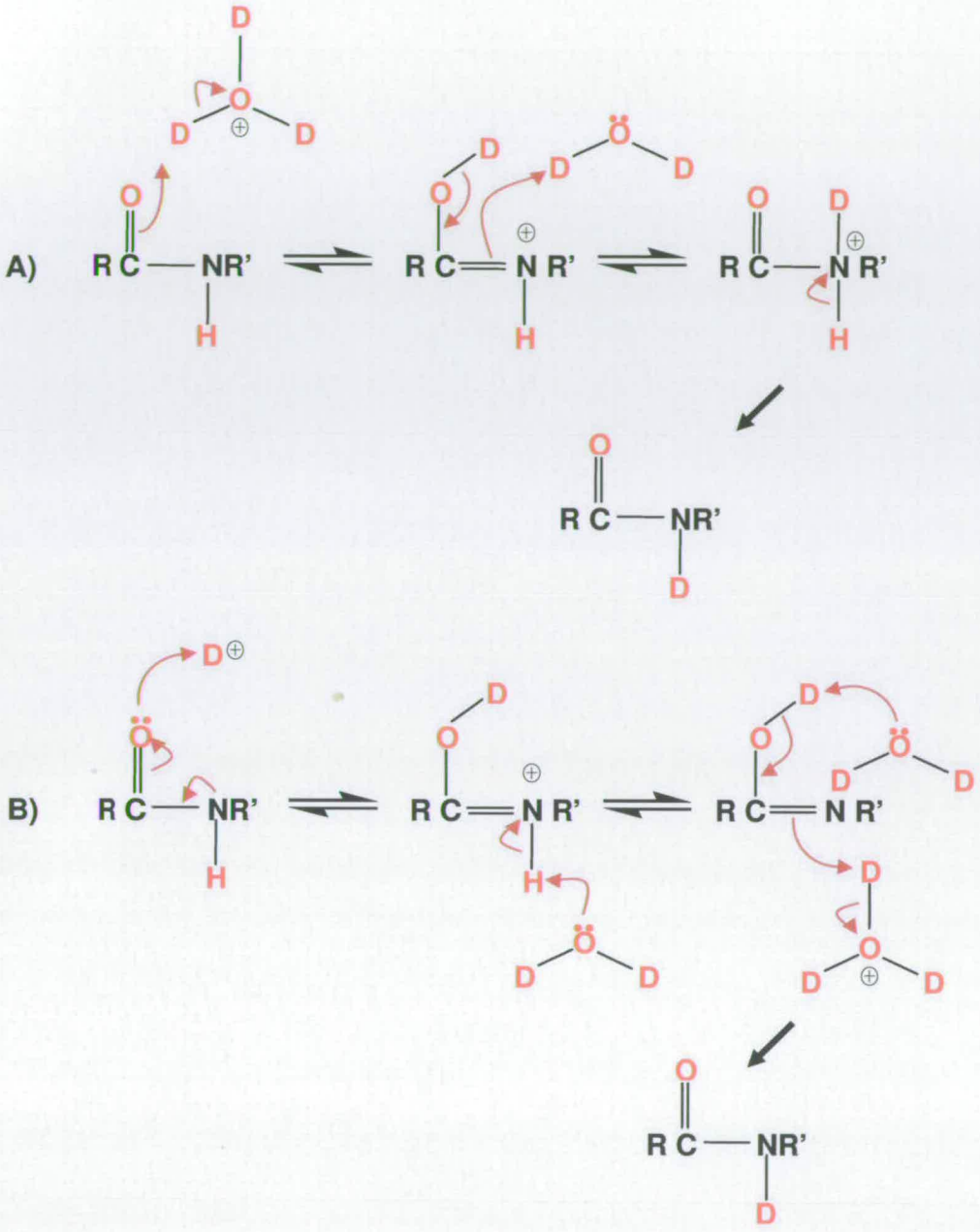

Equations 1-19

1.5.3.2 Gas Phase Exchange

The gas phase HD exchange mechanism that is widely agreed upon, was proposed independently by Green and Lebrilla[144] and Beauchamp and co-workers.[145] Exchange is initiated by the presence of a proton donor group (e.g. R^+NH_3) lying

within 5Å of a proton acceptor group (e.g. C=O:). The gap is bridged by H-bonding from the polar deuterated solvent molecule (*d*-solvent) which results in the formation of an unstable positively charged carbonyl intermediate (Figure 1-26).

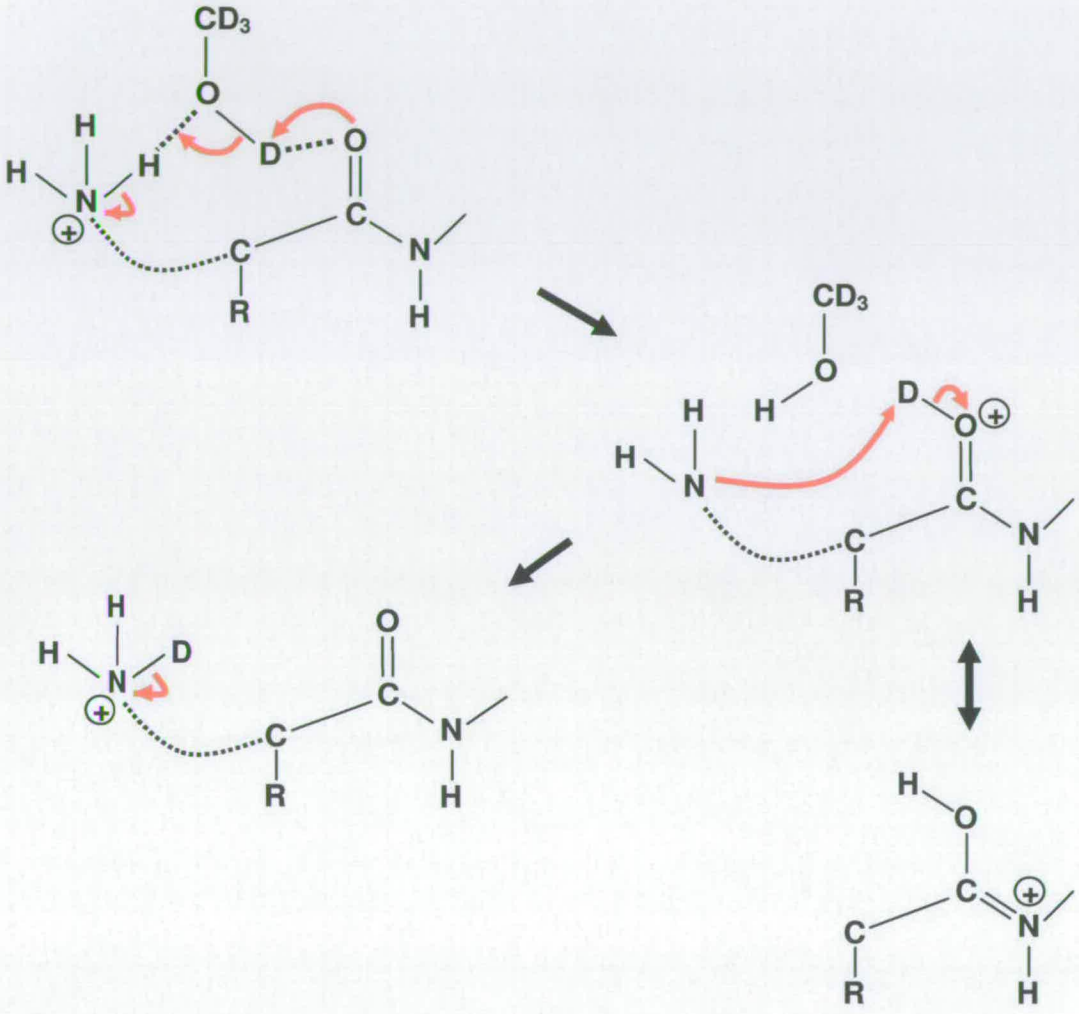

Figure 1-26 The gas phase HDX mechanism as proposed by Green and Lebrilla[144] and Beauchamp and co-workers[145]

1.5.4 Experimental Approaches to HDX using Mass Spectrometry

Measuring *d*-uptake by mass spectrometry provides a global picture of protein conformations unlike NMR which can be amino acid specific.[146] The approach to H/D exchange adopted throughout this thesis has been to measure deuterium uptake. As mentioned previously, Katta and Chait[142] performed one of the first HDX / ESI-MS studies to probe conformational changes in proteins in the early 1990s using native ESI-MS to monitor global *d*-uptake.

HDX-MS is ideally suited to studying intrinsic properties of protein structures (see discussion in Section 1.1.2)[33,32] and noncovalent complexes[147] i.e. a folded protein will exchange less labile hydrogens than a denatured or partially denatured protein. The exchange of one hydrogen for one deuterium results in a mass increase of 1 Da. Direct analysis of this exchange can be monitored over time defining different proton populations of fast (side chain and surface labile hydrogens); intermediate (backbone and less solvent exposed hydrogens) and slow exchanging hydrogens. Although convention dictates calculating *d*-uptake, Kaltashov has monitored back exchange over time due to refolding of a number of protein systems including, partially denatured chymotrypsin and cellular retinoic acid binding protein I (CRABP I) against its ligand all-trans retinoic acid (RA).[148]

Konermann and co-workers[149] developed a pulsed H/D exchange method for identifying conformer populations with individual charge states from *d*-buffer exposure for times of 40 ms up to 3.3 s. These timescales had not been achieved for on-line solution HDX analysis before and he was able to identify multiple conformers for different charge states for inducible nitric oxide synthase core oxygen domain ($iNOS_{COD}$).

1.5.4.1 Solution Phase Approaches to HDX using Mass Spectrometry

There are a number of alternative solution based approaches summarised below. All enable exchange to be carried out in a native environment incompatible with MS.

i) Local exchange analysis can be performed with the aid of peptic digests. Smith and co-workers[150] realised the benefit of being able to minimise exchange at low pH. Pepsin, a largely non-specific protease found in the stomach has high efficiency at pH 2.5. Performing the digest at 0-4 °C slows enzyme activity down further, allowing control over the number of fragments generated. Separated by on-line HPLC-MS, deuterated fragments can be aligned with non deuterated fragments and *d*-uptake monitored over these short peptides. Although these conditions are considered to quench exchange, there will still be some back exchange occurring but, this will largely be due to side chain deuterons rather than those on the backbone. Komives adapted this method to MALDI[151] analysis and used it to map protein-protein binding interfaces by titrating one binding partner against the other. This approach enabled her to monitor rates of dissociation and association.[152]

ii) PLIMSTEX[153] (protein ligand interactions by mass spectrometry, titration and hydrogen / deuterium exchange) and SUPREX[154,155] (stability of unpurified proteins fro rates of H/D exchange) were devised around the early to middle 2000s. They are both used to study protein dynamics in solution and can be used to calculate binding constants of protein-ligand complexes.

The experimental approach in PLIMSTEX is described in Chapter 2, Section 2.5.3. This method takes advantage of the difference in exchange rates between side chain labile hydrogens and amide backbone hydrogens (Section 1.5.2). The protein or protein-ligand mix of interest is incubated under deuterating conditions at physiological pH. At a given time point, exchange is quenched by the addition of acid coupled with rapid cooling. The sample is loaded onto a reverse phase HPLC column and washed under non deuterated conditions until all side chain deuterons are back exchanged and only backbone deuterons are observed. Gross and co-

workers[153] determined stoichiometry and binding constants of a number of complexes. In the example shown below, (Figure 1-27) melittin was titrated against calmodulin (CaM). Deuterium (*d-*) uptake was plotted against the ratio of melittin-CaM which demonstrated that no further *d*-uptake was observed above a 1:1 ratio, which lead to the conclusion that melittin bound to CaM with 1:1 stoichiometry.

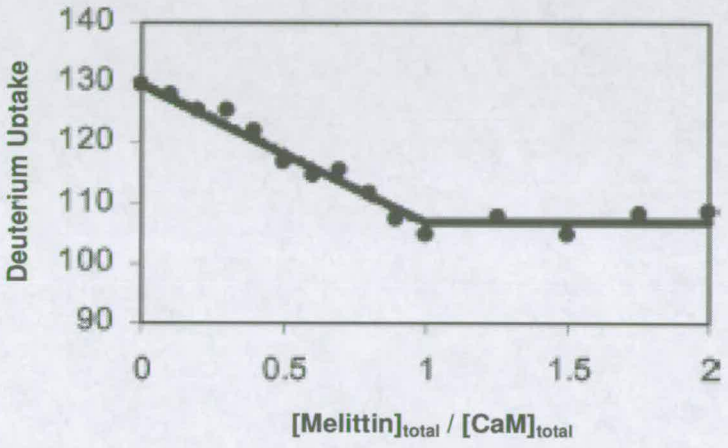

Figure 1-27 Melittin titration against calmodulin showing 1:1 stoichiometry. Reproduced from reference 153

The disadvantage of this technique is that ligands with a low affinity or high k_{off} rate and those which do not induce significant structural changes when binding to the protein, allow exchange to occur at the binding site during the ligand "off" period. This means bound protein may be indistinguishable from unbound protein.

iii) SUPREX involves titrating a *d*-denaturant (guanidine hydrochloride) with the complex[154]. This induces partial or complete denaturation of the protein and as a consequence a dramatic increase in overall exchange. If the presence of a ligand stabilises the protein structure, a difference in denaturant concentration is required to disrupt the protein and its complex. Total exchange plotted against denaturant concentration is used to calculate the free energy of folding and K_ds. A correction factor for intrinsic sequence exchange rates is applied. Wang *et al.*[155] performed thermodynamic analysis of CypA over expressed in lung tumour tissue lysate and

showed it exhibited increased stability when CsA was present. K_d values calculated were shown to be in agreement with those calculated by Wear *et al.*[156]

1.5.4.2 Gas Phase Approaches

The LCQ is used in studies described in this thesis for gas phase HDX studies and similar experiments have been performed by Marzluff and co-workers[157,145] and Clemmer and co-workers.[33] Parallels are drawn between the melittin gas phase studies in Chapter 5 and the work of Marzluff who along with Beauchamp[145] calculated differences in exchange rates between different deuterated solvents (D_2O; CD_3OD; CD_3CO_2D; ND_3) in the gas phase. Much of the gas phase exchange nowadays utilises FT-ICR-MS[158] which has the ability to trap for long periods of time which aren't necessarily achievable with a QIT. Trapping conditions may be manipulated to induce unfolding events.

1.6 References

[1] http://www.ornl.gov/sci/techresources/Human_Genome/home.shtml. Official site of the Human Genome Project
[2] Special Issue - multiple authorship, *Science*, 1998, **282**, 1945-2140
[3] Special Issue - multiple authorship, *Science*, 2000, **287**, 2105-2364
[4] Terwilliger TC. and Eisenberg D, *J. Biol. Chem.*, 1982, **257**, 6010-6015
[5] Hirota N., Mizuno K. and Goto Y., *J. Mol. Biol*, 1998, **275**, 365-378
[6] Liu Y., Jiang J., Richardson PL., Reddy RD., Johnson DD., Kati WM., *Anal. Biochem.*, 2006, **356**, 100–107
[7] Polfer NC., Dunbar RC., Oomens J., *J Am Soc Mass Spectrom* 2007, **18**, 512–516
[8] Gerig JT., *Biophys. J.* 2004, **86**, 3166-3175
[9] Daniel JM., Friess SD., Rajagopalan S., Wendt S., Zenobi R., *Int J Mass Spectrom,* 2002, **216,** 1-27
[10] Benesch JLP., Robinson CV., *Curr Op Struc. Biol.*, 2006, **16**, 245-251
[11] Heck AJR, van den Heuvel RHH., *Mass Spectrom Rev,* 2004, **23**, 368-389
[12] Loo J., Holler TP., Foltin SK., McConnell P., Banotai CA., Horne NM., Mueller WT., Stevenson TI., Mack DP., *Proteins. Struct. Funct Genet.*, 1998, **Suppl. 2**, 28–37
[13] Broberg A., *Carbohydrate Research*, 2007, **342**, 1462–1469
[14] Bhat S., Sorci-Thomas MG., Tuladhar R., Samuel MP., Thomas MJ., *Biochemistry,* 2007, **46**, 7811-7821
[15] Blum W., Schlumpf E., Liehr JG., Richter WJ., *Tetrahedron Letters,* 1976, **7**, 565-568
[16] Fersht A., *Structure and Mechanism in Protein Science*, Freeman, 2000
[17] Mikol, V., Kallen, J., Pflugl, G., Walkinshaw, MD., *J. Mol. Biol.,* 1993, **234**, 1119-1130V
[18] Fuchs E., Weber K., *Annu Rev Biochem*, 1994, **63**, 345-382
[19] Perutz MF., *Nature*, 1962, **194**, 914-917
[20] van Holde KE., Johnson WC., Shing Ho P., *Principles of Physical Biochemistry,* Second Edition, Pearson Prentice-Hall, 2006
[21] Thomas E. Creigton, *Proteins Structures and Molecular Properties,* second edition

[22] Koolman K., Roehm KH., *Colour Atlas of Biochemistry*, 2nd Edition, Thieme 2003
[23] Chang R., *Physical Chemistry with Applications to Biological Systems*, 2nd Edition, Macmillan Publishing Company Inc., 1990
[24] Wain-Hobson S., *Nature*, 2006, **439**, 539
[25] Connelly PR., Aldape RA., Bruzzese FJ., Chambers SP., Fitzgibbon MJ., Fleming MA., Itoh S., Livingston DJ., Navia MA., Thomson JA., Wilson KP., *Proc Natl Acad Sci,* 1994, **91,** 1964-1968
[26] Aplin RT., Robinson CV., Schofield CJ., Westwood NJ., *Journal of Chemical Society, Chemical Communications* , 1994, 2415-2417.
[27] Hernández H., Robinson CV., *J Biol Chem.*, 2001, **276**, 46685-46688
[28] Gross DS., Schnier PD., Rodriguez-Cruz SE., Fagerquist CK., WilliamsER., *Proc. Natl. Acad. Sci. USA* 1996, **93**, 3143-3148
[29] Koeniger SL., Merenbloom SI, Clemmer DE., *J. Phys. Chem. B,* 2006, **110**, 7017-7021
[30] Loo JA., He JX., Cody WL., *J. Am. Chem. Soc.* 1998**, 120**, 4542-4543
[31] Barran PE., Polfer NC., Campopiano DJ., Clarke DJ., Langridge-Smith PRR., Langley RJ., Govan JRW., Maxwell A., Dorin JR., Millar RP., Bowers MT., *Int J Mass Spectrom.*, 2005, **240**, 273-284
[32] Freitas MA., Hendrickson CL., Emmett MR., Marshall AG., *Int. J. Mass Spectrom.,* 1999, **185-187**, 565-575
[33] Valentine SJ., Clemmer DE., *J Am Soc Mass Spectrom* 2002, **13**, 506–517
[34] Hansch C., *Accounts Chem Res*, 1969, **2**, 232-239
[35] Villar HO., Hansen MR., Kho R., *Curr Com Aid Drug Des*, 2007, **3**, 59-67
[36] Shuker SB., Hajduk PJ., Meadows RP., Fesik SW, *Science*, 1996, **274**, 1531-1534
[37] Andersen D., Terwilliger T., Wickner W., Eisenberg, D., *J Biol Chem.*,1980, **255**, 2578-2582
[38] Terwilliger T. and Eisenberg, D. *J Bio Chem,* 1982, **257**, 6016-6022
[39] Marcos J., Beachy R., Houghten R., Blondelle S., Perez-Paya E., *Proc. Natl Acad Sci,* 1995, **92**, 12466-12469
[40] Wachinger, M., Kleinschmidt, A., Winder, D., von Pechmann, N., Ludvigsen, A., Neumann, M., Holle, R., Salmons, B., Erfle, V., Brack-Werner, R., *J Gen Virol,* 1998, **79**, 731-740
[41] Baghian A., Jaynes J., Enright F., Kousolas K., *Peptides,* 1997, **18**, 177-183
[42] Bernèche S., Nina M., Roux B., *Biophys J,* 1998, **75**, 1603-1618
[43] Okada, A., Wakamatsu, K., Miyazawa, T., Higashijima, T., *Biochemistry* 1994, **33**, 9438-9446
[44] Vogel H., *Biochemistry,* 1987, **26**, 4562– 4572
[45] Terwilliger T. C., Weissman L. and Eisenberg D., *Biophys. J.,* 1982, **37**, 353–361
[46] Bachar M and Becker OM., *Biophys J.*, 2000, **76**, 1359-1375
[47] Hristova K., Dempsey CE., White SH., *Biophys J*, 2001, **80**, 801-811
[48] Raghuraman H., Chattopadhyay A., *Biophys J.*, 2007, **92**, 1271-1283
[49] Kaiser ET., and Kezdy FJ., *Proc. Natl. Acad. Sci.,* 1983, **80**, 1137–1143
[50] Morii HS., Honda S., Ohashi S., Uedaira H., *Biopolymers*, 1994, **34**, 481–488
[51] Golding C., O'Shea P., *Biochem. Soc. Trans.*, 1995, **23**, 971–976
[52] Rabenstein, M., Shin YK., *Biochemistry*, 1995, **34**, 13390–13397
[53] Barnham K.J., Monks SA., Hinds MG., Azad AA., Norton RS., *Biochemistry*, 1997, **36**, 5970–5980
[54] Göthel SF., Marahiel MA., *Cell Mol Life Sci,* 1999, **55,** 423-436
[55] Vitikainen M., Lappalainen I., Seppala R., Antelmann H., Boer H., Taira S., Savilahti H., Hecker M., Vihinen M., Sarvas M., Kontinen VP., *J Biol Chem,* 2004, **279,** 19302-19314
[56] Fischer G., Wittmann-Liebold B., Lang K., Kiefhaber T., Schmid FX., *Nature,* 1989, **337**, 476-478
[57] Ke H., Zydowsky LD., Liu J., Walsh CT., *Proc Natl Acad Sci,* 1991, **88,** 9483-9487
[58] Mikol, V., Taylor P., Kallen, J., Walkinshaw, MD., *J. Mol. Biol.,* 1998, **283**, 451-461
[59] Pflugl G., Walkinshaw M., *Nature*, 1993, **361**, 91
[60] Theriault Y., Loga T., *Nature,* 1993, **361**, 88
[61] Eisenmesser EZ., Bosco DA., Akke M., Kern D., *Science*, 2002, **295**, 1520-1523
[62] Ke H., Mayrose D., Cao W., *Proc Natl Acad Sci,* 1993, **90,** 3324-3328
[63] Takahashi N., Hayano T., Suzuki M., *Nature,* 1989, **337,** 473-475
[64] Lui J., Albers MW., Chen C-M., Schreiber SL., Walsh CT, *Proc Natl Acad Sci,* 1990, **88,** 2304-2308
[65] Dornan J., Page AP., Taylor P, Wu S-Y., Winter AD., Husi H., Walkinshaw MD., *J Biol Chem,* 1999, **274,** 34877-34883
[66] Ivery MTG., *Bioorg Med Chem*, 1999, **7,** 1389-1402

[67] Schreiber SL., *Science,* 1991, **251,** 283-287
[68] Waldmeier PC., Feldtrauer J-J., Qian T., Lemasters JJ., *Mol Pharmacol,* 2002, **62,** 22-29
[69] Zhang L-H., Liu JO., *J Immunol,* 2001, **166,** 5611-5618
[70] Zander K., Sherman MP., Tessmer U., Bruns K., Wray V., Prechtel AT., Schubert E., Henklein P., Luban J., Neidelman J., Greene WC., Schubert U., *J Biol Chem,* 2003, **278,** 43202-43213
[71] Towers GJ., Hatziioannou T., Cowan S., Goff SP., Luban J., Bieniasz PD., *Nat Med,* 2003, **9,** 1138-1143
[72] Li Z., Lizaridia T., *J. Phys Chem. B.*, 2006, **110**, 1464-1475
[73] Shirran S., *PhD Thesis*, University of Edinburgh, 2005
[74] Ottiger, M., Zerbe, O., Guntert, P., Wuthrich, K., *J Mol Biol.,* 1997, **272**, 64-81
[75] Dalgarno DC., Harding MW., Lazarides A., Handschumacher RE., Armitage IM., *Biochemistry*, 1986, **25**, 6778-6784
[76] Weber C., Wider G., Von Freyberg B., Traber R., Braun W., Widmer H., Wüthrich K., *Biochemistry*, 1991, **30**, 6563-6574
[77] Handschumacher RE., Harding MW., Rice J., Drugge RJ., Speicher DW., *Science*, 1984, **226**, 544-547
[78] Harrison RK. and Stein RL., *Biochemistry*, 1990, **29**, 3813-3816
[79] Fesik SW., Gampe, Jr. RT., Holzman TF., Egan DA., Edalji R., Luly JR., Simmer R., Helfrich R., V. Kishore RV., D. H. Rich DH., *Science*, 1990, **250**, 1406-1409
[80] Waters LC/MS booklet, Waters European Marketing, France, www.waters.com
[81] Skoog DA., Leary JL., *Principles of Instrumental Analysis*, fourth edition.
[82] http://www-methods.ch.cam.ac.uk/meth/ms/theory/fab.html
[83] Blakely CR., Vestal ML., *Anal Chem*, 1983, **55**, 750-754
[84] Dass C., Principles and Practice of Biological Mass Spectrometry, Wiley Interscience, 2001
[85] Karas M., Doris Bachmann D., Hillenkamp F., *Anal. Chem.,* 1985, **57**, 2935-2939
[86] Karas M., Hillenkamp F., *Anal. Chem.* 1988, **60**, 2299-2301
[87] Takats Z., Wiseman JM., Gologan B., Cooks RG., *Science*, 2004, **306**, 471-473
[88] Whitehouse CM., Dreyer RN., Yamashita M. and Fenn JB., *Anal Chem*,1985, **57**, 675-679
[89] Dole M., Mack LL., Hines RL., Mobley RC., Fergusson LD., Alice MB., *J Chem Phys*, 1968, **49(5),** 2240-2249
[90] Taylor G., *Proc Roy Soc of London. Series A Mathematical and Physical Sciences*, 1964, **280**, 383-397
[91] Kebarle P., Peschke M., *Analytica Chimica Acta,* 2000, **406,** 11-35
[92] Lord Rayleigh, *Proc. Roy. Soc. Of London*, 1882/1883, **34**, 130-145
[93] Znamenskiy V., Marginean I., Vertes A., *J Phys Chem A,* 2003, **107,** 7406-7412
[94] Smith JN., Flagan RC., Beauchamp JL., *J Phys Chem*, 2002, **106**, 9957-9967
[95] Gu W., Heil PE., Choi H., Kim K., *App Phys Letts*, 2007, **91**, 064104
[96] Iribarne JV., Thomson BA., *J. Chem. Phys.,* 1976, **64**, 2287
[97] Iavarone AT., Williams ER., *J Am Chem Soc*, 2003, **125,** 2319-2327
[98] de la Mora JF., *Analytica Chimie Acta,* 2000, **406,** 93-104
[99] Fenn JB., Mann M., Meng CK, Wong SF., Whitehouse CM, *Science,* 1989, **246,** 64-71
[100] LCQ manual, Micromass
[101] Viberg P., Nilsson S., Skog K., *Anal Chem*, 2004, **76**, 4241-4244
[102] Wilm M., Mann M., *Anal Chem,* 1996, **68,** 1-8
[103] Peschke M., Verkerk UH. and Kebarle P., *J. Am. Soc. Mass Spectrom.* 2004, **15**, 1424-1434
[104] Paul W., *Angew Chem Int Ed Engl.*, 1990, **29**, 739-748
[105] Remes PM., Glish GL., *Int J Mass Spectrom*, 2007, **265**, 176–181
[106] March RE., Todd JFJ., *Quadrupole Ion Trap Mass Spectrometry*, 2nd Edition, Wiley Interscience
[107] http://www.chm.bris.ac.uk/ms/theory/
[108] Mamyrin BA., *Int J Mass Spectrom,* 2001, **206**, 251–266
[109] Comisarow MB., Marshall AG., *J Chem Phys.* 1975, **62**, 293-295
[110] Hipple JA., Sommer H., Thomas HA., *Phys Rev Series II,* 1949, **76**, 1877-1878
[111] Breuker K., Oh H-B., Horn DM., Cerda BA., McLafferty FW., *J Am Chem Soc.,* 2002, **124**, 6407-6420
[112] Kaltashov IA., Eyles SJ., *J. Mass Spectrom.,* 2002, **37**: 557–565
[113] Kaltashov IA., *Intl J Mass Spectrom.*, 2005, **240**, 249–259

[114] Chhabil Dass, *Principles and Practice of Biological Mass Spectrometry*, Wiley Interscience, 2001
[115] Zhai H., Han X., Breujer K., McLafferty FW., *Anal. Chem.*, 2005, **77**, 5777-5784
[116] Zubarev RA., Kelleher NL., McLafferty FW., *J. Am. Chem. Soc.*, 1998, **120**, 3265-3266
[117] Jennings KR., *Int. J. Mass Spectrom.*, 2000, **200**, 479-493
[118] Little DP., Speir JP., Senko MW., O'Connor PB., McLafferty FW., *Anal. Chem.*, 1994, **66**, 2809-2815
[119] Zhou H., Watts JD., Aebersold R., *Nat Biotech.*, 2001, **19**, 375-378
[120] Mirgorodskaya E, Roepstorff P, Zubarev RA, *Anal Chem.*, 1999, **71**, 4431-4436
[121] Stryer L., *Biochemistry*, Freeman, 1981, second edition
[122] Carr SA., *Advanced Drug Delivery Reviews*, 1989, **9**, 2-7 (abstract only)
[123] Roepstorff P., Fohlmann J., *Biomed Mass Spectrom.*, 1984, **11**, 601
[124] Paizs B., Suhai S., *Mass Spectrom Rev.*, 2005, **24**, 508-548
[125] Wysocki VH., Tsaprailia G., Smith LL., Breci LA., *J Mass Spectrom*, 2000, **35**, 1399-1406
[126] Tabb DL., Huang Y., Wysocki VH., Yates III JR.., *Anal. Chem.*, 2004, **76**, 1243-1248
[127] Afonso, C., Modeste, F., Breton, P., Fournier, F., Tabet, J-C., *Eur. J. Mass Spectrom.* 2000, **6**, 443-449
[128] Dougre AR., Jones JL., Somogyi A., Wysocki VH., *J Am Chem Soc.*, 1996, **118**, 8365-8374
[129] Wysocki VH., Resing KA., Zhanga Q., Cheng G, *Methods*, 2005, **35**, 211–222
[130] Breuker K., Oh H-B., Horn DM., Cerda BA., McLafferty FW., *J Am Chem Soc.*, 2002, **124**, 6407-6420
[131] Adams CM, Kjeldsen F., Zubarev RA., Budnik BA., Haselmann KF., *J. Am. Soc. Mass Spectrom.*, 2004, **15**, 1087-1098
[132] Wysocki VH., Resing KA., Zhang Q., Cheng G., *Methods*, 2005, **35**, 211–222
[133] Huang Y., Triscari JM., Tseng GC., Pasa-Tolic L., Lipton MS., Smith RD., Wysocki VH, *Anal Chem B.*, 2006, **A-K**
[134] Harrison AG., *Mass Spectrom Rev.*, 1997, **16**, 201-217
[135] Demmers JAA., Rijkers DTS., Haverkamp J., Killian KA. And Heck AJR., *J Am Chem Soc.*, 2002, **124**, 11191-11198
[136] Deng Y., Pan H., Smith DL., *J Am Chem Soc.*, 1999, **121**, 1966-1967
[137] Jørgensen TJD., Bache N., Roepstorff P., Gårdsvoll H., Ploug M., *Mol Cell Proteomics*, 2005, **4**, 1910-1919
[138] Englander SW., *J Am Soc Mass Spectrom*, 2006, **17**, 1481-1489
[139] www.hxms.com designed and maintained by John R. Engen
[140] Hvidt A and Nielsen SO., *Adv Prot Chem*, 1966, **21**, 287-386
[141] Englander SW., Sosnik TR., Englander JJ., Mayne L., *Curr Op Struct Bio.*, 1996, **6**, 18-23
[142] Katta V., Chait BT., *J Am Chem Soc.*, 1993, **115**, 6317-6321
[143] Dempsey CE., *Prog Nuc Mag Res Spec*, 2001, **39**, 135-170
[144] Green MK., Lebrilla CB., *Int J Mass Spectrom and Ion Proc.*, 1998, **175**, 15-26
[145] Campbell S., Rodgers MT., Marzluff EM., Beauchamp JL., *J Am Chem Soc.*, 1995, **117**, 12840-12854
[146] Kaltashov IA., Eyles SJ., *Mass Spectrometry in Biophysics*, 1st Edition, Wiley Interscience, 2005
[147] Xiao H., Kaltashov IA., Eyles SJ., *J Am Soc Mass Spectrom.*, 2003, **14**, 506-515
[148] Kaltashov LA., *Int J Mass Spectrom.*, 2005, **240**, 249-259
[149] Pan J., Wilson DJ., Konermann L., *Biochem.*, 2005, **44**, 8627-8633
[150] Zhang Z., Smith DL., *Prot Sci.*, 1993, **2**, 522-531.
[151] Mandell JG., Falick AM., Komives EA, *Anal Chem.*, 1998, **70**, 3987-3995
[152] Komives EA., *Int J Mass Spectrom.*, 2005, **240**, 285-290
[153] Zhu MM., Chitta R., Gross ML., *Int J Mass Spectrom.*, 2005, **240**, 213-220
[154] Powell KD., Fitzgerald MC., *Biochem.*, 2003, **42**, 4962-4970
[155] Wang M., Shetty JT., Howard BA., Campa MJ., Patz EF., Fitzgerald MC., *Anal. Chem.*, 2004, **76**, 4343-4348
[156] Wear MA. and Walkinshaw MD., *Anal. Biochem.* 2006, **359**, 285-287
[157] Evans SE., Lueck N., Marzluff EM., *Int J Mass Spectrom.*, 2003, **222**, 175-187
[158] Robinson EW., Williams ER., *J Am Soc Mass Spectrom* 2005, **16**, 1427–1437

2 Experimental and Method Development

This thesis employs mass spectrometry to report on the solution structure(s) of peptides and proteins, and also to inform on their gas-phase structure(s). Comparisons between results found with each approach, are insightful, and here aim to determine which methods are most suited to MS based analysis of bio-molecular conformation.

Some of the techniques utilised within this chapter for maintaining non-covalent interactions are well established for examples see work by Robinson,[1] Loo,[2] Konermann,[3] Leary,[4] and have been discussed in Chapter 1. The method development process described in Section 2.4 is used principally for screening small synthetic molecule libraries, one part of a drug discovery program.

This only provides part of the picture. Although dissociation constants (K_ds) are easily calculated, change in protein conformation on ligand binding must also be considered. To this end, various approaches using HDX (reviewed in Chapter 1) are described below using solution and gas phase techniques. Method optimisation is discussed at length within this chapter.

2.1 Reagents

2.1.1 General Buffers

All buffer salts, unless stated otherwise, along with formic acid (FA) and trifluoroacetic acid (TFA), were obtained from Sigma-Aldrich, UK. Organic solvents were analytical HPLC grade and supplied by Fisher. High purity water was either supplied by Fisher or double distilled using a Sartorius Ultrapure Water System. pH was adjusted by the addition of ammonia solution or acetic acid accordingly. Solid reagents were weighed out to an accuracy of ±0.0010g using a Mettler AE550 balance. TBS was prepared using 20 mM Tris (2-Amino-2-hydroxymethyl-1,3-propanediol), 100mM NaCl (Fluka) and pH buffered to range from pH 2.5 – 12.2. 10

mM Phosphate buffer was prepared by mixing 25mM di-potassium hydrogen phosphate and 25mM potassium di-hydrogen phosphate to give pH 7.13.

2.1.2 Deuterated Buffers

Deuterated buffers (prefixed *d*-) were prepared using *d*-water and *d*-methanol (Sigma Aldrich, UK). *d*-Ammonium acetate was prepared by dissolving solid salt with *d*-water to a concentration of 10 mM. Buffering was carried out as described above and subsequent pH values were converted to pD values by the addition of 0.4.[5] *d*-Tris-Cl and *d*-phosphate buffers were prepared in the same way.

2.2 Mass Spectrometry – Sample Introduction

Manual methods for sample introduction are referred to as direct infusion (DI). Front end mechanisms involve both electrospray (ESI) and nanoelectrospray (nanoESI) ionisation.

2.2.1 Electrospray

ESI was carried out using an infusion pump (Harvard Apparatus, USA) coupled to the source probe. Typical flow rates ranged from 2 to 10 μL/min.

2.2.2 Nanoelectrospray

Pre-pulled gold coated nanoESI tips (Proxeon Biosystems, Denmark) were used along with glass capillary nanoESI tips (World Precision Instruments Inc.) which were prepared in house using a Sutter tip puller. Charge was applied to solution in the latter case via an inserted platinum wire.

2.3 Protein and Ligand Preparation

2.3.1 Cyclophilin (CypA)

Purified recombinant human CypA was supplied by members of the Walkinshaw group, University of Edinburgh, at concentrations the range 30 - 200μM.

2.3.1.1 Preparation

CypA was supplied in buffer containing 50 mM HEPES, 100 mM sodium chloride (NaCl). Concentrating protein solutions was occasionally necessary to ensure a stock of greater than 100μM and VivaSpin™ cartridges (Vivascience AG, Germany) with a 5 kDa molecular weight cut off were used to achieve this. Removal of involatile salts was carried out by dialysis into 10 mM ammonium acetate (NH_4OAc), pH 6.8 for a minimum 16 hours at 4°C with one reservoir change. Slide-A-Lyzer™ cassettes (Pierce) with a 3.5 kDa molecular weight cut-off were used for this purpose.

2.3.1.2 Quantitation

Quantitation was performed using both a Bradford assay[6] and Beer's Law with the extinction coefficient at 280 nm. The Bradford assay standard curve was calculated using bovine serum albumin (BSA) from 0.1 – 1 mg/mL. Cyclophilin solutions were diluted to obtain absorbencies at 595nm (A_{595}) in the linear region of the BSA standard curve.

The extinction coefficient (ε) at 280nm was calculated as 8490 $M^{-1}.cm^{-1}$.♥ Protein was diluted to produce solutions with absorbencies at 280 nm within the linear region of the Eppendorf Biophotometer (Eppendorf, Germany).

♥ Calculated in-house by Martin Wear

2.3.2 Cyclosporin

A fresh stock of Cyclosporin A (Clinical Grade, Novartis) was prepared every 4 - 6 weeks to ensure efficacy. Solid peptide was dissolved in methanol at approximately 5 – 15 mM and was stored at -20°C between uses.

2.3.3 Synthetic Ligands

All new ligands were synthesised by members of the Turner group, University of Edinburgh. Stocks of 10 mM were prepared in ethanol and stored at -20°C. Some ligand solutions contained various amounts of DMSO to aid solubility but all had final DMSO concentrations below 2% when used in the MS screen.

2.3.4 Melittin

Honey bee venom melittin (Sigma Aldrich, UK) was reconstituted in methanol or 10 mM ammonium acetate to 10 mg/mL (3.51 mM) and stored at -20°C. Fresh 10 μM solutions were prepared weekly in relevant buffers (as stated in Chapter 4) for DI-ESI and nanoESI analysis.

2.3.5 Insulin

1 mM Insulin (Sigma Aldrich, UK) stock solutions were prepared weekly. Solid was dissolved in 10 mM ammonium acetate pH 3.25 and incubation at 30°C. Increasing the pH above 4 at this concentration resulted in precipitation of the solid. Diluting the stock with solutions of pH 6.8 or 9 and, if necessary followed by pH adjustment enabled working solutions with the correct buffering environment. Working stocks ranging 10 – 200 μM were used.

2.3.6 Horse Heart Myoglobin (HHM)

300μM stock of horse heart myoglobin (HHM) (Sigma Aldrich, UK) in water was prepared and stored at 4°C. This was further diluted to 10 μM in 1:1 water : methanol for calibration purposes and, 10 mM ammonium acetate for analysis.

2.4 Protein - Ligand Screening

2.4.1 Dilutions

Stock CypA was diluted to 20 μM in 10 mM ammonium acetate and 10% methanol for ESI-MS analysis. Ligands were further diluted in methanol to a concentration 10 times that required in the final solution. For complexation of protein and ligands, a solution 9 parts protein in ammonium acetate and 1 part ligand in methanol were mixed together. The resulting solution was incubated at room temperature from 30 minutes to 2 hours. Various ratios were prepared and final concentrations are tabulated below in Table 2-1.

Protein (μM)	Ligand (μM)
20	20
20	40
20	100
20	200

Table 2-1 Protein : ligand dilutions for mass spectral analysis

2.4.2 Mass spectrometry

All in-house screening of complexes was performed using a ZMD Quadrupole mass spectrometer (Micromass, UK) fitted with an electrospray source. Additional analysis used a QTOF instrument (Micromass, UK). Parameters were controlled using MassLynx software version 3.5.

Nitrogen desolvation gas flow was approximately 300 L/h. The capillary probe was held at 3.5 kV and cone voltage at 50 V. The source block and desolvation temperatures were held at 65°C and 90°C respectively. All parameters were modified from conditions used in a previous study[7] aimed at retaining non-covalent interactions.

2.4.2.1 Flow Injection Analysis

Initial studies were carried out manually by direct infusion with a flow rate of 5 – 10 μL/min. One of the first hurdles to overcome was that of low signal / noise (S/N). To this end, the inter-ion scan rate was increased from 0.1 to 0.5 s and the acquisition scan rate was adjusted to 0.5 s for every 100 Da in the range. A compromise was necessary to keep sample consumption to a minimum whilst keeping the S/N ratio to a maximum. Analysis necessitated the use of near neutral, or 'pseudo physiological' pH to enable the detection of native state protein, ensuring biological relevance. At these higher pH values, charging of the sample is much lower and as such desolvation less efficient which also leads to peak broadening, a situation observed in similar studies.[8] Figure 2-1 demonstrates the need for noise reduction without compromising data integrity. The bottom trace is a typical example of raw data averaged over a 2 minute acquisition. The top spectrum shows the same data post Savitzky-Golay smoothing.

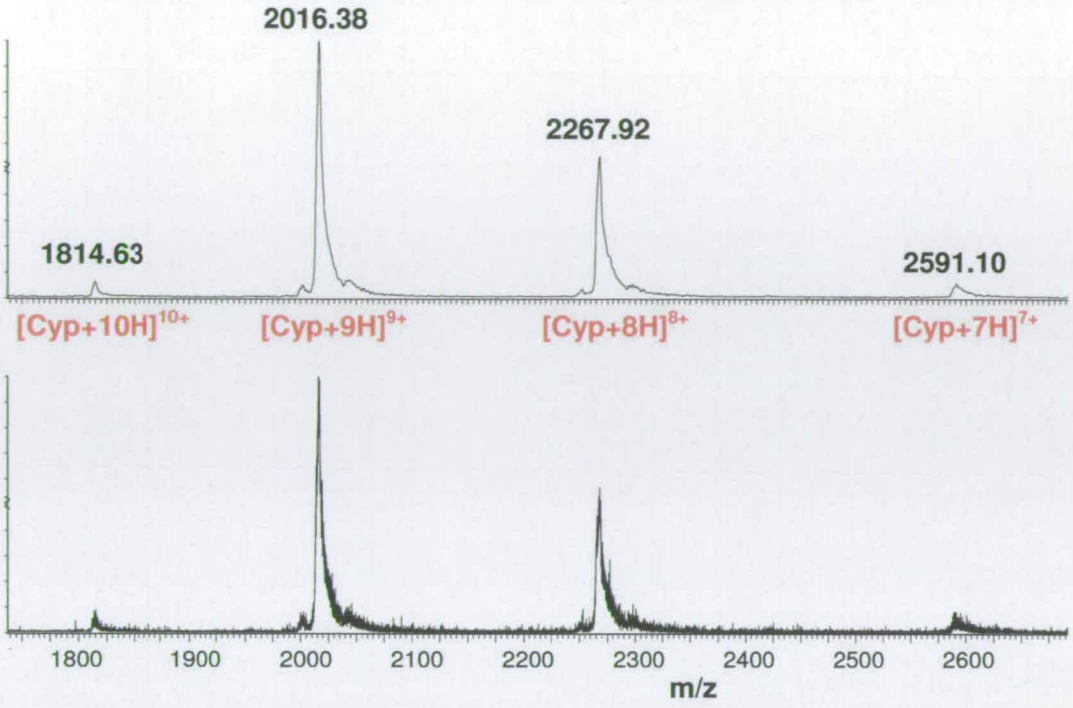

Figure 2-1 Charge state distribution of CypA obtained from 'pseudo native' buffering conditions.

High throughput analysis was carried out using a Waters 2700 autosampler coupled to a Waters 600 HPLC pump (Waters, UK) enabling on-line infusion to the ZMD. The mobile phases, 10 mM ammonium acetate pH 6.8 containing 10% methanol (buffer A) and 95% methanol and 5% water (buffer B), were purged with helium at 50 L/h to ensure de-oxygenation and a flow was maintained at 0.05 mL/min. 50 µL of sample was introduced per run. Source-block and desolvation gas temperatures were increased to 75°C and 120°C respectively to cope with the increased flow rate. It is noted here that complex integrity was not compromised with these increases. The dead volume within the system was approximately 2 - 2.5 min with complete peak elution being after a total of 5 minutes.

Running conditions were kept consistent with those used in manual analysis. As many of the ligands mentioned here were expected to have low binding affinities, the ionisation environment needed to be as non-destructive as possible. An isocratic gradient of buffer A was the first strategy employed. However, immediate washing

with buffer B was required to prevent cross contamination and, this rendered sampling efficiency to equal that of the manual rate (maximum 5 per hour).

Incorporation of a gradient was the obvious strategy to include a wash with high solvent to clean the sample loop and interface tubing (Table 2-2) whilst reducing run time.

Time (mins)	**A :** 10mM ammonium acetate / 10% methanol **(%)**	**B :** 95% methanol / 5% water **(%)**
0	100	0
2.5	100	0
3.0	0	100
3.5	0	100
5.5	100	0

Table 2-2 Initial gradient conditions for high throughput analysis

Carryover was still periodically evident when using the gradient. The peak itself had a tendency to drift when the gradient was applied which inferred an irregular mixing within the pumps. This was not all together unexpected as the HPLC system was working at its lowest limits possibly compromising back pressure. As a consequence, cross contamination was evident. All samples were automatically selected and subjected to the same gradient conditions. Figure 2-2 shows the chromatograms of 4 consecutive samples (run numbers 16 – 19 out of 50). Sample A eluted late at 5.0 min. Samples B and C eluted at the expected time of approximately 2.0 min and D were approximately 1.0 minute after C.

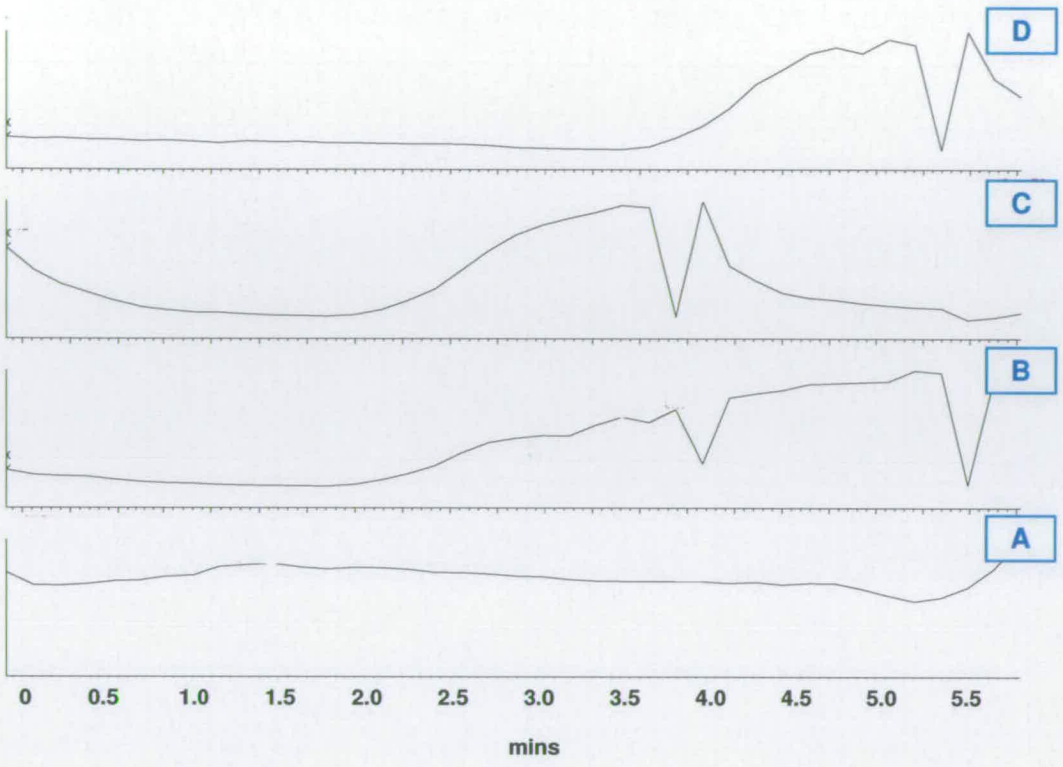

Figure 2-2 Total ion count chromatograms for 4 samples run consecutively from A) Run 16 to D) Run 19

Below (Figure 2-3) are corresponding spectra where sample A (run 16) shows evidence of the preceding sample (run 15) annotated *. This cycle repeats itself throughout the run of 50 samples.

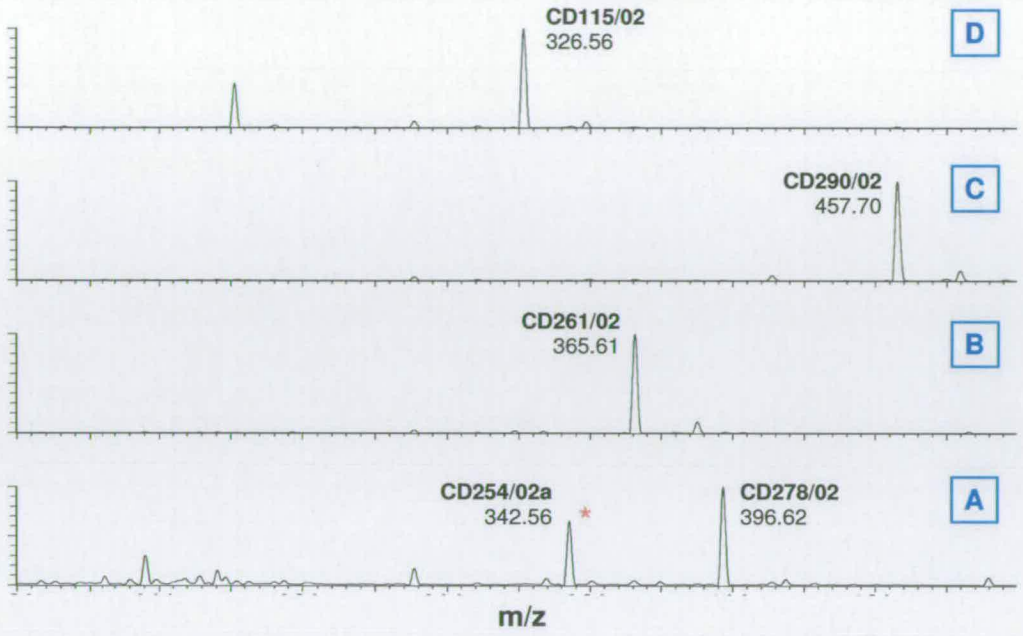

Figure 2-3 Spectrum showing ligand mass peaks detected under the corresponding elution peaks, A) Run 16 (* preceding ligand from Run 15, CD 254/02a), B) Run 17, C) Run 18, D) Run 19

The gradient was further developed to eliminate this issue. Initial changes involved bringing the gradient step forward by 30 s and increasing the length of time the high solvent step was held. This did not compromise complex formation as the dead time ensured no mixing of sample within the tubing. A subsequent increase in the re-equilibration time was incorporated post gradient. This latter step did not solve the peak drift issue but it did combat the sample carryover problem. Although not solved completely, care taken when extrapolating data from under the chromatogram peak itself did substantially reduce the problem. Increasing the time to 7 min did not significantly improve the elution drift and the re-equilibration time was reduced by 1 minute to give a final gradient time of 6 minutes. The delay time between one sample finishing and the next injection was approximately 1 minute.

The final method is tabulated below (Table 2-3). This allowed a sampling rate of 9 ligands per hour. All other MS parameters were maintained as described above and data was acquired in continuum mode.

Time (mins)	**A :** 10mM ammonium acetate / 10% methanol (%)	**B :** 95% methanol / 5% water (%)
0	100	0
2.0	100	0
2.5	0	100
4.0	0	100
5.0	100	0
6.0	100	0

Table 2-3 Optimised gradient for high throughput analysis

2.4.2.2 Nanoelectrospray

Manual low throughput nanoESI was carried out using a QToF I mass spectrometer (Micromass, UK) interfaced with MassLynx versions 3.5 and 4.0. Backing nitrogen pressure was applied to the tip to approximately 5 psi. The capillary voltage was slowly raised to between 0.8-1.6 kV to induce a steady spray to the cone which was set to 50V with the source block set to 65°C. Pressure in the collision cell was raised with the introduction of argon at 7-8 psi to reduce the excess kinetic energy of the projected ions.

The major benefit of using nanoESI was reduced background noise. A comparison of data collected by the different modes is shown in Figure 2-4. It is clear from the spectra that nanoESI produces cleaner spectra with the regulated spray of the NanoMate™ being superior.

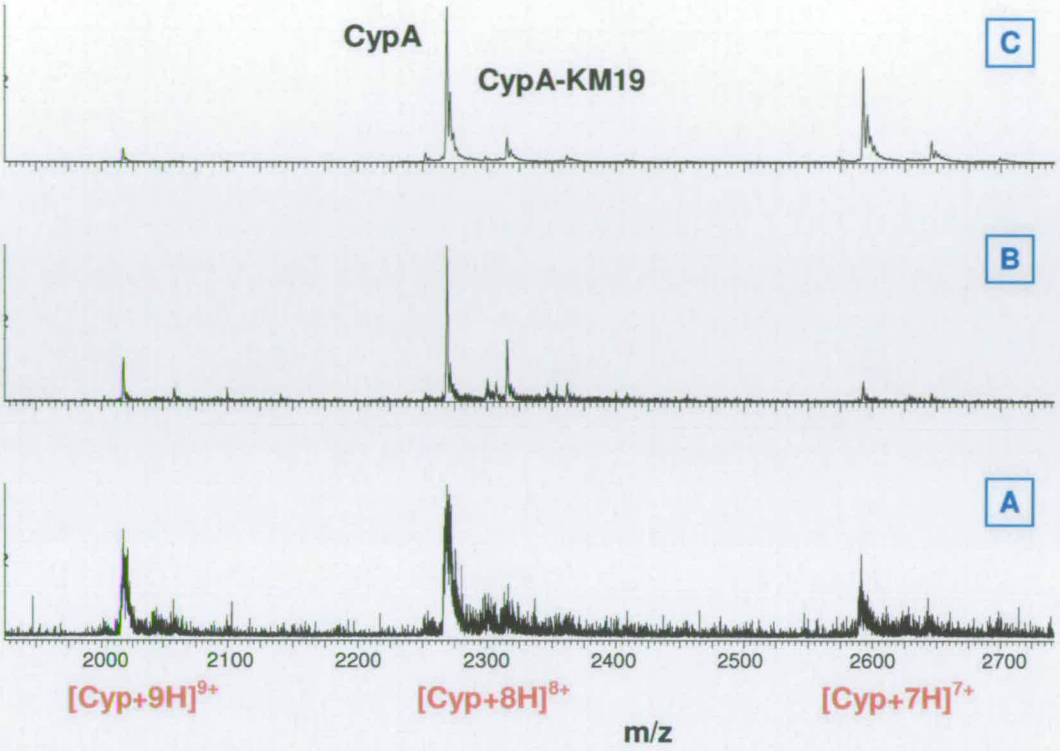

Figure 2-4 Spectra showing data collected by A) ESI-ZMD (S/N=1:6), B) nanoESI-QToF I (S/N=1:20) and C) NanoMate™ -QToF Micro (S/N>1:50)

High throughput nanoESI was carried out with the use of a NanoMate™ (Advion Biosciences, UK) coupled to a QToF Micro (Micromass, UK). NanoMate™ parameters were optimised to maintain reproducible desolvating conditions. Nozzle backing pressure was held at 0.3 psi nitrogen and nozzle voltage 1.7 kV. The calculated flow rate was approximately 200 nL/min. With data acquired in MCA mode over 2 min being averaged, an approximate acquisition rate of 24 samples per hour was achieved.

2.4.2.3 CID

CID analysis was performed using the Q-ToF I. Pressure in the collision cell was maintained at approximately 1E-5 Torr with 7-8 psi argon. An applied voltage ranging from 4 – 50 V increased the ions kinetic energy, promoting fragmentation of the complex.

2.5 Hydrogen/Deuterium Exchange (HDX)

Three different approaches are used, two solution based and one gas phase. The direct method involved incubating the protein in a deuterium rich environment and monitoring the mass shift over time on different charge states. An example of the $[M+4H]^+$ ion of insulin is given in Figure 2-5 below. The majority of exchange occurred within the first 3 minutes rendering much of the readily accessible labile hydrogens difficult to monitor. Whilst exchange rates are calculated using this method, a comparison of this data with that obtained via PLIMSTEX provides a picture of conformational dynamics in solution. By removing the variability found within the side chains and charge state dependent mass increases, a 'snap shot' of the protein in solution is obtained. Gas phase experiments provide further structural information by removing solvent from the environment.

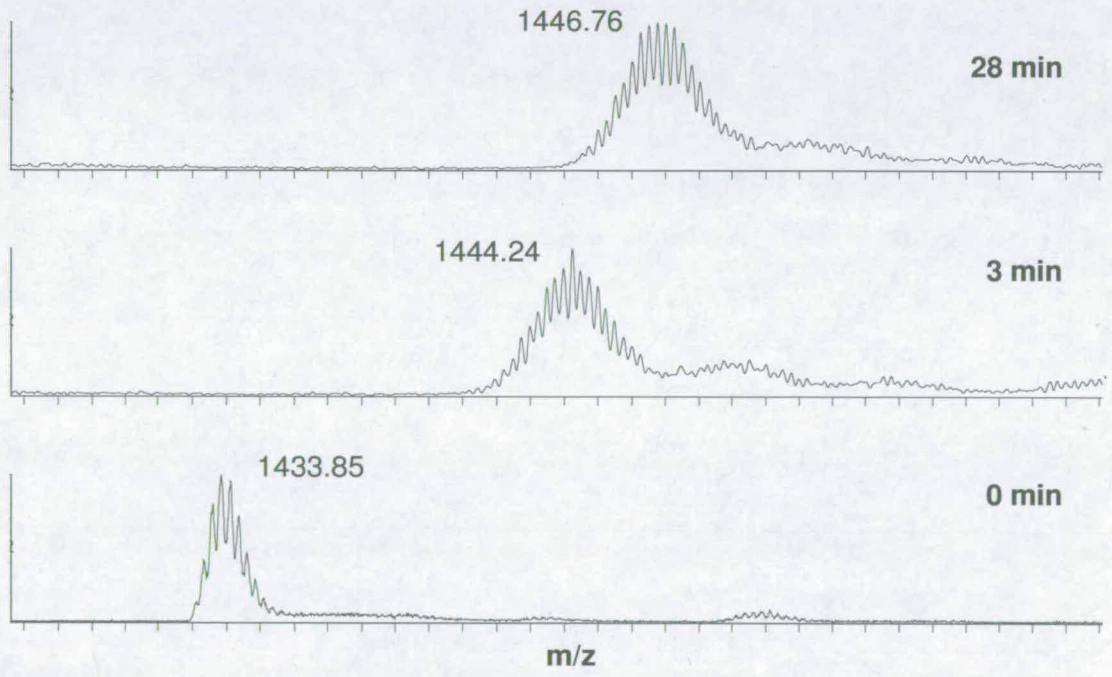

Figure 2-5 Monitoring mass shifts of insulin ($[I+4H]^{4+}$) over time by nanoESI

Using high resolution instrumentation providing isotopic profiles enables calculation of conformational distributions at a given charge state. The LCQ provides the lowest resolution data, followed by the QToF Ultima and 9.4T FT-ICR.

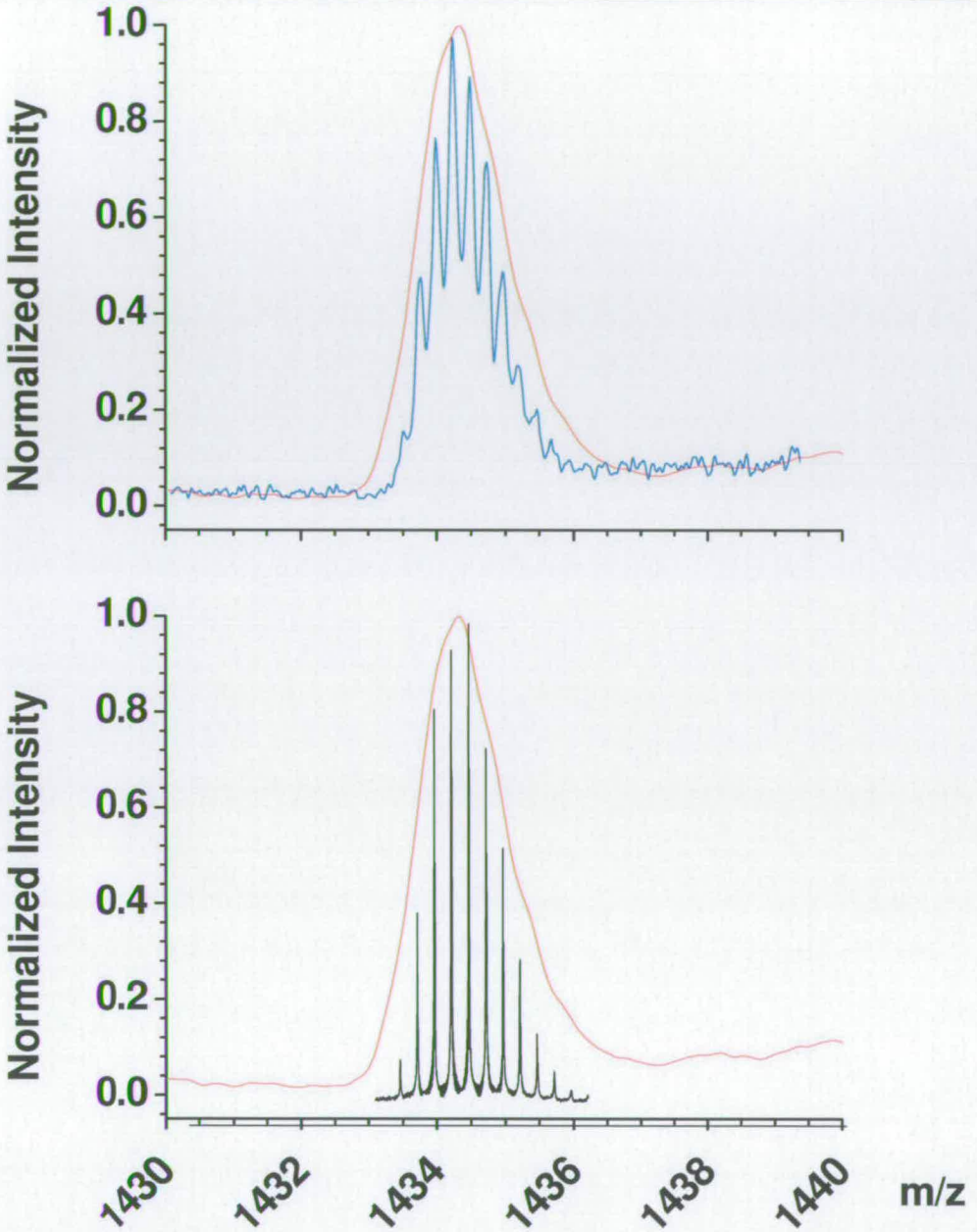

Figure 2-6 Insulin ($[I+4H]^{4+}$) with an LCQ (——) spectrum (Resolution: 2000) overlaid with QToF (—) (Resolution: 10000) and FT-ICR (—) (Resolution 150000) derived data

Above a height cut off of 40% the peak widths and shapes are comparable. Figure 2-6 illustrates this fact with the 4+ charge state insulin. In both examples, low resolution LCQ data is overlaid with each high resolution technique.

2.5.1 Mass Spectrometry – General Settings

An LCQ classic (Thermo Corporation, UK) was fitted with either an ESI or a nanoESI source. A sample flow rate of 3 μL/min with a nitrogen backing pressure of 40-70 psi for electrospray desolvation combined with an applied spray voltage of 4.5 kV ensured a steady aerosol. Capillary temperature was varied between 60°C and 200°C and the capillary and tube lens offset voltages were adjusted accordingly to maintain optimal ion transmission. Values were set to 40 V and 10 V respectively at 200°C and gradually increased to 80 V and 100 V respectively at 60°C. No drying gas was necessary for nanoESI, though a backing pressure of air flowing at 1.5-3 μL/min was used to initiate a steady spray with aqueous buffer conditions and lower capillary temperatures. The applied spray voltage was held at 0.8-1.8 kV. Capillary temperature and voltages were as described for electrospray. Optimal parameters for the ion optics (multipole assembly) were negatively charged for positive ion mode: multipole (1), -2.5 V; Lens, -20.5 V; multipole (2), -5.0 V. Very little adjustment was required between different protein systems. Injection times into the trap were kept to a minimum to prevent space charging effects and ranged 5 – 25 ms in full scan mode and 10 – 100 ms in isolation (MS^n) mode.

All analyses using the QToF Ultima (Micromass, UK) were carried out using nanoESI. Backing pressure was kept below 5psi. The capillary spray voltage was held to between 0.8 and 1.8 kV, cone voltage 40 – 60 V and source block temperature at 65°C. The crucial setting to maintain isotopic resolution was the entrance value, which was optimised to 53. A table containing all parameters can be found in Appendix C.

All analyses carried out using the FT-ICR were in ESI mode. The heated capillary was held at 150°C and the spray voltage 3 kV.

2.5.2 Solution Phase Hydrogen / Deuterium Exchange (HDX) – Direct Infusion

A combination of DI-ESI and self pulled tips for nanoESI were utilised for direct analysis.

2.5.2.1 Sample Preparation

All proteins were diluted using *d*-buffers from non *d*-stocks. A minimum dilution factor of 10 was used. However where possible, factors of 50 and 100 were used. Maximum exchange is limited to the dilution factor and differences in mass shifts can be seen as such in a mass spectrum. Examples of varying the proportion of *d*- to non *d*- buffer are shown in Figure 2-7 where d = 10%, 60%, and 90%, equating to sample dilution factors of 9 in 10, 2 in 5 and 1 in 10 respectively.

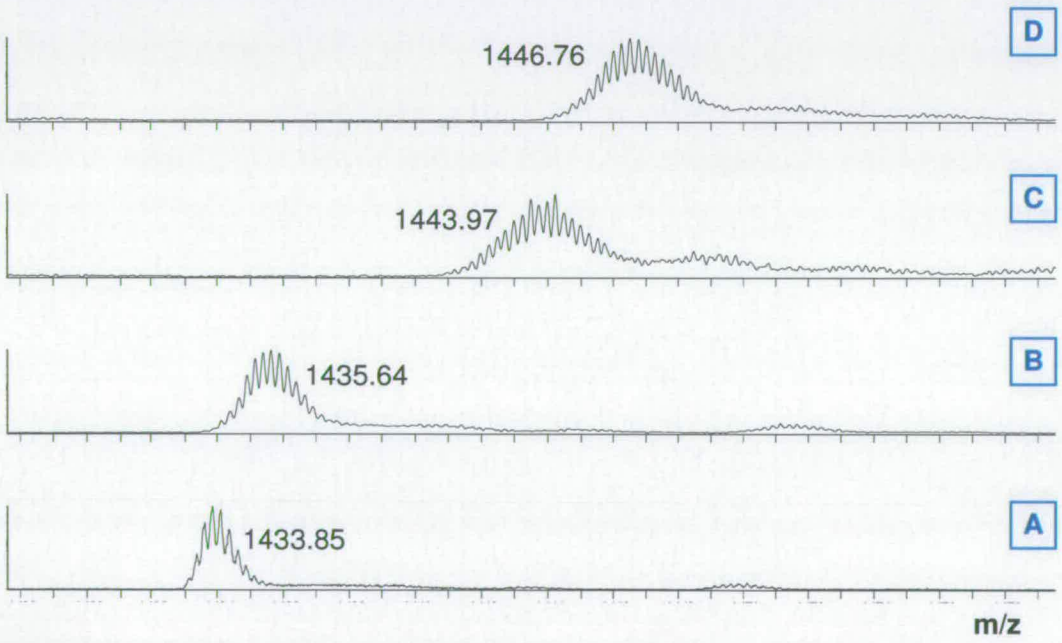

Figure 2-7 Insulin HDX incubated for 26 minutes with varying concentrations of deuterated buffer i.e. A) 0%, B) 10%, C) 60% and D) 90%

2.5.3 Solution Phase Exchange – PLIMSTEX

Protein stocks were diluted to give concentrations ranging 100-500 pM in relevant *d*-buffers. All buffers and samples were incubated on ice at all times. Pictures are shown below of the two cooling systems utilised.

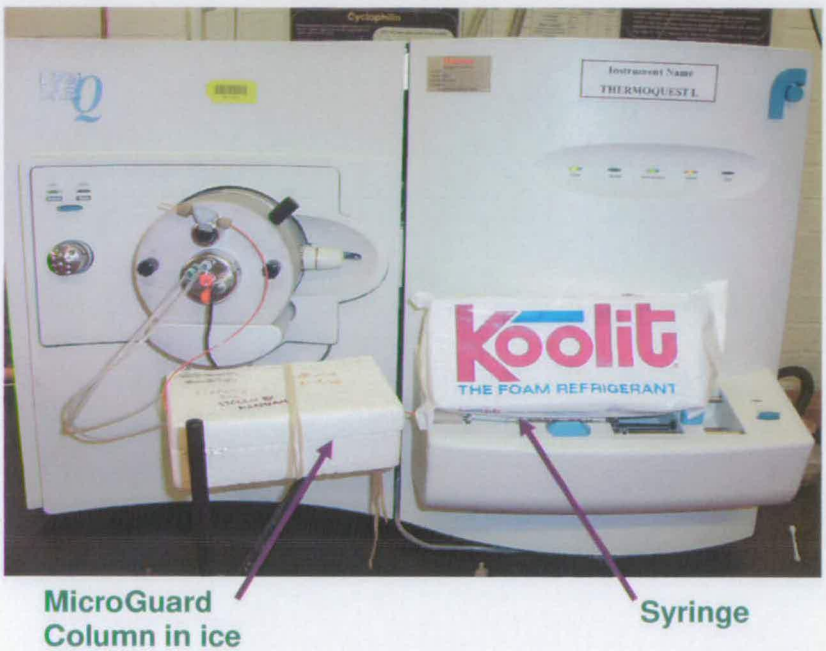

Figure 2-8 Cooling Scheme I : ice

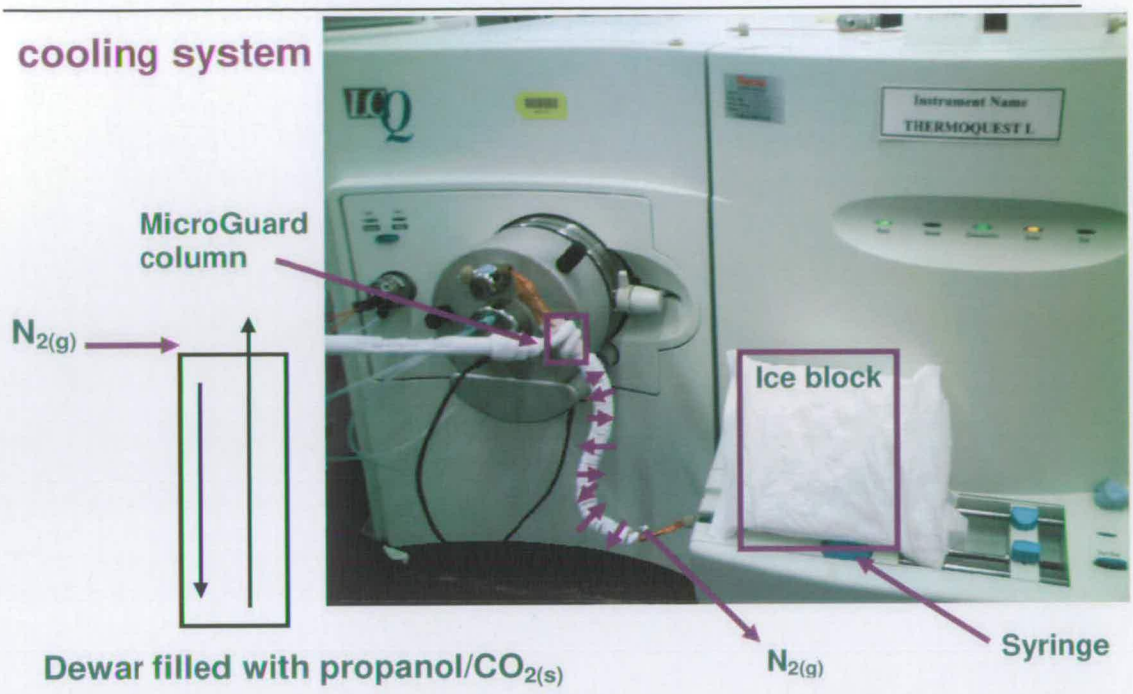

Figure 2-9 Cooling Scheme II : nitrogen coil

The infusion syringe was cooled using an ice pack in both schemes along with keeping transfer PEEK™ tubing to a minimum to limit warming effects. Scheme I (Figure 2-8) demonstrates the column being incubated in ice which, although effective was not as robust as scheme II (Figure 2-9). The cooling system here comprised nitrogen flowing at a pressure of 40 psi through a copper coil pre-cooled in a carbon dioxide / propan-2-ol bath connected to a steel coil jacket surrounding the PEEK™ tubing and column. The majority of the experiments were performed with the LCQ, but where stated, an FT-ICR was used providing isotopic distributions (Figure 2-6).

Samples were incubated in relevant *d*-buffer (prepared as described in Section 2.1.2) where stated at room temperature or on ice. Sample was briefly cooled on ice prior to quenching with 2 µL of cold 1M HCl per 50 µL sample. Loading onto the column (MicroGuard™ C_{18} (melittin), C_8 (insulin), C_4 (CypA), Amersham Biosciences) was achieved by infusion at 1500 µL/min with eluent going to waste. Washing (94% water / 5% acetonitrile / 1% formic acid) of sample on column to remove any salt

impurities and enable amino acid side chain back exchange was optimised for each protein system (Section 2.5.3.1). Flow was connected to the mass spectrometer for on-line sample elution (95% acetonitrile / 4% water / 1% formic acid).

The LCQ nitrogen drying gas was held at 100 psi and the capillary temperature was set to 200°C to ensure effective desolvation. Spray voltage, capillary voltage and tube lens offset voltages were set to 4.5 kV, 40 V and 10 V respectively. Injection time into the trap was 5 ms for full scan and isolation (MS^2) mode.

FT settings were as described in Section 2.5.1.

2.5.3.1 Back Exchange

The most important part of the method to optimise was the back exchange or washing step. The first setup was wholly manual with only the elution being controlled using an infusion pump. As such, initial experiments on CypA followed the strategy that time exposed to non *d*-buffer would be kept to a minimum. Therefore, the wash time was fixed at 30 – 40 s in keeping with literature values (Zhu *et al.*[9]) and the volume varied.

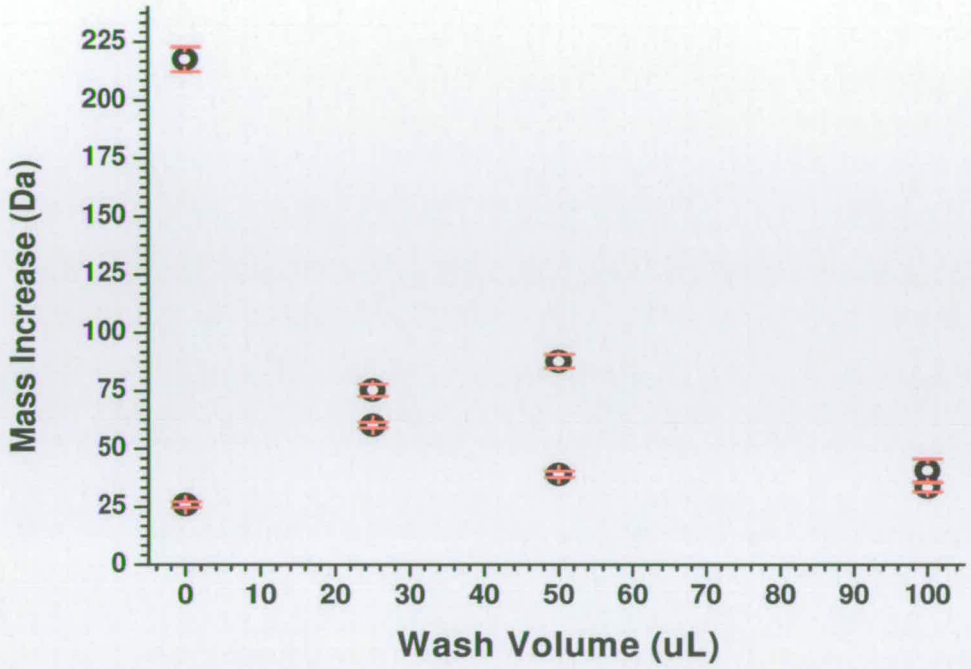

Figure 2-10 Graph of mass increases for CypA averaged over 10 charge states with a fixed washing time (30 – 40 s)

The results shown in Figure 2-10 indicated that this approach was not analytically robust. However, it did suggest some reproducibility across the 30 s time scale. The approach was modified by adjusting washing times and fixing the flow rate but, deviated from the published method by using native wash buffer (10 mM ammonium acetate, pH 6.8). The method was to be used for calculating binding constants of CypA with some of the ligands assayed in Section 2.4. The aim was to titrate ligand into the protein solution, bind the complex to the column, then wash excess ligand away and calculate back exchange rates. The preliminary data is presented in Figure 2-11.

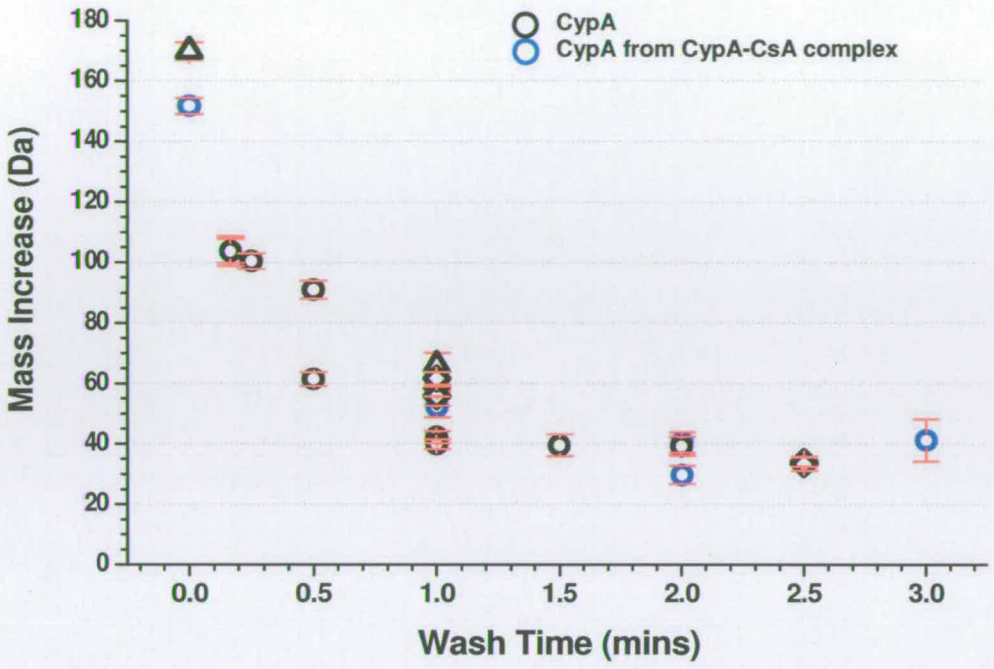

Figure 2-11 Preliminary back exchange of CypA with native washing conditions

Each data point comprises an average of 6-8 charge states. The black symbols represent data derived from *d*-CypA only with increasing washing times and, blue symbols from an incubation of *d*-CypA-CsA. Reassuringly, the error bars (red) indicate very little variation between charge states. There is a rapid decrease of approximately 100 Da between zero and 1 minute of native washing with no significant difference between protein only and protein which was part of a complex. At 1 – 1.5 min, the number of deuteriums levels off at around 40 with approximately 120 of the 160 being readily back exchanged.

In hindsight the data presented here raised the question as to the effect of pH on the back exchange rate. A comparison of data collected using these preliminary CypA experiments with data obtained under further optimised washing conditions (Figure 2-12) is discussed in Chapter 4.

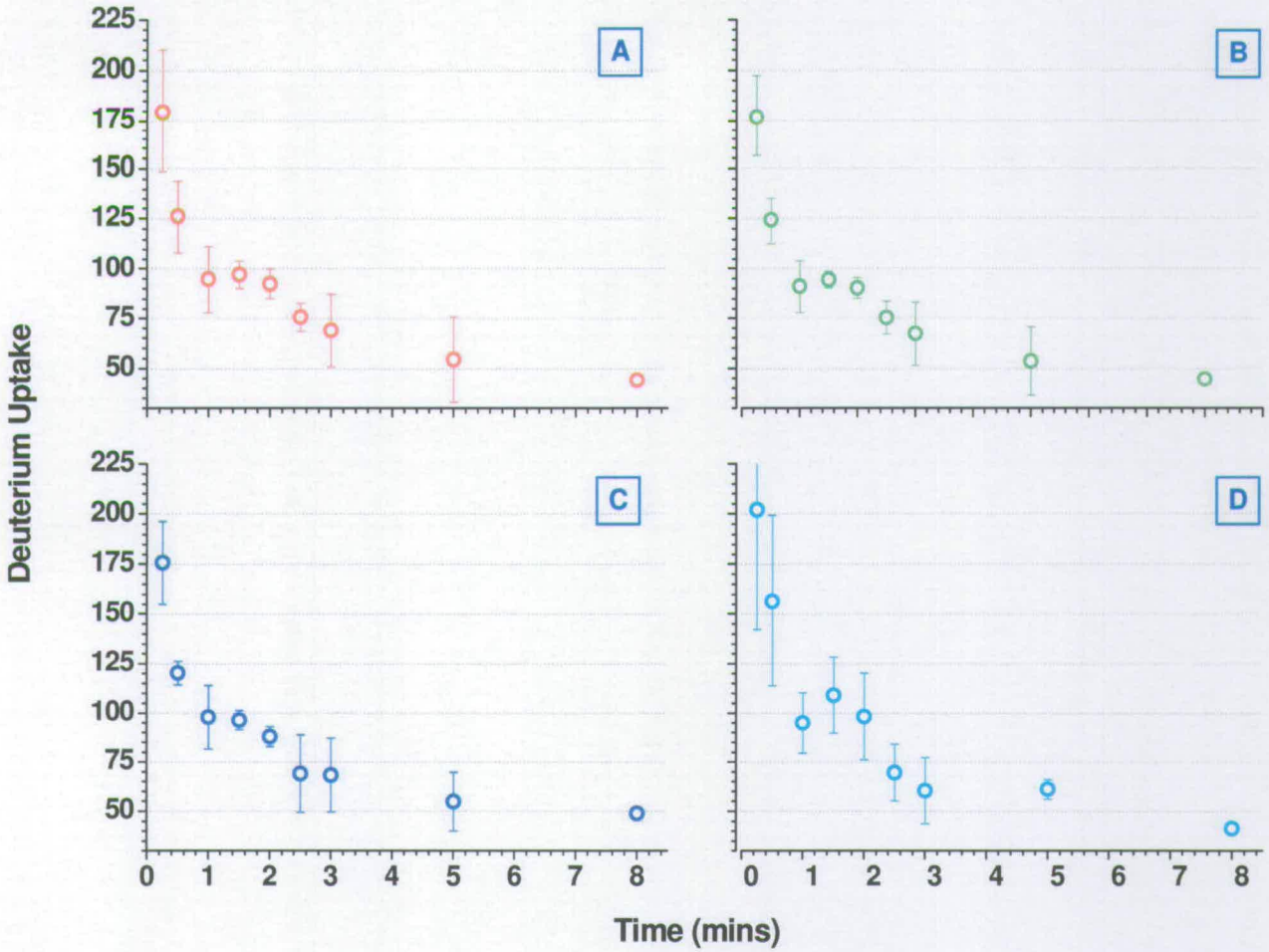

Figure 2-12 Modified back exchange time course of CypA on 4 representative charge states of A) $[Cyp+18H]^{18+}$, B) $[Cyp+19H]^{19+}$, C) $[Cyp+20H]^{20+}$ and D) $[Cyp+22H]^{22+}$

Protein was incubated in relevant *d*-buffer for approximately 1 hour to ensure full exchange. Once on the column, wash solution was infused for increasing periods of time. The back exchange begins to plateau between 60 and 120 s in Figure 2-12 and, it is over this range that the standard deviation also decreases. If there are no available side chain deuteriums left to back exchange, only the less labile amide backbone deuteriums remain. It is then safe to assume in this instance that approximately 100 backbone hydrogens are exposed and labile in 10 mM *d*-ammonium acetate, pD 7.2. The wash time was adjusted accordingly to 90 s to account for this. There is no distinct difference between charge states 18+, 19+ and 20+. Some inconsistency can be seen for charge state 22+ but this is explained by variable peak quality. This result can be compared to Figure 2-11 where back exchange also plateaus at 1 minute 30 s though the masses differ.

For insulin analysis, loading and elution parameters here optimised with CypA, were retained as proposed by Zhu *et al.*[9] who used the same fixed wash time of 30 s for all protein systems regardless of size or complexity.

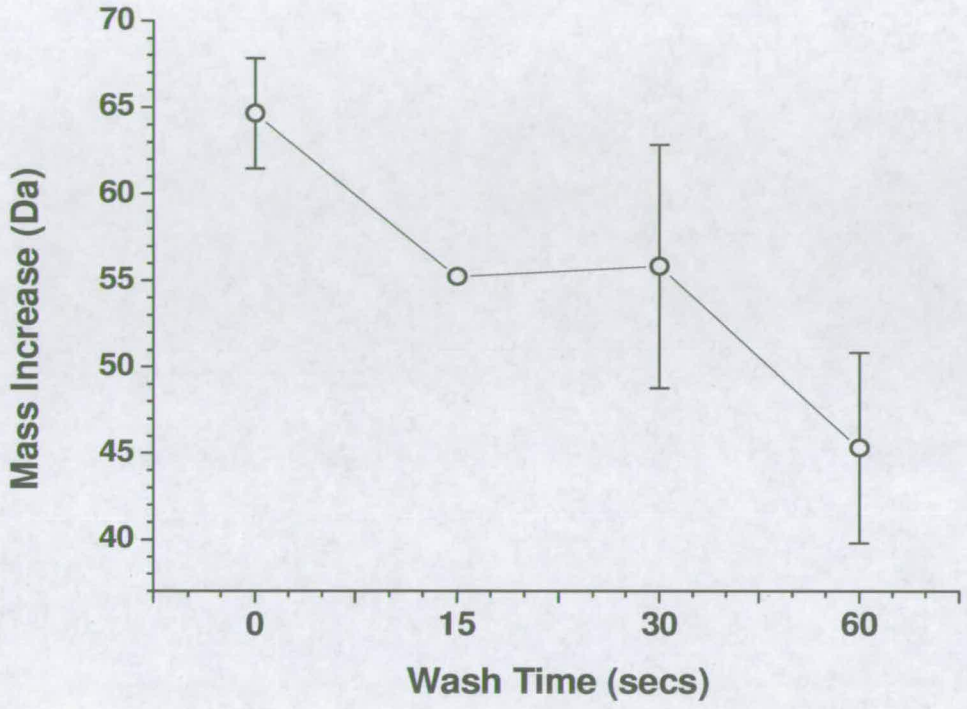

Figure 2-13 Back exchange of insulin on column with increasing time

A wash time of 30 s was used for insulin, where the mass increase does level off (Figure 2-13). The maximum number of labile amide hydrogens is 49. At the time of performing this study it was believed that the insulin had undergone full exchange prior to analysis and therefore the mass increase seen was due to technique variability. It should be noted here that there were issues with reproducibility even with an automated method.[10]

Insulin and CypA data collected using both the LCQ and FT-ICR mass spectrometers are discussed in later chapters and back exchange conditions for these purposes were directly comparable.

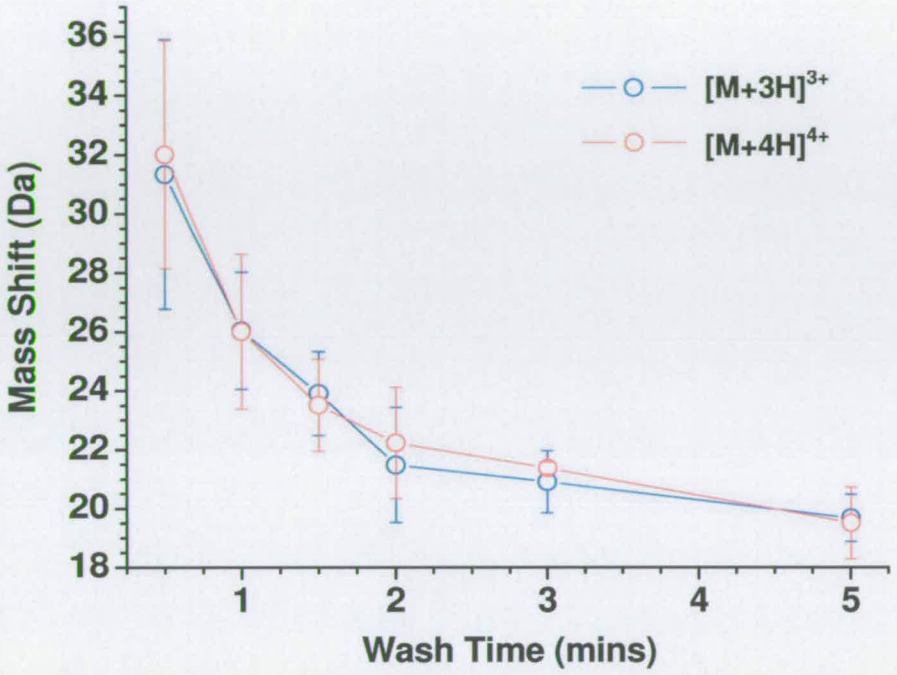

Figure 2-14 Back exchange of melittin with a maximum 5 min wash step

The final protein system studied using the PLIMSTEX technique was melittin. As expected, there is no distinction between the 3+ and 4+ charge states of melittin (Figure 2-14). The amount of exchange begins to plateau after a wash time of 2 min. This, coupled with the standard deviation at 3 and 5 min being reduced, draws the conclusion that all deuterated side chains had been back exchanged to hydrogens. Only the less labile deuteriums (i.e. amide backbone) remained which began to undergo further back exchange at 5 min. Subsequently, a wash time of 3 min 30 s was used for all melittin experiments. From these data, 22 of the maximum 24 amide hydrogens are labile in aqueous conditions (10 mM ammonium acetate, pH 6.8). This was unexpected as data obtained by circular dichroism showed no evidence of secondary structure. It was however later supported using molecular dynamics. These phenomena are further discussed in Chapter 5.

2.5.4 Gas Phase Exchange

2.5.4.1 Inlet Development

Gas phase HDX was achieved by modifying the helium inlet system on the LCQ. Various systems were tested. The first two setups are shown in Figure 2-15. Degassed *d*-water was allowed to diffuse into the trap by taking advantage of the pressure differential and also the aid of heating tape wrapped around the glass bulb reservoir (path A). This proved unsuccessful and the solvent was switched to *d*-methanol. No heating was required and the amount of solvent entering the trap was controlled using the needle valve. The lack of helium in the trap reduced peak resolution considerably and peak broadening became an issue. It was unclear at this stage if this was solely due to methanol being an inefficient dampening gas or partly caused by unresolved issues in trap pressure. To try and overcome this issue an extra helium line was added with the aim of obtaining a helium / *d*-methanol mix (path B).

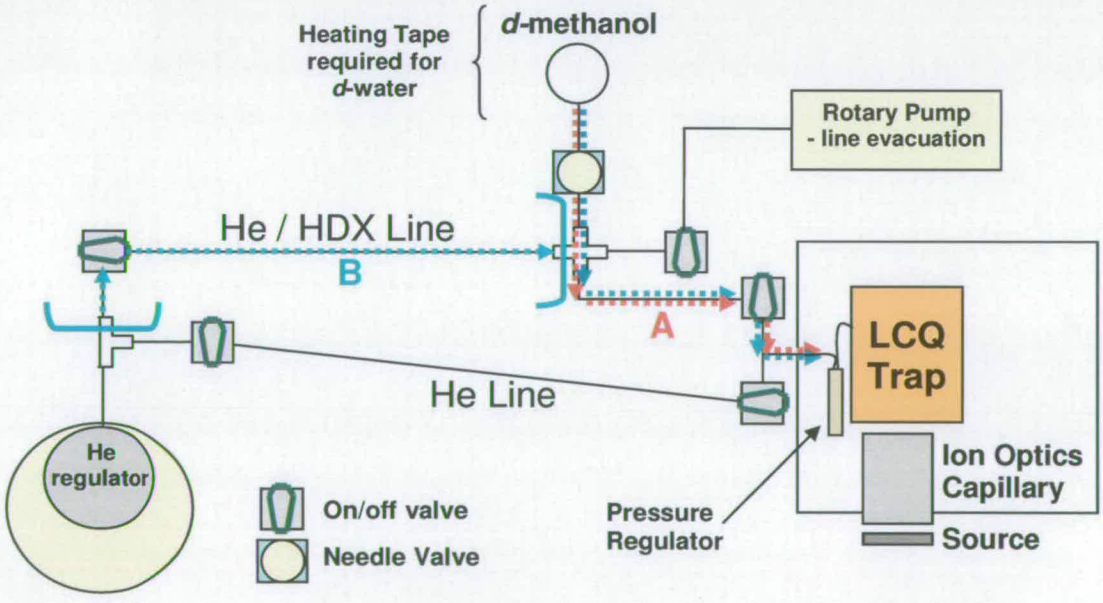

Figure 2-15 First HDX inlet system (A) for enabling the introduction of *d*-water or *d*-methanol into the quadrupole ion trap was later modified to path B

The system shown in Figure 2-16 is almost identical to path B. The crucial difference is the presence of the needle valve denoted NV which was used to adjust i.e. reduce helium flow prior to solvent introduction.

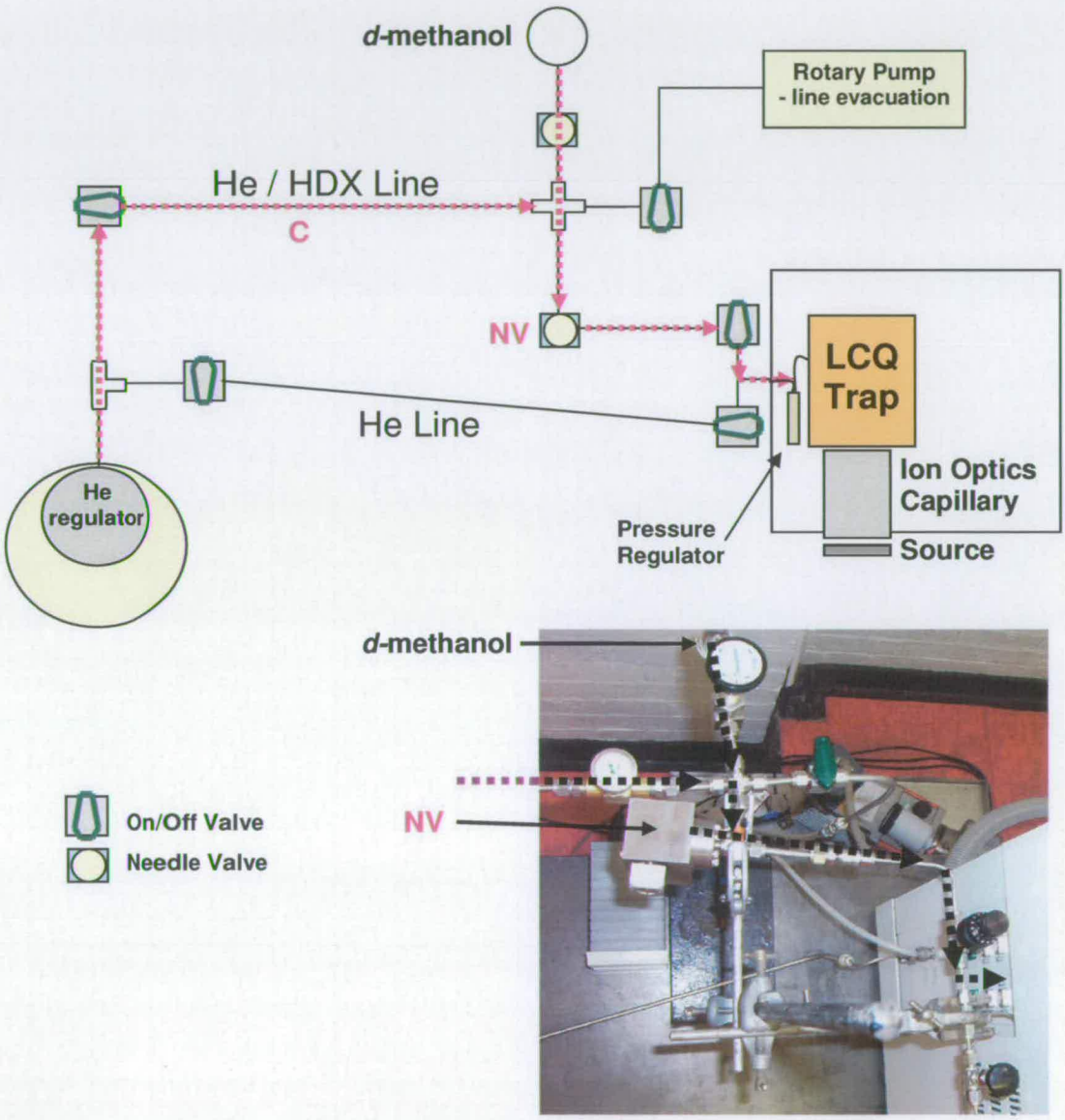

Figure 2-16 Third set up of inlet system (**C**) with helium / d-methanol pressure regulated using needle valve **NV**

The partial pressures of both gases (helium and *d*-methanol) were disproportionate. An apparent increase in pressure relative to helium would be expected on the addition of methanol. This was not seen, so it was assumed the flow of helium dominated, suppressing the incorporation of *d*-methanol. Flooding the trap with *d*-methanol first, reduced the problem but did not solve it completely.

The next course of action involved helium having direct contact with the *d*-methanol by enabling the gas to bubble through the solvent. The first prototype utilised a glass reservoir which proved to be extremely fragile so this was substituted for metal. Figure 2-17 shows the two prototypes with a schematic of the bubbler itself.

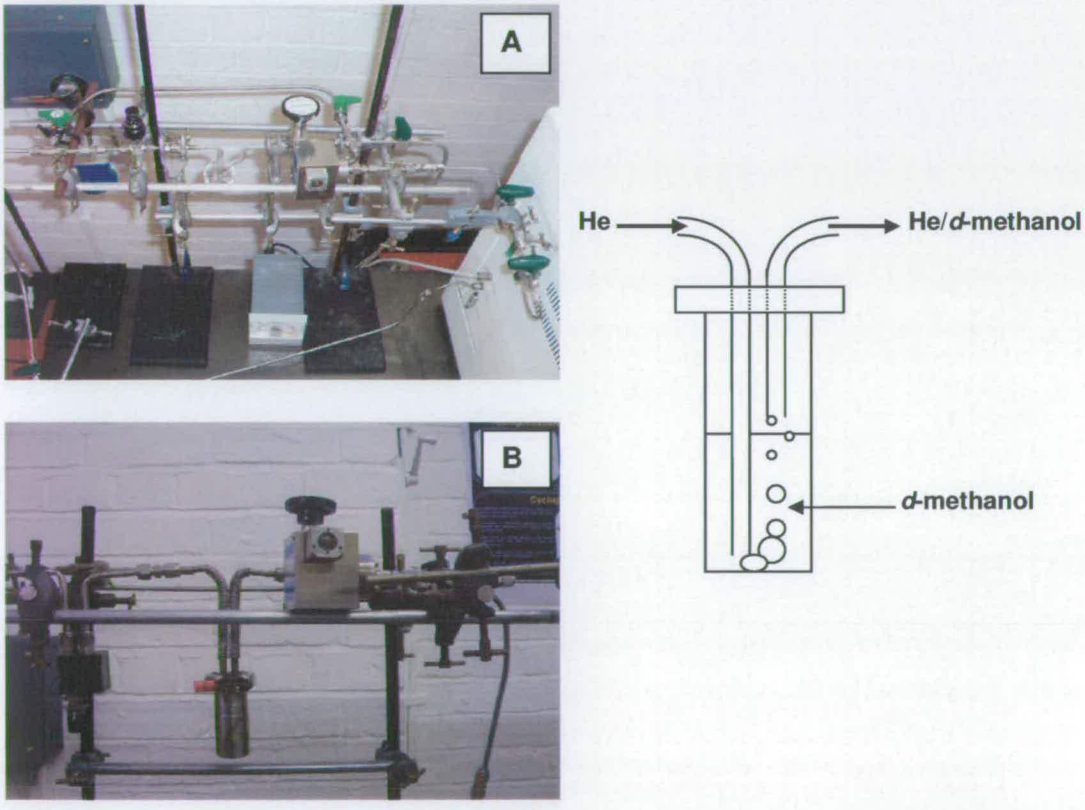

Figure 2-17 Prototypes for the bubbler **A** (glass) and **B** (metal) with an illustration of the bubbler structure

Images of the final inlet system are shown below in Figure 2-18. Helium was regulated at the cylinder head to 40 psi. With a capillary temperature of 200°C, pressure in the trap was calibrated daily to 2.5 – 2.7 E-5 Torr through the He / HDX line using the needle valve. Valve A on the He / HDX line was closed off and the gas redirected to bubble through the solvent reservoir containing *d*-methanol. The system was allowed to equilibrate for 45 min to 1 hour and the ion gauge reading increased to 2.9 - 3.0 E-5 Torr.

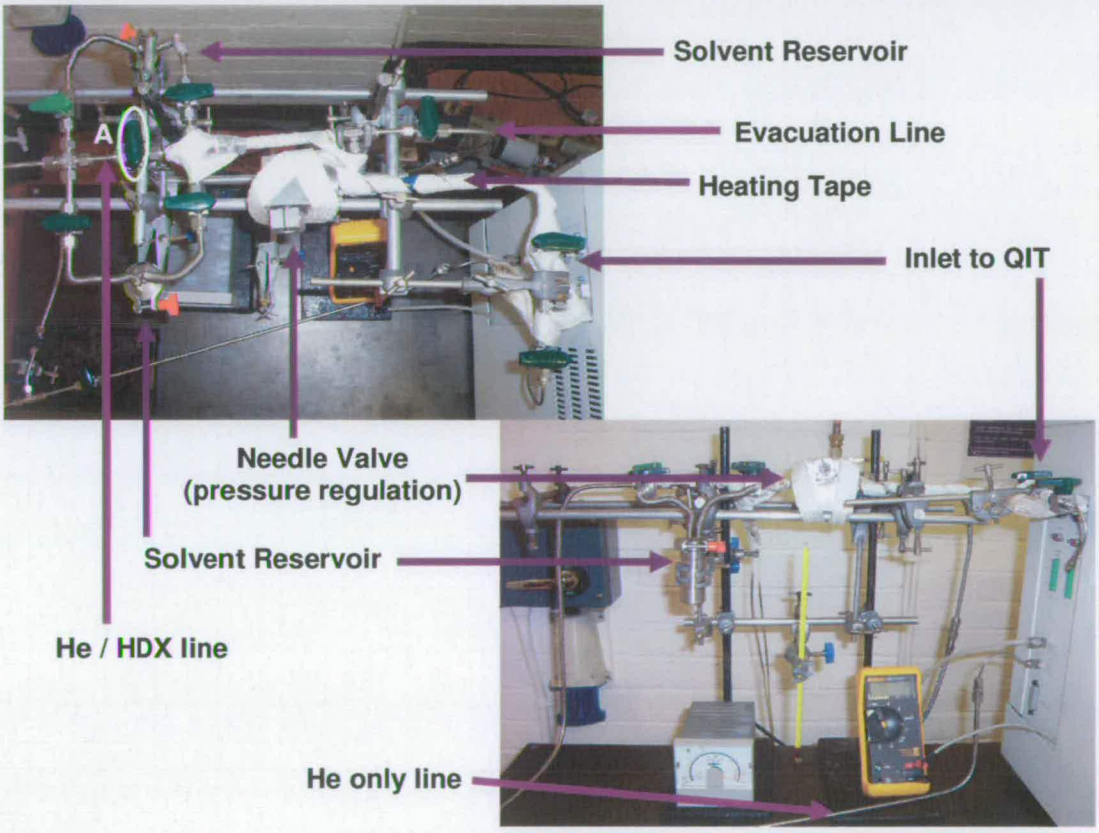

Figure 2-18 Schematic of HDX inlet system

Unless otherwise stated, no further adjustment was required. Pressures above this range at this temperature resulted in mass shifts not attributable to HDX. All proteins were

analysed under *d*-solvent free conditions prior to exchange on a day of analysis. This setup has the facility to switch between different solvents by the presence of two reservoirs. Controls were run using non *d*-methanol to determine the mass of ions over the full range of activation times.

Initial melittin studies used ESI however, nanoESI became the favoured method to minimise desolvation effects on structural integrity. All settings on the LCQ were as described in section 2.5.1.

2.5.4.2 Cell Pressure

There was evidence to suggest that mass shifts of ions were affected by the pressure in the trap. Figure 2-19 illustrates the mass shift found with increasing pressure. The trap was optimised to approximately 2.5 E-5 Torr as it was both easy to obtain and maintain and as a result the signal was found to be stable and reliable.

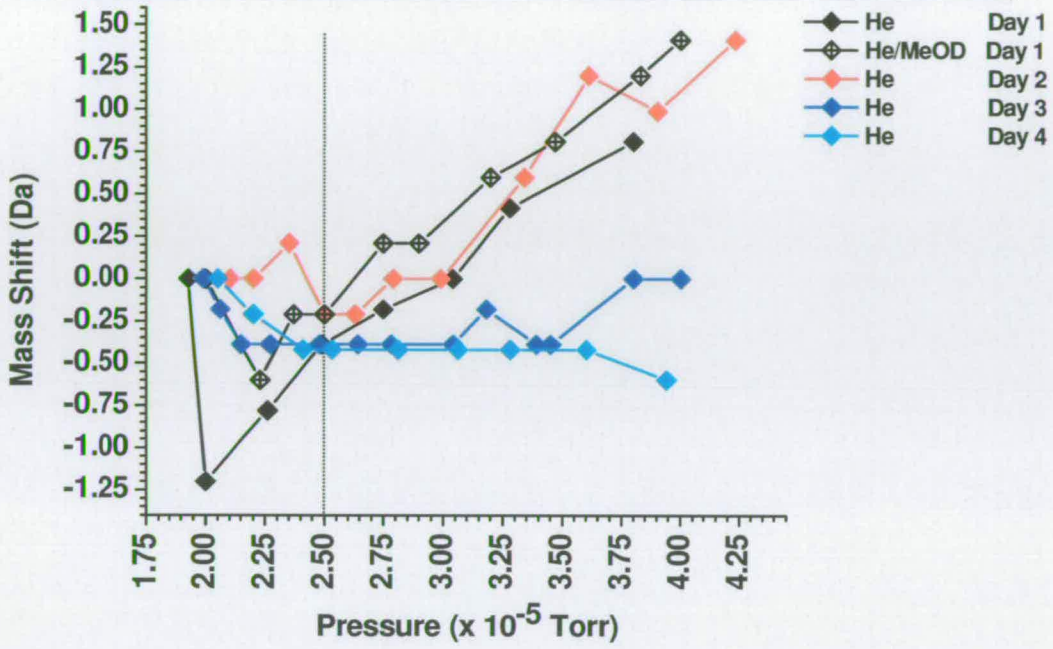

Figure 2-19 Apparent mass shift of melittin ($[M+3H]^{3+}$) with increasing cell pressure with over 4 days

Melittin was analysed by varying the trap pressure using the needle valve. Except for day 1, all readings were taken with helium only in the trap. The latter two days show no significant mass shift whereas days 1 and 2 give a shift of 1.5 Da at 4.00 – 4.25 E-5 Torr. These results show that a pressure effect could not be ignored, although under these conditions it was small. Daily calibration minimised any effect this may have caused.

2.5.4.3 Activation Time

The activation time (AT) determines the length of time ions are retained in the trap. This is defined by the 'tickletime', a term used to describe the length of time between which energy is applied to the ions, which is also necessary to expel unwanted ions, resulting in isolation of the desired species. The AT for full scan mode is controlled by the graphical

user interface (Xcalibur software version 1.2) and as such is fixed at 30 ms. No H/D exchange was detectable under these conditions (Figure 2-20).

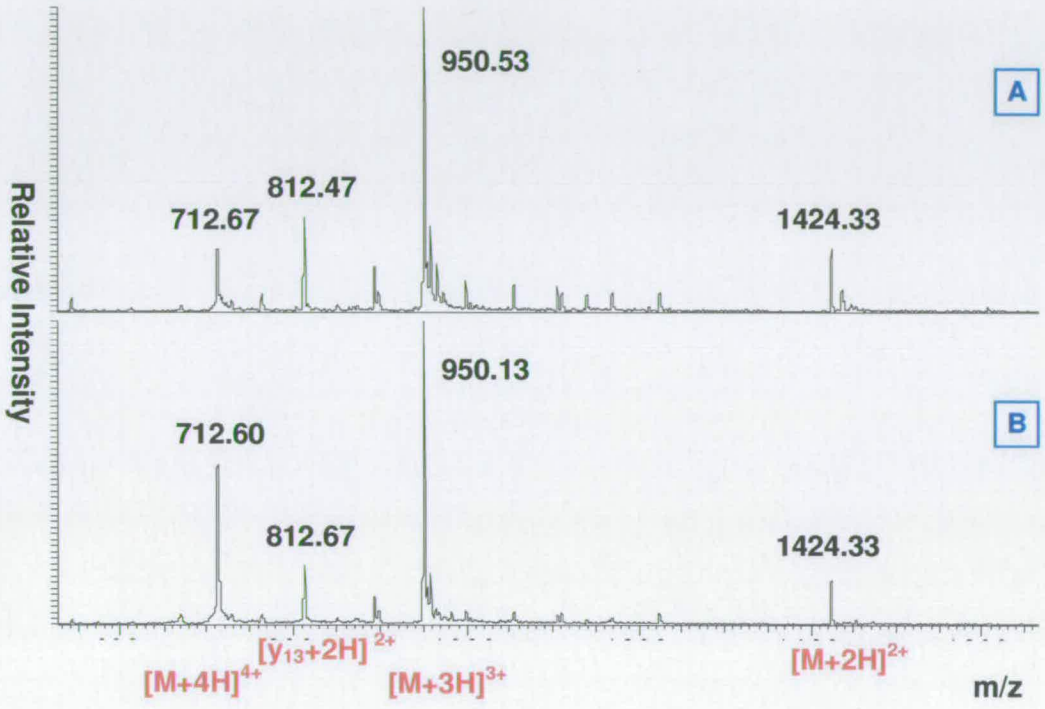

Figure 2-20 Spectra of melittin illustrating lack of gas phase HDX in presence (A) and absence (B) of *d*-methanol in trap during full scan mode (AT = 30ms)

For gas phase exchange studies the ion of interest was isolated (MS^2) and the AT adjusted at intervals from 10 – 10'000 ms. 10 scans were averaged for each AT and the masses plotted. To increase trapping time beyond 10 s, the software made it necessary to perform a re-isolation step. The application of rf required for isolation caused a larger than expected mass increase which is attributed to disruption of the conformation – due to heating. A typical example is illustrated in Figure 2-21 where a plot of increase in mass against AT shows anomalies across each isolation level. Apparent mass shifts i.e. assumed uptake of deuterium, is greater immediately post isolation compared to longer

ATs at the same level. It is also evident that reproducibility is best during the first isolation step inferring the exchange mechanism is consistent, thus implying a uniform structure. This uniformity has visibly decreased by the third (MS^4) isolation. As expected, the rate of deuterium uptake is exponential, levelling off below the maximum. In this example it is unlikely to be due to retained structure but can be attributed either to hydrophilic collapse rendering some hydrogens unavailable or, related to the exchange mechanism becoming less efficient over time with less hydrogens left to exchange.

Melittin, insulin and CypA were studied using gas phase HDX and the effects of exchange in a solvent free environment are discussed in the following chapters.

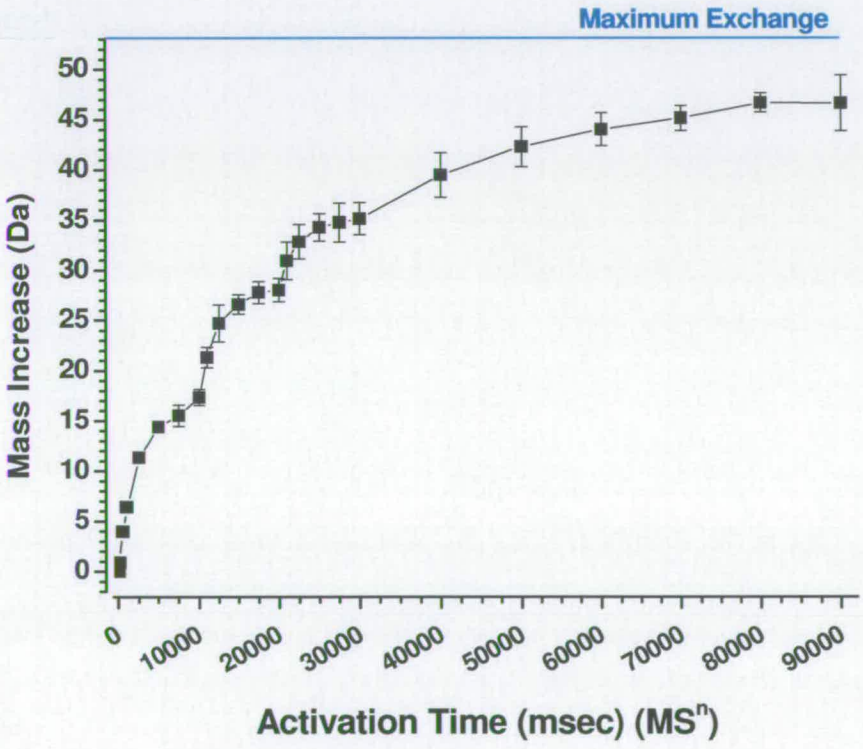

Figure 2-21 Mass increases for $[M+3H]^{3+}$ melittin with increasing ATs with re-isolation every 10000 ms

2.5.4.4 Mass Isolation Width

Isolation sometimes resulted in detection of a peak mass slightly different to that seen in full scan mode. For this reason, the mass isolation width and injection time were optimised. A width of 10.0 Da was to isolate the peak of interest reliably and reproducibly. For smaller proteins and peptides with *m/z* values below 2000Da a width of 5.0 Da was adequate. However, a broader width ensured all relevant ions were retained thereby helping to distribute the applied energy.

2.5.4.5 Activation Q

The Q value was adjusted to obtain optimal fragmentation for CID. Although it largely only affected the acquisition *m/z* range, it was thought to have a bearing on the energy distribution over that region. The instrument was calibrated to a value of 0.5 which was maintained for fragmentation of melittin $[M+3H]^{3+}$ although a value of 0.25 was used for $[M+2H]^{2+}$ melittin. 0.5 was maintained for CypA and insulin though CID had only limited success.

2.5.4.6 Injection Time (IT)

A balance between S/N and ion count in the trap was obtained using the injection time (IT). A high value caused peak broadening, mass shifts not attributable to exchange, potentially creating non covalent complexes and, in the case of CypA, detrimental to overall ion signal. Values of 10 – 15 ms were used for melittin and insulin and, 50 – 75 ms for CypA and CypA-CsA.

2.5.5 Coaxial Exchange

An alternative method named 'coaxial' exchange was attempted to determine if structural conformers could be detected if the exchange time was minimised. This has been shown to be successful by Konermann and co-workers[11] where *d*-buffer was mixed

with sample from 40 ms to 3.3 s prior to desolvation where structural intermediates were shown by partial H/D exchange. In this instance (Figure 2-22), two syringes were infused at 10 μL/min, one containing sample and the other *d*-buffer. They were allowed to mix via a T-piece in 5 cm of PEEK™ tubing.

20 μM melittin in 10 mM ammonium acetate, pH 6.8 was infused against *d*-ammonium acetate at pD7.2 and pD4.6 and 100% *d*-methanol. Although no distinctions in peak shape could be associated with conformation or the presence of intermediates (Figure 2-23), there is a difference in exchange rates due to different solvent conditions (Figure 2-24) which supports research previously discussed in Chapter 1 and Dempsey[12] and Beauchamp and co-workers.[13]

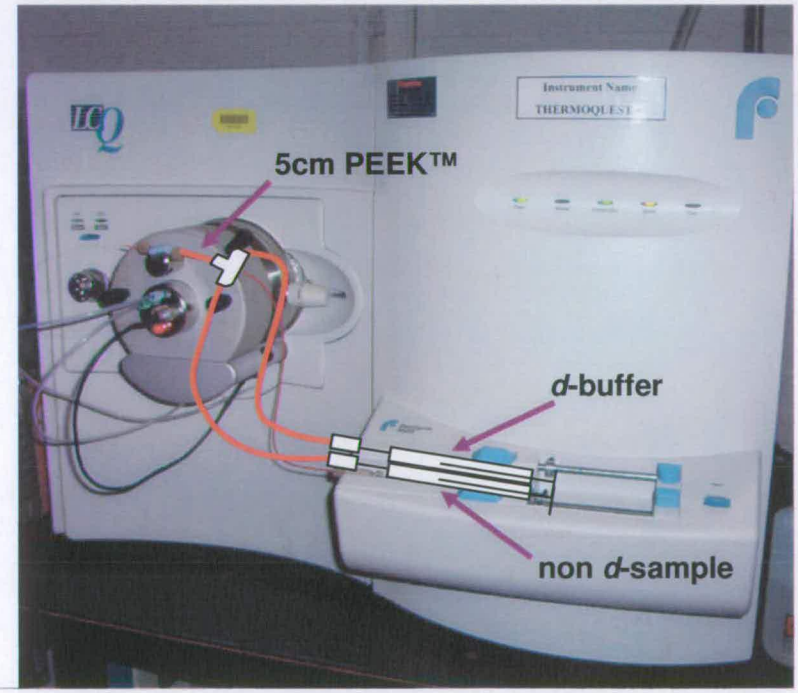

Figure 2-22 Schematic of coaxial HDX

It was assumed there were no differences in the structure of melittin at pD 7.2 and pD 4.6. The difference in mass increase could therefore, be solely attributed to a reduced rate at pD 4.6. The structure of melittin is affected by the presence of methanol (Chapter 4, Section 4.2), in this case equating to 50%. It is possible the lack of exchange compared to the aqueous buffer is attributable to both a conformational change and an inherent slow exchange rate.

This method has potential for elucidating fast conformational changes, but was not optimised here. It is included here as it as a complimentary technique to other solution phase HDX methodologies and will be discussed in Chapter 4.

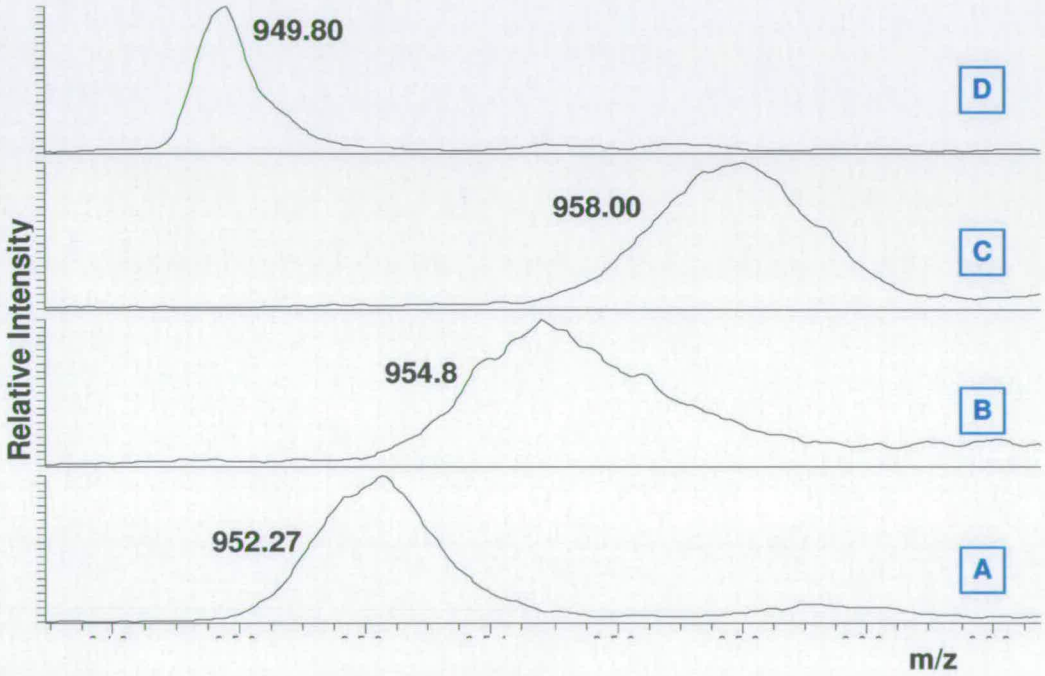

Figure 2-23 Spectra of melittin ($[M+3H]^{3+}$) after coaxial infusion in A) 100% *d*-methanol; B) pD 4.6 10% *d*-methanol / 10 mM ammonium acetate; C) pD 7.2 and D) non-deuterated control pH 6.8

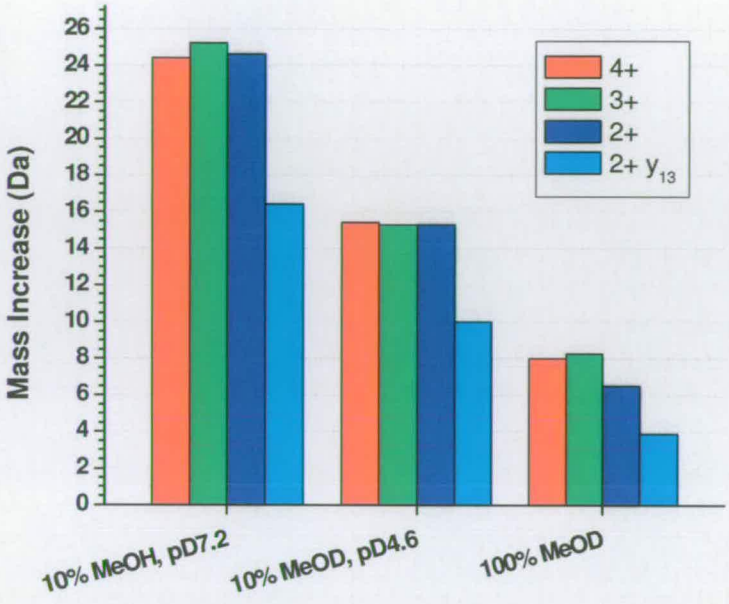

Figure 2-24 Mass increases on melittin after coaxial infusion with 3 *d*-buffers

2.5.6 CID

2.5.6.1 QToF Ultima

CID performed using the Q-ToF Ultima was achieved by applying a collision voltage ranging 4 – 70 V. Pressure in the collision cell was maintained at approximately 1 E-5 Torr with 7-8 psi argon.

2.5.6.2 LCQ - Normalised Collision Energy (NCE)

The LCQ utilises normalised collision energy (NCE) to obtain CID data. NCE was set to 0.0% for all HDX analysis. For fragmentation of melittin $[M+3H]^{3+}$ a value of 20 - 30% was sufficient and 35 - 40% for $[M+2H]^{2+}$. Increasing the NCE was useful for improving signal of the larger proteins.

2.5.7 Gaussian Fitting

Isotopically resolved spectra were imported into Origin® and fitted using 4 Gaussian distributions with fixed peak widths of 1.5 Da at half their height for the 4+ charge state of insulin. Theoretical isotopic distributions were calculated using XMass software where the numbers of deuteriums and hydrogens were adjusted to fit each Gaussian peak. In the example in Figure 2-25 the 4 peaks were assigned with deuteriums equalling 25, 30, 36 and 41. This equates to a weighted average mass increase of 32.03 Da representing exchange of 32 hydrogens. Although there was some inconsistency in mass shifts, the peak widths and shapes were very reproducible. The differences in mass were mainly attributable to instrument calibration but experimental variation cannot be disregarded. This did not compromise results as all mass increases were calculated relative to a non deuterated control run daily.

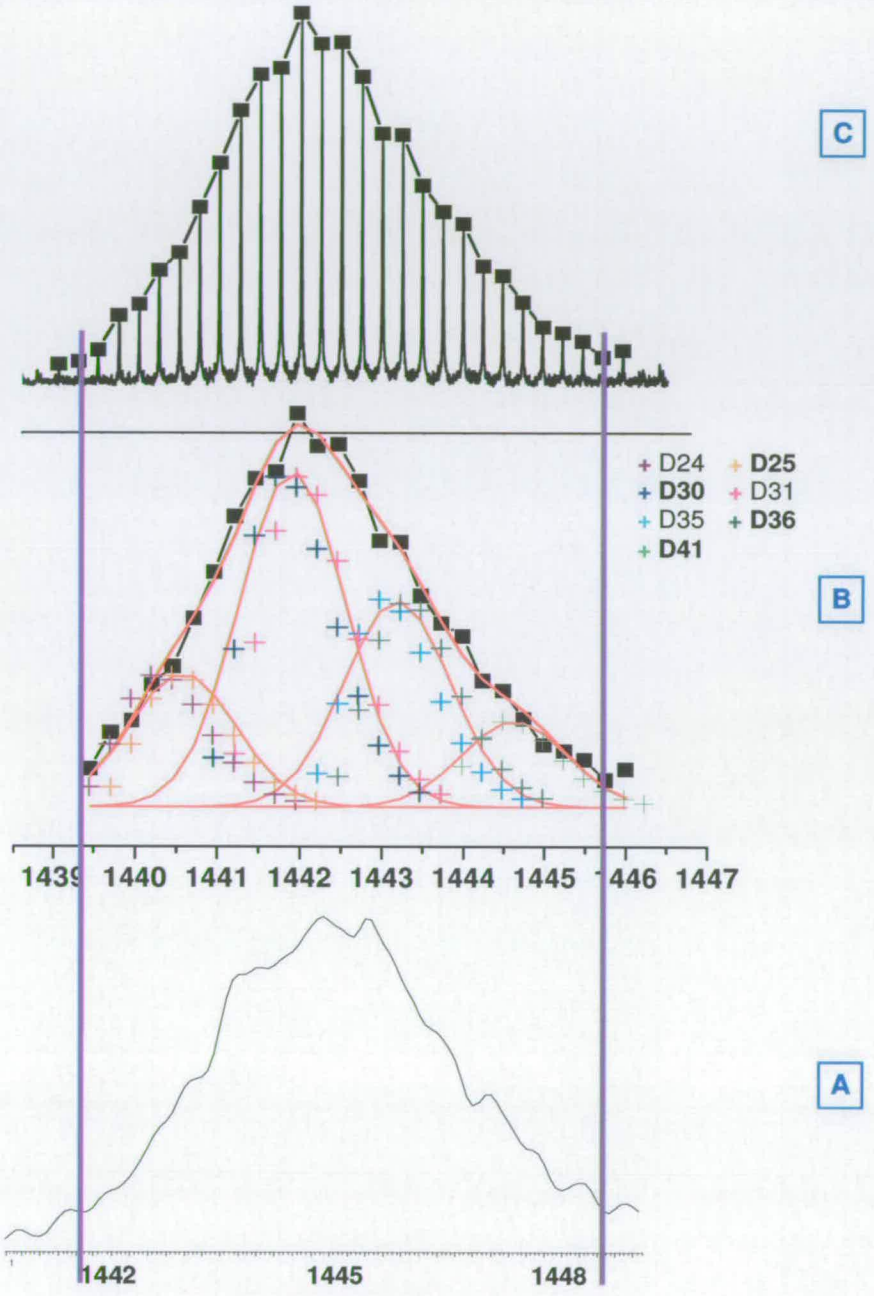

Figure 2-25 Spectrum of insulin ($[I+4H]^{4+}$) exchange with LCQ (A), FT-ICR (C) and Gaussian fitting (B) with calculated exchange assignments

2.6 Circular Dichroism

All data was acquired using a Jasco J-810 Cicular Dichroism Spectrometer. Melittin stock (10 mg/mL) was diluted to 0.15 mg/mL (52.8 μM). Spectra were acquired in continuous mode from 250 – 190 nm (band width of 1nm), averaging 3 scans at 20nm/min. The following solvent conditions were used to induce various conformational states: 10% - 100% methanol in 10 mM ammonium acetate, pH 6.8, 10 mM phosphate buffer, pH 7.13 and 20 mM TBS at pHs ranging 2.25 – 12.2.

2.7 References

[1] Robinson CV., Chung EW., Kragelund BB., Knudsen RTA., Poulsen FM., Dobson CM., *J. Am. Chem. Soc.,* 1996, **118**, 8646-8653
[2] Loo JA., Hu P., McConnell., Mueller WT., Sawyer TK., Thanabal V., *J Am Soc Mass Spectrom,* 1997, **8**, *234-243*
[3] Clarke SM., Konermann L., *Anal. Chem.,* 2004, **76**, 1257-1263
[4] Gao H., Yu Y., Leary JA., *Anal. Chem.* 2005, **77**, 5596-5603
[5] Krężel A., Bal W., *J Inorg Biochem.,* 2004, **98**,161–166
[6] Bradford, M., *Anal. Biochem,* 1976. **72**, 248-254
[7] Shirran S., *PhD Thesis,*University of Edinburgh, 2005, unpublished data
[8] Ockey DA, Dotson JL, Struble ME, Stults JT, Bourell JH, Clark KR, Gadek TR, *Bioorg Med Chem,* 2004, **12,** 37-44
[9] Zhu MM., Chitta R., Gross ML., *Int J Mass Spectrom.,* 2005, **240**, 213-220
[10] verbal communication with Justin Sperry, Gross group
[11] Pan J., Wilson DJ., Konermann L., *Biochemistry,* 2005, **44**, 8627-8633
[12] Dempsey CE., *Biochemistry,* 1988, **27**, 6893-6901
[13] Campbell S., Rodgers MT., Marzluff EM., Beauchamp JL., *J. Am. Chem. Soc.,* 1995, **117,** 12840-12854

3 Cyclophilin A - High Throughput Screening

3.1 Introduction

The role played by mass spectrometry (MS) in drug development has become more significant over the last 10 years. The flow chart in Figure 3-1, depicting the preclinical phase of drug development illustrates the integral role mass spectrometry plays in this study. As a rapid method for ranking binding affinity of large numbers of ligands by comparing detection of complex with unbound protein, it has the potential to reduce the number of ligands submitted for *in vitro* assays by up to a factor of 10. Feedback to a core database, (e.g. the EDULISS (Edinburgh University Ligand Selection System)) allows progress to be monitored and can highlight potential candidates or libraries of compounds. This provides a means of driving improvements to ligand design.

The use of mass spectrometry for determining both stoichiometry information and dissociation constants for biological complexes is a growing field.[1,2,3] ESI-MS lends itself to both high throughput sampling and direct stoichiometric analysis. Zhang *et al.*[4] have been involved with the development of NanoMate™ technology for automating the application of nanoESI for native bio-molecular complexes. This technology has been put to good use by Veros *et al.*[5] for calculating the affinities of lysozyme to N-acetyl-glucosamine oligomers. The development of a high throughput system is discussed in this chapter.

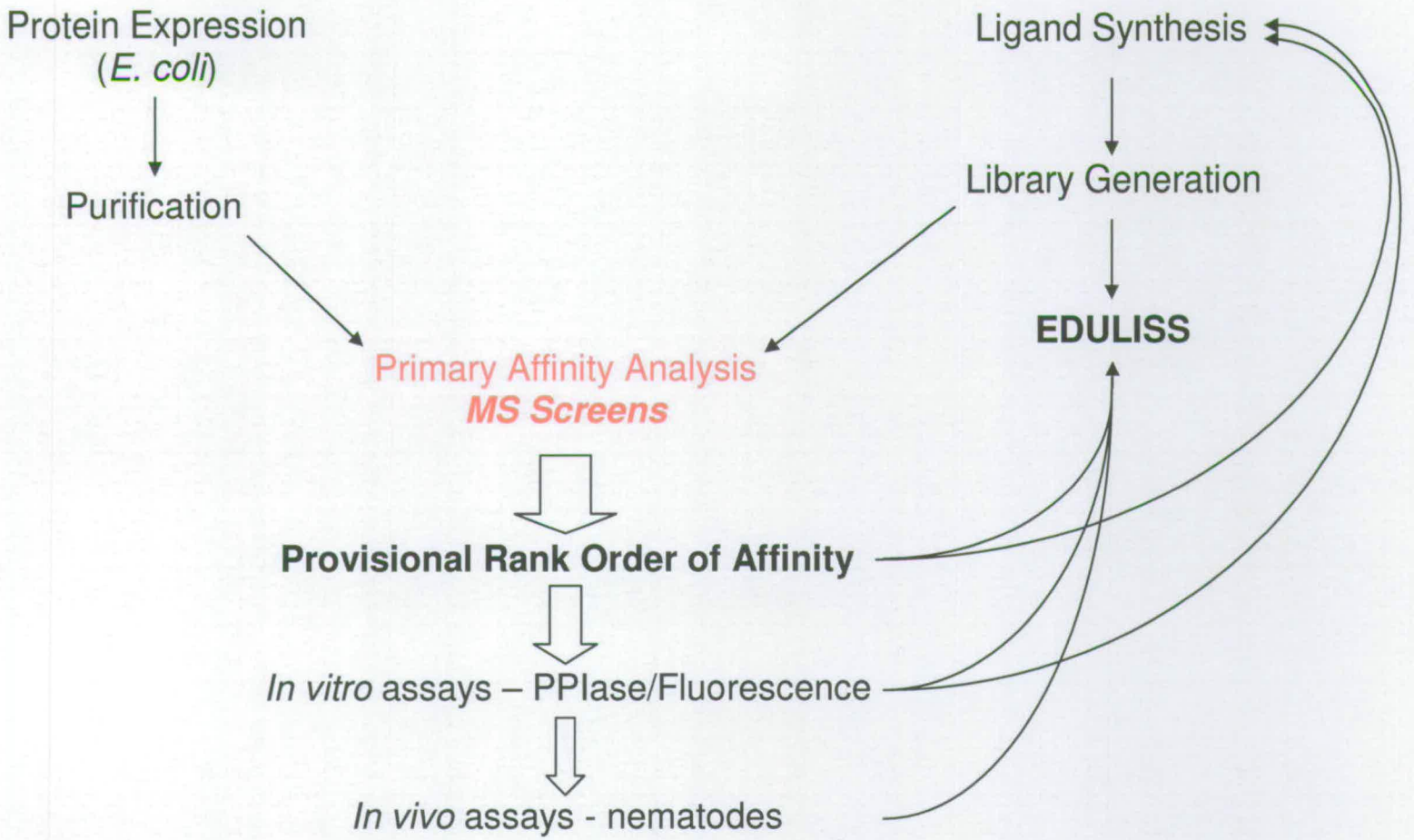

Figure 3-1 Preclinical drug development with regards to CypA with the role of mass spectrometry highlighted

3.1.1 Cyclosporin and New Synthetic Ligands

A primary aim here was to discover new compounds able to bind to CypA without affecting the T-lymphocyte antigen activation cascade (Chapter 1).

Two key residues within the CypA binding pocket are Arg-55 and Phe-113 which form strong interactions with residues 10 and 11 of CsA respectively (Chapter 1 Section 1.2.2). The C=O backbone group of the MeLeu (residue 10) has a link with Arg-55. The second, strong hydrophobic interaction involves the two methyl groups of MeVal linking to the phenyl group of Phe-113. These interactions led to the development of the so called dimedone derivatives. The Abu pocket of CypA relates to interactions formed with Abu-2 of CsA. Incorporation of water molecules into the complex structure has been shown to play a structural role within the binding site of some systems.[6]

Previous work carried out showed the interaction of MeVal on CsA can be mimicked by the dimethyl group on dimedone[7] (Figure 3-2). To this end libraries of ligands were synthesised following 3 different strategies.* A basic schematic of the compounds development is described in Figure 3-2. The binding interface is discussed further in Chapter 3.

For Series 1, groups R' and R" were found to be most effective with the alkyl groups that are illustrated, (Figure 3-2) leaving the N-terminal R group open to modification. The cyclised ring in Series 2 was developed from its precursor because although positive results were found with some versions of the first compound, it was thought the tetrahydropyrrol ring would stabilise the structure. Series 3 was designed and synthesised based on candidate molecules obtained via molecular modelling. A library of tetrahydrochromene compounds (also derivatives of dimedone) were developed using high throughput microwave synthesis. Many of the compounds in the first mass spectrometry screen were successful. Using molecular modelling, different aldehyde chains were added to the structure with the specific purpose of

* Synthesised, modified and supplied by Turner group members Kirk Malone (KM), Colin Dunsmore (CD) and Kevin Bailey (KB) at the University of Edinburgh

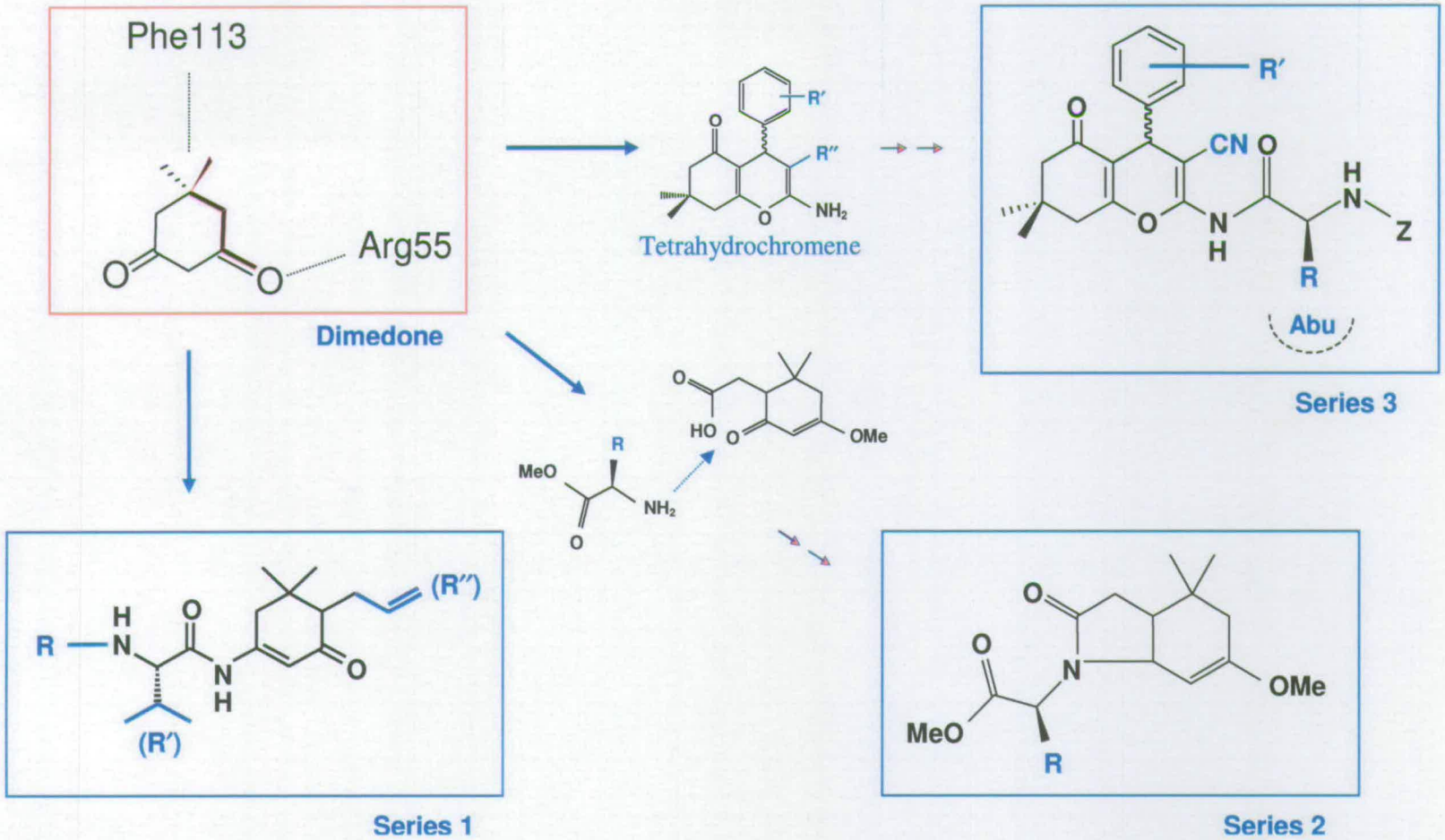

Figure 3-2 Schematic showing the derivation of the 3 ligand libraries

binding into the area of CypA known as the Abu pocket. The initial library developed maintained a CN group at position R″. Modifications to the amine group were developed by the addition of aldehyde groups with a variable R chain which, it was hoped, would show affinity for the Abu pocket of CypA.

3.1.2 The Dissociation Constant, K_d

An association constant K_a is a measure of the affinity a protein and ligand have for each other. It is calculated by measuring the free ligand in solution. Therefore, the K_a value will remain constant under a given set of conditions. The ratio of bound to free protein is directly proportional to the concentration of free ligand (Equation 3-1).

$$P + L \underset{K_d}{\overset{K_a}{\rightleftharpoons}} P \cdot L \qquad \text{hence} \qquad K_a = \frac{[P \cdot L]}{[P]\,[L]}$$

Equation 3-1

K_a units are defined as concentration^{-1}, so the reciprocal K_d is used in its place which has its units quoted as concentration (Equation 3-2).

$$K_d = \frac{[P]\,[L]}{[P \cdot L]} \qquad \text{therefore} \qquad \frac{[P \cdot L]}{[P]} = \frac{1}{K_d}\,[L]$$

Equation 3-2

It follows that if the concentration of free ligand is less than the K_d there is little association as binding conditions are favoured by having excess ligand. However when the concentration of ligand is equal to the K_d, half the protein molecules are bound with

ligand. Similarly, to have 90% of the protein bound, the free ligand concentration must be in the order of 9X that of the K_d.[8] The calculations may be simplified therefore by having the ligand in such excess of the protein binding sites that uptake does not significantly deplete the unbound ligand reserve.

Peak intensities are assumed to be proportional to the concentration of each species in solution i.e. unbound protein P or complexed protein P·L. To this end, the addition of all P and P·L peak intensities is equivalent to the solution protein concentration [P]. By the same logic, the concentration of free ligand [L] is calculated by subtracting the now known concentration of the complex [P·L] from the initial solution concentration of ligand [L_{init}]. As such, Equation 3-2 is modified to give Equation 3-3.

$$K_d = \frac{[P]\,([L_{init}]-[P \cdot L])}{[P \cdot L]}$$

Equation 3-3

The equations derived above can be utilised for obtaining a K_d for a single protein – ligand ratio. A more accurate means would be to carry out a ligand titration. Whilst [P] represents the concentration of unbound protein, [L], unbound ligand, using Equation 3-2 for non-competitive binding, a plot of [PL] / [P] versus [L_{init}] – [PL] produces a gradient equivalent to 1 / K_d. An example is provided in Section 3.4.1. Competitive binding, although not relevant to this study, is discussed in Appendix D.

3.2 Optimisation of Complex Analysis

3.2.1 Effect of pH on Charge State and Complex Formation

Initial studies performed by Shirran[9] established the optimal pH for detecting 'native' CypA and its complex CypA-CsA. Further experiments incubating CypA and CsA at a

range of pHs were performed to ascertain the probability of non-specific binding (Figure 3-3). Protein and ligand were incubated at a 1:1 (mol/mol) ratio.

There is no evidence of complex formation at pH 3.3 confirming the inability of the denatured protein to bind CsA suggesting that non-specific binding under these conditions is not an issue. Raising the pH to 6.0 results in the detection of both bound and unbound protein. There is still a significant amount of unbound protein at charge states associated with 'native' conformations. The impact is greatest on charge state 8+ ($[CypA + 8H]^{8+}$). The charge state assumed to represent the most 'native' conformer. It can therefore be inferred that slightly acidic buffering conditions result in changes in the protein structure. These issues are addressed by simply raising the pH to 6.8 where the unbound form with charge state 8+ is significantly depleted relative to the complex. Increasing the pH to 9.0 does not appear to have a detrimental effect on either the charge state distribution or bound / unbound ratios although, ionisation conditions did have to be re-optimised. With physiological pH being 7.4, the data here suggests pH 6.8 is suitable for screening analysis.

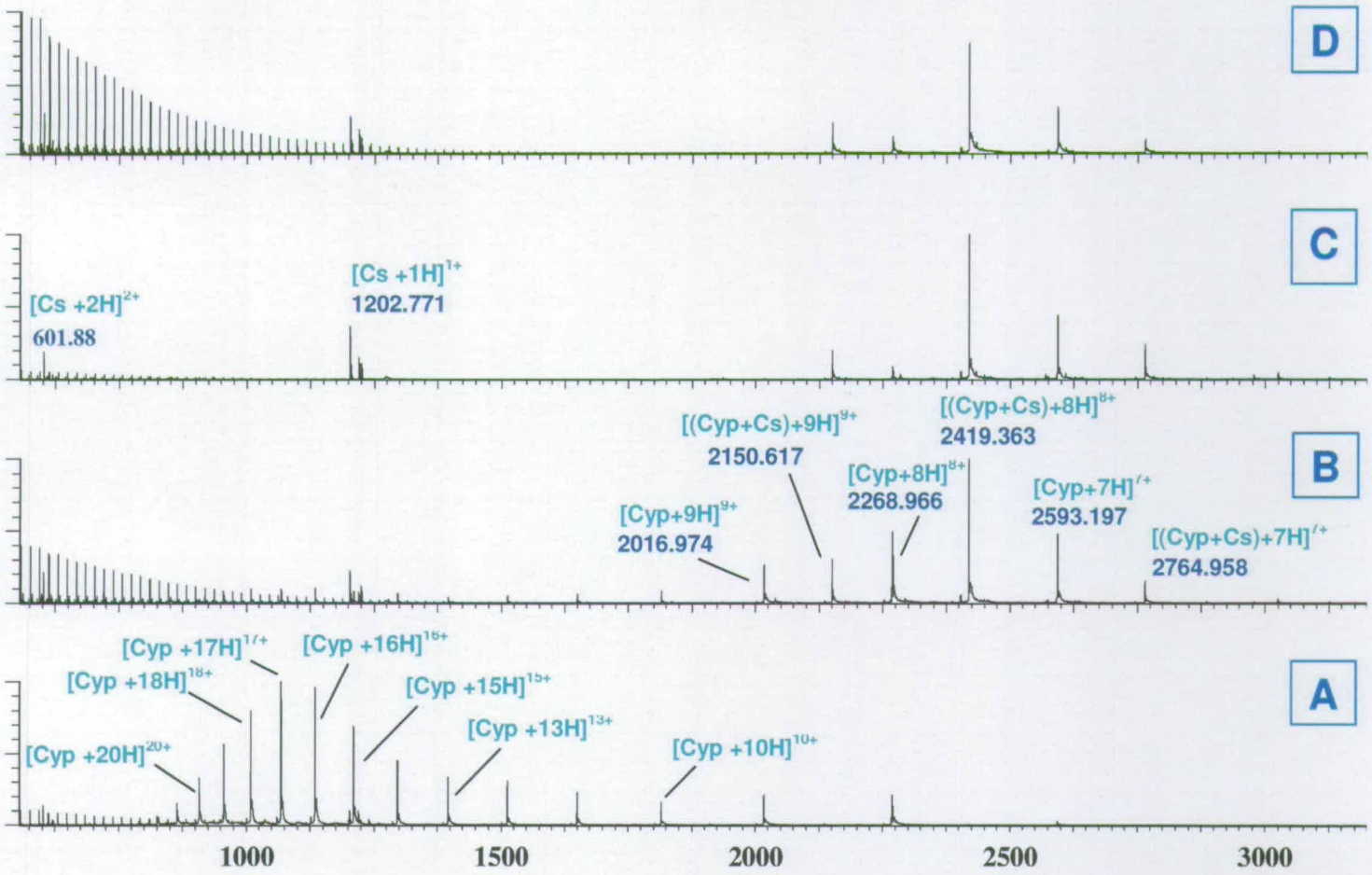

Figure 3-3 Determination of non specific binding of CsA on CypA by comparing incubations at varying pHs, A) 3.3, B) 6.0, C) 6.8 and D) 9.0

3.2.2 Stoichiometry of Ligand Binding

3.2.2.1 Analysis of CypA-CsA and CsA Aggregates

CypA possesses a single binding pocket conducive to interaction with CsA.[10,11] This binding is readily detected by mass spectrometry when CypA and CsA are incubated at a 1:1 ratio. CsA is hydrophobic and has limited solubility in aqueous media. Serial dilution steps into increasingly aqueous solutions resulted in aggregation. The detection of singly charged multimers of CsA is common in 90% aqueous, 10% organic solvent solutions at concentrations of 20 μM after incubation for several hours at 4°C. The effect is almost immediate in solutions of 40 μM CsA. The consequences of this are reflected in the detection of more than one ligand bound to the protein (Figure 3-4). The $[Cyp+nCs+8H]^{8+}$ complex shows evidence of up to three CsAs molecules binding, and the $[Cyp+nCs+9H]^{9+}$ associates with up to two. There is also evidence of a doubly charged unbound tetramer of CsA.

The unbound tetramer provides evidence that multiple ligands binding to CypA is a result of ligand aggregation rather than non-specific binding. Further evidence supporting this is obtained by subjecting the complex to CID. Figure 3-5 depicts the release of CsA with increase in collision voltage (CV). Fragmentation of $[Cyp+2Cs+9H]^{9+}$ with a collision voltage of 20 V principally results in the loss of one CsA and a subsequent reduction in charge state to $[Cyp+Cs+8H]^{8+}$. Increasing the CV to 30.8V results in an increase of $[Cyp+7H]^{7+}$ protein only which becomes the dominant fragment by the time 50.3V is applied. The ease with which both CsAs are removed as protonated species does not distinguish between two stacked ligands or one specific and one non-specifically bound. At the highest voltage however, both ligands are removed simultaneously as a singly charged species leaving protein only as $[Cyp+8H]^{8+}$. This is only possible if the ligand is associated as a singly charged dimer.

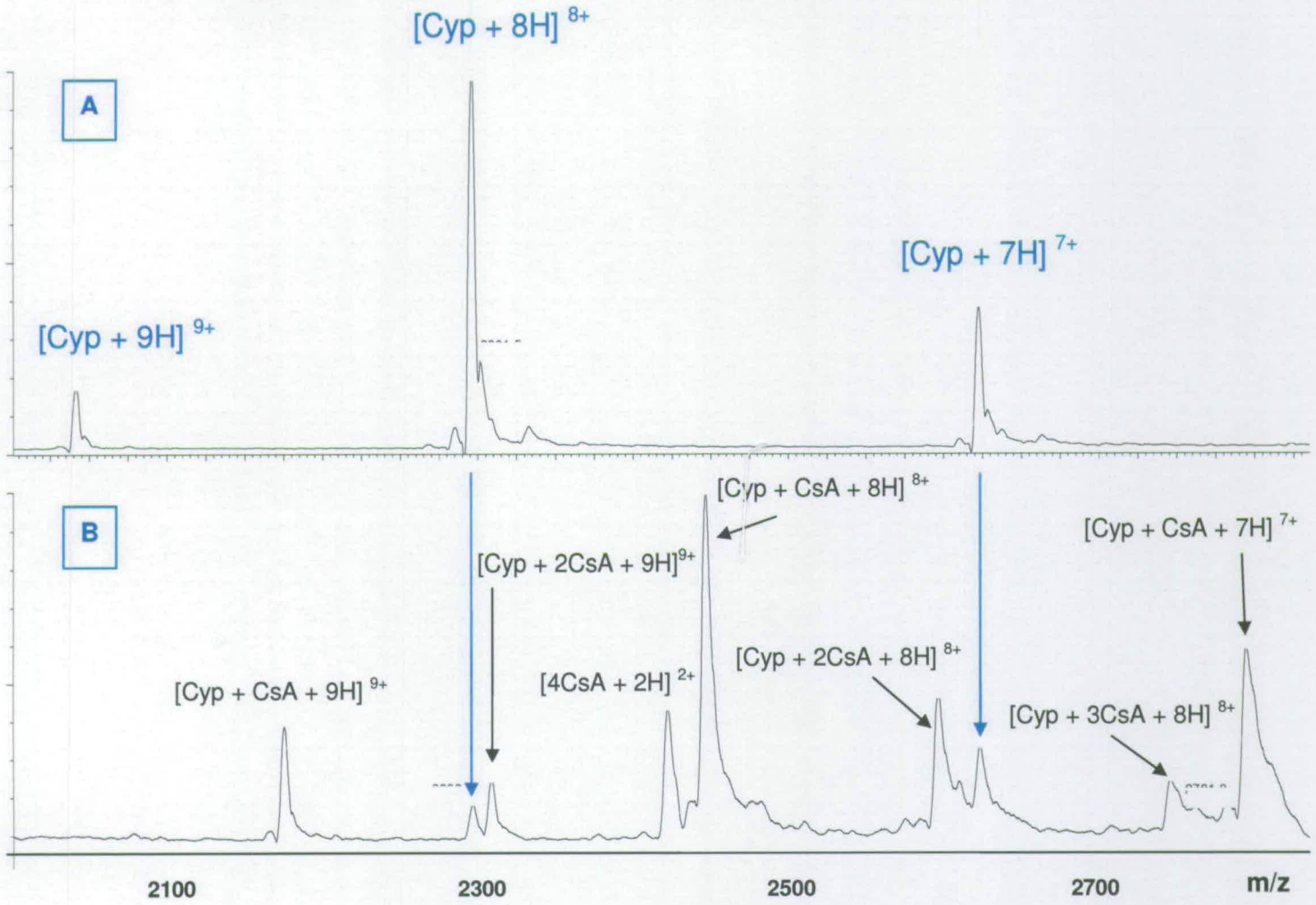

Figure 3-4 Spectrum of A) CypA and B) CypA-CsA complex where dimers of ligand bind to protein

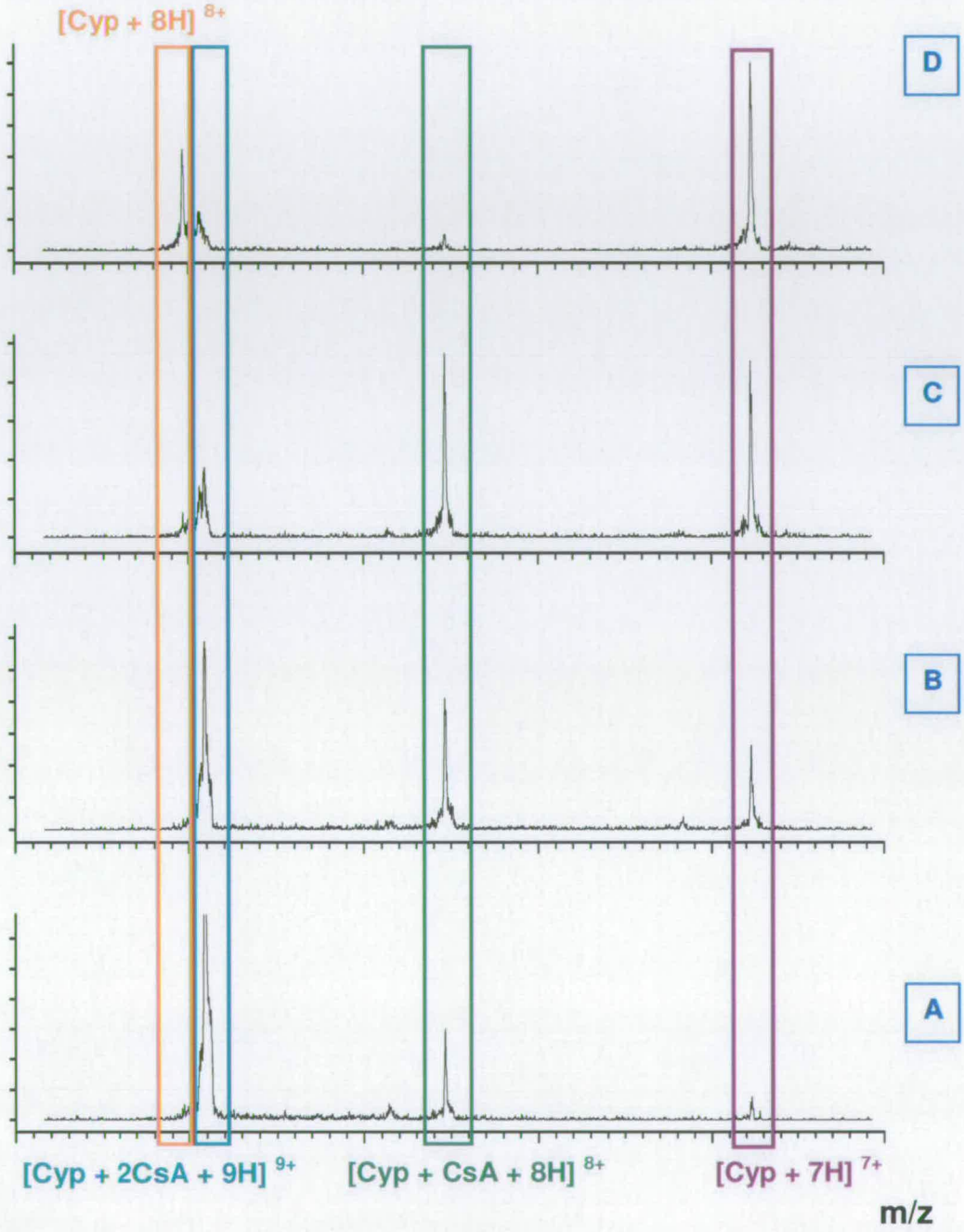

Figure 3-5 Fragmentation of $[CypA + 2CsA + 9H]^{9+}$ by CID with increasing collision voltages A) 20.0V, B) 30.8, C) 39.2 and D) 50.3

3.2.2.2 Synthetic Ligands : Aggregation and Noncovalent Complexes

The synthetic ligands also had a tendency to aggregate. As with CsA, following dilution into aqueous conditions, the hydrophobic groups on the ligands form strong interactions with each other, creating a structure comparable to that of a micelle. The masses of the CypA-Ligand complexes detected demonstrate up to six ligands binding. Figure 3-6 illustrates unbound ligand aggregates in solution and Figure 3-7 illustrates the same ligand bound to CypA. These aggregates may suppress or alter the binding affinity of complex formation.[12]

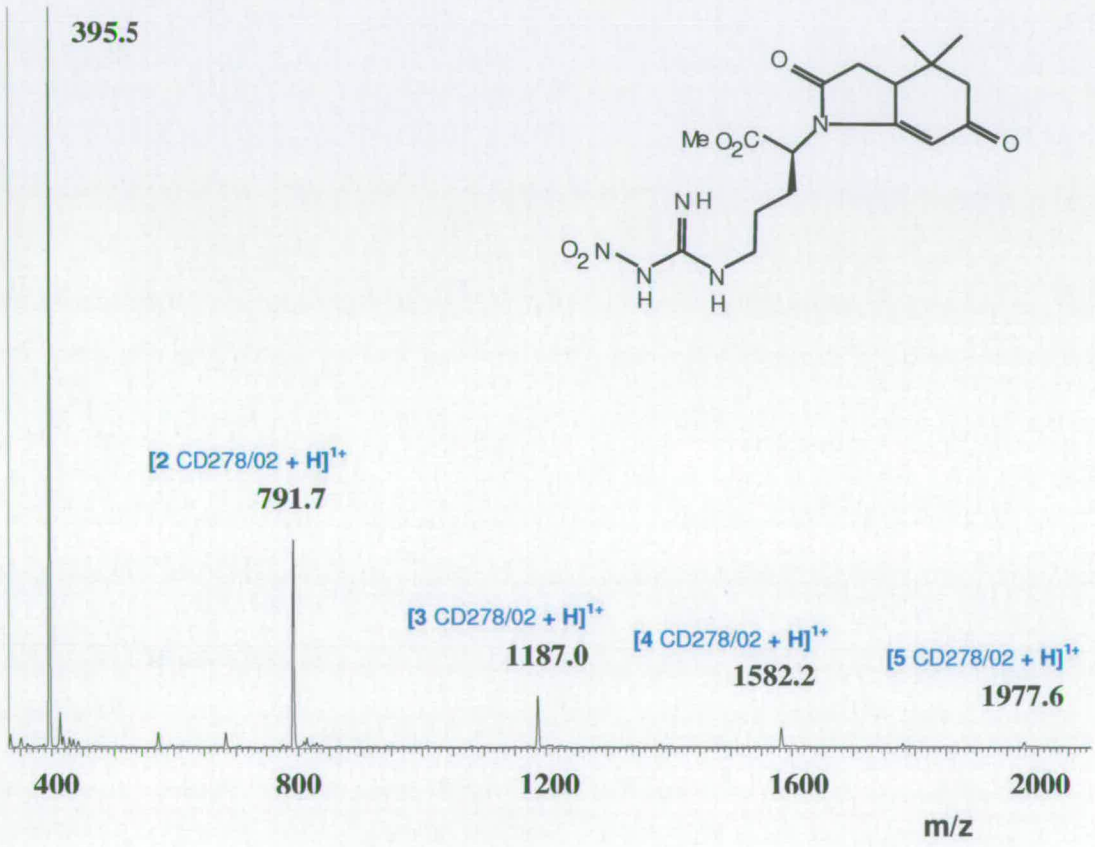

Figure 3-6 Singly charged aggregates of CD278/02 the monomer represented with m/z 395.5

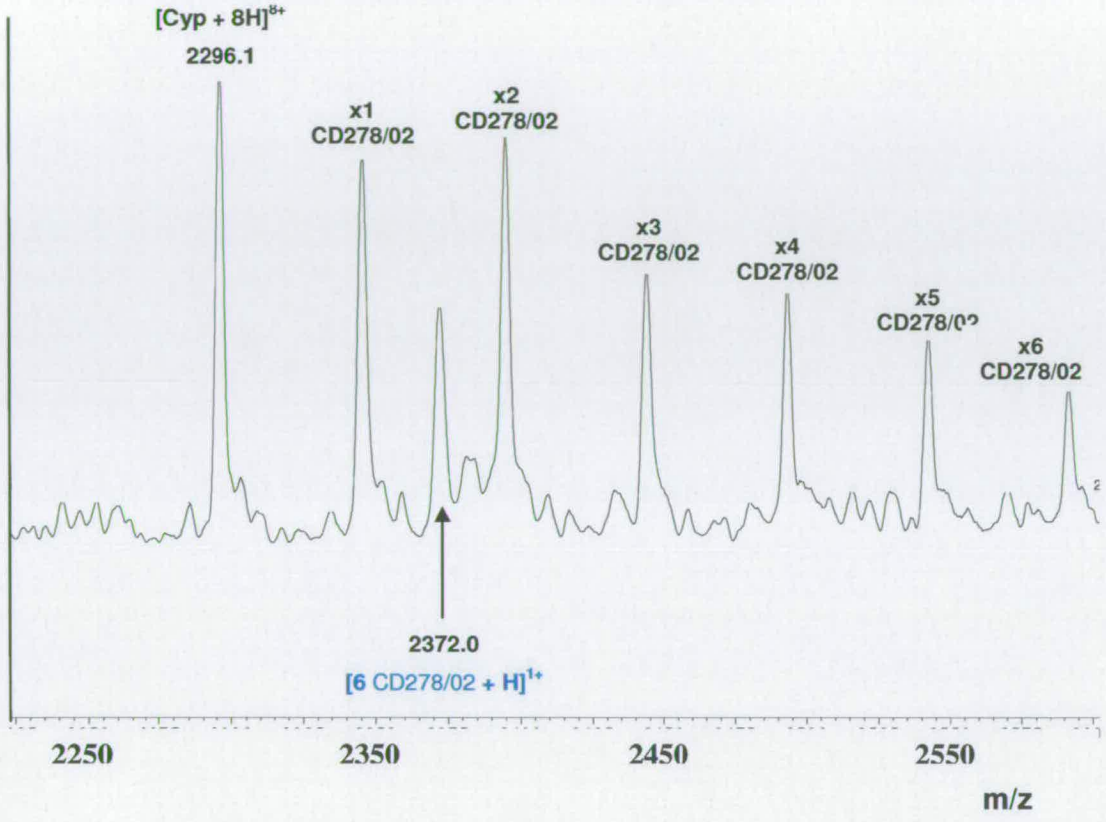

Figure 3-7 Spectrum of [Cyp + *n*CD278/02 + 8H]$^{8+}$ with multiple ligand aggregates (x***n*** CD278/02)

DMSO was used to solubilise the more hydrophobic ligands (principally Series 3). There were two concerns regarding the overall effect on protein-ligand complexes; 1) DMSO binds to CypA and 2) DMSO affects the ionisation process. To avoid these pitfalls the ligands known to be problematic for dilution in methanol, acetonitrile or aqueous buffers were reconstituted in DMSO or a DMSO / methanol mix. Figure 3-8 shows the increased binding affinity of KB6217/7 in the presence of DMSO. This was probably aided by the increased solubility of the ligand with DMSO but it did not prevent the formation of aggregates. The most abundant charge state now becomes [Cyp+*n*CD278/02+7H]$^{7+}$, perhaps due to charge stabilisation by DMSO.

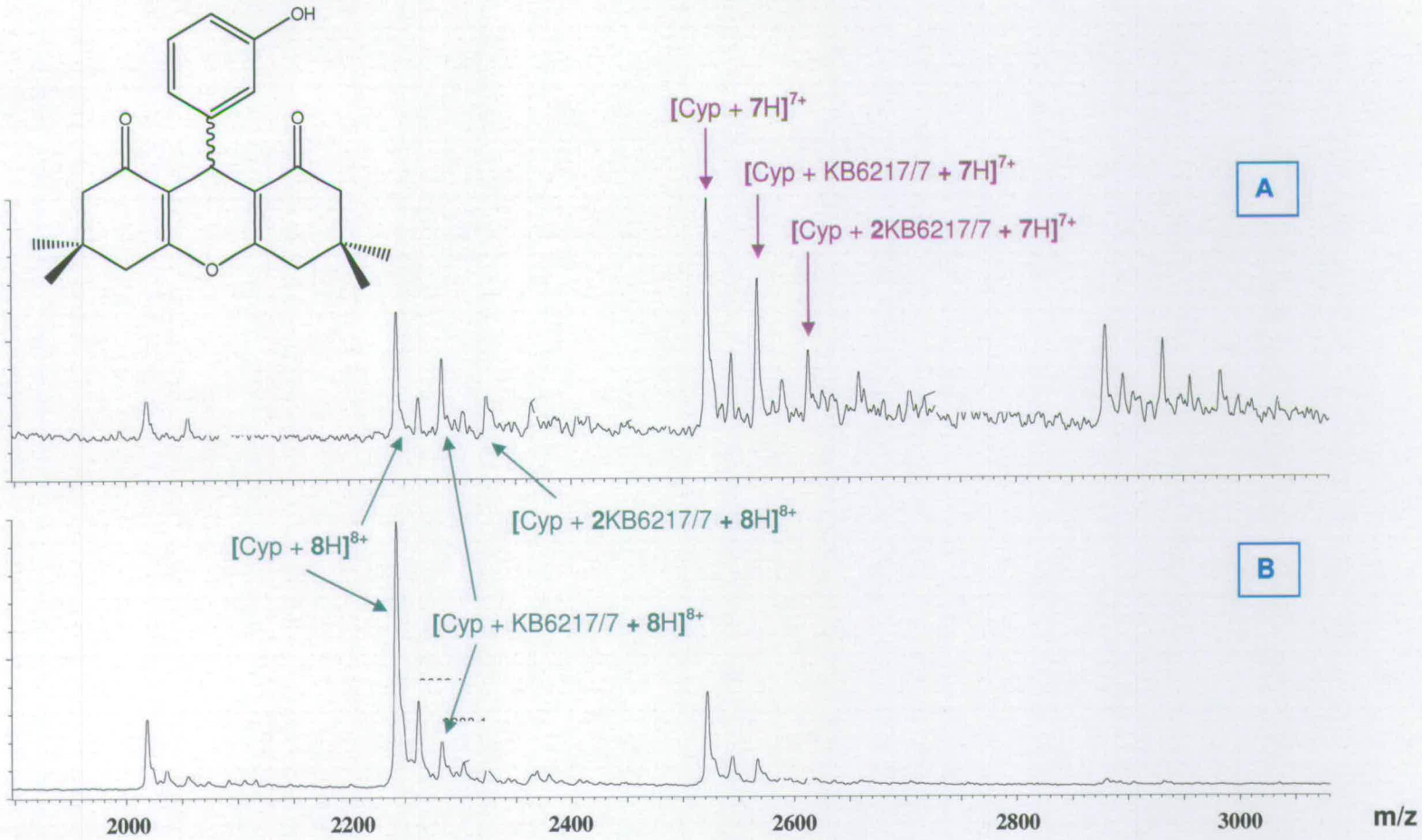

Figure 3-8 Noncovalent complex spectra of $[Cyp + n\text{KB6217/7} + xH]^{x+}$ with (A) + DMSO and (B) - DMSO

3.3 Comparison of sampling techniques and ionisation

Variability between spectra on a daily basis was noted when using the ZMD. This can be attributed to both the ionisation technique and capability of this single quadrapole mass spectrometer. The NanoMate™ as discussed in Chapter 2 demonstrates the benefits of high throughput nanoESI to produce a highly reproducible ionisation source for desolvation. A reproducibility study was performed using KM184 at two different concentrations, 40 μM and 100 μM.

Screening data was obtained using 3 different mass spectrometry systems, ESI-ZMD, nanoESI Q-ToF and NanoMate™ Q-Micro. Figure 3-9A shows some variability in measured K_ds. There is an apparent increase in K_d with increase in ligand concentration for data generated using the QToF. Intermolecular interactions between CypA and the respective ligands are likely to be weakened *in vacuo* due to their hydrophobic nature. As a result of this, the increased probability of complex dissociation causes the ratio of unbound ligand relative to bound ligand to increase. An increase in initial ligand concentration ($[L_{init}]$) will increase the amount of unbound ligand $[L_{unbound}]$ which may aggregate more, and this may in turn compete with protein binding. That this effect is most marked in Q-ToF data implies desolvation and / or source conditions are more disruptive or that the aggregation of ligands is more favoured. Interestingly, the K_d for 100μM KM184 is of the same order as that obtained using ESI-ZMD. The reproducibility of the latter decreases with increase in ligand concentration suggesting the ligands influence the desolvation and ion detection processes. It is apparent that the data is most reliable at lower ligand concentrations.

Using the Nanomate™ shows high reproducibility. Figure 3-9 B shows K_ds of CypA with KM184 over 6 identical injections performed periodically throughout the screen run. All K_ds lie within 1 standard deviation suggesting this to be a desirable method for sample introduction.

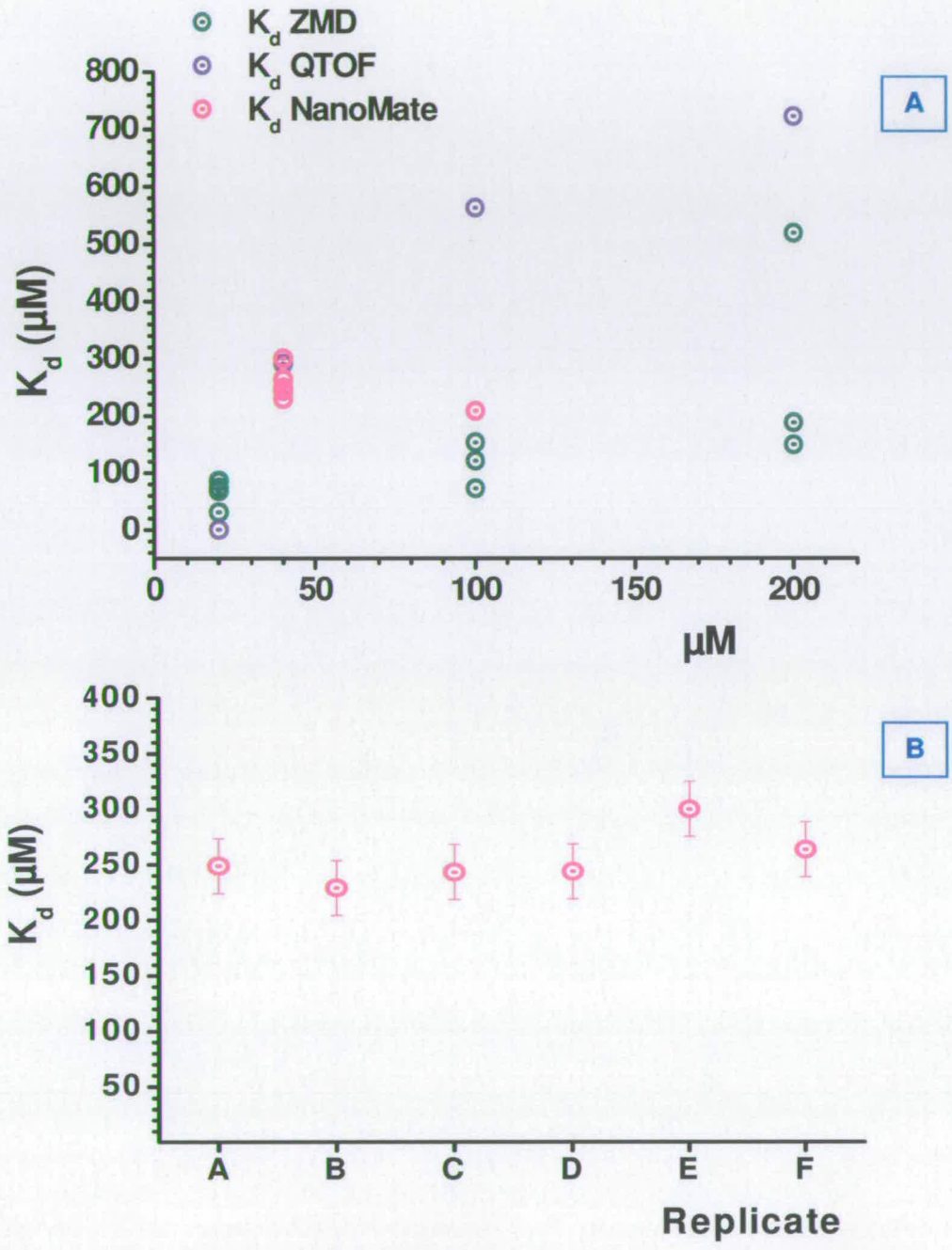

Figure 3-9 K_ds on replicate incubations of KM184 with CypA (A) comparing each mass spectrometer with varying concentrations of ligand and (B) 40µM by NanoMate™ only

3.4 Calculating K_d Values using Mass Spectrometry

K_ds for each ligand were calculated from mass spectra in two ways; i) peak areas and ii) peak intensity. Each approach was used to calculate K_ds using charge state 8+ ($[Cyp+nLig+8H]^{8+}$), the most abundant peak under 'native' ESI conditions and from deconvoluted mass spectra, which incorporates all charges states.

Binding of ligand aggregates frequently occurred (described in section 3.2.2.2). $[Cyp+8H]^{8+}$ appeared predisposed to binding ligand multimers, an observation minimised in deconvoluted data where the relative amount of multimer was reduced. It was initially assumed the ligand clusters provided conditions equivalent to a competitive environment (Appendix C).[13] This approach was modified to use a non-competitive strategy whereby peak areas of each complex (PL_1, PL_2, etc) were combined. It was assumed the ligand always bound in the same way irrespective of aggregate size, a factor which may have imposed steric hindrance. However, large ligand clusters did show a reduced binding affinity but were not thought to be significantly competitive with ligand monomers.

Data was collected on different days and at different ligand concentrations relative to the protein. When studying the calculated K_d values there was a large discrepancy not only between days but between concentrations (further discussed in Section 3.4.2). This is in agreement with the assertion above that affinities must always be calculated with respect to their relative concentrations to the protein and other components or ligands within the environment.

3.4.1 K_ds Calculated from Multiple Ligand Concentrations

Section 3.3 and in particular Figure 3-9 demonstrates that K_ds derived from direct infusion peak intensities may alter with ligand concentration. All experiments therefore, were performed with comparable protein:ligand ratios. Performing a titration of ligand

against the protein of interest takes this into account. This is therefore the most reliable method for calculating K_ds.

20μM CypA was incubated at room temperature with KM184 at concentrations 20μM (1:1), 100μM (1:5) and 200μM (1:10). The ratio [PL]/[P] is plotted against [L] (derived from $[L_{init}]$-[PL]) in Figure 3-10. A linear relationship between the concentration of ligand and its binding affinity with CypA is clearly seen. Using Equation 3-2, the K_d for CypA-KM184 is calculated to be 189 ± 43 μM.

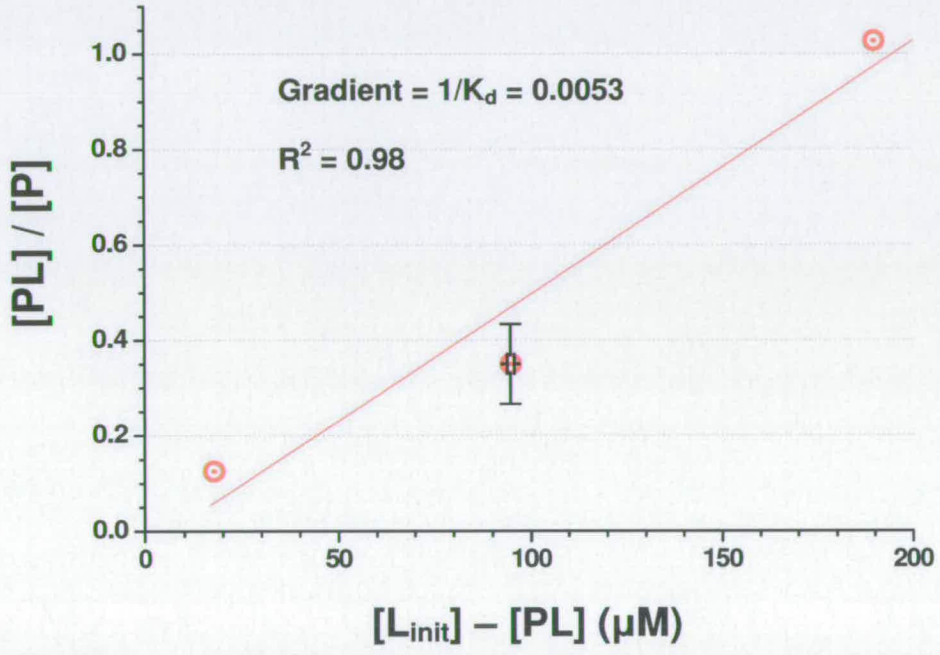

Figure 3-10 Plot of CypA titrated against KM184

3.4.2 Rank Order of Ligand Affinity using MS derived K_ds

For the purposes of this study, a list of relative binding affinities was required. To achieve this, the following questions were addressed:

i) Does using a single ligand concentration affect the order?

ii) Is the order affected by using peak intensity rather than peak area?

iii) Is the order affected by using the most abundant charge state (in this case $[Cyp+L+8H]^{8+}$) rather than transformed data?

iv) Is the order affected by the ionisation source?

3.4.2.1 The Effect of Ligand Concentration

Tjernberg *et al.*[14] showed that although multiple points are beneficial for determining accurate K_ds, single point analysis does not affect the reliability of ranking. The K_d values listed in Table 3-1 are derived from two concentrations of ligand. The rank order shown is derived using K_ds calculated using 40 μM ligand solutions. The general trend shows strong agreement between ligand concentration and order of affinity. Therefore, K_ds can only be directly compared where ligand concentrations are identical. There are a few exceptions where the 100 μM ligand e.g. KB 22/8; KB 17/7; KM 198; KM 5 do not agree with the original list. On the whole however, affinities lie within the same order of magnitude. These differences may result from the different solution properties. e.g. an extremely hydrophobic ligand may show increased self aggregation in solution at higher concentrations, thus reducing its availability for CypA binding. In agreement with the NanoMate™ example KM 184 in Figure 3-9, the ligands show a tendency for decreased apparent K_ds with increased ligand concentrations, which contradicts the result seen with nanoESI-Q-ToF.

LIGAND	$CONC^N$ (μM)	Kd (μM) Transformed	n
KB69/12	40 100	96.09 41.41	1 1
KB22/5	40 100	97.66 63.00	1 1
CD278/02	40 100	104.05 31.95	1 1
KB17/4	40 100	112.54 72.68	1 1
CD359/02	40 100	142.84 120.60	1 1
CD357/03	40 100	152.69 133.19	1 1
CD361/02	40 100	153.56 113.19	1 1
CD358/02	40 100	166.85 159.42	1 1
KM198	40 100	168.38 113.50	1 1
KB69/3	40 100	171.50 227.10	1 1
KB17/7	40 100	196.88 157.08	1 1
KB22/6	40 100	209.44 202.83	1 1
KM257	40 100	221.92 253.43	1 1
KB22/8	40 100	232.53 158.99	1 1
KM184	40 100	254.68 218.11	6 2
KM249/02	40 100	285.85 313.86	1 1
KM19	40 100	301.58 390.50	1 1
KB69/15	40 100	605.38 362.80	1 1
KM183	40 100	876.50 1720.69	1 1
KM5	40 100	1053.62 271.97	1 1
KM249/04	40 100	1442.81 841.97	1 1
CD354/02	40 100	2228.29 1868.34	1 1

Table 3-1 K_ds calculated for a selection of ligands using the NanoMate™ at two concentrations (n = replicate runs)

3.4.2.2 Comparing Peak Intensity with Peak Area

Native proteins pick up salts and buffer debris during the desolvation process which, along the contribution of the isotopic distribution at low charges states results in peak broadening. The question arises as to whether the width of the peak is affected proportionally to the intensity i.e. do the causes of the increased peak width affect its ability to ionise or, does binding a ligand or multiple ligands cause the peak to broaden. If it does then the relative contribution must be accounted for. In this instance, there is no evidence of significant broadening as a result of multiple ligand complexes so no compensation is necessary.

LIGAND	Kd (μM)		Ratio
	Peak Areas	Peak Intensity	
CD 278/02	19.13	31.95	1.7
KB 69/12	97.70	41.41	0.4
KB 22/5	57.64	63.00	1.1
CD 361/02	116.37	113.19	1.0
KM 198	103.95	113.50	1.1
CD 359/02	181.57	120.60	0.7
CD 357/03	143.08	133.19	0.9
KB 17/7	163.88	157.08	1.0
KB 22/8	168.30	158.99	0.9
CD 358/02	150.89	159.42	1.1
KM 257	298.79	253.43	0.8
KM 5	760.76	271.97	0.4
KM 249/2	343.55	313.86	0.9
KM 183	2039.20	1720.69	0.8

Table 3-2 Comparison of K_ds for a selection of ligands (100 μM) calculated using peak intensities and peak areas

Table 3-2 shows a comparison of a selection of K_ds obtained using the NanoMate™ with ligand concentration 100 μM. All values were calculated using transformed data using either relative peak intensities obtained using MassLynx™ software or by exporting data

into Origin® and calculating peak areas. The general trend for intensity and areas is in agreement, with the ratios remaining close to 1. There are two notable exceptions, KM 5 and CD 359/02. KM 5 showed erratic binding when analysed using the ESI-ZMD throughout the duration of the project so this value may not be a true reflection of the K_d. Origin® also suffered periodic problems with peak recognition and as such not all the complex states were accounted for. This also contributes to the discrepancies seen between the two methods of calculation and is clearly evident for CD 278/02. This is an issue which needs tackling if high throughput data analysis is to be used.

The K_ds calculated above using areas and intensities differ by greater than 1 standard deviation however, the values do not change by more than one order of magnitude. In light of this, using peak intensities rather than peak areas is valid when obtaining a rank order, and when wanting a rapid screen.

3.4.2.3 Comparing Transformed Data with a Single Charge State

K_d values calculated from both transformed and $[Cyp+Lig+8H]^{8+}$ spectra are listed below in Table 3-3. As above, all values are calculated from single ligand concentrations with the protein concentration maintained at 20 μM. The optimum concentration for ligand was determined to be 100 μM, a 5-fold excess with respect to protein ensuring maximum opportunity for detecting the complexes without suppressing the signal. They are not derived using the titration method as not enough points were obtained to generate a curve.

Again, barring one or two exceptions, the general trend between K_ds obtained using the $[Cyp+n Lig+8H]^{8+}$ and transformed data agree. Some of the KB ligands which required DMSO for solubilisation showed higher intensities for $[Cyp+n Lig+7H]^{7+}$. For this reason it is preferable to use transformed data, taking account of all bound and unbound species detected.

It is assumed that whilst a complex may fragment as a result of nozzle/skimmer dissociation the voltages and heating necessary for ion desolvation do not induce complex formation. The relative intensities detected and subsequent K_ds calculated are therefore assumed to reflect what is seen in solution. The most abundant charge state implies it represents the most favoured conformer in solution. However, other charge states, although of a lower abundance, still show some evidence of complex retention and are therefore considered representative of 'native' protein and complex. These should not be ignored but included in the calculation.

LIGAND	K_d (μM)	
	$[Cyp + L + 8H]^{8+}$	[Cyp + L]
CD 278/02	14.88	31.95
KB 69/12	24.81	41.41
KB 22/5	33.67	63.00
CD 361/02	34.98	113.19
KM 198	27.09	113.5
CD 359/02	45.54	120.60
CD 357/03	37.72	133.19
KB 17/7	39.06	157.08
KB 22/8	67.97	158.99
CD 358/02	57.84	159.42
KM 257	71.31	253.43
KM 5	78.78	271.97
KM 249/2	82.48	313.86
KM 183	320.08	1720.69

Table 3-3 K_ds calculated for $[Cyp+nLig+8H]^{8+}$ and transformed data [Cyp+*n*Lig] from a single ligand concentration of 100 μM and CypA at 20 μM

A list incorporating K_ds of all ligands screened can be found in Appendix E using transformed data at a single concentration. The method of sample introduction with regards to reproducibility has been discussed in Section 3.3. Comparisons of S/N values obtained using DI-ESI, on-line LC-MS and Automated nanoESI (NanoMate™) have been discussed in Chapter 2. Each method of sample introduction is listed separately. The differences noted between ZMD Auto and ZMD manual are a result of inconsistent flow rate using the HPLC system. Problems with sample carryover are discussed in Chapter 2 although a summary is tabulated in Section 3.5.

3.4.3 Comparison with Biological Assays

Fluorescence and PPIase IC_{50} assays were performed by Martin Wear (Walkinshaw group) and K_ds were obtained for a selection of ligands. Values between all three methods vary considerably confirming that deriving K_ds is extremely method dependent although they do all lie within one order of magnitude of each other. The general trend is in agreement validating the use of MS as an initial screen. ESI-MS also provides the most reproducible data supporting this conclusion.

The fluorescence assay is a measure of the intrinsic fluorescence Trp-121 with and without ligand present. Therefore, how the ligand binds, i.e. does it significantly alter the electronic environment in the pocket may affect the result. Mass spectrometry data is not dependent on which amino acids the ligands associate with but will be influenced by the proportion of hydrophobic and electrostatic interactions. The benefit being that intrinsic properties are being studied.

LIGAND	STRUCTURE	K_d (μM)		
		ESI-MS	Fluorescence	IC_{50}
CD365/01	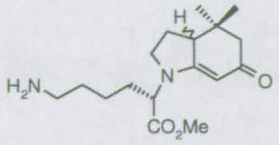	No binding	-	No inhibition
CD278/02	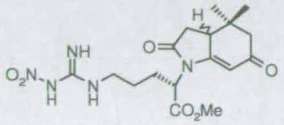	31.9 ± 3.1	5.0 – 30.0	No inhibition
CD291/02	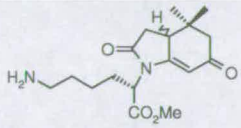	72.6 ± 16.2	15.9 ± 2.3	6.8 ± 1.9
CD261/02	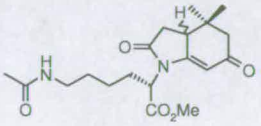	85.1 ± 19.0	-	No inhibition
CD357/03	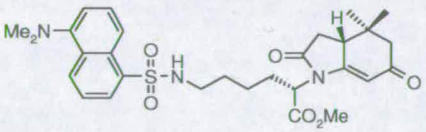	113.2 ± 11.0	21.9 ± 3.5	207.0 ± 57.8
CD290/02	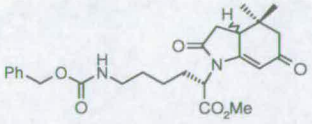	128.1 ± 28.6	5.0 – 20.0	No inhibition

Table 3-4 Comparison of K_ds obtained using ESI-MS, fluorescence and PPIase IC_{50}.

3.5 Conclusion

The principle of using mass spectrometry during phase I drug discovery has been proven in this study. A rank order of binding affinity has been generated for all ligands supplied and where present show broad agreement with bio-assays.

K_ds calculated from a single ligand concentration can be used to generate a rank order. K_ds calculated using multiple ligand concentrations produce more accurate absolute value. The precise route by which K_ds are obtained can be altered, but to make comparisons between ligands a single method for analysing the MS data should be taken.

Table 3-5 below provides a summary of the different techniques used within this study for high throughput noncovalent protein-ligand screening.

Method	Pro's	Con's
Manual Infusion	•Control sample introduction •Non-destructive ionisation	•Slow, 5-6 samples / h •High sample consumption •Day to day variability •Low S/N
Automated Injection	•Faster, up to 10 samples / h •Decreased sample handling	•High sample consumption •Day to day variability •Low S/N •Risk of sample carryover
Manual nanoESI	•Low sample consumption •Improved S/N	•Low throughput
Automated nanoESI – NanoMate™	•Low sample consumption •Up to 60 samples / h •Highly reproducible	•Cost

Table 3-5 Summary of the pro's and con's of each screening technique

3.6 References

[1] Daniel JM., Friess SD., Rajagopalan S., Wendt S., Zenobi R., *Int J Mass Spectrom.* 2002, **216**, 1-27
[2] Sannes-Lowery KA., Griffey RH., Hofstadler SA., *Anal Biochem,* 2000, **280**, 264-271
[3] Gao H, Yu YH, Leary JA, *Anal Chem*, 2005, **77**, 5596-5603

[4] Zhang S., Van Pelt CK., Wilson DB., *Anal Chem,* 2003, **75**, 3010-3018
[5] Veros CT., Oldham NJ., *Rapid Comm Mass Spectrom.,* 2007, **21**, 3505-3510
[6] Kitova EN., Bundle DR., Klassen JS., *J Am Chem Soc,* 2002, **124,** 5902-5913
[7] Elizabeth Moir, thesis, unpublished data
[8] Creigton TE., *Proteins Structures and Molecular Properties,* second edition
[9] Shirran S., *PhD Thesis*, unpublished data
[10] Ke H., Zydowsky LD., Liu J., Walsh CT., *Proc Natl Acad Sci,* 1991, **88,** 9483-9487
[11] Pflugl G., Walkinshaw M., *Nature*, 1993, **361**, 91
[12] Wang W., Kitova EN., Klassen JS., *Anal Chem,* 2003, **75,** 4945-4955
[13] Zhang S., Van Pelt CK., Wilson DB., *Anal Chem,* 2003, **75,** 3010-3018
[14] Tjernberg, A., Carno S., Oliv F., Benkestock K., Edlund P-O., Griffiths WJ., Hallen D., *Anal Chem,* 2004, **76**, 4325-4331

4 Melittin – Solution Phase H/D Exchange

This chapter describes the use of solution phase HDX-MS to probe the structure of melittin, a small 26 amino acid protein.[1] Melittin has been chosen as a model for developing in-house HDX techniques. Solvent conditions are varied to induce well documented conformational changes and, by comparing data obtained with different techniques, a picture of its structural dynamics in solution is obtained.

4.1 Introduction

Melittin is small, cheap and extremely well characterised, all major considerations for comparing and contrasting novel mass spectrometric techniques with other traditional complimentary methods such as CD, NMR and X-ray crystallography. Melittin can exist in a variety of structural forms, in aqueous solution it is a disordered polypeptide chain which converts to a helix in more hydrophobic solvents. The helix in turn aggregates, and the postulated dimer that is formed is thought to be the active form of this peptide. The ease with which helical conformations and aggregates can be induced in the presence of organic solvents,[2,3] and at high pH[4] and high peptide concentrations[5] (Section 4.2.1), which simulates the hydrophobic lipid bilayer of cell membranes, make it an ideal candidate for validation studies.

Fully structured melittin comprises two α-helices flanking either side of Pro-14 (Figure 4-1) and several studies ascertaining the exact positioning of the α-helices have been carried out over the last 25 years. Gerig[2] determined the positioning of the α-helices from residues 2-8 and 13-25 with NMR in a hexafluoro-2-propanol / water mix. Hirota *et al.*[3] had previously used CD to study how these assignment of helical regions alters depending on the type and concentration of alcohol used. In a 'pseudo-native' environment i.e. buffered aqueous conditions at very high concentration[5] (10 mM) the two helical regions span residues 2-11 and 15-23 with a kink of approximately 46° as part of a tetramer. The angle of the kink and relationship

between the individual monomers was found to be temperature dependent. Naito *et al.*[6] used solid state NMR to calculate the angle of the kink at residues 12-14 as 140° which compares with the work of Lam *et al.*[7] who report 160°. Both NMR studies contrast somewhat with findings using X-ray diffraction[1] which places the value at 120°. The structure depicted in Figure 4-1 was obtained from a dimer found using X-ray diffraction.[1]

NMR has also been extensively used to study the effect of high pH and salt concentration in inducing the helical nature and monomer aggregation.[4] Wang and Polavaropu[8] used vibrational CD to study the same effect (CD data for this study is presented in Section 4.2.2).

Much of the work performed on melittin is driven by a desire to study the mechanism by which it interacts with cell membranes and in particular its role as a voltage gated channel involved in cell lysis.[6,9,10] Channel forming proteins require a degree of flexibility; to probe this, Pawlak *et al.*[11] synthesised melittin attached to a hydrophilic template and studied its oligomerisation by monitoring the formation of a functional tetramer.

Gross and co-workers studied melittin indirectly using its interaction with calcium saturated calmodulin (CaM) to illustrate the development of PLIMSTEX[12] (See Section 4.4) as this is a well known interaction.[13] By titrating melittin into a CaM solution and monitoring deuterium uptake as a function of ligand concentration, he established a 1:1 binding stoichiometry and a binding constant of K_d 54μM compared to a value of 330 μM.[14]

Anderreg *et al.*[15] used HDX and mass spectrometry on melittin to determine proton populations and carried out CID to map the exchange.

The following two chapters aim to consolidate these findings using mass spectrometry both as a structural probe (CID and gas phase HDX) and simply as a mass detector of solution phase HDX (DI-ESI and PLIMSTEX). To this end, the

labile Leu-13 – Pro-14 amide bond is crucial in trying to determine where helicity is retained within the structure. Mass shifts resulting from H/D exchange enable a comparison of secondary structural elements of the y13 (C-terminal) fragment with the whole protein. Table 4-1 and Table 4-2 list the most common fragments obtained using CID along with of the maximum number of exchangeable hydrogens. This assumes the N-terminal amide group of glycine to be neutral and hence exchange only 2 hydrogens.

Figure 4-1 Melittin taken from a crystal structure dimer[♣] exhibiting a full α-helix partially arrested at Pro-14

[♣] X-ray diffraction structure: Protein Data Bank (Gribskov, M., Wesson, L., Eisenberg, D.)

b^{1+} Fragments	1	2	3	4	5	6	7	8	9	10	11	12	13	14	15	16	17	18	19	20	21	22	23	24	25	26	
	G	I	G	A	V	L	K	V	L	T	T	G	L	P	A	L	I	S	W	I	K	R	K	R	Q	Q	NH_2
y^{2+} Fragments	26	25	24	23	22	21	20	19	18	17	16	15	14	13	12	11	10	9	8	7	6	5	4	3	2	1	
N° Labile Hydrogens	2	1	1	1	1	1	3	1	1	2	2	1	1	0	1	1	1	2	2	1	3	5	3	5	3	3	2

Table 4-1 b and y fragment annotation and numbers of labile hydrogens per amino acid on neutral melittin

Fragment	Labile Hydrogens	Fragment	Labile Hydrogens
b5	6	y13	32
b6	7	y15	34
b7	10	y17	38
b8	11	y18	39
b9	12	y19	40
		y20	43
		y21	44
		y22	45

Table 4-2 Common fragments with respective numbers of labile hydrogens denoting mass increase according to charge state

4.2 Circular Dichroism (CD) - A 'Traditional' Analytical Approach to Determine the Secondary Structure of Melittin

Following the work described above, to probe the effect of solvent environment on the structure of melittin we here have used methanol to create an increasingly 'pseudo lipid' or non-polar medium. A simple titration of methanol against 10mM ammonium acetate showed that increasing the hydrophobic environment promotes the formation and stability of the α-helix. Initial work employed circular dichroism (CD) to describe the ease with which melittin moves into and out of its helical conformation. This confirms studies performed by Hirota *et al.*,[3] Terwilliger and Eisenberg[1], and Bernèche *et al.*[16] amongst others.

4.2.1 Hydrophobicity and the α-Helix

Figure 4-2 illustrates the shift in ellipticity to produce the typical α-helical signature with increasing methanol content. This is followed by plotting the values at 220 nm. There is no evidence of helical conformation at less than 11.8% methanol. However, there is an apparent transformation when increasing the methanol to 26.5%. The random coil signature is less predominant inferring a potential shift in structural conformation. At 51% and above, the presence of the α-helix is increasingly prevalent.

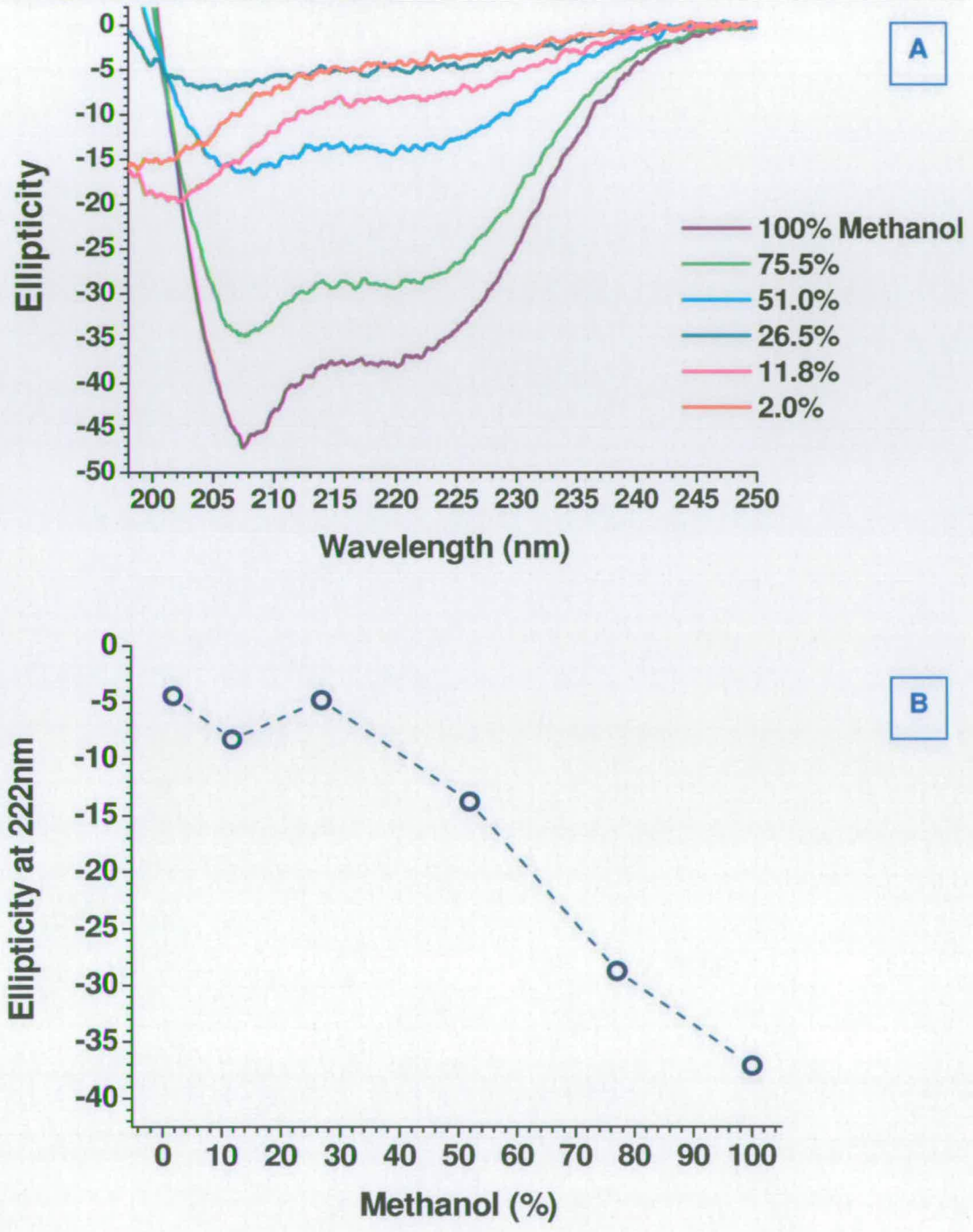

Figure 4-2 (A) CD chromatograms of melittin with increasing methanol content and (B) a plot of ellipticity at 222 nm. The dashed line is included to guide the eye.

4.2.2 The Effect of pH and Salt on α-Helical Formation

The effect of salt on melittin is also demonstrated by the use of CD although the effect of pH remains inconclusive under buffered solvent conditions. Figure 4-3 illustrates the effect buffer and salt have on the formation and retention of the α-helix. A random coil is detected in ammonium acetate (pH 6.8) in agreement with data shown in Figure 4-2. The negative ellipticity detected over the range 202-195 nm and a sharp increase at 212 nm provides a clear signature. In the presence of phosphate buffer (pH 7.4) ellipticity values produced by the presence of random coil is reduced, illustrated by a shift in wavelength corresponding to 210-205 nm indicating the presence of some α-helical nature. The ellipticity at 222 nm however, is much less than that of the TBS solutions where the melittin favours the helical form at all pHs ranging 2.25 – 12.20. Excessive charging expected at pH 2.25 should result in coulombic repulsion forcing the protein to elongate, however the structure is retained, implying the presence of salt has a far greater stabilising effect on the secondary structure than pH. The spectra show a degree of variability around the pH range but this is deemed insignificant for the reason previously stated. The formation of the helix under these conditions must therefore be attributed to the presence of salt.

Once outwith the pH range of tris i.e. pH 10 and above, a question which remains is whether the helix is only retained by the high salt content. Although not answered here, both of these buffers are routinely used in biological assays, and can induce and retain protein folds on small flexible proteins. In summary, the conformational change from random coil to α-helix can be manipulated using methanol whereas this work suggests the influence of pH is much less marked.

For the purposes of comparing melittin conformations in solution and the gas phase, methanol is the preferred solvent for inducing a conformational change. This represents the simplest route for direct infusion ESI-MS studies, although pH is also a parameter that can be changed. Direct infusion ESI is not a viable method for studying the effect of high salt concentrations, due to the involatile nature of TBS. However, here PLIMSTEX[12] (Chapter 1, Section 1.5.4.1) could be an ideal technique

to pursue. PLIMSTEX in turn would not be appropriate for methanol induced conformational changes as the organic solvent content necessary to mimic the membrane environment will prevent melittin from binding to the reverse phase column. As a consequence of these physical constraints, several techniques are evaluated.

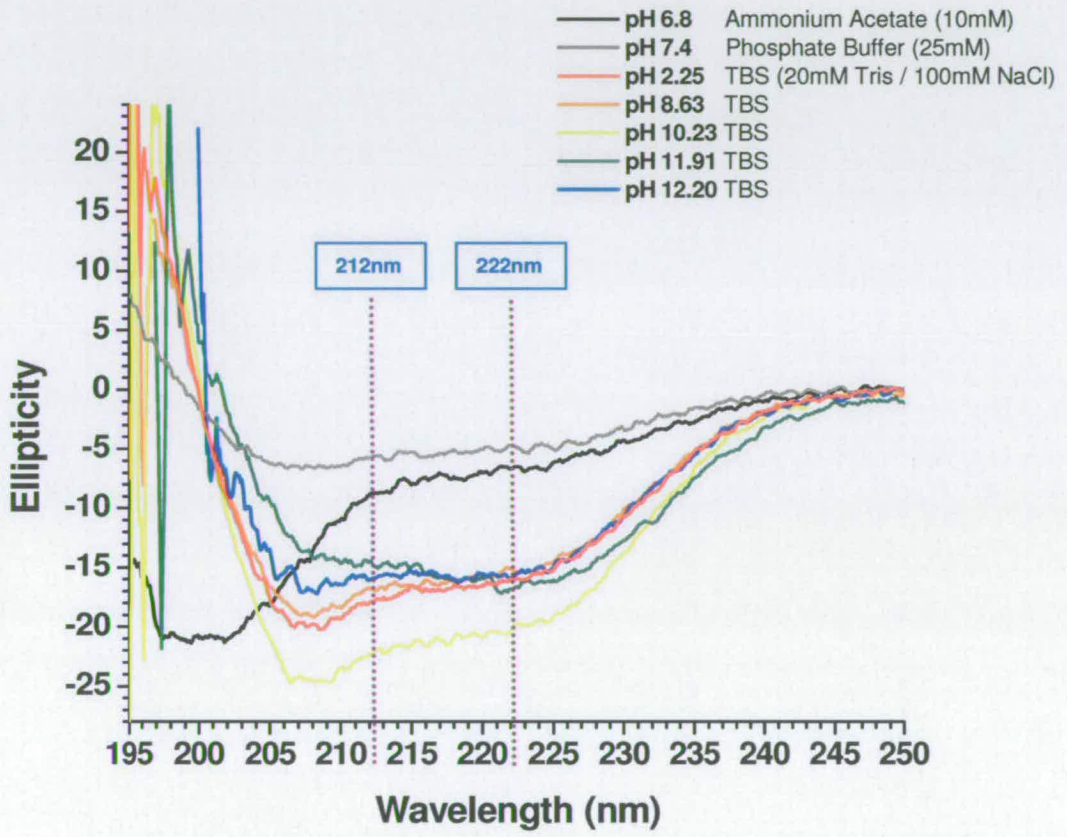

Figure 4-3 CD spectra comparing melittin in tris buffered saline (TBS) at low (pH 2.25), 'near pseudo native' (pH 8.63) and high pH (pH 10.23 – 12.20) with the 'pseudo native' conditions of ammonium acetate and phosphate buffer

4.3 Direct Infusion HDX-MS

Melittin exhibits increased stable secondary structure as conditions become more hydrophobic (Figure 4-2). It was possible to predict a decrease in total H/D exchange as the α-helical nature became increasingly predominant. 10 μM melittin was

incubated in *d*-methanol / 10mM *d*-ammonium acetate at varying ratios, and the rate of deuterium exchange monitored with time. Figure 4-4 shows typical spectra of melittin incubated in non-*d*- and *d*-ammonium acetate. CID analysis was used to map these exchange patterns.

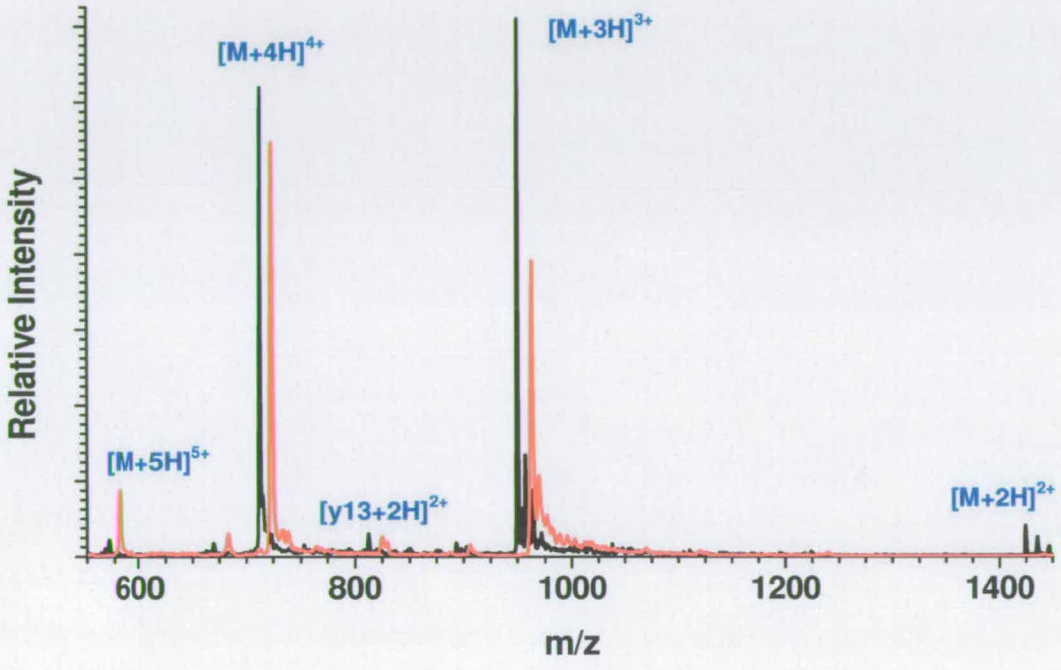

Figure 4-4 DI-ESI on melittin incubated in 10mM ammonium acetate (black) and *d*-ammonium acetate (red)

4.3.1 The Effect of Altering Solvent Hydrophobicity

Anderreg *et al.*[15] demonstrated three distinct H/D exchange rates when melittin was incubated in 79% *d*-methanol / 19% *d*-water / 2% *d*-acetic acid. *d*-uptake of 35 deuteriums was detected during the first 0.8 min, (a time frame comprising protons from a primary population). These are attributed to freely available protons not involved in secondary structure. This increased to 45 after 14 mins and designated as a secondary (intermediate) population. These labile hydrogens are assumed to have some involvement in secondary structure. Protons in the third phase were only slowly exposed, exchanging 48 after 45 mins. These are thought to be involved in

hydrogen bonds stronger than that of the secondary population. Some structure is putatively maintained here as exchange did not go to completion.

A close inspection of the solution structure of melittin (Figure 4-1) can provide information about which groups will be free to exchange. The amide hydrogens of residues 2-11 and 15-23[5] are locked into a helix. The side chains of these amino acids will be free in solution and hence available for exchange - at least if the peptide is monomeric.

Experimental data in Figure 4-5 illustrates the observed shift in mass with an increase in *d*-incubation time at 4°C. Low temperatures were employed by incubating the sample and infusion needle on ice, thus reducing the exchange rate and increasing sampling time.[17,18]

Rapid exchange of 5 to 20 labile hydrogens occurs during the initial 6 minutess, and is lower than that observed by Anderegg *et al.*[15] Exchange between 6 and 8 minutes has high errors, which is attributed to incomplete equilibration of the infusion lines resulting in some back exchange. As a result, data obtained within 6-10 minute incubations in deuterated buffer provides information on exchange rates which are a combination of hydrogens exchanged from the primary and intermediate populations defined by Anderegg.

Rates between 10 and 24 minutes elicit two further distinct exchange patterns. Here there are qualitative similarities with data generated by Anderegg *et al.* In both studies a decrease in the rate of exchange occurs after a mass increase of ~35 leading to the conclusion that exchange has completed for the so called primary population. With solvent (80% methanol 2% acetic acid) and source conditions used by Anderegg, the primary population has completed exchange by ~0.8 mins. In this work, as might be expected, the time taken to reach 35 increases as a function of methanol concentration, but in all cases takes over 8 mins i.e. an order of magnitude greater time than that found by Anderegg. For the 50 and 100 % methanol solutions, it appears that our primary population involves ~30 exchangeable sites rather than

~35 (which is what is seen here with lower concentrations of methanol). In this study it is difficult to distinguish between the primary and secondary populations as the rate of *d*-uptake is greatly reduced after 10 minutes, in line with the tertiary population described by Anderegg. This difference can be attributed to solvent conditions which are acid free in these experiments with near neutral pH. Exchange under these buffering conditions occurs much faster than at the low pH used by Anderegg (pH 3.2), but conversely melittin should retain its fold more at pH 6.8. We have here considered the effect of solvent on the conformation of melittin. For the 0% methanol we see the fastest uptake of deuterium and for the 50 and 100% methanol the slowest. It is apparent therefore that solvent conditions do affect the exchange rates and that this in turn is related to the solvent imparted conformation(s) of the peptide.

Reducing the temperature of the infusion solution reduces exchange rates but distinction between the populations becomes harder. There are problems when maintaining a low temperature throughout the experiment which may also contribute to some of the variability of exchange over the time course. Reducing the pH as described above may be a more effective approach.

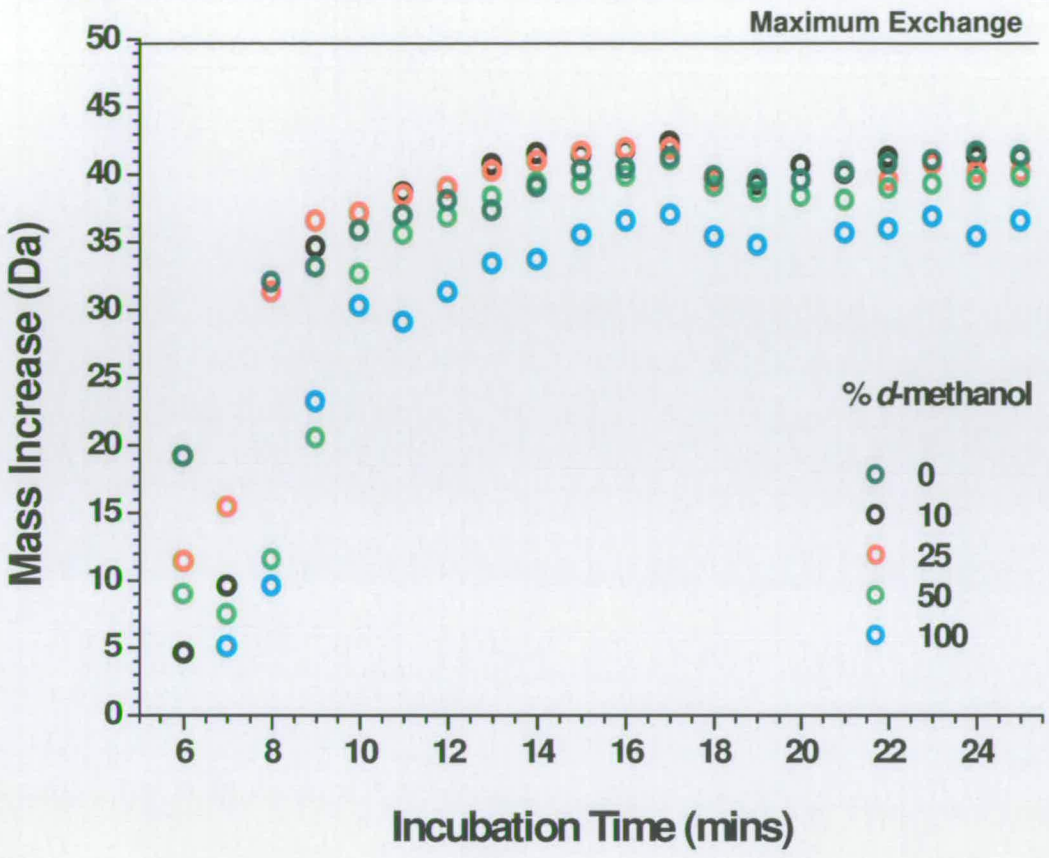

Figure 4-5 HDX time course comparing exchange of melittin ($[M+3D]^{3+}$) against a titration of *d*-methanol in *d*-ammonium acetate

10% *d*-methanol shows the most dramatic mass increase of the molecular ion increasing over 30 Da between 7 and 9 minutes. It is impossible to distinguish between the gradients of the 25%, 50% and 100% *d*-methanol solutions although the latter two increase between 8 and 10 minutes as opposed to 6 and 8 minutes. Similar observations can be made for the central or intermediate region. Gradients from 10 to 16 minutes also exhibit differences but reach a maximum at ~17 mins. In 100% *d*-methanol, melittin only achieves a maximum 37 exchanges as opposed to the average 42 reached under the other conditions suggesting the presence of a more rigid conformation, perhaps held by hydrogen bonds due to a short stable α-helix. None of the solutions achieve maximum exchange suggesting either a) some overall structural retention / aggregation preventing solvent accessibility or b) back exchange during desolvation.

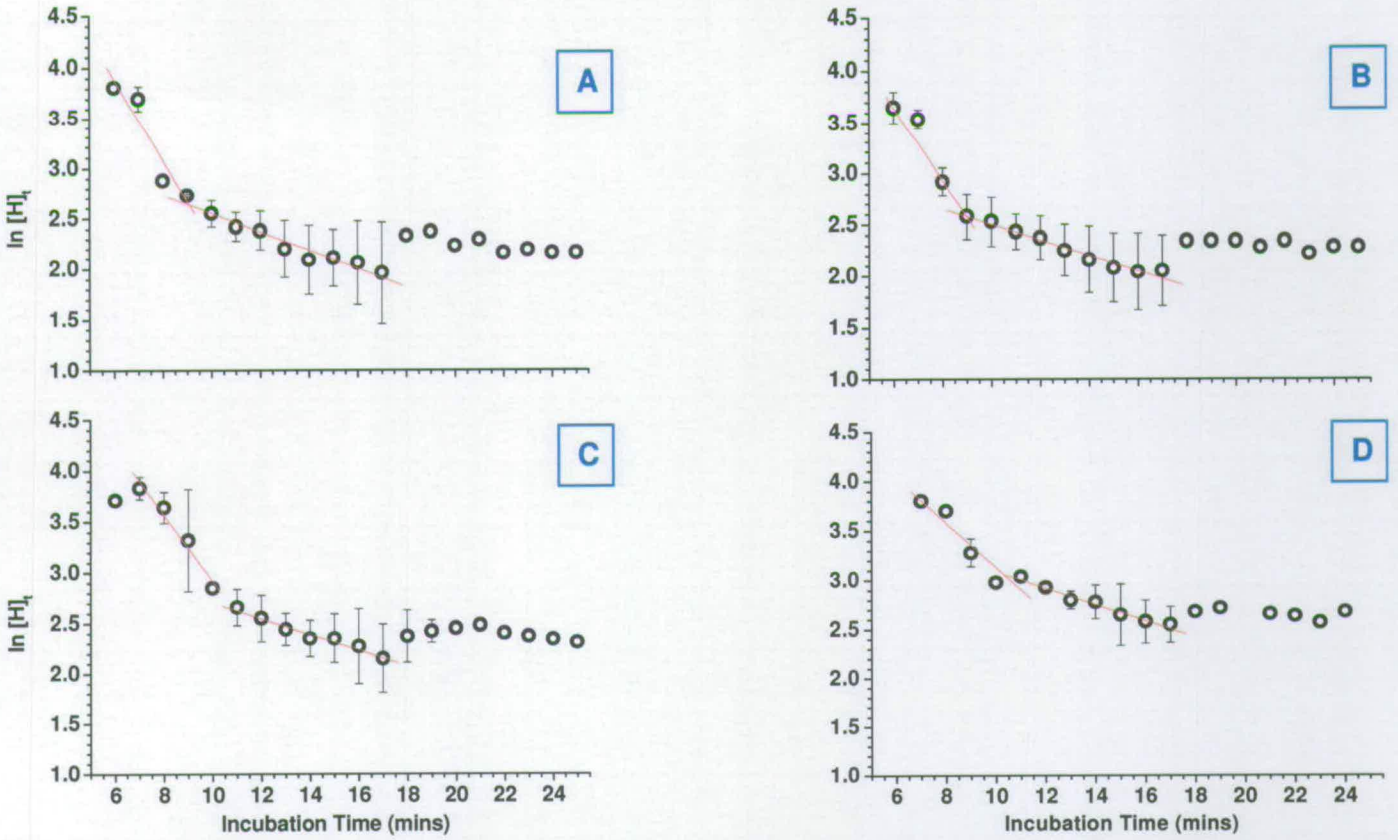

Figure 4-6 Hydrogen depletion in (A) 10%, (B) 25%, (C) 50% and (D) 100% *d*-methanol solutions to distinguish between the intermediate and tertiary proton populations for the $[M+3D]^{3+}$ charge state

Population	% *d*-methanol	$[M+4D]^{4+}$ -*k* (Slope)	$t_{1/2}$ (mins)	R^2	$[M+3D]^{3+}$ -*k* (Slope)	$t_{1/2}$ (mins)	R^2	$[y_{13}+2D]^{2+}$ -*k* (Slope)	$t_{1/2}$ (mins)	R^2
Intermediate	0	0.286	2.42	1.00	0.301	2.30	1.00			
	10	0.550	1.26	0.97	0.406	1.71	0.95	0.404	1.72	0.97
	25	0.327	2.12	1.00	0.358	1.94	1.00	0.318	2.18	0.98
	50	0.241	2.88	0.93	0.326	2.13	0.98	0.370	1.87	0.99
	100	0.123	5.64	0.98	0.224	3.09	0.94			
Tertiary	0	0.063	11.00	0.91	0.074	9.37	0.98			
	10	0.047	14.75	0.87	0.091	7.62	0.97	0.127	5.46	0.96
	25	0.074	9.37	0.94	0.075	9.24	0.98	0.139	4.99	0.97
	50	0.058	11.95	0.95	0.078	8.89	0.98	0.070	9.90	0.98
	100	(0.009)	(77.02)	0.64	0.082	8.45	0.99			

Table 4-3 Summary of rates ($mins^{-1}$), calculated half-lives and linear correlation coefficients for charge states 4+, 3+ and y13 fragment

Hydrogen depletion ($ln[H]_t$) for $[M+3D]^{3+}$ is plotted against time (Figure 4-6) to illustrate the presence of intermediate and tertiary proton populations exhibiting linear 1st order distributions. It is difficult to distinguish between the results when plotted in this manner so half lives are calculated to enable a comparison of exchange rates.

Exchange half-lives are calculated for each proton population for charge states 3+, 4+ and the y_{13}^{2+} fragment (Table 4-3) and illustrated in Figure 4-7 showing a comparison between the two exchange populations. The $t_{½}$ values calculated for the intermediate population are much smaller than those of the tertiary populations. This supports the proposed hypothesis that hydrogens held in more stable hydrophobic interactions or hydrogen bonds take longer to undergo exchange.

Half life values quoted by Anderegg *et al.* are calculated using $[M+4H]^{4+}$ to be 47 s (primary), 10 mins (intermediate) and 37 mins (tertiary). All mass shifts however represent a snapshot of exchange on melittin in solution at any given time point. If

there is no relation between the resultant charge state and the solution conformation for this flexible small peptide, *d*-uptake should be similar for each charge state.

As the hydrophobicity of the environment increases, there is a general trend for the intermediate exchange rates of the 3+ and 4+ charge states to decrease (Figure 4-7 (A)). Identical solvent conditions for CD demonstrate increased α-helical formation. It takes time for these hydrogen bonds to be disrupted to then allow H/D exchange to occur. The two charge states show strong similarities in solutions up to 50% *d*-methanol after which they diverge. $[M+4D]^{4+}$ exhibits much longer half lives than $[M+3D]^{3+}$. The differences may arise from two factors:

(i) More than one conformation exists in 100% methanol. Side chains not involved in helical stability may be solvent exposed in the less rigid state, increasing the rate at which deuterium is taken up. This is unlikely as these conformers are attributed to $[M+3D]^{3+}$, the more native state, and not $[M+4D]^{4+}$, the charge state expected to represent more unfolded forms.

(ii) $[M+4D]^{4+}$ may be derived from solution aggregates which undergo nozzle skimmer dissociation. This would reduce solvent exposure, slowing exchange.

Explanation (ii) is also favoured as the two exchange populations seen with the other solutions were generally found to be less defined. Averaging data of $[M+4D]^{4+}$ resulted in detection of a single rate of *d*-uptake across the time course. Labile hydrogens on the complex surface would exchange out rapidly with detection time, whilst gradual exchange embedded within complex interface occurs slowly.

The high value noted for the methanol free solution is attributed to unknown conformation(s) and hence unknown H-bonding patterns of the 'random coil' detected using circular dichroism. The intermediate populations of both $[M+4D]^{4+}$

and $[M+3D]^{3+}$ exhibit half lives that lie within the experimental error suggesting they are derived from similar conformational states.

The tertiary population (Figure 4-7 (B)) does not suggest any significant difference in exchange rates across the range of charge states or solvent environments. This implies the structures retain the same or similar hydrogens within the more involved secondary i.e. α-helical structure. The anomalous half life value of 77 mins for $[M+4D]^{4+}$ from 100% methanol is explained by experimental variability and is supported by explanation (ii) discussed above.

The y13 fragment shows no difference in exchange rates for either population in solutions containing 10% – 50% *d*-methanol. Therefore no apparent differences in the structure of the C-terminal fragment can be ascertained within these three environments. This suggests the C-terminal fragment has an overall more open structure than the 3+ parent ion inferring structural retention is at the N-terminal region. This would be expected as the N-terminal region has only one basic residue compared to 4 on the C-terminal region, which would cause it to be more likely to unfold due to coulombic repulsion.

Establishing a steady spray by ESI on the LCQ proved a limiting factor for determining initial exchange which in turn may provide crucial information on the diversity of conformers. The same problem regarding the rate at which initial HDX happens is apparent here for nanoESI on the LCQ. Protons not involved in H-bonding or weak hydrophobic bonds exchange rapidly. If the structure is very dynamic, hydrogens involved in H-bonding may exchange on unfolding to exhibit D-bonding on refolding.

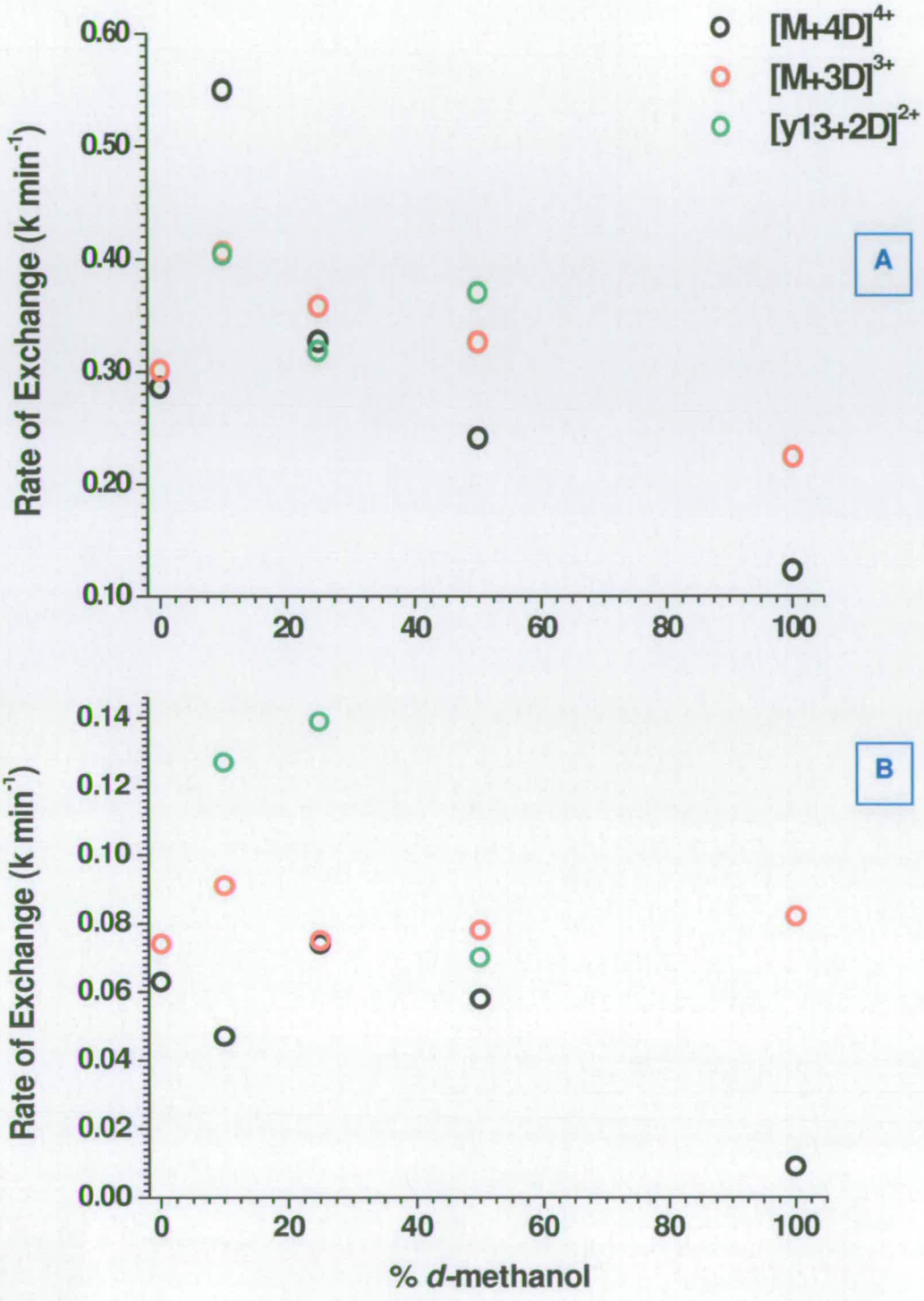

Figure 4-7 Rates of exchange for both the intermediate (A) and tertiary (B) proton populations

Figure 4-8 illustrates the effect of increasing the relative proportion of methanol has on the number of labile hydrogens for $[M+2H]^{2+}$, $[M+3H]^{3+}$ and $[M+4H]^{4+}$. There is no significant difference between charge states and any variability is likely to be as a result of peak quality. No further increases in mass are detected after an incubation of 1 h 15 mins so it was assumed that an exchange equilibrium had been reached in the melittin solution. 100% *d*-methanol exchanged a maximum of 32 hydrogens whereas 100% *d*-ammonium acetate exchanged an average of 38. An almost identical pattern emerges for the y13 fragment implying the effect of increasing hydrophobicity causes the whole protein to respond in a uniform manner.

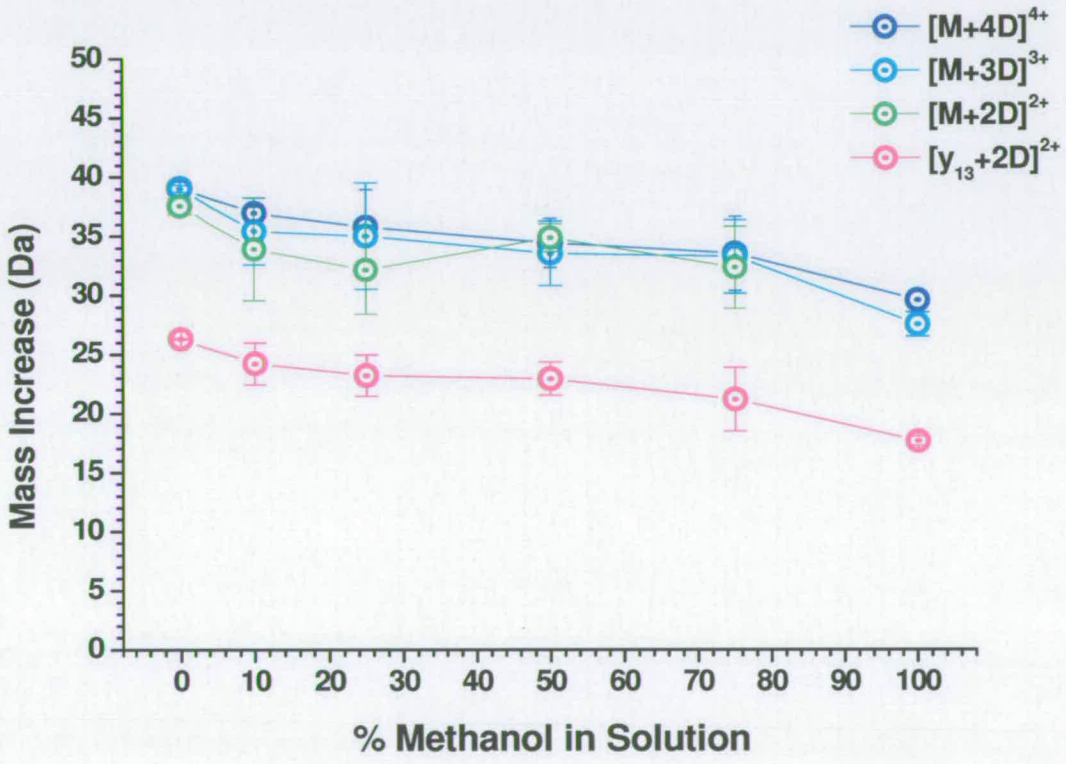

Figure 4-8 DI-ESI of melittin incubated 1 h 15 mins in *d*-methanol titrated against *d*-ammonium acetate

As discussed in Chapter 1, discrete charge states do not exist in solution in the same way as they do in the gas phase. An equilibrium exists between protonated forms and the surrounding solvent. As pH is lowered and proton availability increased, so the

protein receives those protons. This results in coulombic repulsion forcing the protein towards an open denatured conformation rendering the whole protein available to H/D exchange.

Differences in the extent of exchange between charge states are observed in the following nanoESI data. Figure 4-9, an equivalent direct infusion experiment using nanoESI rather than ESI with melittin in 50% *d*-methanol also favours the 3+ and 4+ charge states. However, $[M+4H]^{4+}$ has an elevated exchange of 2-3 Da more than $[M+3H]^{3+}$ inferring a marginally more solvent exposed structure consistent with higher charge. Neither undergoes complete exchange suggesting some structural retention probably due to H-bonding. The protein ions represented by the 5+ charge state have been fully exposed to *d*-solvent. Two explanations can be given here, (a) an open, linear conformer is refolding at a slower rate than exchange is happening or (b) there is no refolding at all. The latter is the most likely as the majority of the protein detected is retaining some form of structure. A typical spectrum shown in Figure 4-10, shows $[M+5D]^{5+}$ to be a minor component relative to $[M+4D]^{4+}$ and $[M+3D]^{3+}$. This may also explain the gap between the lower charge states. If a portion of protein is slightly denatured it may not refold efficiently and the slightly more open structure favours the extra charge on desolvation. This allows distinctions to be made between folded and fully denatured protein in solution. The y13 fragment is not formed under these desolvation conditions so no conclusions can be drawn to determine whether the structure is preferentially stabilised on the N- or C-terminus. NanoESI conditions help to retain conformational stability.

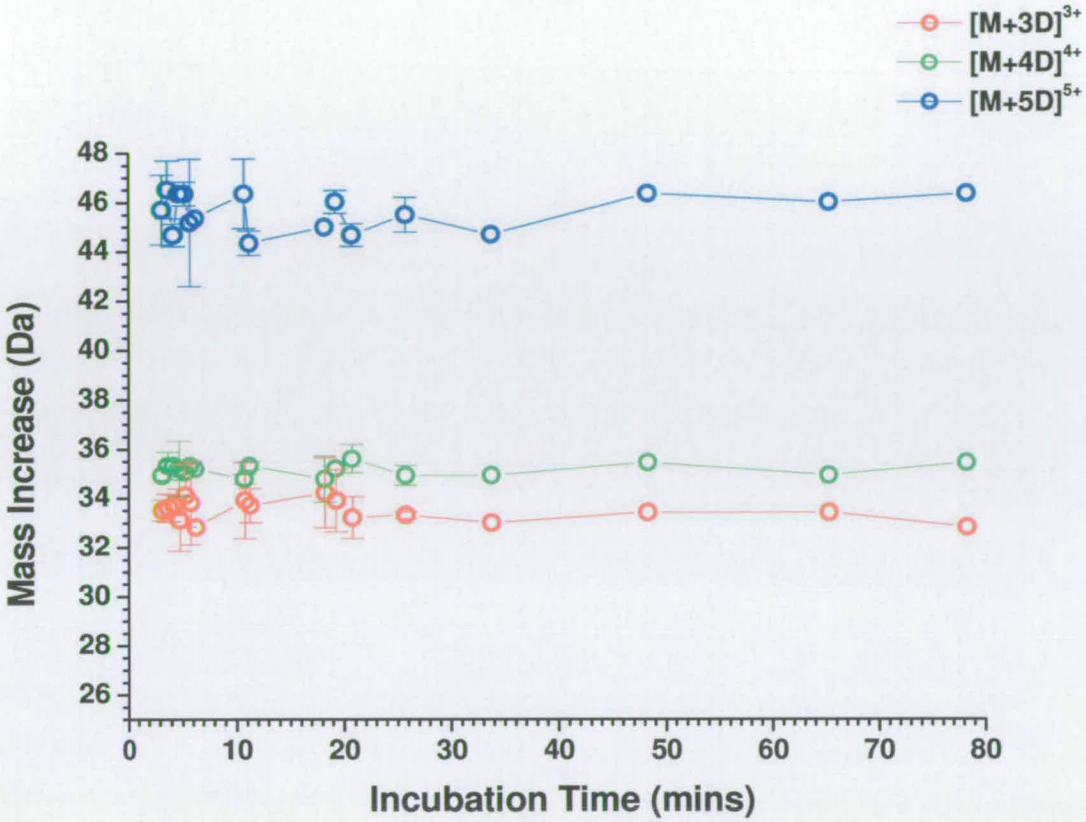

Figure 4-9 nanoESI on melittin exposed to 50/50 *d*-methanol / *d*-ammonium acetate over a period of 80 mins

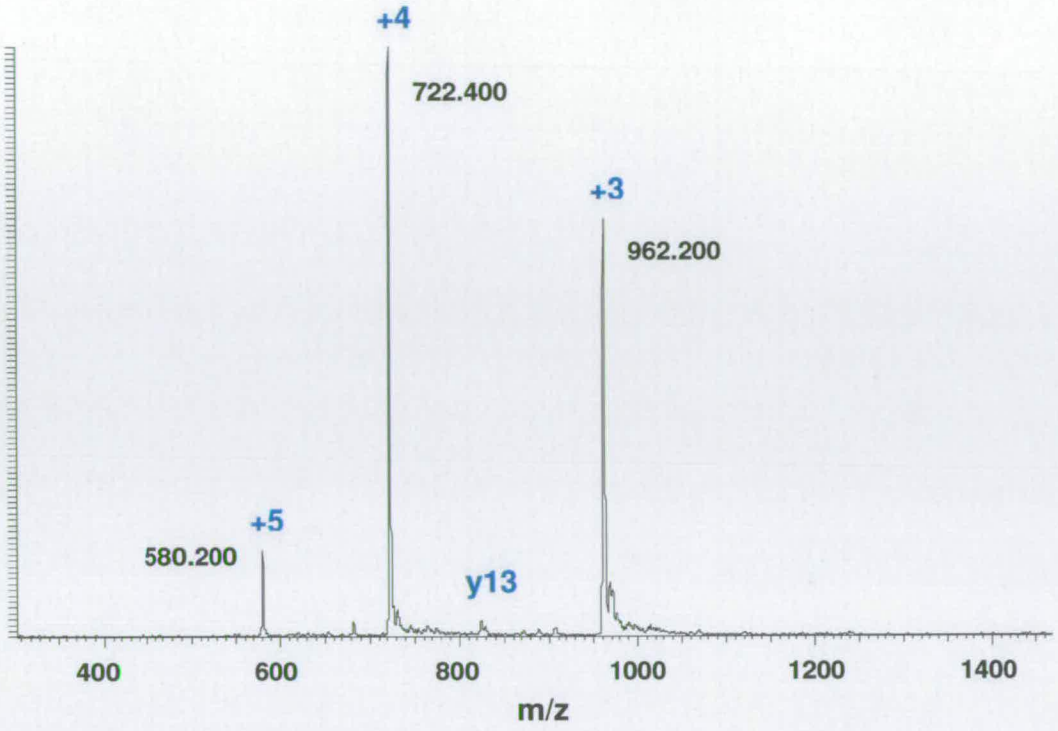

Figure 4-10 Spectrum illustrating different intensities of melittin charge states analysed by nanoESI-LCQ from 50/50 *d*-methanol / *d*-ammonium acetate

4.3.2 The Effect of pH on HDX of Melittin - Ammonium acetate

A reduction in rate of deuterium uptake with increase in pH is discussed in this section, supporting NMR studies which show high pH and high salt concentrations can induce melittin dimerisation.[4,8]

Using ESI, mass shifts for charge states 4+, 3+, 2+ and fragment y13 from 10μM melittin solutions at pD 7.6, 8.6 and 10.0 are plotted against time in Figure 4-11. pD 8.6 is shown to be the most conducive to exchange exhibiting the greatest increase in mass over the first 10 mins. $[M+3D]^{3+}$ and $[M+4D]^{4+}$ exchange approximately 46 of the available 50 labile hydrogens respectively and the y13 fragment exchanges 30 of the maximum 34.

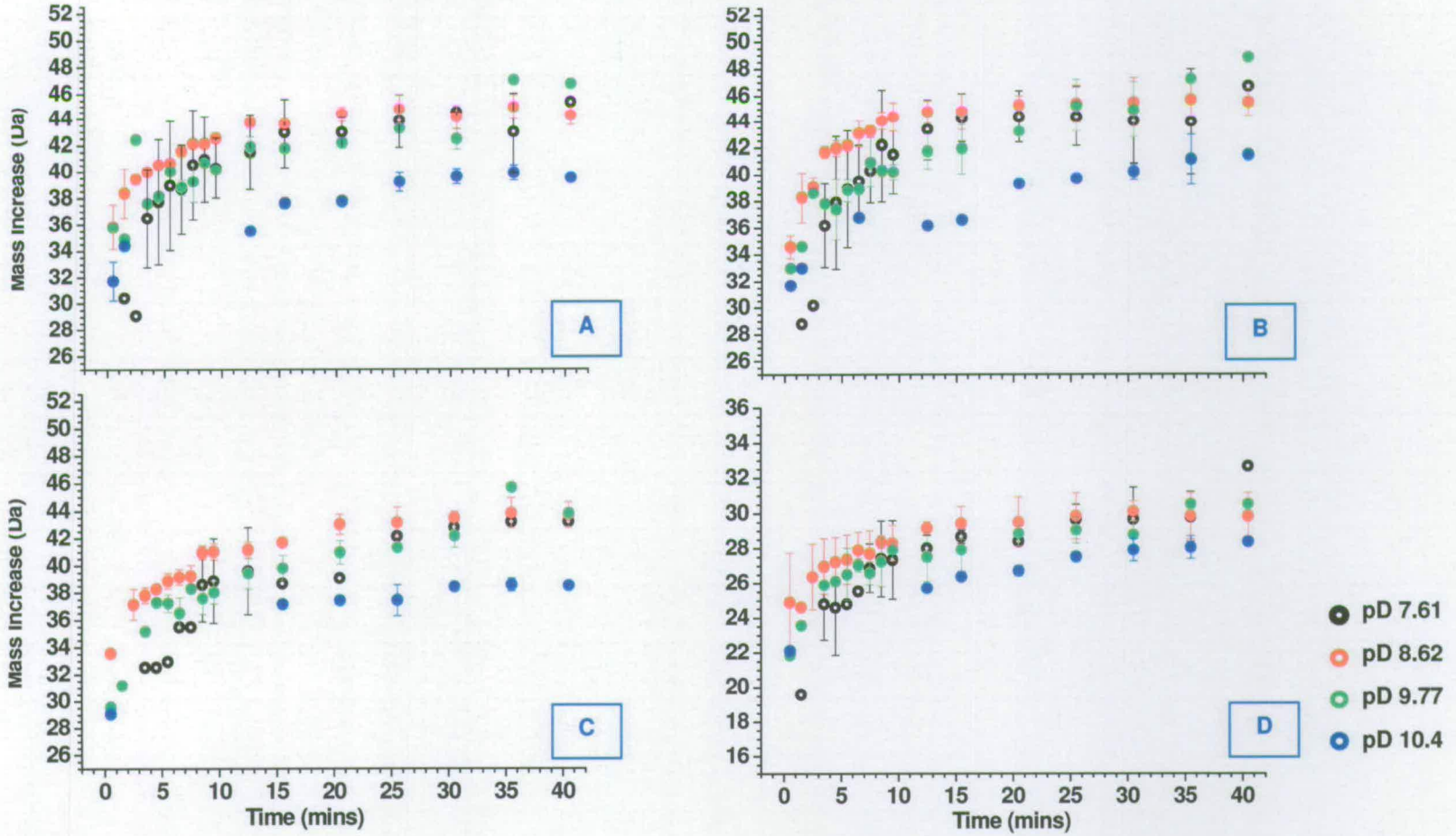

Figure 4-11 Deuterium uptake by melittin ((A) $[M+4D]^{4+}$, (B) $[M+3D]^{3+}$, (C) $[y13+2D]^{2+}$ and (D) $[y13+2D]^{2+}$) over time buffered to pDs 7.61, 8.62, 9.77 and 10.40 in *d*-ammonium acetate.

d-uptake by $[M+2D]^{2+}$ is consistently 3-4 Da less than the other charge states inferring the presence of a conformer containing a more stable secondary structure preventing exchange, but this again represents a small fraction of the total.

pD 7.61 as expected exchanges more slowly than pD 8.62 consistent with studies by Englander and co-workers[19] stating that exchange rates increase with pH. However, above pD 8.62 uptake decreases suggesting another factor is slowing and possibly preventing exchange. This could be due to a) aggregation or b) an increase in helicity. NMR studies by Takei *et al.*[4] suggest dimerisation.

As with the methanol studies the most interesting exchange happens within the first few minutes of exposure to *d*-ammonium acetate. The data here shows at least 2 exchange rates for each solution. Rate constants are calculated for each population with exchange half lives for each solution and, where possible the charge states are compared. The second or 'intermediate' rate is shown to be the most reproducible region within these data. This is probably attributable to the time taken to achieve a steady flow rate.

The data displayed in Figure 4-11 has been converted to exchange rates by plotting the natural logarithm of hydrogens remaining ($\ln(H_t)$ against time (t)) ($[M+3D]^{3+}$ is shown in Figure 4-12). Protons from the same population types exhibit straight lines inferring first order kinetics to produce a gradient being inversely proportional to the rate constant, *k*. Three population types are clearly seen with buffers pD 8.62 and pD 9.77 inferring ion stability within the solution possibly aiding efficient desolvation. These rate constants show similarities with the hydrophobicity data discussed above in that the intermediate population elucidates the information pH has on structure.

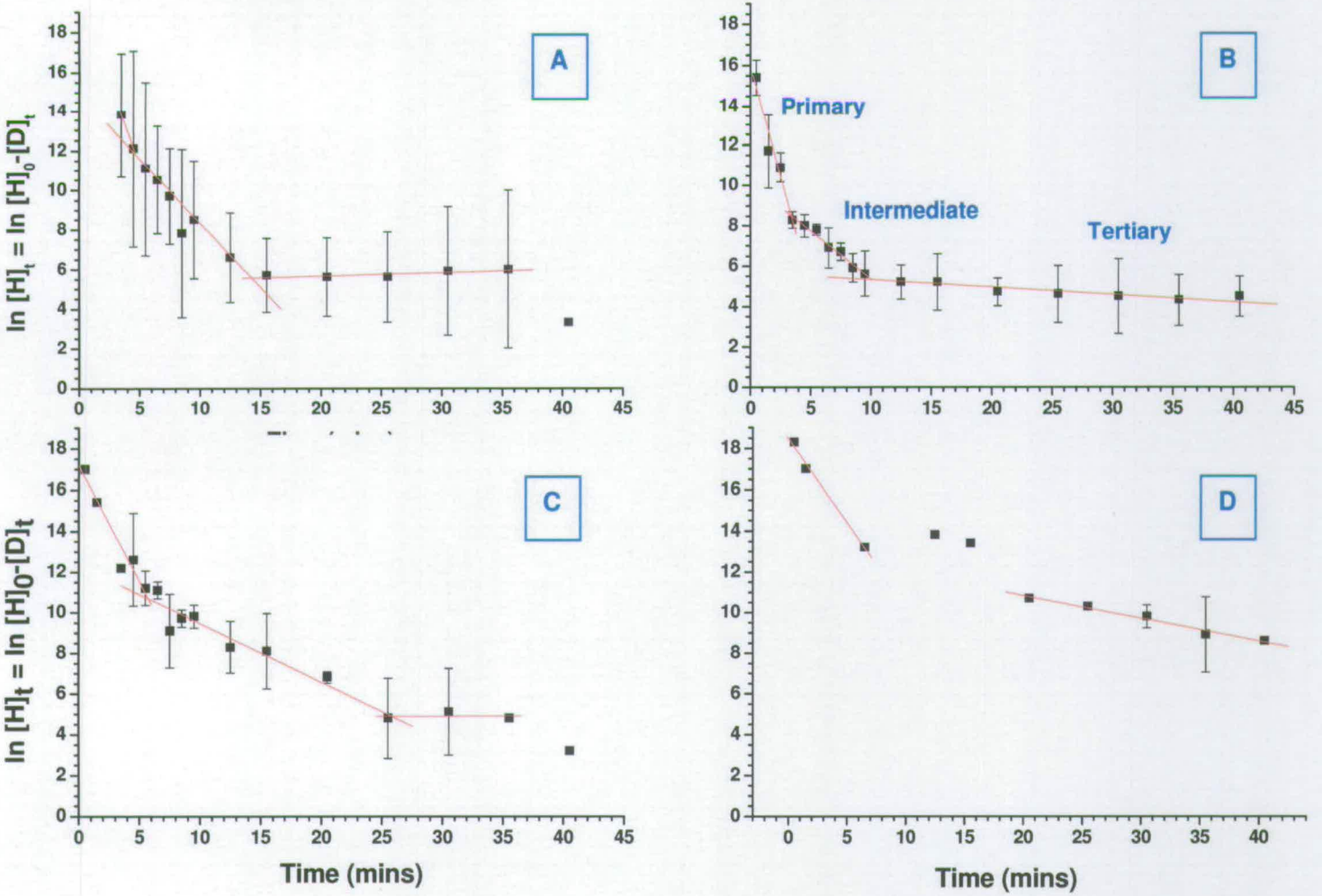

Figure 4-12 Hydrogen depletion on Melittin ($[M+3D]^{3+}$) with time at pD 7.61 (A); pD 8.62 (B); pD 9.77 (C) and pD 10.40 (D)

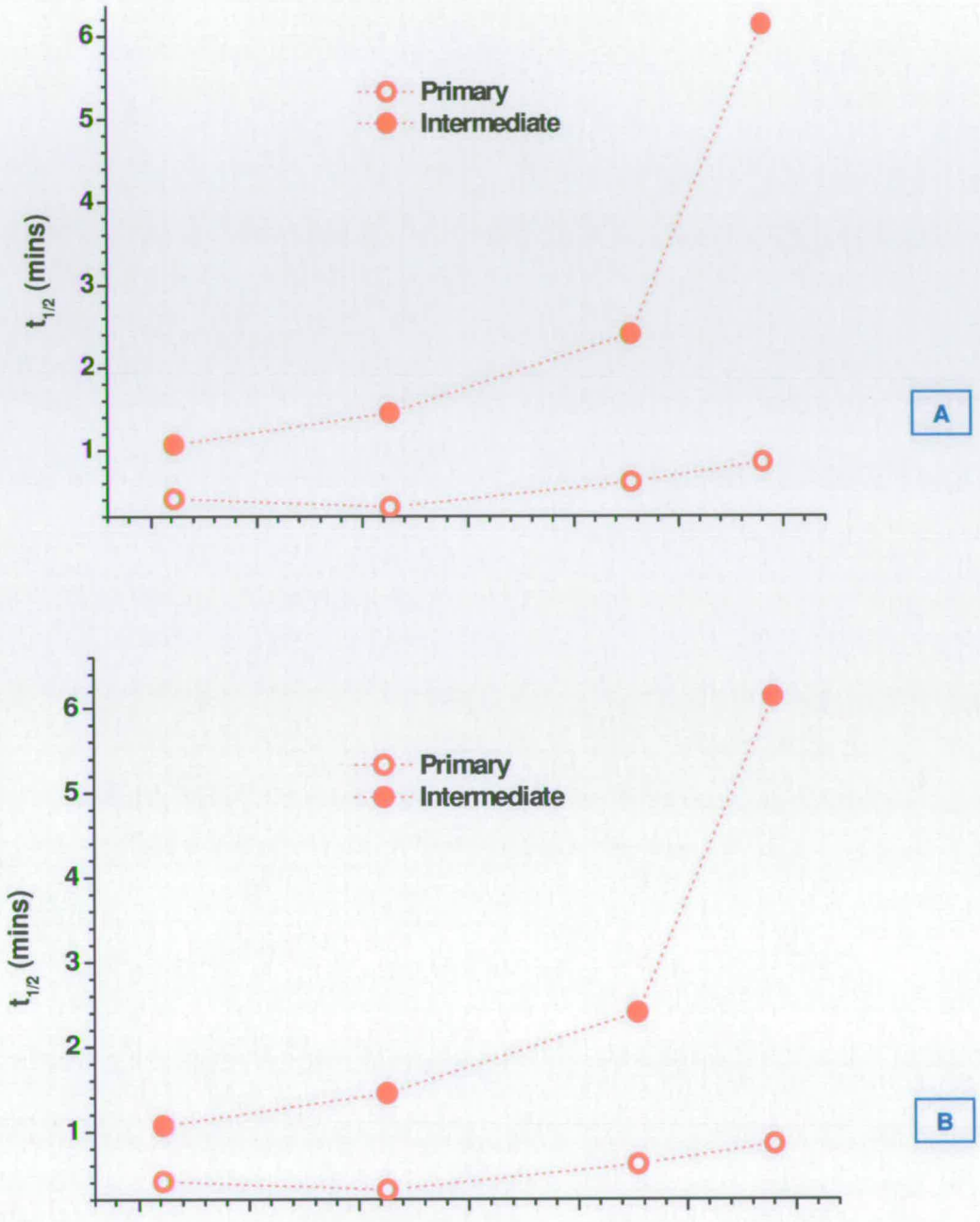

Figure 4-13 Comparison of half lives of up to 3 proton populations for (A) $[M+3D]^{3+}$ and (B) $[y13+2D]^{2+}$ with increasing pD

Half lives for $[M+4D]^{4+}$, $[M+3D]^{3+}$ and $[y13+2D]^{2+}$ are listed in Table 4-4 with values for each population of $[M+3D]^{3+}$ and $[y13+2D]^{2+}$ plotted in Figure 4-13.

The primary populations all show rapid exchange regardless of pD. Exchange rates were difficult to achieve and only single data sets were obtained for 4+, 2+ and y13. To establish a trend, a more efficient sample introduction and desolvation technique and additional time points would be necessary. Where data is available for $[M+3D]^{3+}$, exchange is only marginally affected by pD ($t_{½}$ remains constant across the pD range) reasserting their lack of significance with respect to secondary structure. The very nature of the primary population representing labile hydrogens not involved in secondary structure renders them difficult to study.

Intermediate populations show an increase between pD 7.61 and pD 8.62. The effect of increasing the pD to 10.40 is more dramatic where the half lives increase by at least a factor of 3. This suggests aggregation of melittin at the higher pD. The half lives for the intermediate exchange population for all detectable ions are plotted in Figure 4-14. Evidence of partial aggregation is particularly relevant for the 2+ species. Aggregates present in solution result in reduced solvent exposure due to increased folding or aggregation (as stated in NMR[4] and CD[8] studies). Labile hydrogens on the complex surface would exchange rapidly whereas a gradual perturbation of the complex occurs slowly. These complexes are not retained during desolvation and undergo nozzle skimmer dissociation.

The tertiary populations show low reproducibility and little consistency with the trends already shown. It is likely therefore, that intermediate and tertiary exchange populations are indistinguishable. This was seen in the hydrophobicity studies where melittin was incubated in 100% methanol.

Population	pD	$[M+4D]^{4+}$			$[M+3D]^{3+}$			$[y13+2D]^{2+}$		
		$-k$ (min^{-1})	$t_{1/2}$	R^2	$-k$ (min^{-1})	$t_{1/2}$	R^2	$-k$ (min^{-1})	$t_{1/2}$	R^2
Primary	7.61				1.695	0.41	0.96	2.60	0.27	1.00
	8.62	2.526	0.27	1.00	2.213	0.31	0.97			
	9.77				1.129	0.61	0.97	1.327	0.52	0.99
	10.0	2.99	0.23	1.00	0.818	0.85	1.00			
Intermediate	7.61	0.483	1.44	0.94	0.65	1.07	0.79	0.372	1.86	0.94
	8.62	0.464	1.49	0.98	0.477	1.45	0.99	0.360	1.93	0.93
	9.77	0.551	1.26	0.94	0.289	2.40	0.97	0.159	4.36	0.93
	10.0	0.202	3.43	0.95	0.113	6.13	0.99	0.092	7.53	0.98
Tertiary	7.61	0.105	6.60	0.98	0.018	38.51	1.00	0.085	8.15	0.83
	8.62	0.029	23.90	0.61	0.037	18.73	0.91	0.019	36.48	0.70
	9.77	0.066	10.50	0.87				0.007	99.02	0.25
	10.0	11.2	0.06	0.51						

Table 4-4 Summary of calculated rates, half-lives and linear correlation coefficients for $[M+4D]^{4+}$, $[M+3D]^{3+}$ and $[y13+2D]^{2+}$

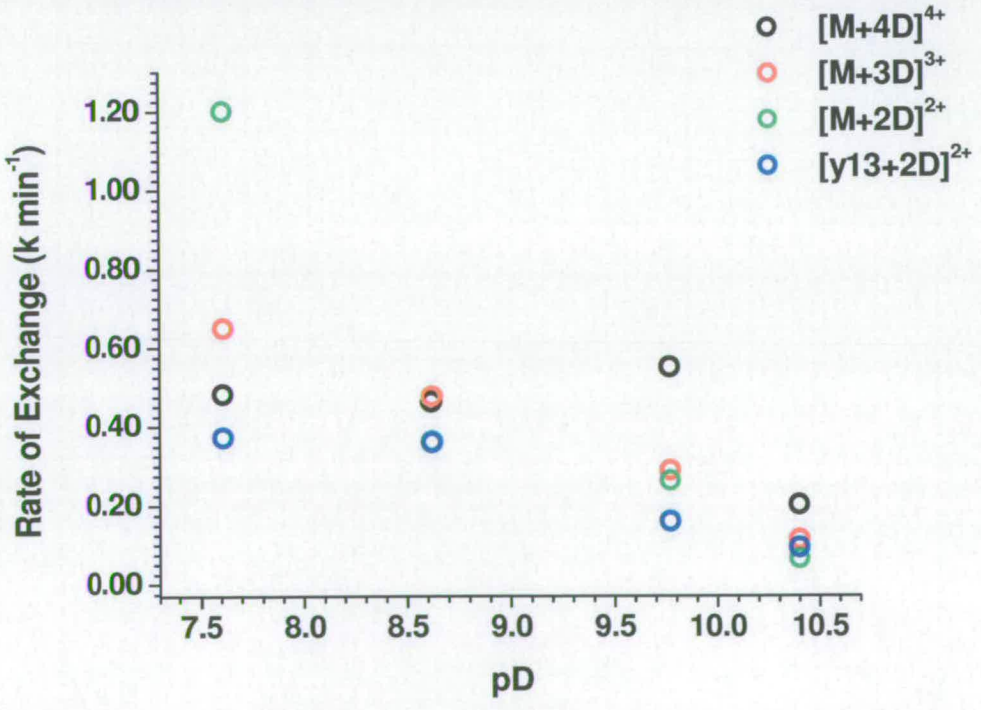

Figure 4-14 Comparison of intermediate rates with increasing pD

4.3.3 Mapping *d*-Uptake by CID

An amount of information has already been elicited with respect to the C-terminus. Exchange kinetics of the y13 fragment formed during desolvation indicates some evidence of secondary structure. CID however, when used in conjunction with whole protein analysis is a potential tool for mapping regions of exchange, although proton scrambling in the gas phase during this process can mislead the assignment of exchange positions.[20,21] Heck and co-workers[22] performed a series of HDX experiments on transmembrane peptides which were charged with either H^+ or Na^+. They showed that post CID, protonated species have a greater tendency to exhibit exchange across the whole peptide whereas it remains much more localised on the sodiated species. Smith and co-workers[21] conclude that most scrambling occurs during the formation of y ions, a potential issue regarding melittin where the majority of the product ions are indeed from the C-terminus. Kaltashov and Eyles[20] on the other hand ascertain that scrambling only becomes an issue with low collision energies and is negligible at high collision energies.

A typical CID spectrum derived from $[M+3D]^{3+}$ melittin is shown in Figure 4-15. Using the mobile proton model[23] discussed in Chapter 1, Section 1.4.1.2, it was expected that melittin would fragment primarily into doubly charged y type daughter ions. The C-terminus is highly basic with a KRKR domain and predicted to be a site for protonation. The likelihood of these protons being released to produce b ions is low.

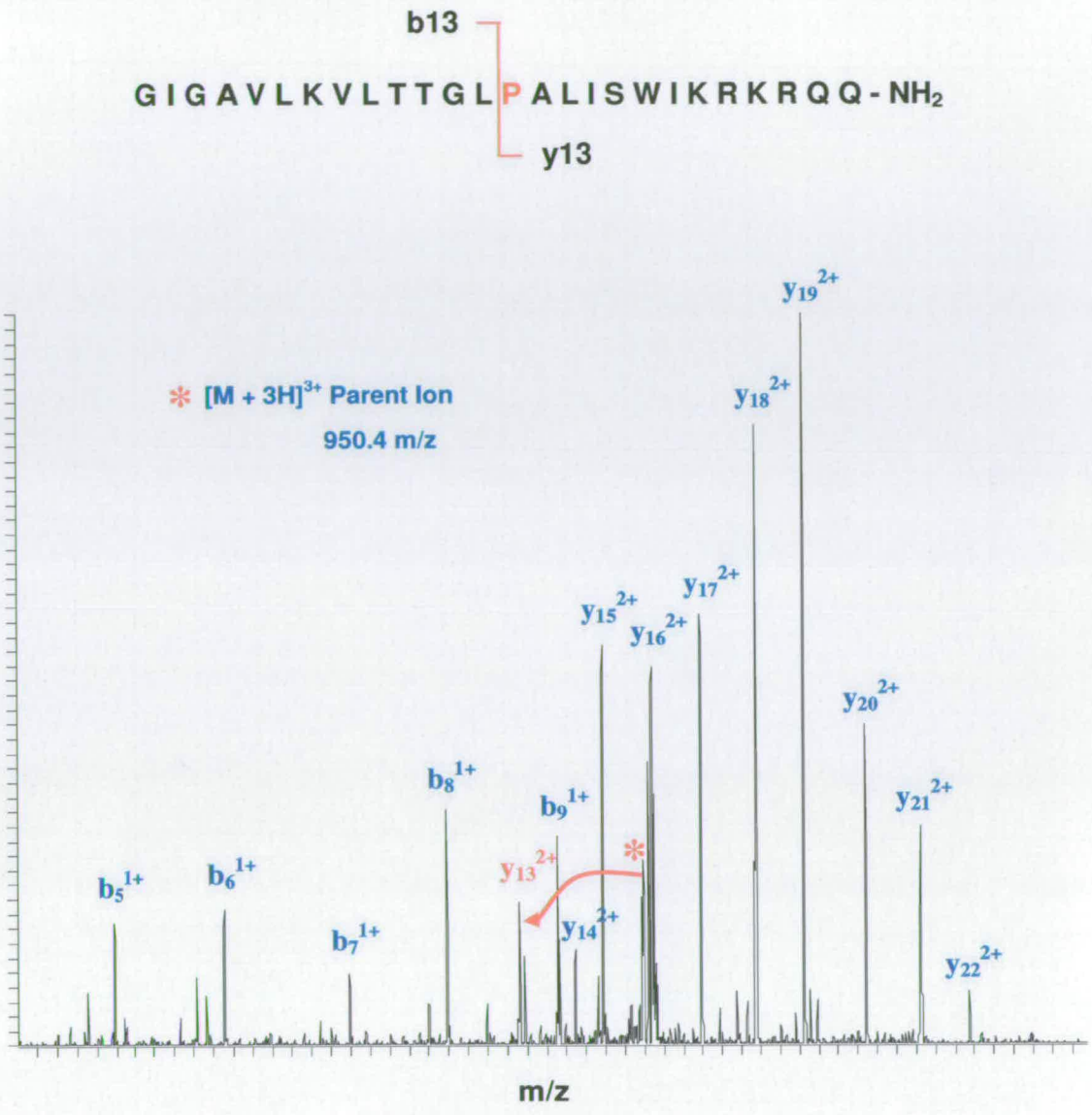

Figure 4-15 Typical CID spectrum derived from $[M+3H]^{3+}$ parent ion

Figure 4-16 and Figure 4-17 compare the major fragments obtained for the 3+ and 4+ charge states of solutions incubated in *d*-methanol / *d*-ammonium acetate. All the major fragments are derived from the C terminal region. No CID data was obtained for the $[M+5D]^{5+}$.

The numbers of labile hydrogens for each b fragment derived from the $[M+3D]^{3+}$ parent remains constant at 4. No conclusions can be made regarding GIGAVL except

the exchange is incomplete with 4 out 7 non-exchanged hydrogens. The next three fragments incorporating residues K, V and L lose a deuterium exhibiting 5 out of 12 non-exchanged suggesting it is taken by the sister y19 fragment on dissociation. This is unexpected as lysine has a greater gas phase basicity than valine.[24] The 5 non-exchanged labile hydrogens are not available for exchange and therefore remain incorporated in some form of secondary structure, assumed to be helical. b ions derived from the $[M+4D]^{4+}$ parent follow the same trend except in b9 which has undergone near full exchange (exchanging an extra 3 hydrogens). This implies a disruption of the N-terminal structure and rapid scrambling during dissociation. Anderegg *et al.* shows agreement with this, with Val-5 and Leu-6 showing much slower exchange than the rest of the N-terminal region during the first 10 minutes.

The daughter ions y20 to y17 all show 15 non-exchanged hydrogens. This supports the evidence found with the b ions that the same N-terminal region (KVLT) is not vulnerable to exchange. y17 derived from $[M+4H]^{4+}$ ion however, shows in increase of 6 exchanges whereas y15 decreases by 6. When the peptide bond between Leu-9 and Thr-10 is cleaved, no more b ions are identified which suggests that a b10 ion will not favourably support a proton, which according to the mobile protein model[23] implies an interaction between one of the two most likely protonatable sites on the N terminus (Gly-1 and Lys-7) and an acceptor in the C-terminal region.

Both y13 ions show greater uptake from the $[M+4H]^{4+}$ parent compared to the $[M+3H]^{3+}$ parent implying as previously suggested that either a) there is scrambling across the fragment during fragmentation or b) $[M+4H]^{4+}$ represents a more solvent exposed conformer in solution.

In broad agreement, Anderegg showed that the basic region of the C-terminus shows partial exchange of the KRKR domain. This is assumed to be a result of helical retention, with exchange occurring on the side chains. There is an argument to suggest scrambling i.e. back exchange with non-exchanged groups during fragmentation. Due to the prevalence of y fragments and the high gas phase basicity

of lysine and arginine it is possible these may act as proton acceptors on fragmentation.

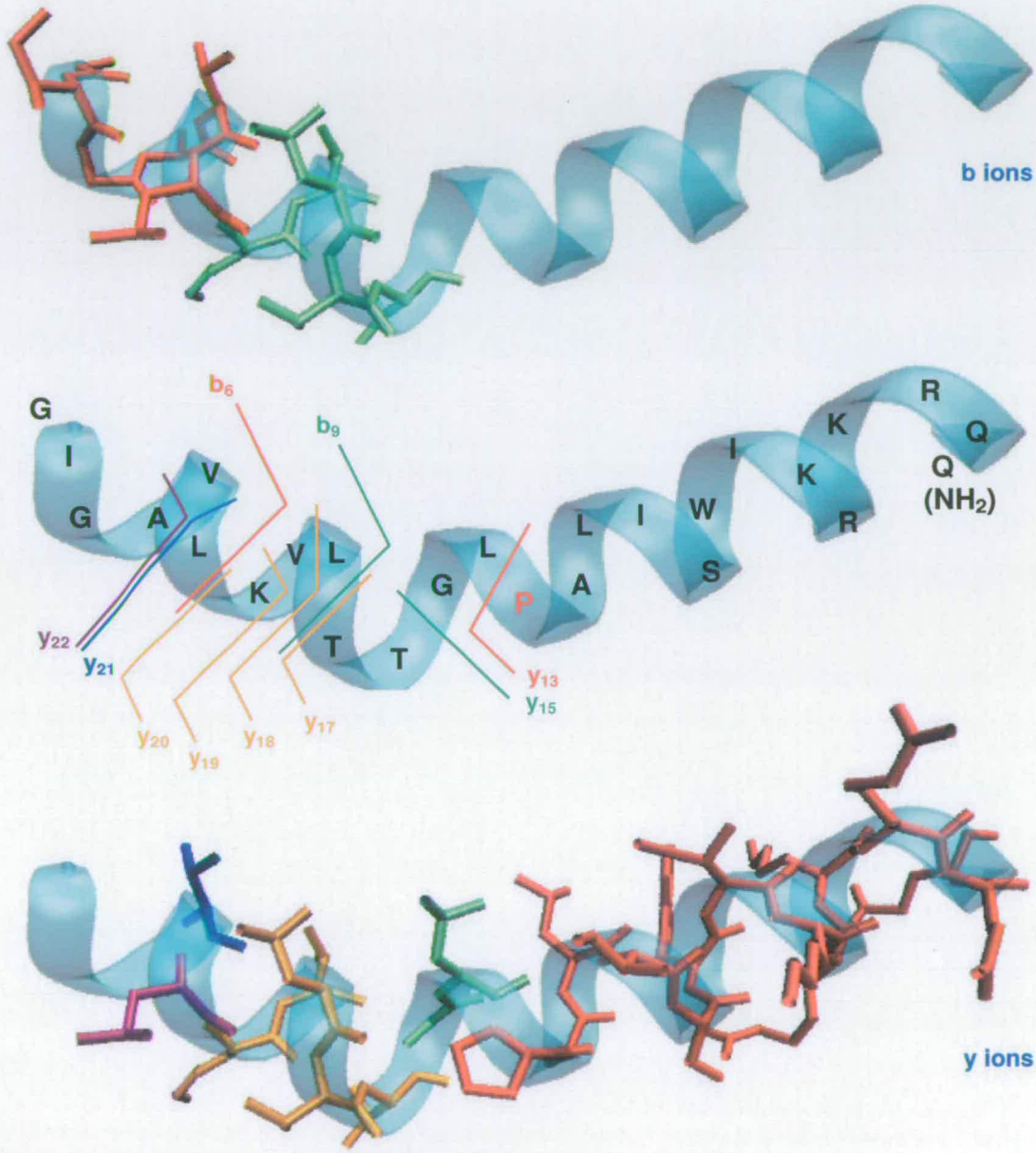

Figure 4-16 Schematic illustrating b and y ion fragments where colour change signifies a mass shift due to deuteration

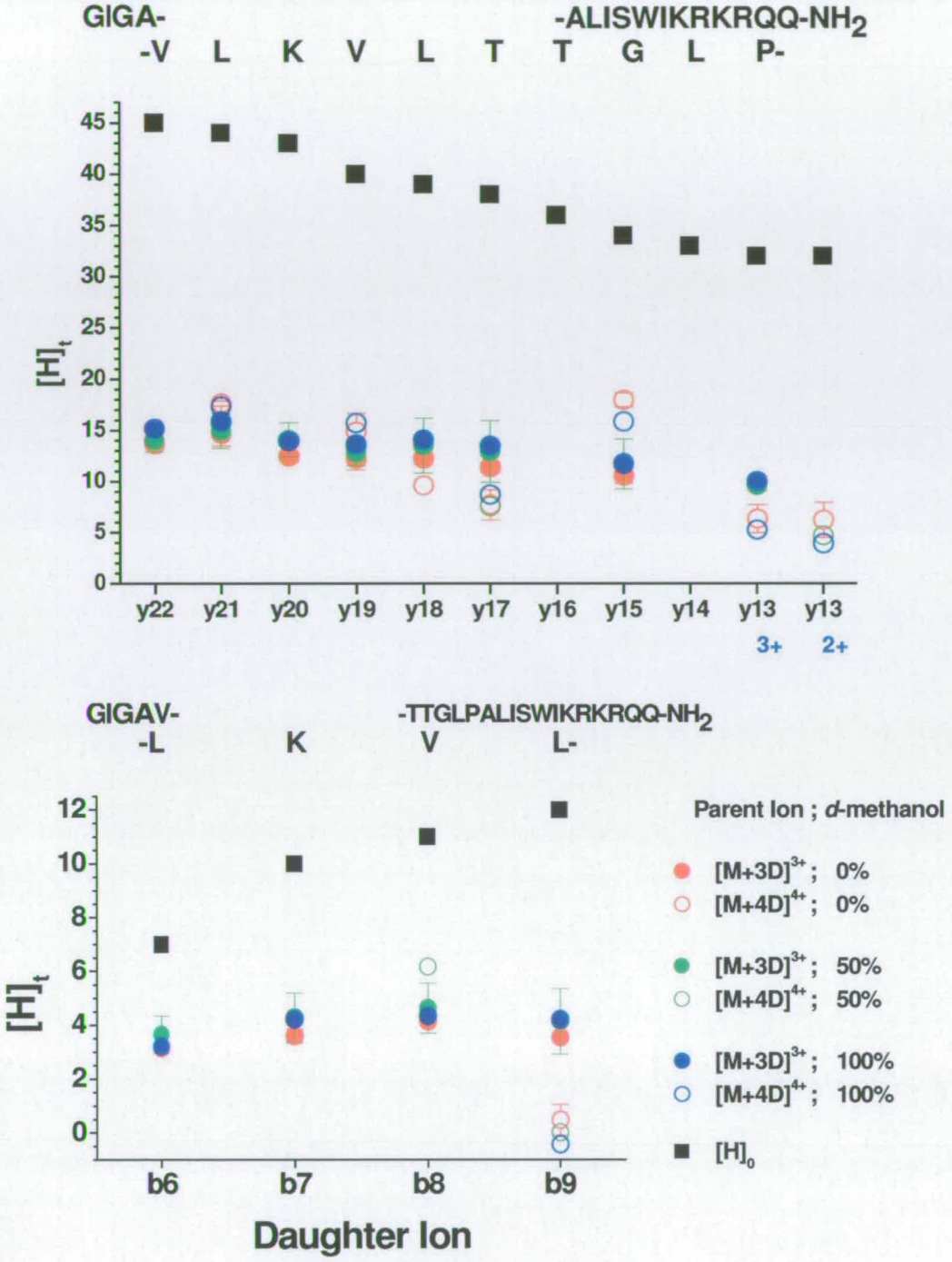

Figure 4-17 Labile hydrogens *remaining* on daughter ions after CID of parent ions $[M+3D]^{3+}$ and $[M+4D]^{4+}$ after 2 hours incubation in *d*-methanol titrated against *d*-ammonium acetate. The inclusion of points labelled $[H]_0$ is to illustrate the theoretical number of labile hydrogens on each fragment.

4.4 PLIMSTEX

The first step in the study of melittin by PLIMSTEX was carried out in standard buffering conditions of 10mM ammonium acetate, pH 6.8 or pD7.2. Further studies using differing concentrations, pH and salt environments were also employed to compliment the CD and direct infusion data.

4.4.1 Standard PLIMSTEX conditions

Results shown in Figure 4-18 uphold the evidence already given of some structural retention under 'pseudo-native' buffering conditions. A maximum 24 amide backbone hydrogens are available for exchange of which approximately 20-22 exchange within minutes of *d*-solvent exposure. Lower levels of exchange are not obtainable within the experimental error of the technique. As with the direct infusion analysis, the proton population not involved in secondary structure exchanges too rapidly for isolation and detection. There should be no significant difference between charge states so although average $[M+2H]^{2+}$ values sit up to 2 Da higher than $[M+3H]^{3+}$ and $[M+4H]^{4+}$ this may be attributable to peak quality or the ion may be derived from another source such as a dimer in solution. The maximum 12 amide hydrogens on the C-terminal y13 fragment have undergone exchange. Comparing this to the whole protein exchange, this could be due to the amide hydrogen of two or three amino acids in the N-terminal region being unavailable for exchange, but it is more likely that due to the nature of the PLIMSTEX experiment, two or three of the amide hydrogens in the N terminal region are actually back-exchanged in the washing step, i.e. are *more* solvent accessible.

This illustrates that because melittin will not readily form a helix at low concentrations and pH 6.8, standard PLIMSTEX is not appropriate. However, it is used to explore the effect of pH on conformation.

Data obtained after a 10 minute incubation show a mass increase greater than the number of labile hydrogens. These data are ignored as the presence of exchanged side chains complicates the interpretation.

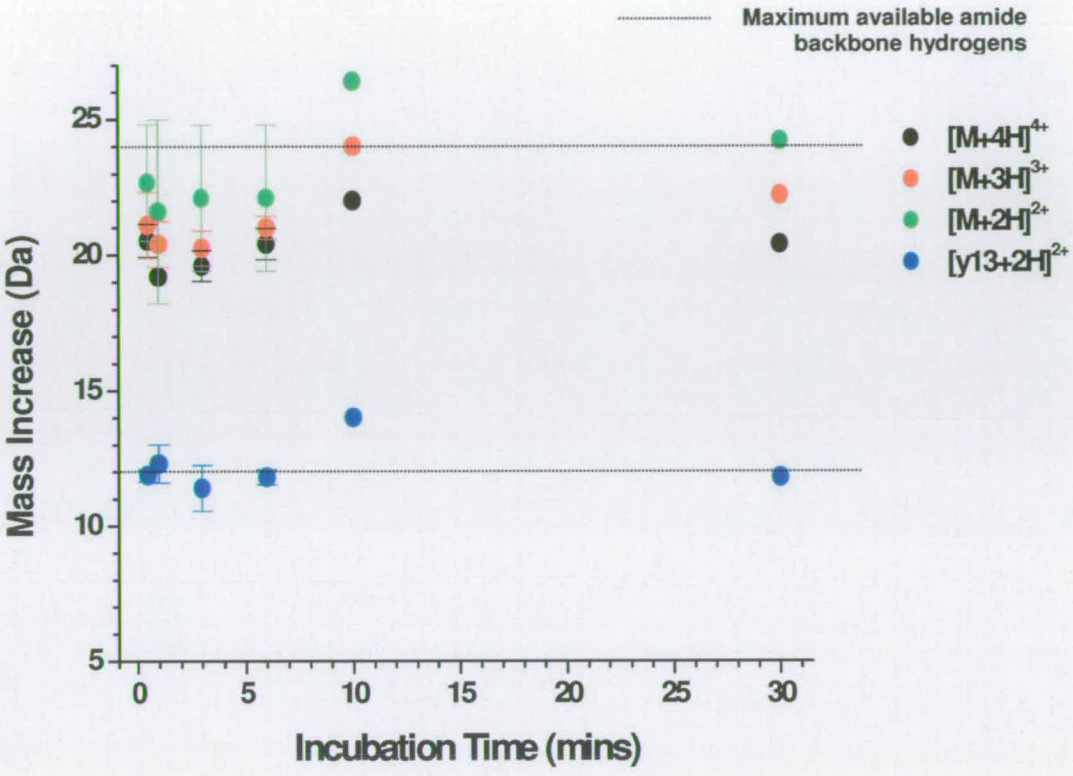

Figure 4-18 PLIMSTEX data on 3+ and 4+ charge states using 10mM *d*-ammonium acetate with increasing incubation times

4.4.2 The Effect of Concentration vs. pH

Demspey and co-workers[4] reported that by increasing the pH, formation of melittin aggregates can be induced. The present study shows increasing the peptide concentration can influence this pH effect. The data below in Figure 4-19 illustrates the effect of pD on deuterium uptake for four concentrations of melittin. The general trend for the lower concentrations (0.055 mM, 0.22 mM and 0.44 mM) supports the literature. As the pD is increased, there is a small decrease in deuterium uptake caused by reduced proton accessibility, which we attribute to aggregation. This becomes more notable on increasing the pD over 10.0 (outside the buffering capacity of ammonium acetate) with a full drop of 1 mass unit. This is in contrast to results

obtained by direct infusion of a 10 μM solution where the rate increased with increase in pD.

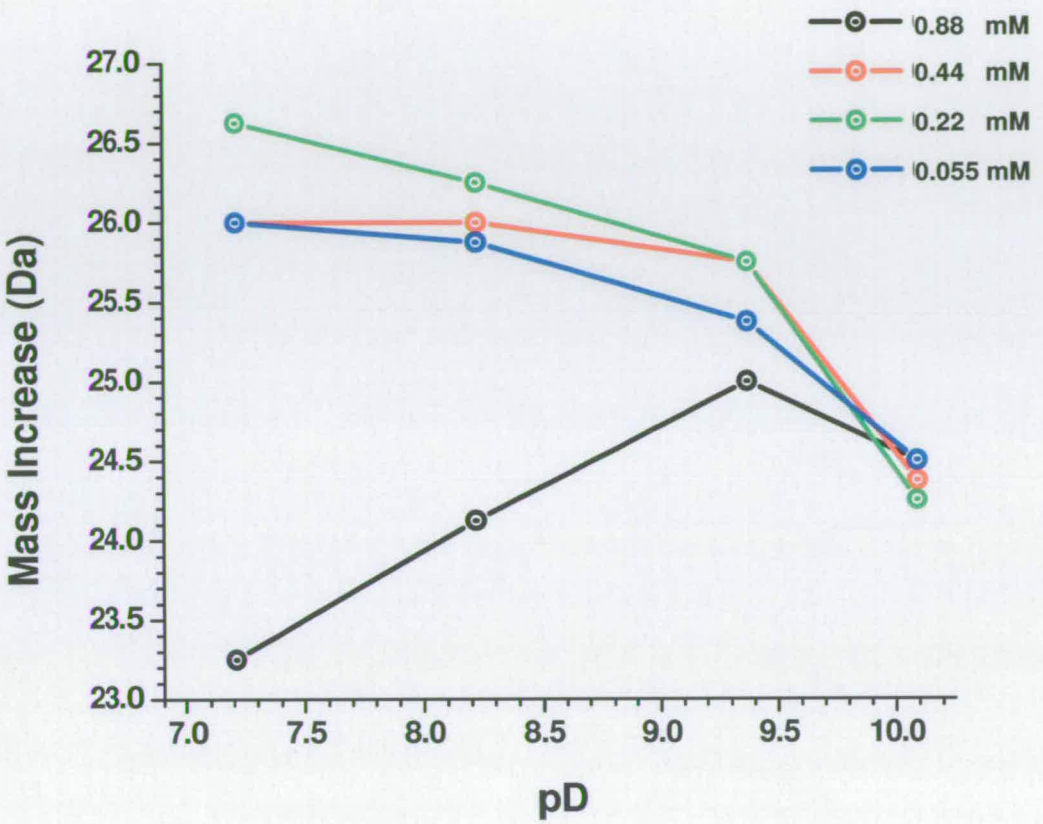

Figure 4-19 Comparison of $[M+3H]^{3+}$ exchange rates for increasing concentrations of melittin as a function of raising the pD

At 0.88 mM a different effect is seen. At near neutral pD the deuterium uptake is approximately 3 less than the other concentrations. This steadily increases by 2 with each unit rise in pD suggesting a decrease in aggregation as the pD is increased, up until pD 10.0 where the values converge on those obtained for the lower concentrations. A possible explanation for this effect is that at the high concentration (0.88 mM), higher order aggregates are formed, which become less stable as the pD is increased. At this point a lower order aggregate (probably a dimer) becomes more stable with increasing pD and competition between these two states results in the behaviour observed above.

4.4.3 The Effect of Salt on the α-Helix - PLIMSTEX

As previously established using CD (section 4.2) the pH effect can be rendered insignificant in the presence of salt for inducing and maintaining a helical structure. PLIMSTEX is the ideal technique to complement these findings as all involatile salts are removed during the back exchange step.

A preliminary experiment was performed uisng the FT-ICR 9.4T mass spectrometer. PLIMSTEX was carried out after a 15 minute incubation with a range of buffers, pD 7.61 phosphate buffer and pDs 8.63, 10.23 and 12.20 in TBS. Due to instrument access limitations, data points are derived from a single data set. The general trend of the data supports the findings by CD.

The data was difficult to process as large numbers of sodium adducts were detected as a result of the high quantities of salt present in the buffer. A typical mass spectrum obtained is shown in Figure 4-20. This raised a question with regards to the role of sodium. The data does not provide evidence on whether salt bridges form a) within the helix stabilising it preferentially to H-bonds, b) if sodium is exchanging in place of deuterium or c) binding to the –COOH group.

The presence of random coil cannot be excluded by CD when using phosphate buffer at near native pH since it shows exchange of 20 of the 24 available amide hydrogens using PLIMSTEX (Figure 4-21). This is in agreement with HDX performed with ammonium acetate at an equivalent pH where there is some structural integrity. Exchange at higher pHs using TBS show a reduced level of exchange also in agreement with the presence of increased helicity, rendering some of the amide hydrogens inaccessible.

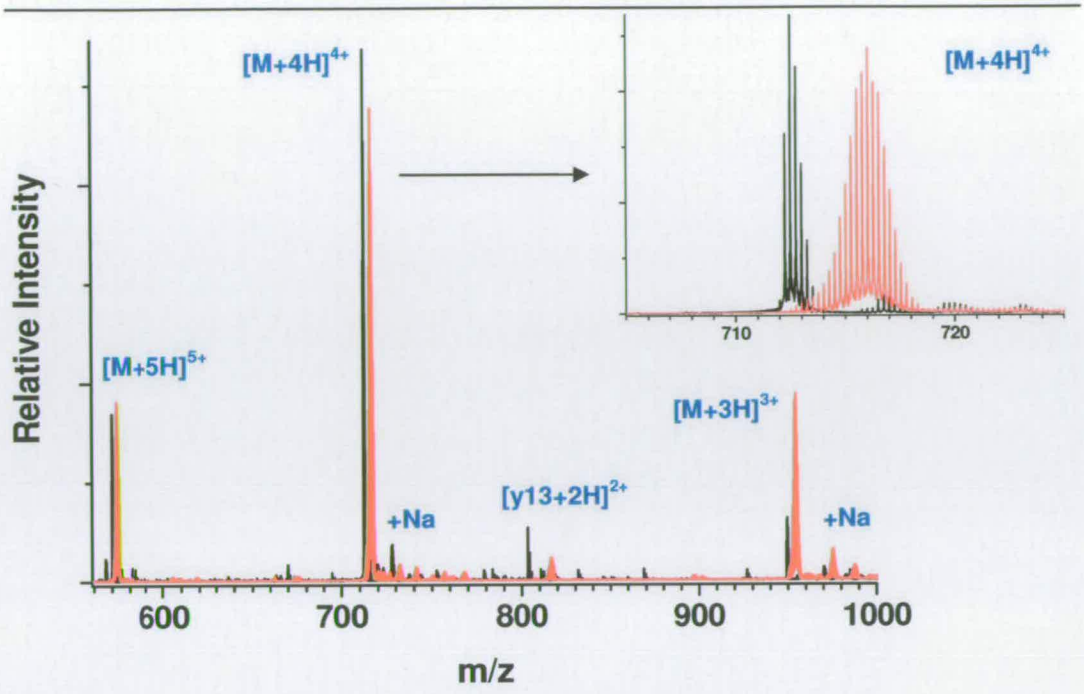

Figure 4-20 Typical FT mass spectrum of PLIMSTEX on melittin after 15 min incubation with TBS pH 7 (black) and *d*-TBS pD 7 (red)

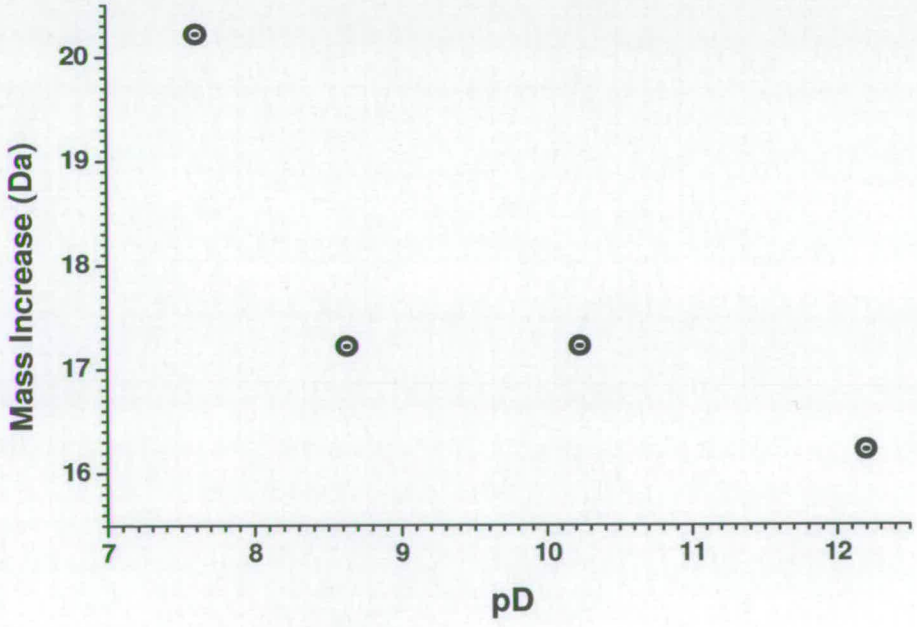

Figure 4-21 PLIMSTEX performed using an FT-ICR 9.4T across a range of pDs using TBS and phosphate buffer (pD 7.61)

The experiment was also performed on the LCQ (Figure 4-22) where, unpredictably, after incubation times spanning the first 2 minutes, 22 of the 24 amide hydrogens exchange in solutions pD 8.54 to 12.00. Only 13 hydrogens exchange during the first 60 mins at pD 2.25. If there was no evidence of an α-helix and, maintaining this exchange was assured, full exchange within 60 mins would be expected. Whereas this evidence suggests an overnight incubation is required.

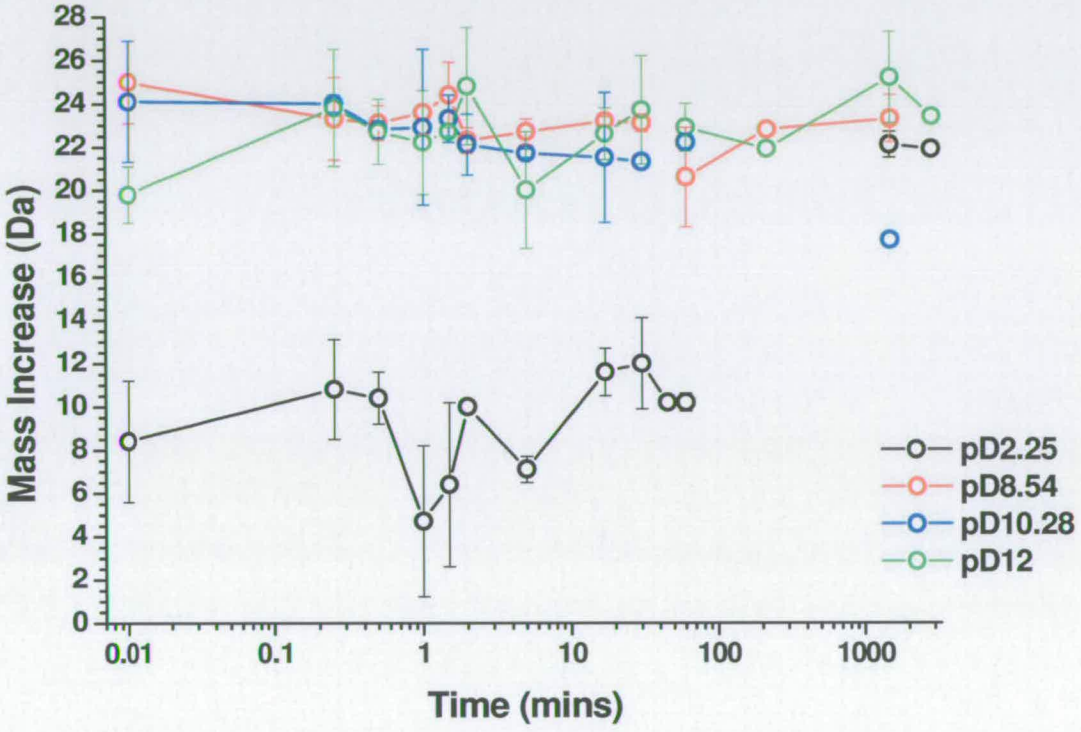

Figure 4-22 PLIMSTEX performed using the LCQ ion trap at pDs 2.25, 8.54, 10.28 and 12.00 in TBS

4.4.3.1 Mapping Backbone Exchange Using CID

CID was performed on samples diluted in TBS. Results are taken from a mixture of single and duplet data and illustrated in Figure 4-23. pD 7.47 shows an increase in uptake between b5 and b6 in the 1 minute incubation. There is no further exchange on the remaining b fragments 7 – 9 (residues KVL). This is in agreement with studies using ammonium acetate described earlier in section 4.3.3. This is reinforced by analysis of y ions 20 – 18 (also spanning residues KVL) where the trend in

experiments pD 7.47 and 12.00 agree. One (pD 7.47) and two (pD 12.00) amide backbone hydrogens remain unexchanged. The higher pD results show variability across the range and no other comparisons are drawn at this stage especially as the results at pDs 8.54 and 10.28 indicate over-exchange and as such are regarded as unreliable.

The picture is very different after 60 minutes. The results at pD 2.25 shows increased exchange, and the fragments y20, 19, 17 and 15 show mass increases of the same ratio whereas y 21 and 18 show enhanced exchange. This would be expected if residues 7, 8 and 9 (y20-18) preferentially retain a helical nature but this is not supported by the b ions where inhibition of exchange is seen between residues 5-7.

These data are preliminary and as such cannot be taken as statistically viable. They do however provide an insight for the use of CID for mapping exchange sites on the amide backbone.

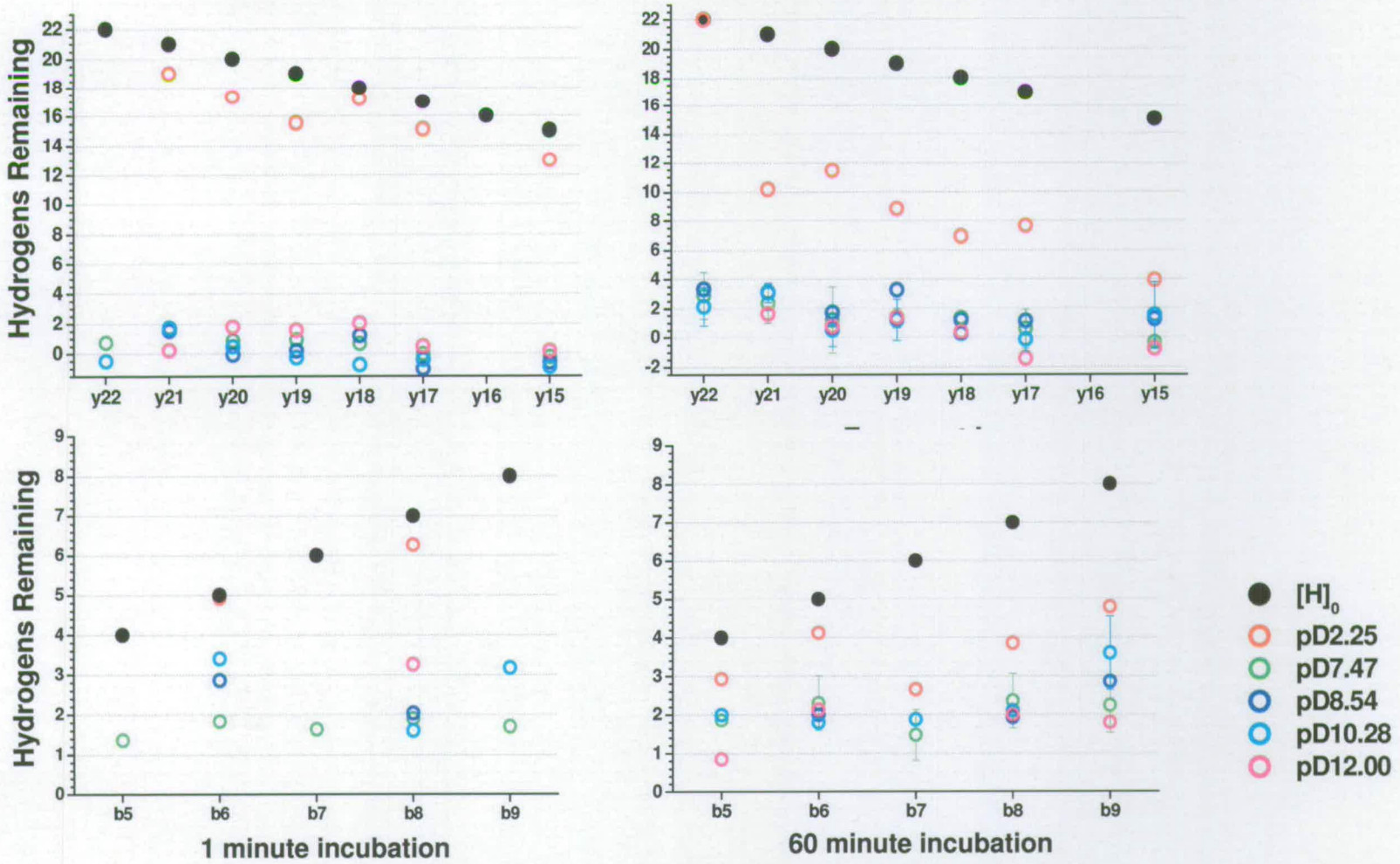

Figure 4-23 CID on PLIMSTEX of melittin incubated in *d*-TBS after 1 and 60 minute incubations

4.5 Conclusions

Two proton populations were detected using direct infusion techniques. The rates of exchange decrease with increase in α-helical nature. Confirming this, a number of solvent conditions induce and maintain the α-helical nature of melittin:

i) CD data shows α-helical formation which is onset at 25% methanol.

ii) Incubation in 100% methanol can induce aggregation.

iii) Salt induces and stabilises an α-helical conformation irrespective of pH, as shown by CD and PLIMSTEX.

iv) Increasing the pH of ammonium acetate buffer and the peptide concentration simultaneously induces aggregation.

Charge states can be used as an indication of the presence of denatured protein. Exchange levels relating to $[M+5H]^{5+}$ exhibited near maximum exchange suggesting it represented an open structure which undergoes full exchange. $[M+2H]^{2+}$ represents the most 'native-like' conformation and hence the least solvent accessible.

Fragmentation by CID enabled positioning of the helix at the N-terminus under 'pseudo native' aqueous conditions of ammonium acetate and TBS.

4.6 References

[1] Terwilliger TC. and Eisenberg D, *J. Biol. Chem.*, 1982, **257**, 6010-6015
[2] Gerig JT., *Biophys. J.* 2004, **86**, 3166-3175
[3] Hirota N., Mizuno K. and Goto Y., *J. Mol. Biol*, 1998, **275**, 365-378
[4] Takei J., Remenyi A., Clarke AR. and Dempsey CE., *Biochemistry*, 1998, **37**, 5699-5708
[5] Iwadate M., Asakura T. and Williamson MP., *Eur. J. Biochem.* 1998, **257**, 479-487
[6] Naito A., Nagao T., Norisada K., Mizuno T., Tuzi S. and Saito H., *Biophys. J.*, 2000, **78**, 2405-2417
[7] Lam Y.-H., Wassell S.R., Morton C. J., Smith R. and Separovic F., *Biophys J.*, 2001, **81**, 2752-2761
[8] Wang F. and Polavarapu PL., *Biopolymers (Biospectroscopy)*, 2003, **70,** 614-619
[9] Bachar M. and OM., *Biophys. J.*, 2000, **78**, 1359-1375
[10] Hristova K., Dempsey CE., White SH., *Biophys J.*, 2001, **80**, 801-811
[11] Pawlak M., Meseth U., Dhanapal B., Muter M. and Vogel H., *Protein Science*, 1994, **3**, 1788-1805
[12] Zhu MM., Rempel DL., Du Z., and Gross ML., *J. Am. Chem. Soc.* 2003, **125**, 5252-5253
[13] Wong JW., Maleknia SD., Downard KM., *J Am Soc Mass Spectrom.*, 2005, **16**., 225-233
[14] Comte, *Biochem J.* 1983, **209**, 269
[15] Anderegg RJ., Wagner DS., Stevenson CL. and Borchardt RT., *J. Am. Soc. Mass Spectrom.* 1994, **5**, 425-433

[16] Bernèche S., Nina M., Roux B., *Biophys J,* 1998, **75**, 1603-1618
[17] Connelly GP., Bai Y., Jeng M-F. and Englander SW., *Prot Struct Funct Gen.,* 1993, **17**, 87-92
[18] Zhang Z. and Smith DL, *Protein Sci*, 1993, **2**, 522–531
[19]Bai Y., Milne JS., Mayne L. and Englander SW., *Prot Struct Funct Gen.,* 1993, **17**, 75-86
[20] Kaltashov IA., Eyles SJ., *J Mass Spectrom,* 2002, **37**, 557-565
[21] Deng Y., Pan H., Smith DL, *J Am Chem Soc.,* 1999, **121**, 1966-1967
[22] Demmers JAA., Rijkers DTS., Haverkamp J., Killian KA. And Heck AJR., *J Am Chem Soc.,* 2002, **124**, 11191-11198
[23] Dongre AR., Jones JL., Somogyi A., Wysocki VH., *J Am Chem Soc,*1996, **118**, 8365-8374
[24] Harrison AG., *Mass Spectrom Rev.,* 1997, **16**, 201-217

5 Melittin – Gas Phase Studies (H/D Exchange, Ion Mobility, Molecular Modelling)

5.1 Introduction

The effect of desolvation on the structural integrity of native proteins and the complexes they form has been discussed in Chapters 1 and 2 with regard to non-covalent protein-ligand screening. It is further discussed here applied to melittin HDX in the gas phase. As has been established, the conformation of melittin is easily manipulated by varying the solvent environment, and consequently it is possible that ionisation / desolvation processes may also be particularly disruptive. Maintaining structural integrity in the gas phase will rely on the hydrogen bonding within the α-helix playing a more significant role in stabilising the conformation than that of solvent. Thermal stability of melittin ions in the trap is challenged by sequential isolation steps necessary to increase activation (trapping) times.

In an early study of the gas phase structure of melittin, Kaltashov and Feneslau[1] used mass-analysed ion kinetic energy (MIKE) spectrometry to measure kinetic energy release on dissociation of amide bonds, inter- and intramolecular hydrogen bonds in melittin and melittin dimers. Using CHARMm22 force field software they energy minimised the x-ray structure of melittin in order to estimate the coulombic repulsion energy released upon peptide or dimer cleavage. Distances between protonated Lys-7 and Arg-22 and Arg-24 were interchangeable in the gas phase and dynamics studies showed hydrogen bonds responsible for α-helix formation were preserved.

Gronert built on the kinetic model of Goeringer and McLuckey[2] and experimentally attempted to calculate the temperature of the quadrupole ion trap using the well characterised reaction of thiophenolate and trifluoroethanol.[3] The internal energy of ions entering the trap was shown to be unaffected by capillary temperature, with the trap maintaining a constant temperature of around 300K. This is the assumed temperature of the ion trap for the studies within this and the following chapters, the

aim of which is to ascertain if capillary temperature invokes protein unfolding, leading to increased *d*-uptake.

Marzluff and co-workers[4] performed gas phase experiments on a series of proteins (lysozyme, cytochrome C, thioredoxin, ubiquitin, insulin and also melittin). All proteins were dissolved in 49:49:1 water:methanol:acetic acid. A bath gas of He / *d*-methanol in the trap was achieved by infusing the solvent into the ion trap using an inlet system designed by Gronert.[3] They observed a maximum exchange on melittin was 5.7 Da for the $[M+3H]^{3+}$ ion and 0.7 for $[M+2H]^{2+}$. Evidence in this chapter suggests the amount of *d*-methanol in the trap at the start has a major influence on primary rates of exchange and as such may explain the differences in exchange between the literature and our experimental values. On all occasions the peak width described the presence of multiple conformers by broadening with increased time within the trap. After 10 seconds however, the peaks narrow indicating a synchronisation or minimising of the number of conformational states. Each protein was studied with at least two charge states to determine whether gas phase exchange is dependent on the number of protons. Two out of the six, thioredoxin and ubiquitin, showed a reduced total exchange with the higher charge state. In both instances the peaks widths were greater for the higher charge state suggesting a greater number of conformers.

Green and Lebrilla[5] also postulate that arginine location plays a significant role in exchange. If they are positioned in a single region, as in the case of lysozyme, the exchange is slowed which adds credence to the relay mechanism.[5,7]

Solution phase experiments on melittin described in Chapter 4 confirmed $[M+3H]^{3+}$ and $[M+2H]^{2+}$ ions were the most native-like of the charge states studied. These were subjected to gas phase exchange with deuterium uptake being compared with differences attributed to charge and conformations.

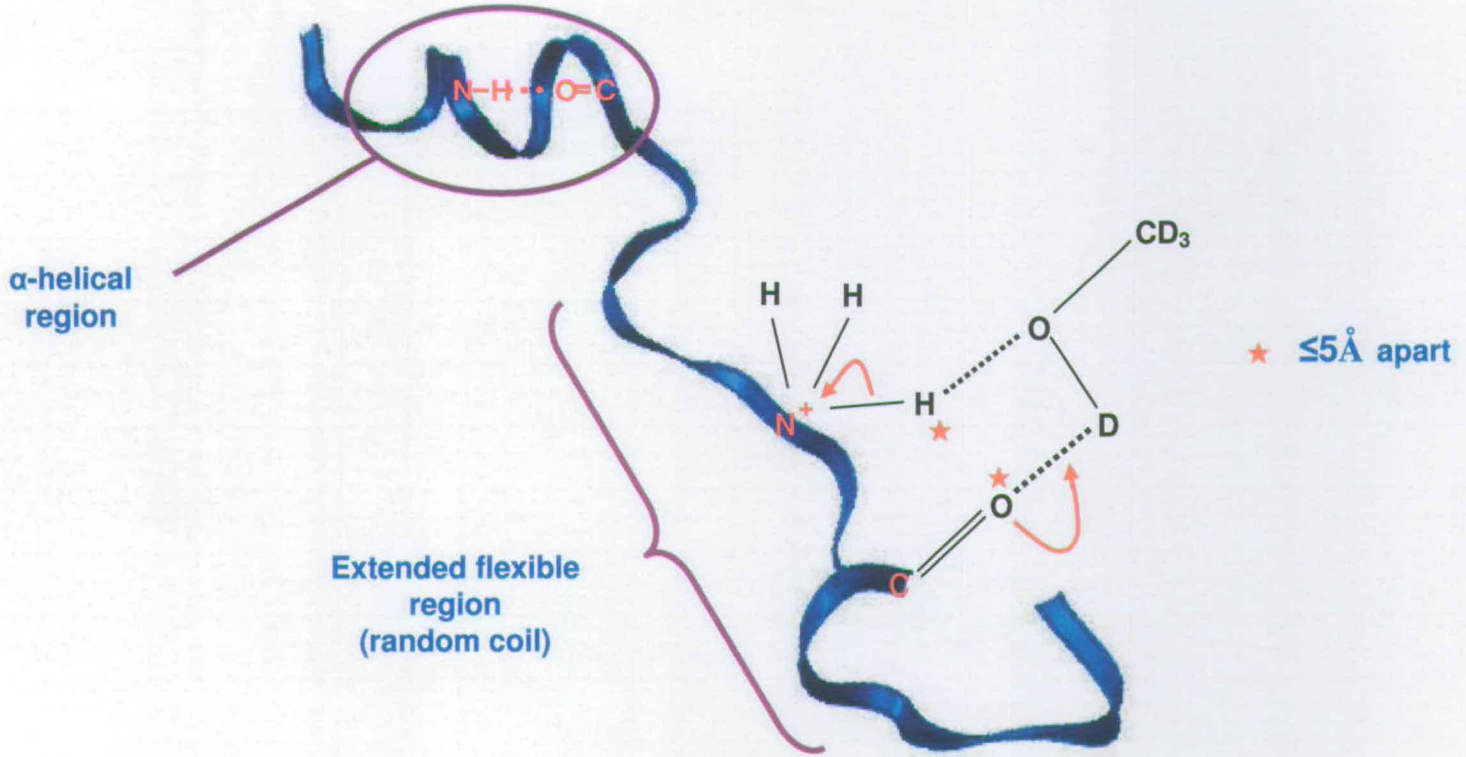

Figure 5-1 Empirical illustration of melittin $[M+3H]^{3+}$ generated by molecular dynamics[♣] with a cartoon of a proton donor ($-NH_3^+$) – acceptor (-C=O) placement enabling gas phase exchange by the relay mechanism.[5-7]

[♣] Molecular Dynamics performed by J. Lippens and J. Kalapothakis

A rigid helical structure involving H-bonding reduces both dynamicity and availability of the donor sites such as amide groups,[6] which in turn decreases the probability of successful collisions with *d*-methanol in the trap. Consequently, an α-helical region is expected to show reduced exchange whereas the flexible random coil region is more likely to have donor – acceptor sites within the required maximum 5Å distance.[6,7] Figure 5-1 provides an empirical example for exchange opportunities via the relay mechanism and hindrances caused by the α-helix.

5.2 ESI Analysis of Melittin from Hydrophilic and Hydrophobic Solutions

Preliminary studies were performed using ESI with a high capillary temperature (200°C). 10 μM melittin was prepared in solutions ranging from 100% aqueous (10 mM ammonium acetate, pH6.8) to 100% methanol and infused at 3 μL/min. Helium was bubbled through a reservoir of *d*-methanol at a maximum pressure of 40 psi. The trap pressure was regulated to ~2.5 x 10^{-5} Torr using an external needle valve. Ions were held in the trap for activation times ranging from 10 to 10000 ms.

Figure 5-2 shows typical peaks obtained from $[M+2H]^{2+}$ and $[M+3H]^{3+}$ ionised from aqueous solutions with ammonium acetate or 100% methanol after exposure to *d*-methanol and with various activation times. There is a clear increase in mass with increase in activation time. The mass shift between 5 and 10 seconds is much less than the first 5 seconds for $[M+3H]^{3+}$. In all cases, there is a general trend of peak broadening with increase in trapping time. In Chapter 4 similar changes in peak shape are attributed to more than one conformer being present on the time scale of the experiment. The same conclusion can be drawn here with the conformer population increasing as the protein unfolds due to a combination of destabilisation of hydrogen bonds due to the solvent free environment and ion - bath gas collisions. In the case of $[M+2H]^{2+}$, peaks continue to broaden and become less smooth with increased time in the trap. In contrast however, $[M+3H]^{3+}$ shows little broadening.

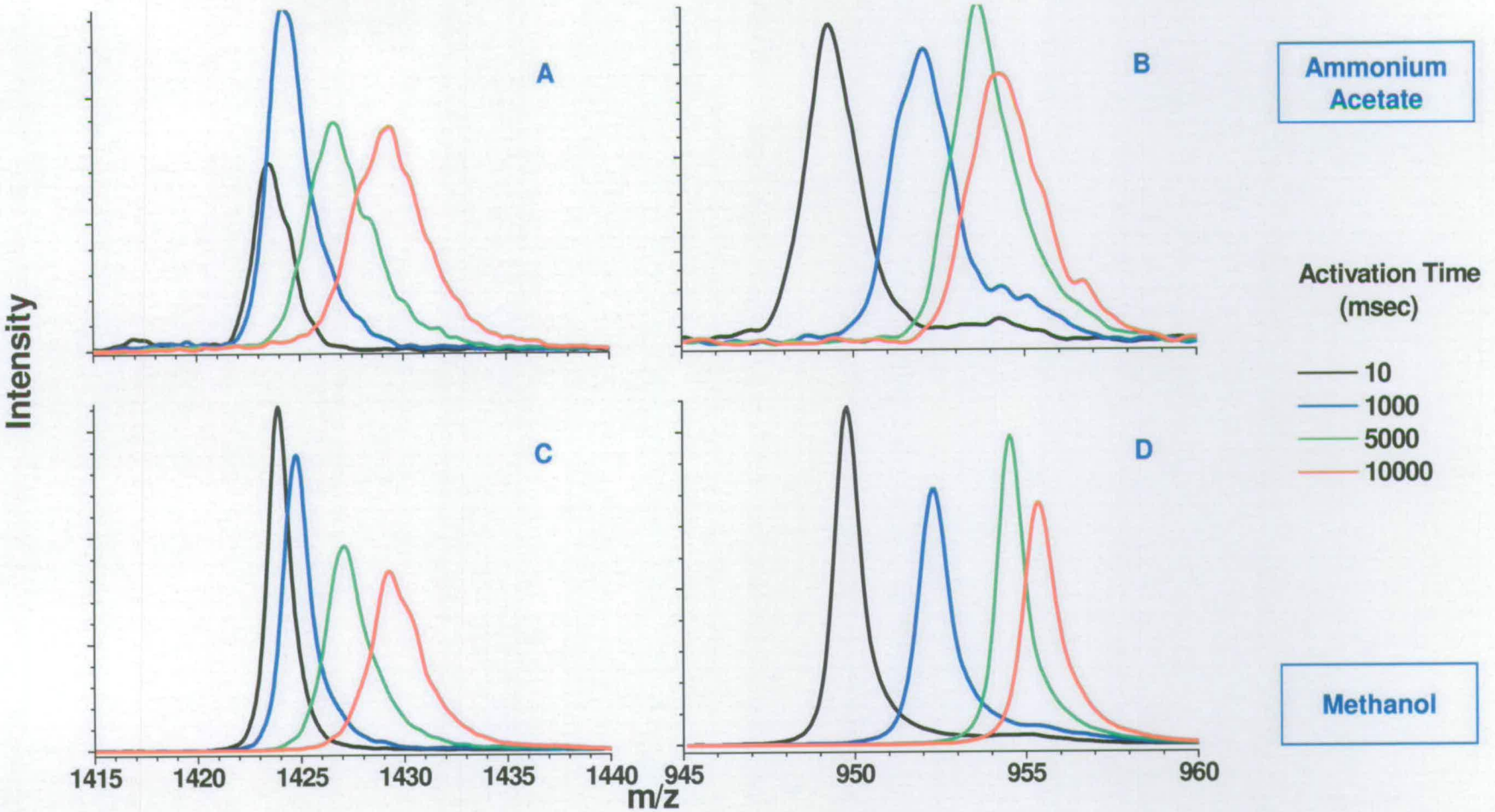

Figure 5-2 Typical examples of peak shapes of $[M+2H]^{2+}$ (A and C) and $[M+3H]^{3+}$ (B and D) from ammonium acetate and methanol after increasing activation times

The implication of possessing a third proton is assumed to result in increased intramolecular repulsion during ionisation and, with no solvent to counteract this effect, the protein is likely to be more 'elongated' as a $[M+3H]^{3+}$ ion than the $[M+2H]^{2+}$. On this basis the third proton is probably carried by Arg-22 or Arg-24 and not Lys-7 as postulated by Kaltashov and Feneslau in reference 1.

Peak widths calculated at half peak height are illustrated in Figure 5-3 highlighting these differences between the charge states. It appears that the 2+ charge state undergoes unfolding throughout the 10 second activation window. The biggest difference in peak width occurs in the first 5 seconds suggesting the majority of unfolding occurs within this time. The 3+ charge state shows an increase of less than 0.5 *m/z* over the same time period.

There is some indication to suggest 'solvent memory' in the desolvated structure. In both charge states, the sample sprayed from aqueous buffer displays peak widths approximately 1 Da broader than the methanol derived species, suggesting more conformers are present, resulting in slightly higher levels of exchange. This again, supports the data described in Chapter 4 indicating a hydrophobic environment is favoured for helical formation.

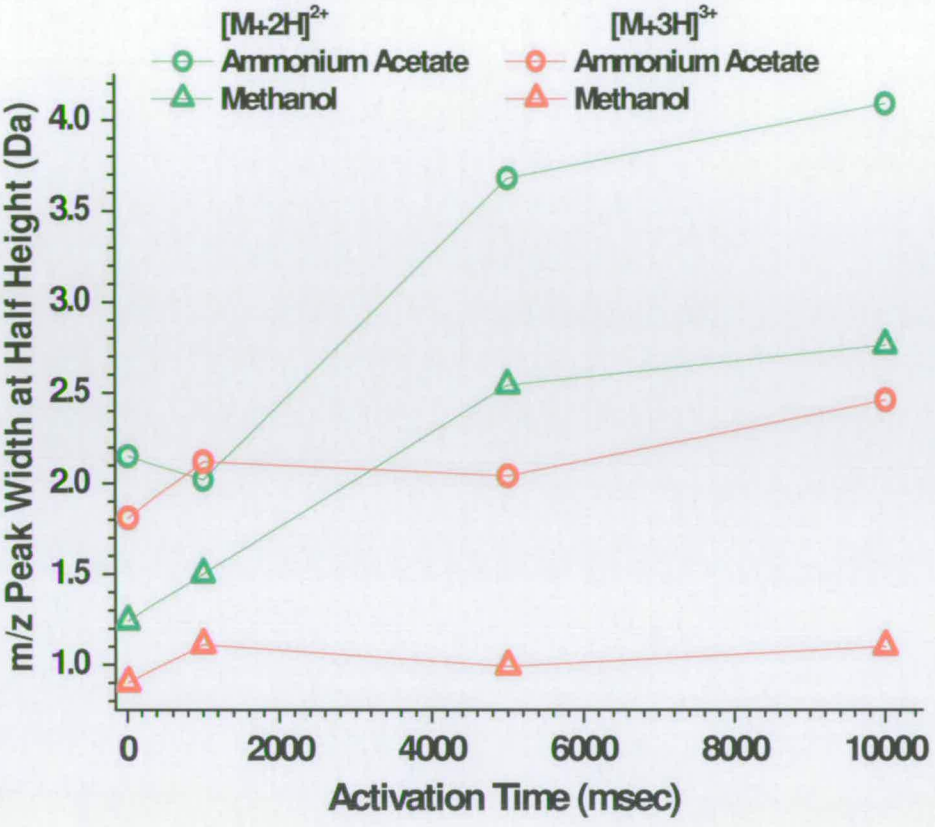

Figure 5-3 Peak widths at half peak height for $[M+2H]^{2+}$ and $[M+3H]^{3+}$ with activation time

Insignificant exchange was found to occur with a 10 ms activation time so all mass increases were relative to this value. Mass shifts over the 10 second activation time are plotted in Figure 5-4 for solutions sprayed from an increasingly hydrophobic solvent environment.

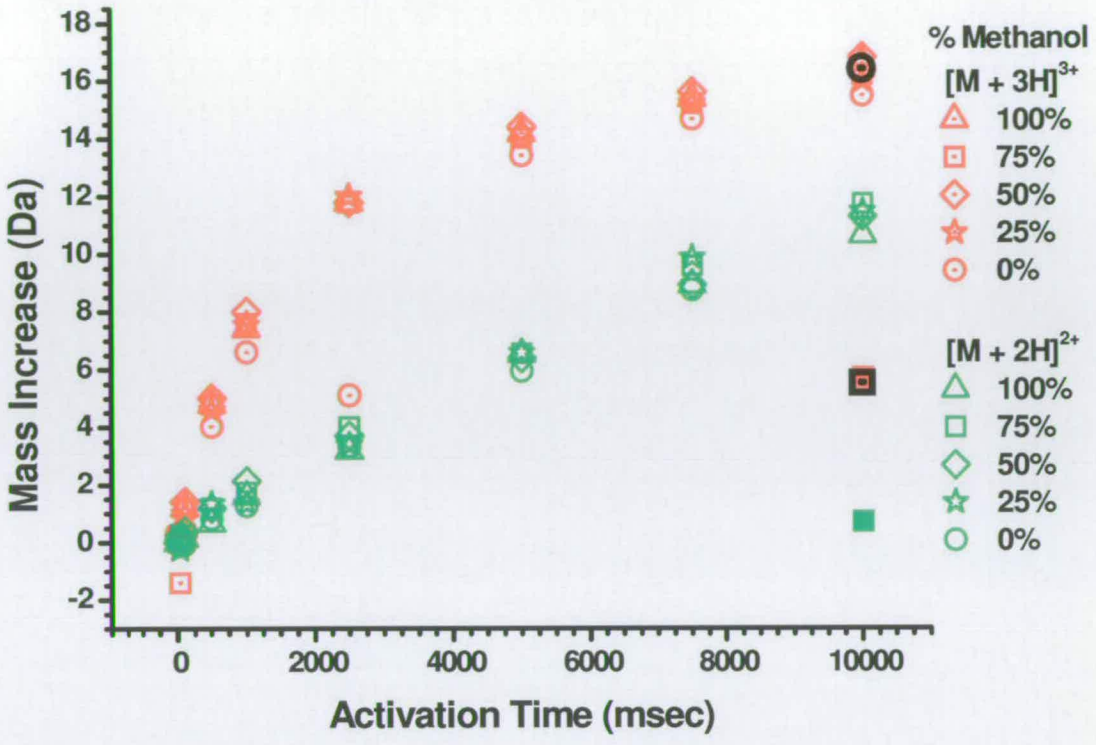

Figure 5-4 Gas phase exchange of melittin $[M+3H]^{3+}$ and $[M+2H]^{2+}$ by ESI with a capillary temperature 200°C and maximum trapping time 10 s (solid squares are exchange values quoted from Reference 4, Black data points used identical buffering conditions as Reference 4: $[M+3H]^{3+}$ (circle) and $[M+2H]^{2+}$ (square))

All solutions appear to exhibit near identical *d*-uptake under these conditions, the implication being that despite the differences exhibited by the peak shapes above (Figure 5-2) no distinguishable conformational differences are evident from mass increases observed post desolvation and ion isolation. The action of isolation involves rf heating which imparts energy to the parent ion. Elevated internal energy may also result in thermal unfolding. This renders conclusions on ion conformation open to question when making comparisons with solution phase structures. The LCQ does not have the facility to manipulate the activation time in full scan mode so studies could not be carried out to compare the effects of isolating a single ion species. Marzluff and co-workers[4] report maximum exchange values for $[M+3H]^{3+}$ which are 3 times less than those seen here. In addition their results for $[M+2H]^{2+}$ show only one exchange over a 10 ms incubation inferring a fully folded protein with

labile hydrogens protected. We have a higher amount of deuterated methanol in our experiments than used by Marzluff,♠ and so we would expect a higher rate of exchange, nonetheless the relative difference between our results and those of Marzluff[4] is somewhat puzzling, and indeed when we use identical solution conditions we still obtain higher exchange for $[M+3H]^{3+}$ (akin to that that we see from all solvents) and somewhat higher for $[M+2H]^{2+}$ (although this *is* lower than what we observe without 1% acetic acid - green open diamonds Figure 5-4). So it appears that in Marzluff's laboratory under solvent conditions (49% aqueous / 50% methanol / 1% acetic acid) which we might expect to denature melittin, they are able to retain an unexchangeable possibly helical conformation for the $[M+2H]^{2+}$ although the difference between the two sets of data may be attributable to an error in their low measurements for the $[M+2H]^{2+}$ ion. Despite trying solvent conditions which are known to provide a helix in solution (Chapter 4, Section 4.2) it has not been possible to retain one here. Although it is possible that conformation(s) from solution are here destroyed in the desolvation process in all cases, it is more likely that the isolation stages we employ impart more thermal energy to the peptide ions, which at least partially denatures them. Nonetheless we do see a difference in the exchange as a function of charge state, which supports conformational differences for the gas phase structure of these two types of ion.

These significant differences between charge states support a mobile proton exchange process.[8] With proton donor sites positioned throughout the molecule, the $[M+3H]^{3+}$ exhibits at least two linear exchange phases ranging from 10 – 1000 ms and 2500 – 10000 ms. To ascertain whether this is due to different proton populations (and by inference conformation), as with the solution phase experiments described in Chapter 4 or, attributable to an annealing process due to collisional cooling within the trap, the half lives were calculated and are displayed in Figure 5-5 and Figure 5-6. From the mass increase data shown in Figure 5-4 the $[M+2H]^{2+}$ ion, containing one less proton donor site, exhibits linear exchange with no evidence of a decrease in exchange rate over the 10 seconds irrespective of solvent. This implies there may be enough of a structural difference from $[M+3H]^{3+}$ in the gas phase to

♠ De Cecco M., Unpublished work (private communication)

assume the presence of discrete proton populations and hence conformations. Half-lives for the exchange of $[M+2H]^{2+}$ following electrospray ionisation from different solvents are calculated across the 10 second activation time and plotted in Figure 5-5. Here subtle differences as a function of solvent which are not apparent in Figure 5-4 are evident. The rate of exchange decreases linearly with increase in methanol content from 25% upwards with the anomalous result for 75% which has been discarded.♠ This is in agreement with that observed in the solution phase. As the data in Figure 5-4 demonstrates, the differences between samples is small but becomes exaggerated when expressed as hydrogen depletion.

$[M+3H]^{3+}$ half lives are plotted in Figure 5-6 and infer the presence of two proton populations. In contrast to $[M+2H]^{2+}$, no trends can be ascertained between the different starting solutions for either exchange phase. This supports the hypothesis that the $[M+2H]^{2+}$ parent ion bears the most 'native-like' conformation by distinguishing between the different solutions. These slight differences appear too subtle for the more denatured $[M+3H]^{3+}$ and as such, all solutions appear to have the same conformation. However, there is a distinction between two proton populations. Initial exchange is much more rapid than the $[M+2H]^{2+}$ ion as a direct result of possessing an extra mobile proton. The exchange rate of the $[M+3H]^{3+}$ ion decreases after 12 protons are exchanged which is approximately equal to the maximum value achieved on the $[M+2H]^{2+}$ ion. Further studies with increased trapping times were necessary to ascertain whether the secondary exchange rate on the $[M+3H]^{3+}$ is replicated for the $[M+2H]^{2+}$ ion.

♠ $t_{½}$ for 75% methanol was obtained from data showing greater variation than the other samples due to issues with back exchange in the gas inlet lines.

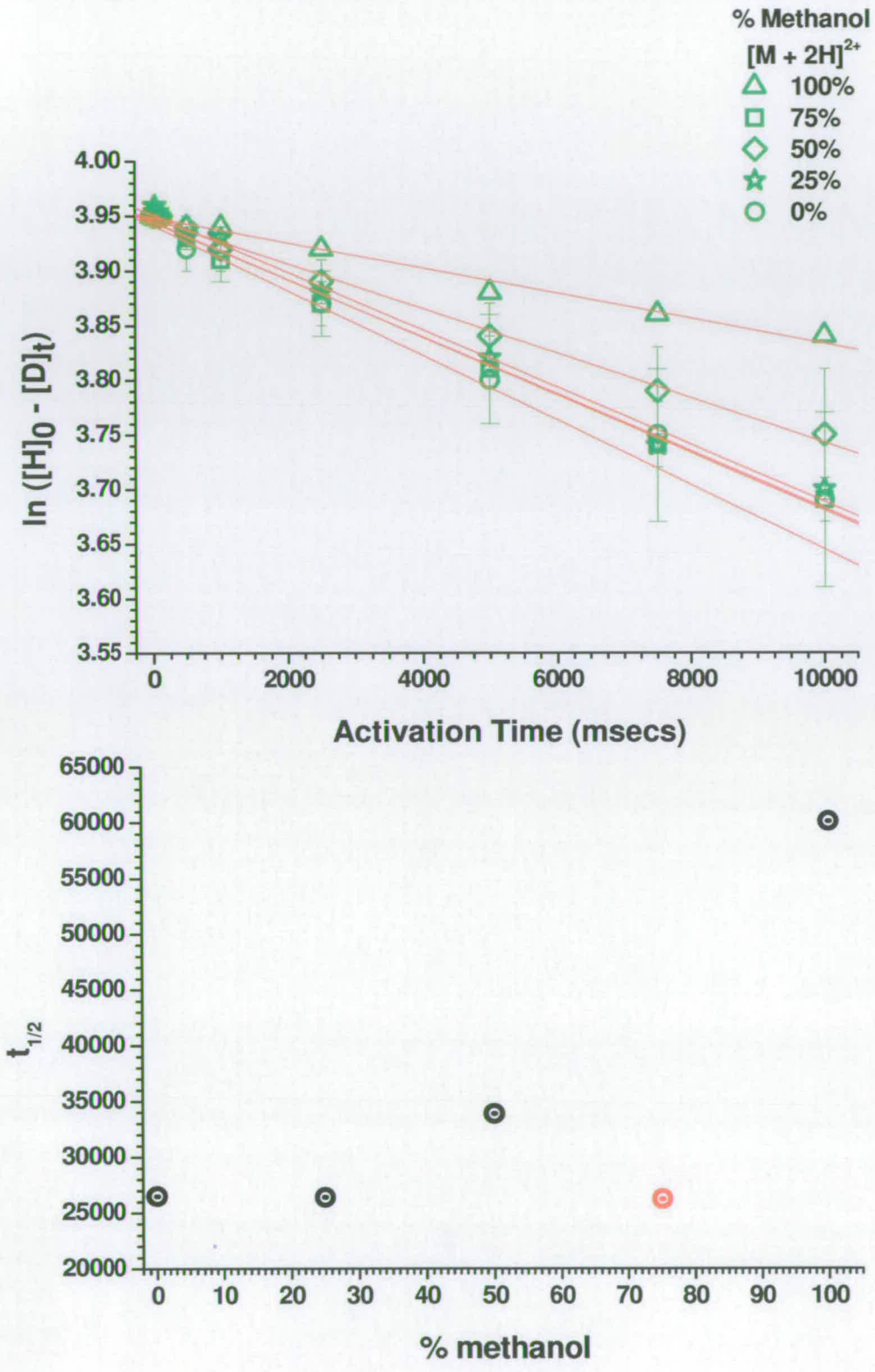

Figure 5-5 Half-lives of $[M + 2H]^{2+}$ with increasing methanol composition

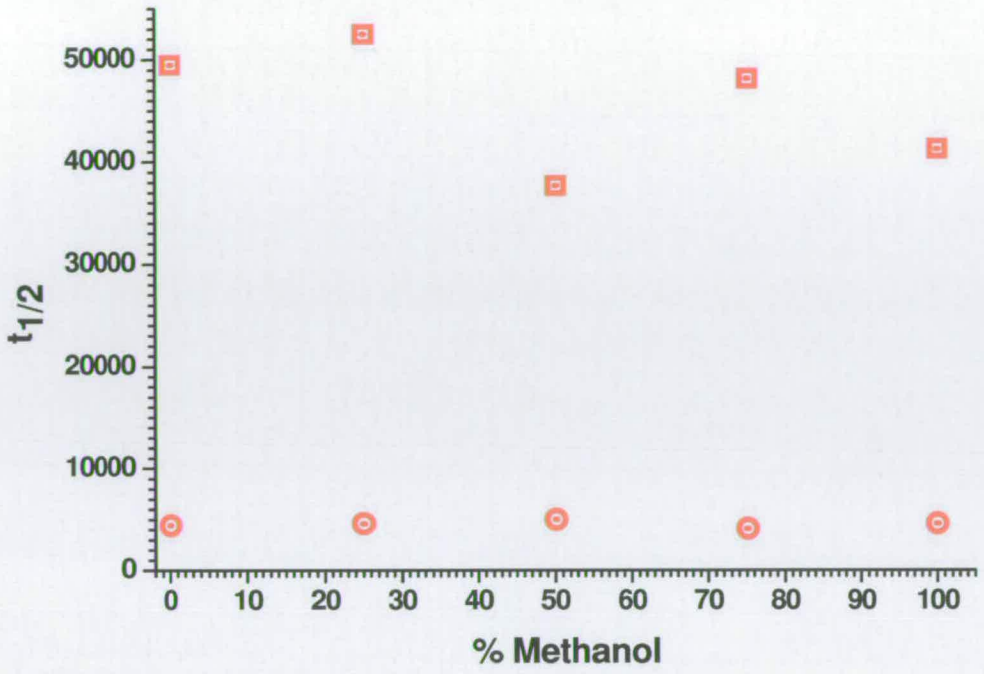

Figure 5-6 $[M+3H]^{3+}$ half lives for two exchange populations

5.3 Increased Activation Times on Melittin by ESI

The experiments described above were repeated using nanoESI and with activation times up to 90 seconds, which was achieved by re-isolating the parent ion 9 times (equivalent to MS^{10}) at 10 second intervals. To determine whether mass shifts occur as a direct result of re-isolation, non *d*-methanol was used as a control. A mass increase of no more than 3.2 Da is incurred over the full 90 seconds (Figure 5-7). For the purposes of this study the amplitude of the base mass was small enough to be regarded as insignificant and so was taken as zero.

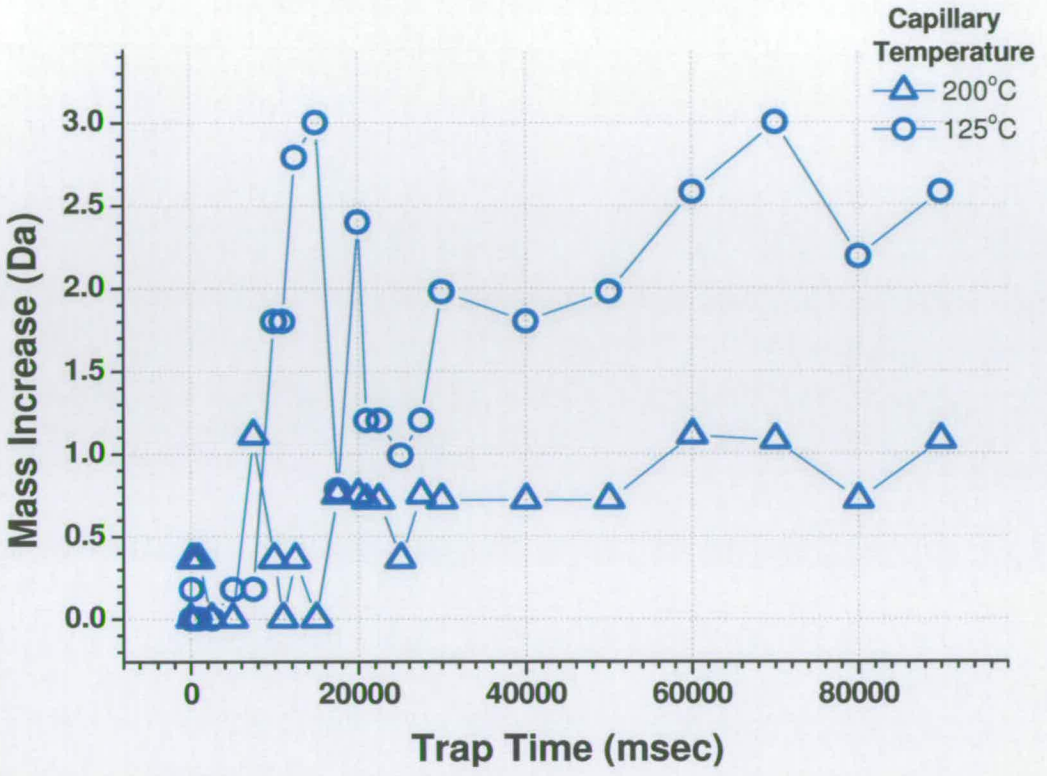

Figure 5-7 Mass increase of $[M+3H]^{3+}$ over 90 s with non *d*-methanol / He in the ion trap with two different capillary temperatures

5.3.1 Factors Affecting the *d*-Uptake by the Isolated Ion

A hypothesis that lower capillary temperatures would be more likely to preserve native structure was investigated. Initial interpretation of primary data suggests this to be the case. Figure 5-8 indicates a clear decrease in exchange rate with a capillary temperature of 125°C compared to that at 200°C for activation times up to 40 s.

A drop in capillary temperature results in an increase of the pressure gauge reading. This is counter intuitive on two levels. Firstly, the vacuum should increase with a decrease in temperature. Molecules and ions in the trap land on the turbo blades causing them to be pulled through to waste (with smaller molecules being evacuated more efficiently than larger).[9] Secondly, as mentioned in the introduction, research was performed by Gronert[3] proving the temperature in the ion trap to be ambient.[3]

The capillary temperature has no bearing on ion trap temperature so trap experiments could be judged as independent of source conditions. The assumption therefore was that air entered via the capillary and this can be attributed to the source seal becoming less effective at lower temperatures.

The effect of rf heating during ion isolation and the resulting thermal unfolding is illustrated here. Figure 5-8 shows exchange is accelerated during the first 5 seconds of each isolation window, the effect being more pronounced with a capillary temperature of 200°C. When the 125 °C data (Figure 5-8) was obtained, the pressure of *d*-methanol in the trap was manually adjusted to compensate for the observed change in pressure and to maintain a constant gauge pressure reading in the ion trap.

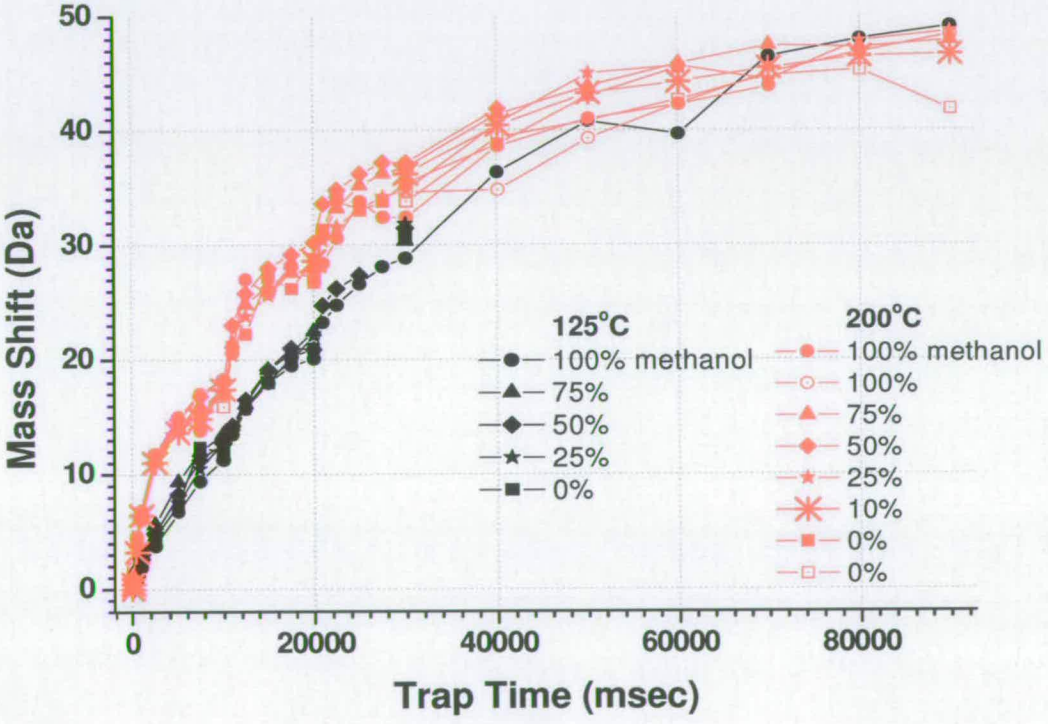

Figure 5-8 Gas phase exchange on melittin [M+3H]3+ over 90 s with capillary temperatures 125°C and 200°C

This readjustment, as the capillary temperature was lowered for the 125°C experiments, resulted in a lower concentration of *d*-methanol entering the trap.

However, any exchange post 40 seconds for both temperatures was not constrained by structure as nearly 100% exchange was achieved within a 90 second activation time. To this end, data collected between 40 and 90 seconds cannot be used to distinguish between different conformers. It also suggests that any exchange detected after this point is independent of *d*-methanol abundance and suggests that rf heating over the first four isolation stages has resulted in full denaturation and opening up of the structure.

.

Figure 5-9 shows the logarithmic relationship of hydrogen depletion over 10 and 90 seconds for $[M+2H]^{2+}$ and $[M+3H]^{3+}$ ionised either from 100% methanol or from 10 mM ammonium acetate with the half lives listed in Table 5-1. The same issues surrounding *d*-methanol concentration in the bath gas remain i.e. overall trap pressure was maintained at 2.5-2.8 E-5 Torr resulting in a reduction of *d*-methanol with decrease in capillary temperature which means that the effect of capillary temperature on its own cannot be seen here. Several conclusions can be inferred from this data:

i) The effect of elevated levels of *d*-methanol for the 200°C data. *d*-uptake is much greater at the higher temperature for both the 10 and 90 seconds trapping times for $[M+2H]^{2+}$, whereas there is no significant difference in uptake for $[M+3H]^{3+}$ over 90 seconds.

ii) The half life of the $[M+2H]^{2+}$ ion derived from methanol at 125°C is 4 times greater than at 200°C over 90 seconds and 3 times over 10 seconds. Although the same comparison cannot be made for ammonium acetate derived species, the magnitude of the half life at 125°C is in agreement with that from a methanol solution suggesting loss of the slight solvent memory effect shown in Figure 5-5 post isolation.

iii) The half life data for $[M+3H]^{3+}$ with both solutions are indistinguishable over the 90 second time scale. As with $[M+2H]^{2+}$ this infers that no solvent memory exists after isolation.

iv) The extra proton on $[M+3H]^{3+}$ allows rapid uptake of deuterium during the initial 2.5 seconds at 200°C before slowing down over the remainder

of the time course, an effect not seen at 125°C. The lower levels of *d*-methanol in the trap presumably result in decreased rates of exchange. This could provide another explanation for the difference between Marzluff's data and that shown here.

As discussed in the previous section, the extra proton on $[M+3H]^{3+}$ helps to destabilise the structure *via* coulombic repulsion, exposing the labile hydrogens early on. This is enhanced by rf heating during the isolation process (see Figure 5-8). This evidence supports the assumption that *d*-methanol levels in the bath gas and not capillary temperature play a significant role in *d*-uptake. If this is not the case, one must assume the extended form of $[M+3H]^{3+}$ relative to $[M+2H]^{2+}$ at the higher capillary temperature results in rapid uptake on entering the trap.

Methanol

Capillary Temperature	$[M+3H]^{3+}$ 10 s (i) t ½	(i) -k	(ii) t ½	(ii) -k	90 s t ½	90 s -k	$[M+2H]^{2+}$ 10 s t ½	10 s -k	90 s t ½	90 s -k
200°C	7223.3	9.60×10^{-5}	33324.4	2.08×10^{-5}	22733.6	3.05×10^{-5}	37732.6	1.84×10^{-5}	44805.9	1.55×10^{-5}
125°C	27440.5	2.43×10^{-5}			24202.1	2.86×10^{-5}	115910.9	5.98×10^{-6}	182263.3	3.80×10^{-6}

Ammonium Acetate

Capillary Temperature	$[M+3H]^{3+}$ 10 s (i) t ½	(i) -k	(ii) t ½	(ii) -k	90 s t ½	90 s -k	$[M+2H]^{2+}$ 10 s t ½	10 s -k	90 s t ½	90 s -k
200°C	7145.8	9.70×10^{-5}	42265.1	1.64×10^{-5}	27670.5	2.51×10^{-5}				
125°C	25662.6	2.70×10^{-5}			25530.3	2.72×10^{-5}	103609.4	6.69×10^{-6}	148584.6	4.67×10^{-6}

Table 5-1 Comparison of methanol and ammonium acetate half lives (sec) and rates (sec^{-1}) for activation times of 10 and 90 s (error bars present on graphs plotted in Figure 5-9). (Error range: $-k \pm (0.01 - 0.9) \times 10^{-5}$ s)

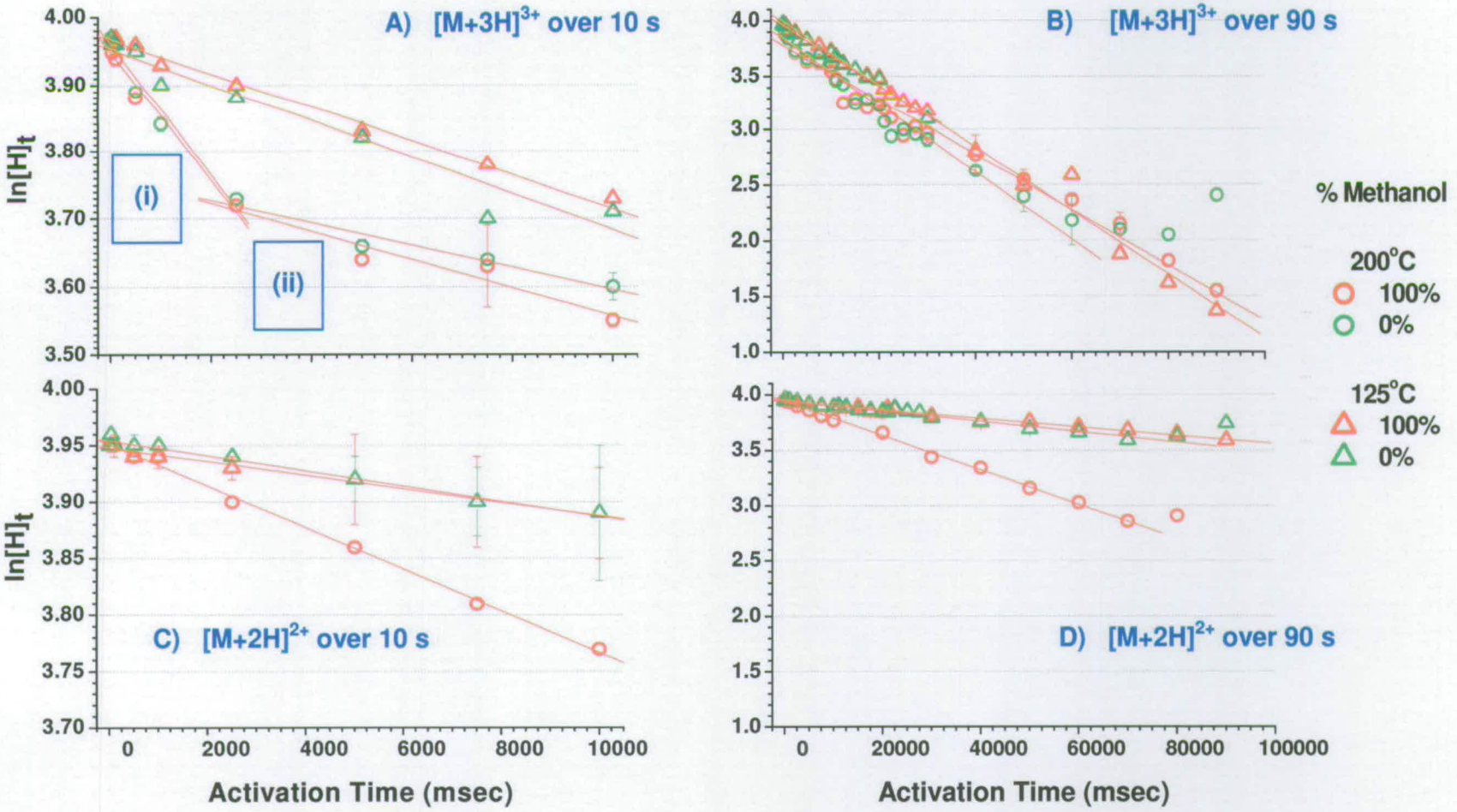

Figure 5-9 Demonstration of the logarithmic relationship of hydrogen depletion by gas phase exchange using ESI over 10 s (A and C) and 90 s (B and D) activation times for $[M+3H]^{3+}$ and $[M+2H]^{2+}$

5.3.2 The effect of Capillary Temperature on Gas Phase *d*-Uptake by Melittin using nanoESI

The experiments described in Section 5.3.1 infer capillary temperature is not a significant factor in gas phase exchange rates of melittin. However, the following studies repeat these experiments using nanoESI in an effort to confirm these findings. Data is compared with and without the trap pressure being maintained at 2.5E-5 - 2.8E-5 Torr as the capillary temperature is lowered using the external needle valve.

NanoESI, regarded as a less invasive ionisation technique, is used to help minimise any change in structure caused by desolvation. Consequently it is used for all subsequent gas phase studies in this thesis. Lower capillary temperatures favour the transmission of more highly protonated ions. The optics were therefore adjusted accordingly to assist $[M+2H]^{2+}$ transmission and, although ion abundance was low, gross mass shifts can still be calculated.

5.3.2.1 Maintaining a Constant Trap Pressure at Different Capillary Temperatures

As with ESI, similar trends of peak broadening were found to occur relative to activation time. As discussed in Chapter 4 and Section 5.2, peak shape is attributed to conformer populations with differing isotopic distributions. There is evidence to suggest structural integrity is retained during the first 10 s. The high kinetic energies of the ions entering the trap are efficiently quenched by the bath gas. The high number of collisions required to dissipate the energy and reduce the velocity returns the ion to its stable trajectory[10] and also more rapid exchange at this stage. This goes some way to explaining why exchange is accelerated during the first half of the 10 second activation window.

Figure 5-10 shows typical spectra obtained over multiple isolation steps. In agreement with solution phase HDX, peaks representing non-deuterated melittin are narrow (*m/z* ~1 Da). Analysis of $[M+3H]^{3+}$ shows peak broadening after 10 seconds

with tailing towards the higher *m/z* end. Again, this is assumed to be due to a combination of partial unfolding of the ions giving a wide distribution of *d*-uptake due to the occurrence of exchange happening at distinctly different rates. This continues with MS^3 (20 s) with peaks becoming more symmetrical though there is still evidence of more than one conformer present by a shoulder in the peak. By 90 s (MS^{10}), the peak has narrowed again suggesting the majority of ions present are now fully unfolded or at least occupying a similar conformational space. An almost identical pattern is followed for $[M+2H]^{2+}$ except the peak shape is less defined. There are a number of arguments to explain these observations:

i) $[M+3H]^{3+}$ already shows partial unfolding before exchange takes place due to intramolecular repulsion. Fewer unfolding steps lead to fewer intermediate conformers, hence a more stable doubly protonated ion will undergo a more complex unfolding pathway and widen the peak.

ii) $[M+2H]^{2+}$, as previously mentioned, is much less abundant at lower capillary temperatures. It is highly probable therefore that increasing the acquisition time would increase the signal to noise ratio and hence average out and smooth the shape.

iii) The ions are 'thrown off' their trajectory each time they are re-isolated. This may also result in the isolated ions moving at different velocities. The trajectory is increased with each subsequent step forcing the ion to be ejected 'out of sync' with the calibration. These two factors frequently result in either peak broadening or peak splitting.

iv) Peak splitting may also result from an electrical pulse dispersing the ion cloud, again causing ejection out with instrument calibration.

The second point may be another suggestion as to why the value for $[M+2H]^{2+}$ obtained by Marzluff and co-workers was so low. No spectra were available but if peak abundance for this ion was limited the question is raised as to whether they were genuinely observing the 2+ ion. This is a difficult argument to qualify, and perhaps it is more plausible that lower *d*-methanol content in the trap is the overriding factor.

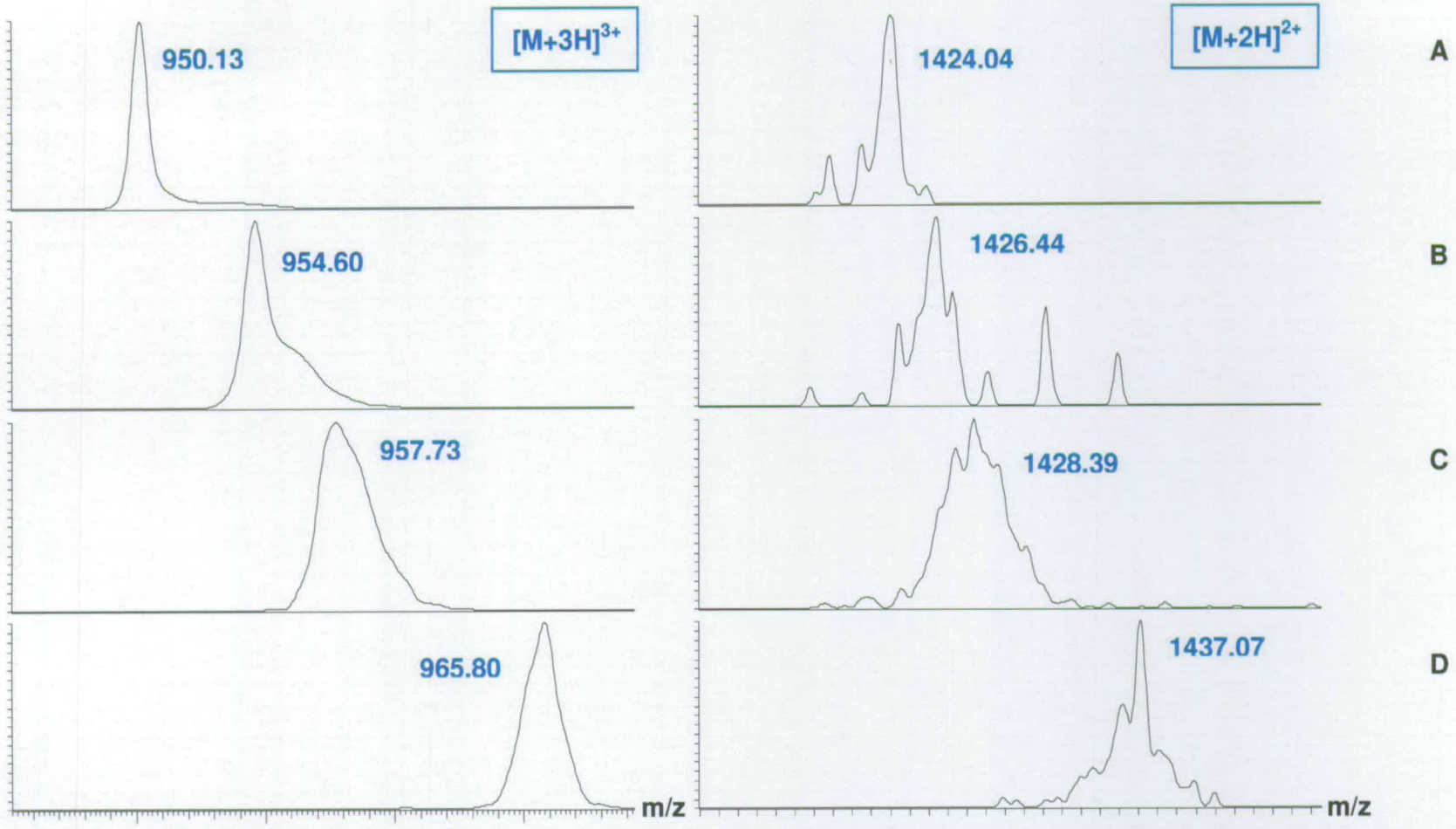

Figure 5-10 Peak shapes (capillary temperature 80°C) of $[M+3H]^{3+}$ and $[M+2H]^{2+}$ at activation times (A) 10 ms; (B) 10 s; (C) 20 s and (D) 90 s

Plots depicting hydrogen depletion over the two trapping times of 10 and 90 seconds are shown in Figure 5-11. There are strong similarities between the general trends of *d*-uptake here and those shown by ESI (Figure 5-9), i.e. greater levels of exchange are seen with higher capillary temperatures. In this instance, the nanosprayed solution has no bearing on the outcome.

d-Uptake of $[M+2H]^{2+}$ is logarithmic across both time intervals. Approximately 50% exchange is achieved after 90 seconds whereas $[M+3H]^{3+}$ exchanges 87% of its labile hydrogen population. Again, statistics are comparable to the ESI data presented earlier. This can be explained in one of two ways:

a) The $[M+2H]^{2+}$ ion never fully unfolds exposing all labile hydrogens or,
b) There is rapid interchange between conformers (i.e. the protein unfolds, which is implied by peak widths and shape) but the lack of intramolecular charge repulsion allows rapid hydrophilic collapse in the vacuum preventing further solvent exposure.

The second scenario is the most probable as the energy imparted to the ions during isolation by rf heating as been shown to cause loss of structural integrity. This has been discussed previously.

The magnitude of the half lives obtained using nanoESI (Table 5-2) were of the same order as the previous data shown in (Figure 5-9 and Table 5-1) with the exception of $[M+3H]^{3+}$ from methanol at 125°C which reaches a plateau after 40 seconds. The $t_{½}$ values for $[M+2H]^{2+}$ after 90 seconds, like electrospray, were at least a factor of three longer than values obtained for $[M+3H]^{3+}$, irrespective of solvent system.

The $[M+3H]^{3+}$ data taken over 10 seconds shows a small effect of capillary temperature[♦] and of solvent on the exchange profiles. There are two exchange populations which are distinguishable at the low temperatures for the 100% methanol solution and at 125 °C for the 0% methanol solution.

♦ The effect here could be augmented by the elevated pressure as the capillary temperature decreases as discussed previously.

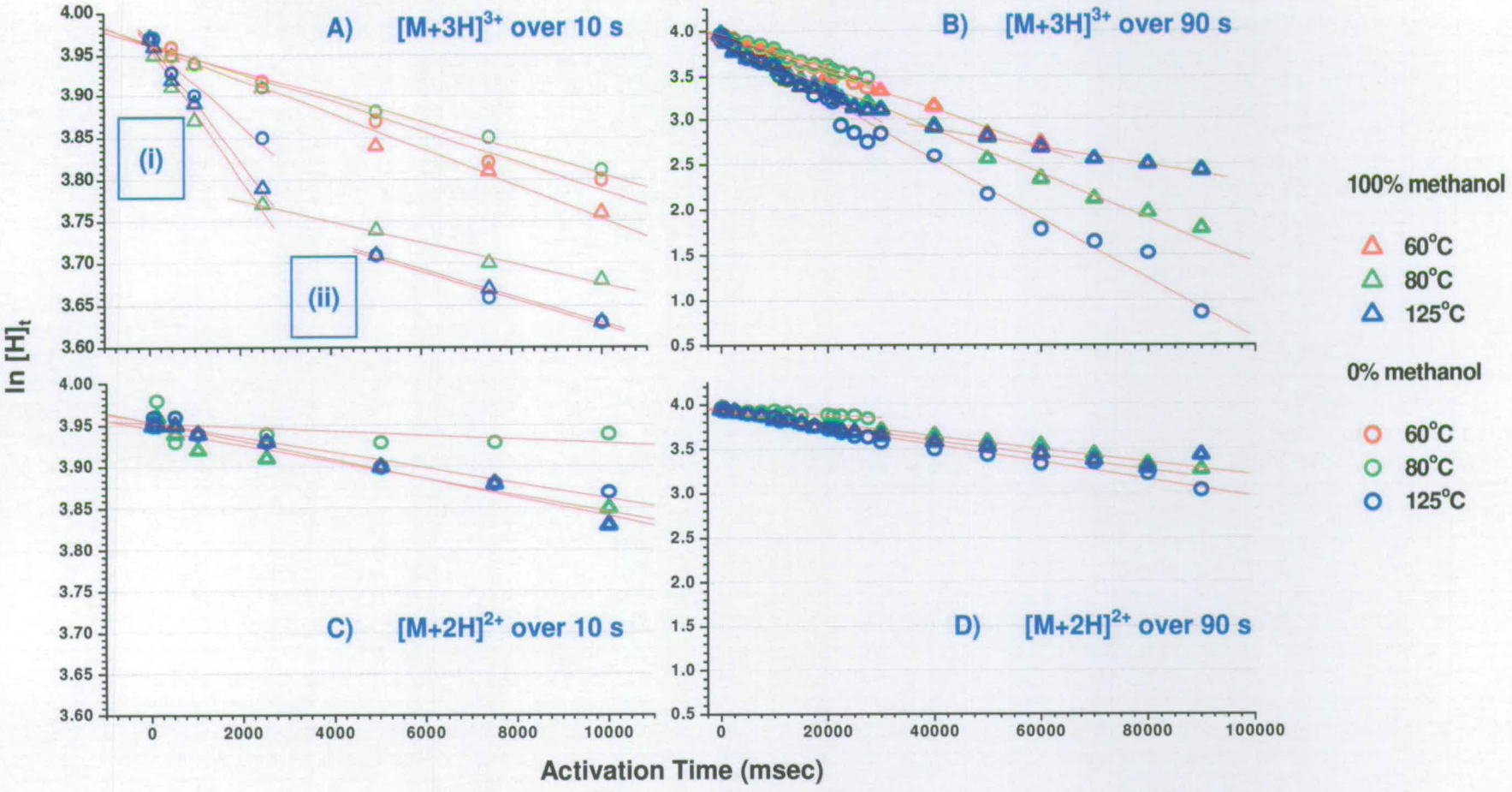

Figure 5-11 Demonstration of the logarithmic relationship of gas phase exchange using nanoESI over 10 s and 90 s activation times for $[M+3H]^{3+}$ (A and B) and $[M+2H]^{2+}$ (C and D) as derived from hydrogen depletion.

Methanol

Capillary Temperature	$[M+3H]^{3+}$ 10 s (i) t ½	(i) -k	(ii) t ½	(ii) -k	90 s t ½	90 s -k	$[M+2H]^{2+}$ 10 s t ½	10 s -k	90 s t ½	90 s -k
125°C	9624.4	7.20×10^{-5}	43321.7	1.60×10^{-5}	22060.7	3.14×10^{-5}	61668.0	1.12×10^{-5}	83171.0	8.33×10^{-6}
80°C	8724.3	7.95×10^{-5}	55899.0	1.24×10^{-5}	28108.2	2.47×10^{-5}	69245.5	1.00×10^{-5}	94049.8	7.37×10^{-6}
60°C	330384.7	2.10×10^{-6}			32944.3	2.10×10^{-5}				

Ammonium Acetate

Capillary Temperature	$[M+3H]^{3+}$ 10 s (i) t ½	(i) -k	(ii) t ½	(ii) -k	90 s t ½	90 s -k	$[M+2H]^{2+}$ 10 s t ½	10 s -k	90 s t ½	90 s -k
125°C	13580.5	5.10×10^{-5}	43321.7	1.60×10^{-5}	20985.4	3.30×10^{-5}	75572.1	9.17×10^{-6}	71194.3	9.74×10^{-6}
80°C	44318.9	1.56×10^{-5}			38788.3	1.79×10^{-5}	288691.0	2.40×10^{-6}	202378.7	3.43×10^{-6}
60°C	38919.0	1.78×10^{-5}			33977.8	2.04×10^{-5}				

Table 5-2 Comparisons of half lives (sec) and rates (sec^{-1}) using nanoESI calculated over 10 and 90 s activation times with needle valve readjustments. (Error range: -k ± (0.01 - 0.9) x 10^{-5} s)

5.3.2.2 Comparing ESI and nanoESI

Deuterium uptake using different methods of ionisation is plotted in Figure 5-12. As described above, the trapping time was increased from 10 seconds to 90 seconds in increments up to 10 seconds. Although temperature was shown to not significantly affect H/D exchange (see data obtained using the same desolvation method in Section 5.3.1), for purposes of convenience, different data sets are identified by capillary temperature.

The isolation steps have a greater effect on *d*-uptake than ionising solvent and capillary temperature because:

a) Melittin ions produced *via* nanoESI with the capillary at 125°C undergo slightly more exchange than with ESI. This is surprising since nanoESI is arguably a gentler technique.
b) Using 100% methanol solution and nanoESI at 80°C the protein undergoes greater exchange than at 125°C. This may be attributable to slightly harsher desolvation.
c) There is a slight decrease in uptake at long activation times between 100% methanol and 0% methanol. This is not thought to be significant and does not have much effect on the rates (see above)

These minor observations aside, there seems little difference between the two ionisation methods.

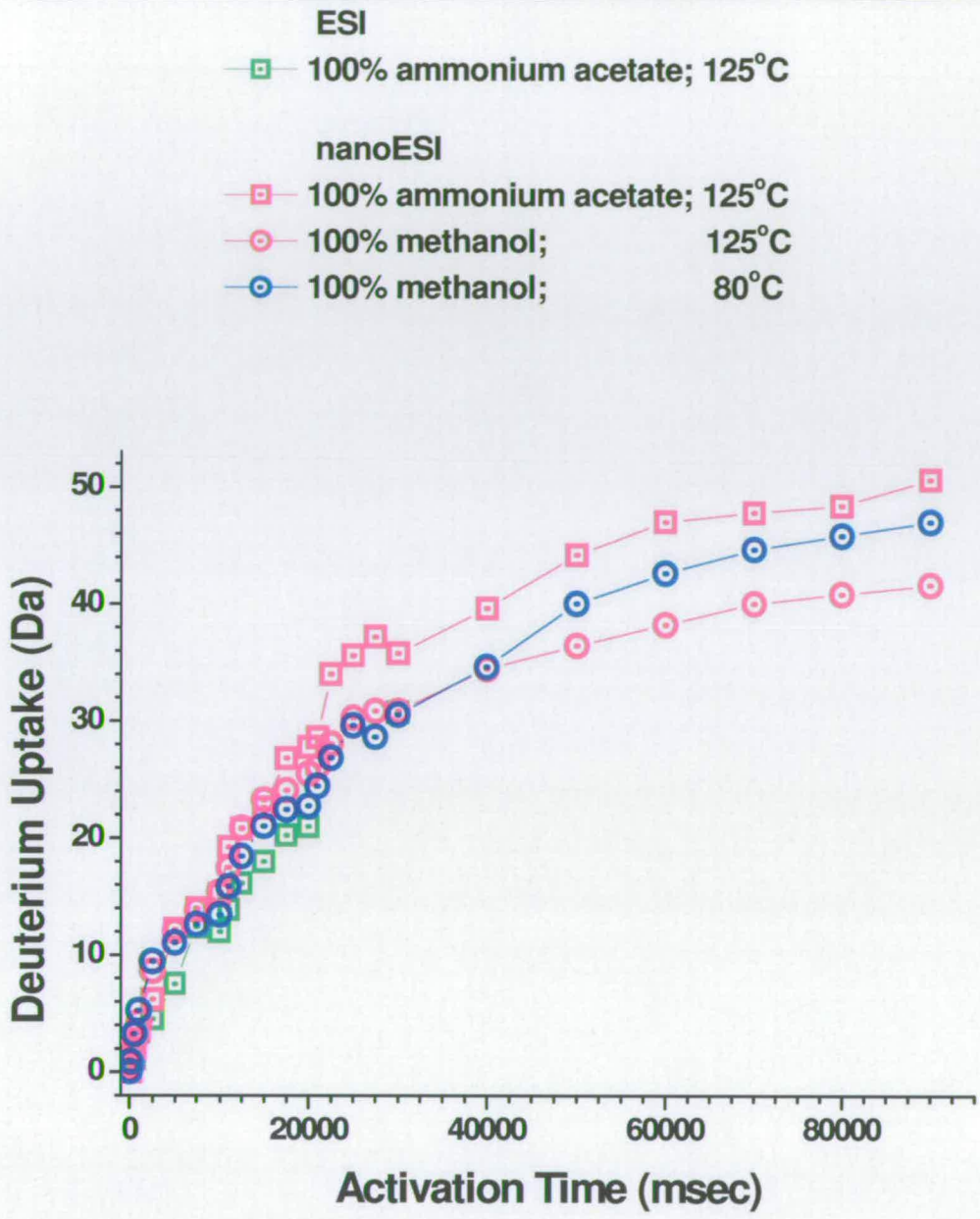

Figure 5-12 Comparison of nanoESI and ESI deuterium uptake. In these experiments the pressure of *d*-methanol is comparable.

5.3.2.3 The Effect of Different Capillary Temperatures with nanoESI

NanoESI of melittin was performed without adjustment of the He / *d*-methanol inlet valve. The gauge was calibrated with helium on a daily basis to achieve a constant base pressure then left to equilibrate with *d*-methanol. There was a slight rise in gauge reading at this point due to the first ionisation potential differences in the two gases. The approach was modified by discontinuing data acquisitions across the full 90 seconds. All subsequent experiments were limited to a single isolation step with a maximum 10000 ms activation time as defined by the LCQ software interface. Half lives listed in Table 5-3 were calculated from data acquired across a 10secondrange with no needle inlet valve readjustment. The capillary temperature was then lowered and the ion gauge left to equilibrate for 1 hour.

As shown above (Figure 5-2), peak widths can reveal conformer interconversion. Figure 5-13 shows typical spectra observed for both the 3+ and 2+ charge states with capillary temperatures 60°C and 125°C. Differences between two extreme solution environments, ammonium acetate and methanol are directly compared.

i) In contrast with earlier studies, no significant peak broadening is observed with $[M+3H]^{3+}$ from ammonium acetate at either temperature suggesting no complex unfolding mechanisms were necessary to increase solvent exposure.

ii) $[M+3H]^{3+}$ from methanol at 60°C does exhibit some structural retention which is not observed at 125°C. Peaks are immediately much broader with a loss of symmetry which has already been established as a sign of multiple conformers. The peak maximum shifts from a lower mass at 1 second to a higher mass after 10 seconds, a clear indication of increased solvent exposure attributed to conformer interconversion.

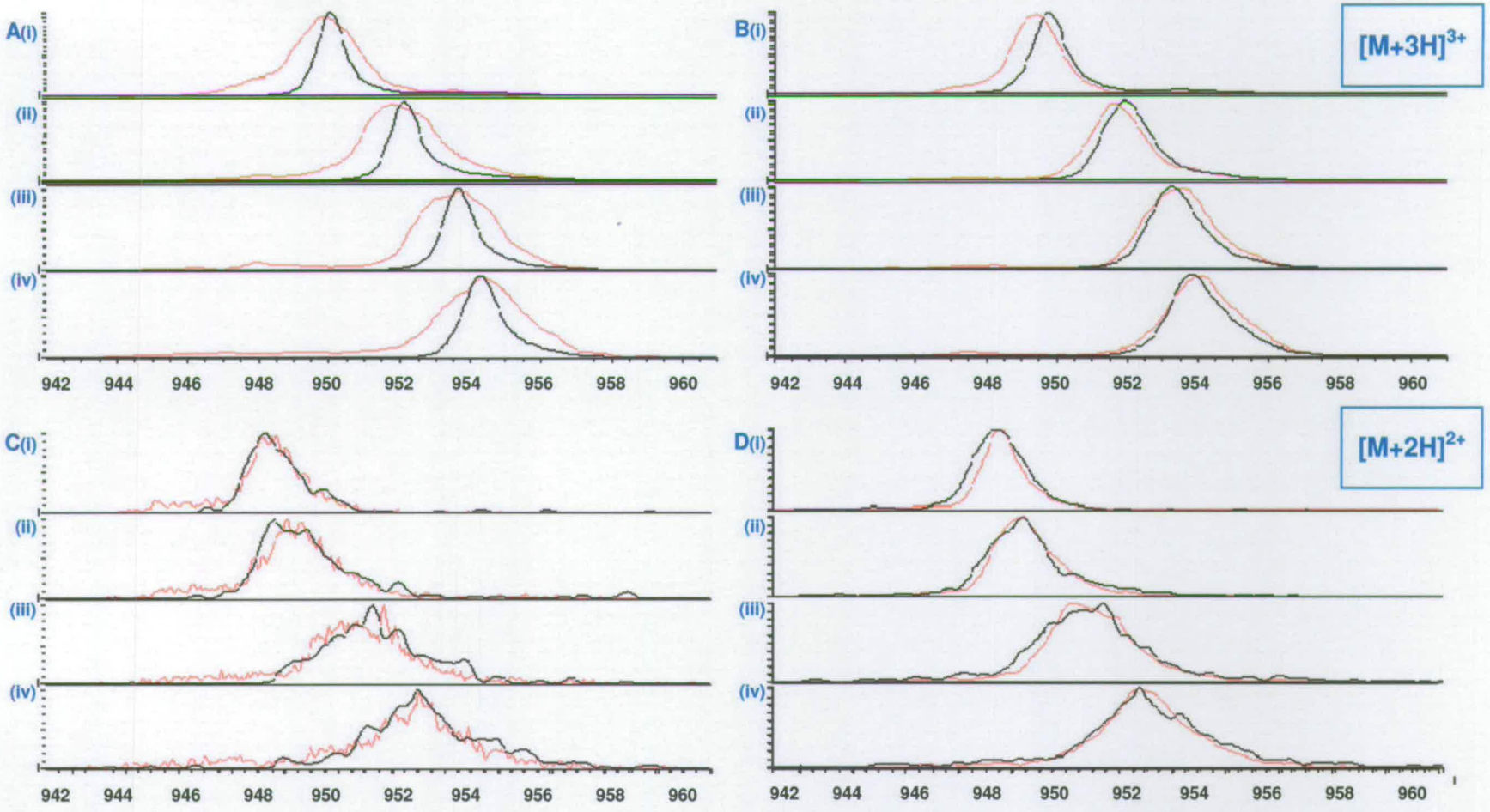

Figure 5-13 Typical spectra of $[M+3H]^{3+}$ and $[M+2H]^{2+}$ ionised from ammonium acetate (black) or methanol (red) using nanoESI, with capillary temperatures 60°C (A and C) and 125°C (B and D) with activation times (i) 10 ms; (ii) 1 s; (iii) 5 s; (iv) 10 s

iii) The shape of the $[M+2H]^{2+}$ ion suggests some unfolding or interconversion mechanism is necessary. Peak broadening is apparent with both capillary temperatures and solvent environments. As with $[M+3H]^{3+}$ peak maximum is biased to lower *m/z* values at shorter activation times and higher *m/z* values after 10 seconds. After 10 seconds the peak narrows again in keeping with previous data inferring all ions occupy the same or similar conformational space.

iv) Peaks are much smoother at 125°C. A direct consequence of more efficient desolvation.

This data confirms that dropping the capillary temperature considerably can indeed help retain some structural integrity for low charge states of melittin derived from hydrophilic and hydrophobic solution environments. Reducing the temperature results however at a cost of sensitivity. $[M+2H]^{2+}$ is much harder to observe under such gentle desolvating conditions.

With the use of this lower capillary temperature there may be some retention of solvent conforamtion. For $[M+3H]^{3+}$ sprayed from methanol the rates of exchange for the second population are significantly different as a function of capillary temperature, although notably they are not for the first population. For the ammonium acetate solution and for $[M+2H]^{2+}$ in both cases the exchange rates over 10000 ms with four capillary temperatures all lie within experimental error of each other (Table 5-3). The exchange rates for $[M+3H]^{3+}$ from both solutions are faster than $[M+2H]^{2+}$ from which we can infer a more open conformation(s) for the $[M+3H]^{3+}$ ion.

Methanol

Capillary Temperature	$[M+3H]^{3+}$ 10 s (i) t ½	(i) -k (sec^{-1})	(ii) t ½	(ii) -k (sec^{-1})	$[M+2H]^{2+}$ 10 s t ½	-k (sec^{-1})
200°C	3481.4	$2.07x10^{-4}$	38508.2	$1.80x10^{-5}$	15949.1	$4.35x10^{-5}$
125°C	2968.5	$2.13x10^{-4}$	36870.0	$1.88x10^{-5}$		
80°C	3257.3	$2.34x10^{-4}$	25483.4	$2.72x10^{-5}$	17085.2	$4.06x10^{-5}$
60°C	3342.1	$1.99x10^{-4}$	25114.0	$2.76x10^{-5}$	16795.4	$4.13x10^{-5}$

Ammonium Acetate

Capillary Temperature	$[M+3H]^{3+}$ 10 s (i) t ½	(i) -k (sec^{-1})	(ii) t ½	(ii) -k (sec^{-1})	$[M+2H]^{2+}$ 10 s t ½	-k (sec^{-1})
200°C	3195.7	$2.17x10^{-4}$	33977.8	$2.04x10^{-5}$	15137.5	$4.58x10^{-5}$
125°C	3182.5	$2.18x10^{-4}$	35364.7	$1.96x10^{-5}$	15865.1	$4.37x10^{-5}$
80°C	2994.2	$2.32x10^{-4}$	34657.4	$2.00x10^{-5}$	15127.6	$4.58x10^{-5}$
60°C	3080.7	$2.25x10^{-4}$	29370.6	$2.36x10^{-5}$	14203.8	$4.88x10^{-5}$

Table 5-3 Calculated half lives (sec) of melittin exchange over 10 s activation time with no readjustment to the inlet valve

Differences between ESI and nanoESI have been shown to be minimal (Figure 5-12). However capillary temperature does become a factor when using nanoESI at temperatures below 125°C. As reported throughout this thesis it is a challenge to maintain native structural conformations during desolvation, and it seems that this is particularly true for a protein as small as melittin. Most ESI studies have been performed on large complex proteins where multiple intramolecular interactions allow the retention of a greater degree of structural integrity *in vacuo.*[11,12,13]

5.3.3 CID Analysis of Gas Phase Melittin

The $[M+3H]^{3+}$ parent ion was easy to fragment and obtain a high sequence coverage comprising principally of y ions. Selecting $[M+2H]^{2+}$ as the parent generated c and z daughter ions which suggested a fragmentation pathway akin to that following electron capture dissociation (ECD) (Figure 5-14). Limited sensitivity, coupled with higher normalised collision energies (NCEs) lead to fragmentation of the $[M+2H]^{2+}$ ion being irreproducible and so it not discussed further.

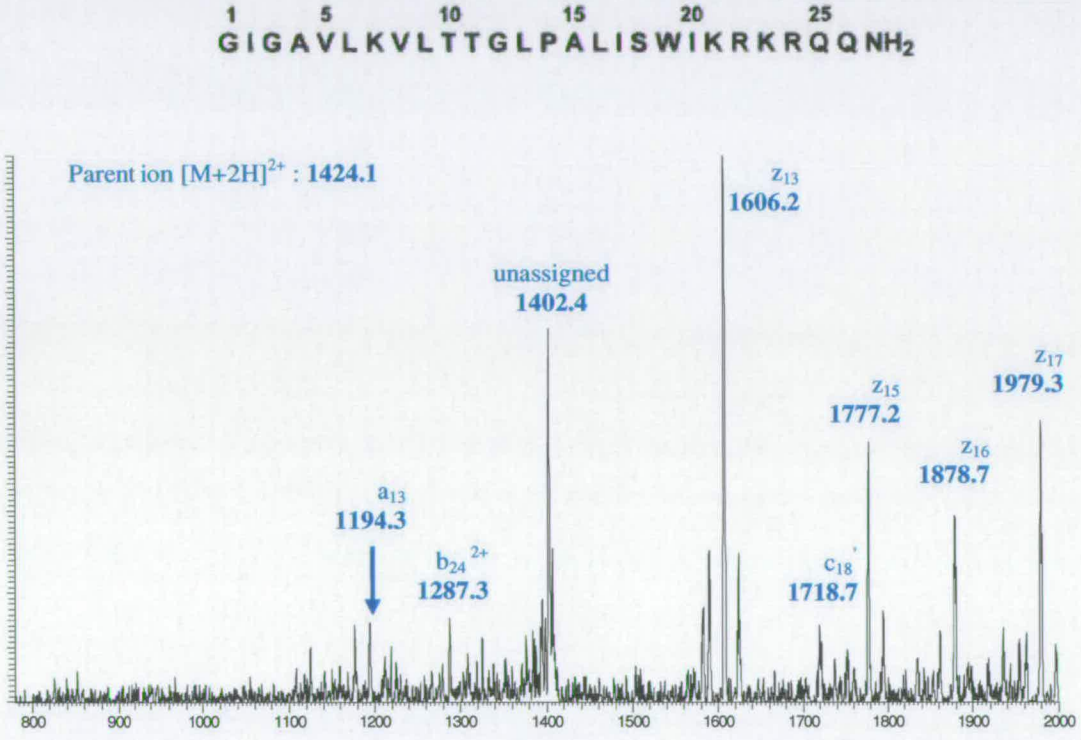

Figure 5-14 CID of Melittin $[M+2H]^{2+}$ produced fragments equivalent to ECD

5.3.3.1 Peak Shapes of Fragment Ions

Chapter 4 demonstrated the use of CID to locate regions of a protein where labile hydrogens are protected from exchange – in the case of melittin this is assumed to be by the presence of at least a partial α-helix. Arginine is the amino acid with the highest gas phase basisicity[14] and hence the residues within melittin (Arg-22 Arg-24)

are likely to be proton carriers. Lys-7 possesses a flexible side chain and due to its location surrounded by neutral amino acids and high gas phase basisicity[14] is a favoured site within the N terminus for protonation.[1] As shown in Chapter 4, the high abundance of fragments arising from dissociation around this residue enable the calculation of *d*-uptake on the daughter peptides. This allows mapping of the solvent exposed parts of the protein. The same approach is adopted here and typical examples of spectra are shown in Figure 5-15. Analysis of the y18 fragment, one of the most abundant fragments comprising the C-terminal region from Leu-9, shows that peak width and shape provide information on conformer diversity. Again the peak broadens up to ~10 seconds followed by a narrowing after 90 seconds. This can be related to the parent ion conformation as the mass shift due to exchange occurs prior to CID, although the same caveats regarding deuterium scrambling that were discussed in Chapter 4 are also relevant here.[15] The ions were not reisolated and subjected to further exchange as restructuring may occur during fragmentation thus negating any meaningful structural interpretation.

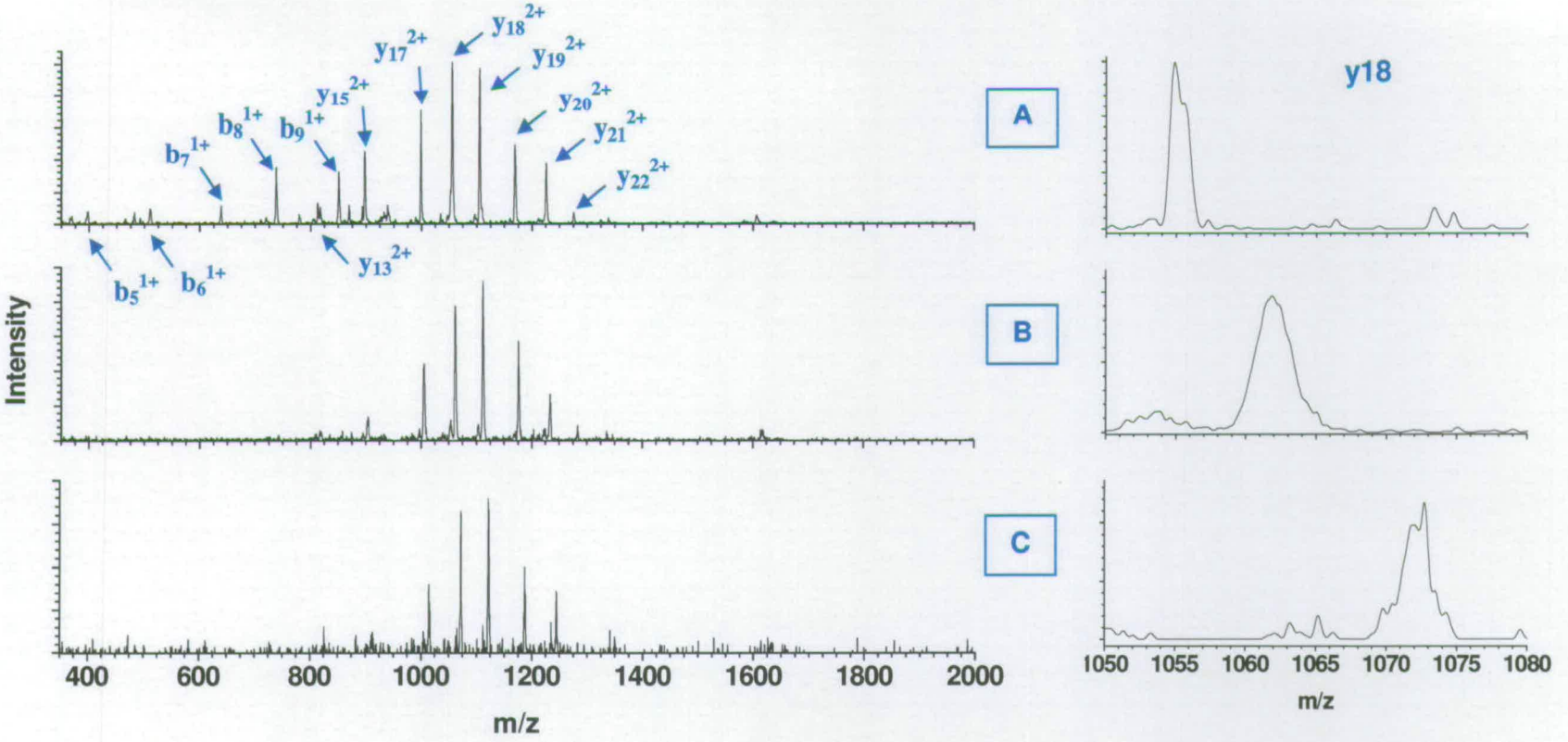

Figure 5-15 CID spectrum resulting from fragmentation of $[M+3H]^{3+}$ after 10msec (A), 10sec (B), 90sec (C) with an amplified view of fragment y18 for peak shape and width comparisons

5.3.3.2 Analysis of C-Terminal Region *via* y13

The sequence contains a KRKR motif rendering the C terminal end of melittin extremely basic. The high gas phase basicity of arginine[14] is conducive to the sequestering of protons thus increasing the amount of energy required to mobilise them and initiate fragmentation.[16] The N-terminus contains one lysine which readily protonates, but having a lower gas phase basicity than arginine lends itself to initiating the formation of oxalozone intermediates. The presence of Pro-14 weakens the molecule and a y13 fragment is often formed by nozzle-skimmer dissociation during desolvation. This was examined in Chapter 4 to locate the presence of some α-helical structure in the N-terminal region. To confirm this, y13 was isolated and its *d*-uptake monitored and compared to that of the parent ions (Figure 5-16).

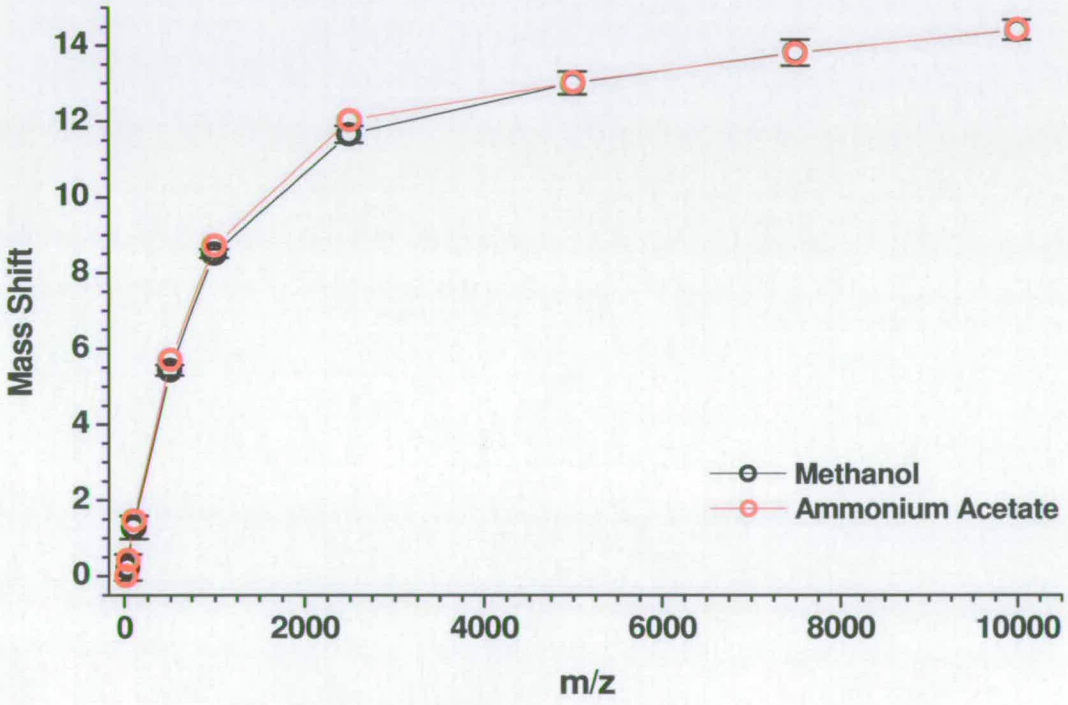

Figure 5-16 *d*-uptake of y13 over 10 s (only the major peak in the bimodal distribution shown above has been analysed)

Analysis of the peak shapes shown in Figure 5-17 present interesting outcomes regarding differences between aqueous and non-aqueous solution structure. Both are identical after 1secondexposure. After being held in the trap for 5 seconds, the fragment generated from ammonium acetate shows the peak to be a doublet whereas the methanol derived ion retains a mono-modal distribution. This suggests a more stable structure on the methanol derived fragment. After 10 seconds, a bimodal distribution is resolved with the lower *m/z* peak maximum being the same as the most abundant conformer of the ammonium acetate derived peak.

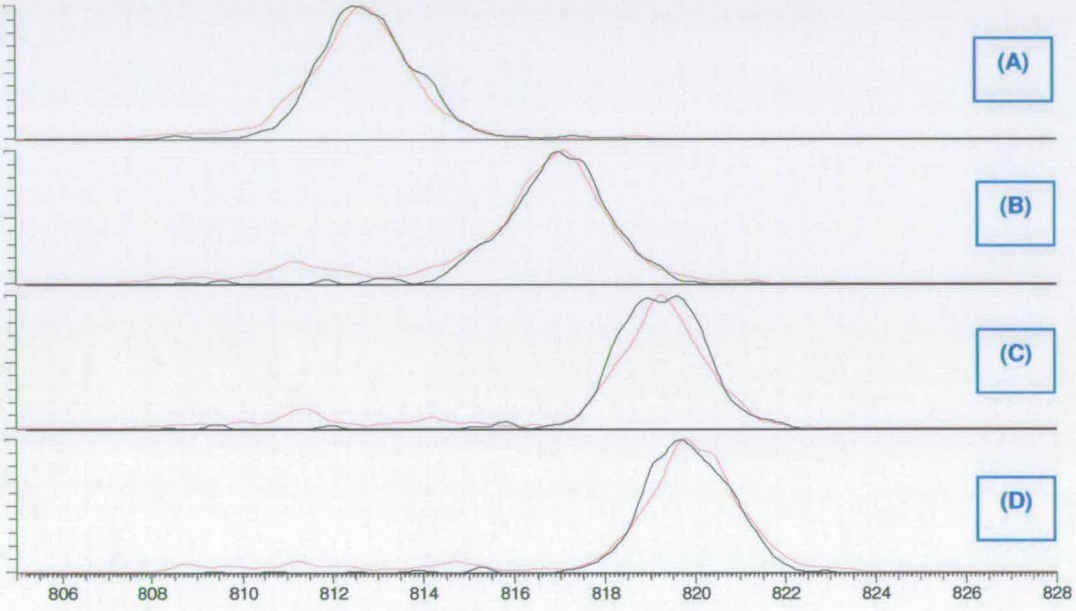

Figure 5-17 Exchange of isolated y13 fragment from ammonium acetate (black) and methanol (red) with capillary temperature 60°C at activation times (A) 10 ms; (B) 1 s; (C) 5 s; (D) 10 s

14 hydrogens are exchanged after 10 seconds accounting for 82 % of the total uptake by $[M+3H]^{3+}$. The sister b13 ion was not detected and as such its uptake is not calculated. From these data the majority of the exchange occurs within the C-terminal region. All solution phase experiments agree with this conclusion.

5.3.3.3 Locating the α-Helix by CID

Melittin was trapped for 10 seconds then re-isolated for 10 ms to perform CID. This does not compromise the data as no significant exchange occurs during this activation time. Hydrogen depletion of the fragment ions is plotted in Figure 5-18.

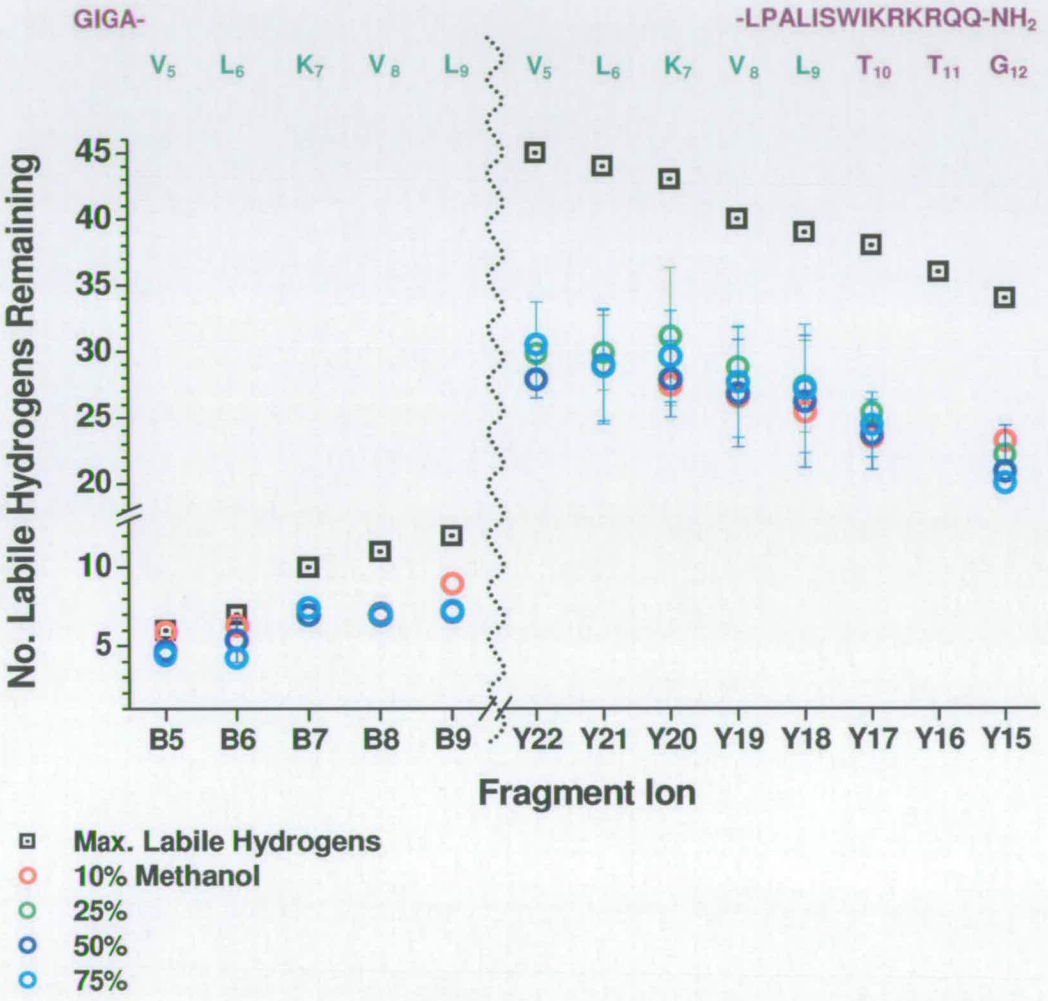

Figure 5-18 CID fragments of $[M+3H]^{3+}$ (capillary temperature 125°C) after 10 s activation time

Residues 1-5 show full exchange but the larger b fragments reveal that no exchange occurs between residues Val-5 and Leu-6 and, Lys-7 and Leu-9. This correlates with solution phase data where the same residues show no solvent exposure.

This data overlaps with that obtained from the corresponding y fragments where y22, y21, y19, y18 show no change in exchange. The residues involved, apart from lysine, are aliphatic and as such show hydrophobic qualities. This encourages helical formation when in a hydrophobic environment. The backbone amide hydrogens are subsequently shielded from exchange. The protons in the amino group of Lys-7 will be amongst the first to exchange on entering the trap so some albeit limited *d*-uptake is seen.

5.4 Complimentary Techniques

Two additional analytical methods were employed served to corroborate the HDX findings above.

5.4.1 Molecular Modelling

CID post HDX data presented in the previous section 5.3.3 indicate the similarities between a hydrophobic solution phase environment and a vacuum. These findings are now used to justify emulating the conditions of a hydrophobic lipid bilayer found in cell membranes using molecular dynamics based on the fully helical crystal structure calculated by Terwilliger and Eisenberg[17] minimised at 300K. A typical structure is illustrated in Figure 5-19. This preservation of a strong helical character correlates with other studies (including CD data in chapter 4) which show melittin maintains its helicity in organic and membrane environments.[18,19]

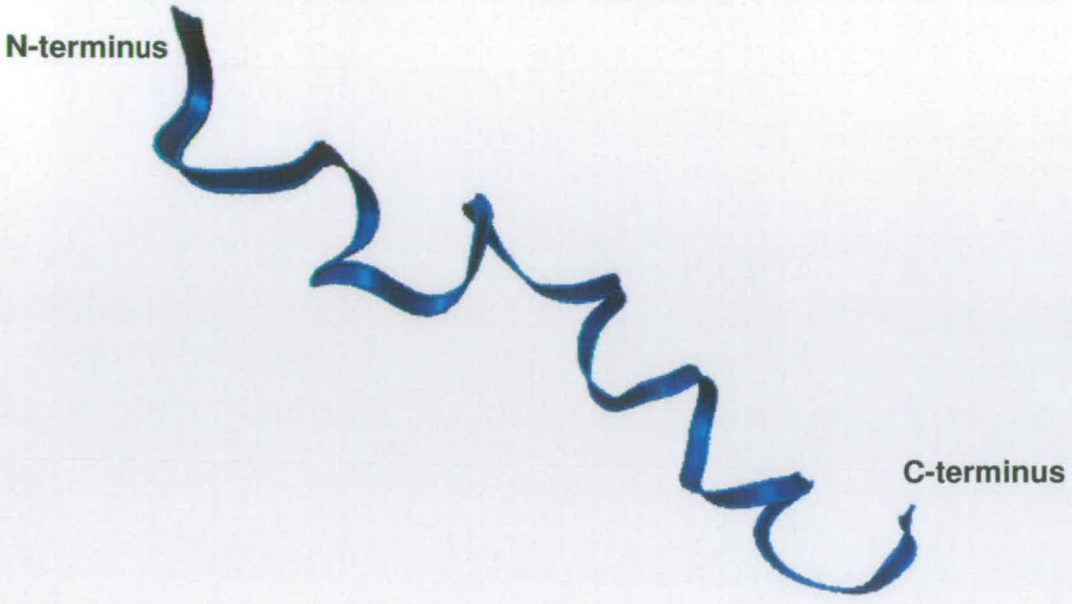

Figure 5-19 Molecular dynamics snapshot of the $[M+3H]^{3+}$ species in solution phase

Born-Solvent simulations show a complete collapse in overall structure with the majority of the helical moiety being lost except at the N-terminus which is illustrated in Figure 5-20. This is in agreement with solution phase HDX studies presented in Chapter 4 where there incomplete exchange of whole protein is observed but there is complete exchange of the C-terminal (y13) fragment. The low energy structures show a degree of fluctuation with no strong trend emerging. This said, they often contain one helical terminus starting just after or ending just before the central Pro-14 residue – the helix breaker. This is supported by studies performed by Inagaki *et al.*[20] and Okada *et al.*[21] who disagree however, on both the region possessing greatest helical retention and which terminus unravels first.

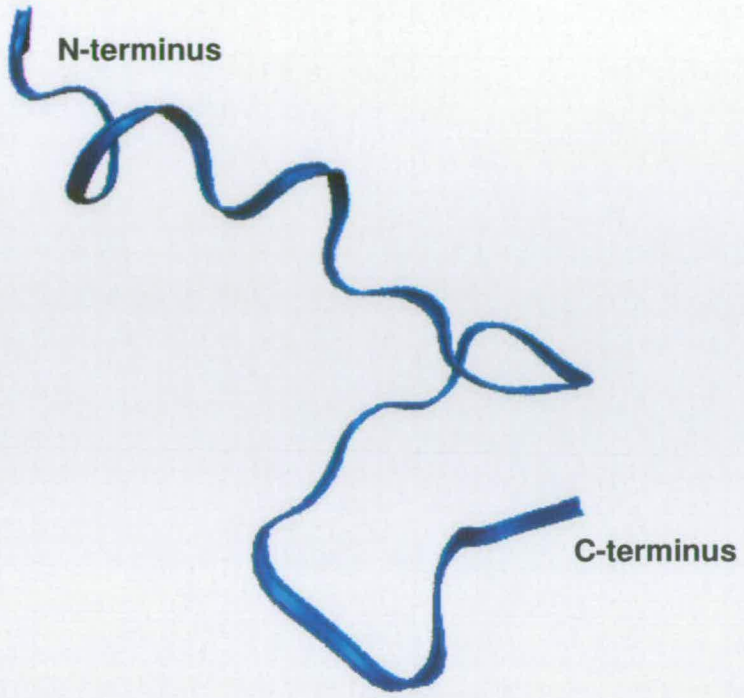

Figure 5-20 Molecular dynamics snapshot of the $[M+3H]^{3+}$ species in solution phase exhibiting partial helical retention at the N terminus

5.4.2 Ion Mobility

As shown in Chapter 4, the characteristic presence of the y_{13} fragment ion produced as a result of in source dissociation was used as an aid for establishing the most robust helical region of melittin. The following data was obtained using ion mobility quadrupole time of flight mass spectrometry newly developed at Edinburgh and referred to here as the MoQToF.[22] The aim was to substantiate the solution phase data that an increasing hydrophobic environment promotes an α-helical structure. A tightly coiled structure would exhibit a smaller collision cross section than a conformer comprising random coil.

In high methanol concentration solutions, the y_{13}^{2+} fragment is the dominant species while the y_{13}^{3+} ion is the dominant species in aqueous solutions. This immediately indicates the molecule is less structured in an aqueous solution than in a predominantly organic solution.

Charge	% Methanol in Water					50% MeOH
	0	25	50	75	100	50% Am Ac
3+	544	543	523	530	566	516
4+	584	576	572	561	587	578
5+	605	602	-	-	-	-
y_{13}^{2+}	340	339	328	332	350	332
y_{13}^{3+}	359	351	-	337	356	362

Table 5-4 Collision cross sections ($Å^2$) of melittin from different solvent conditions♥

Table 5-4 lists the collision cross sections measured for melittin under each solvent condition. The trends in these data do not reveal a clear shift in cross section with solvent concentration that would indicate a large structural change caused by the transition from random coil to α-helix. This supports our HDX findings. Melittin did not show distinct differences in *d*-uptake when it was ionised from ostensibly the same solutions as those listed above. This maybe attributed to the difficulty in maintaining the structure of this small dynamic protein in a solvent free environment.

There is however a clear trend of collisional cross section increasing with charge state for both the parent and y13 fragment ions, indicating that the presence of protonated residues force a more open structure, a now well established fact. In addition the y13 fragments, which form half of the peptide sequence, have a measured collision cross section which is more than half that of the respective parent ions. This suggests that the C terminal region is more unfolded and by inference the N terminal region is more helical. This supports the findings using CID.

♥ Unpublished data obtained in collaboration with B. McCullough

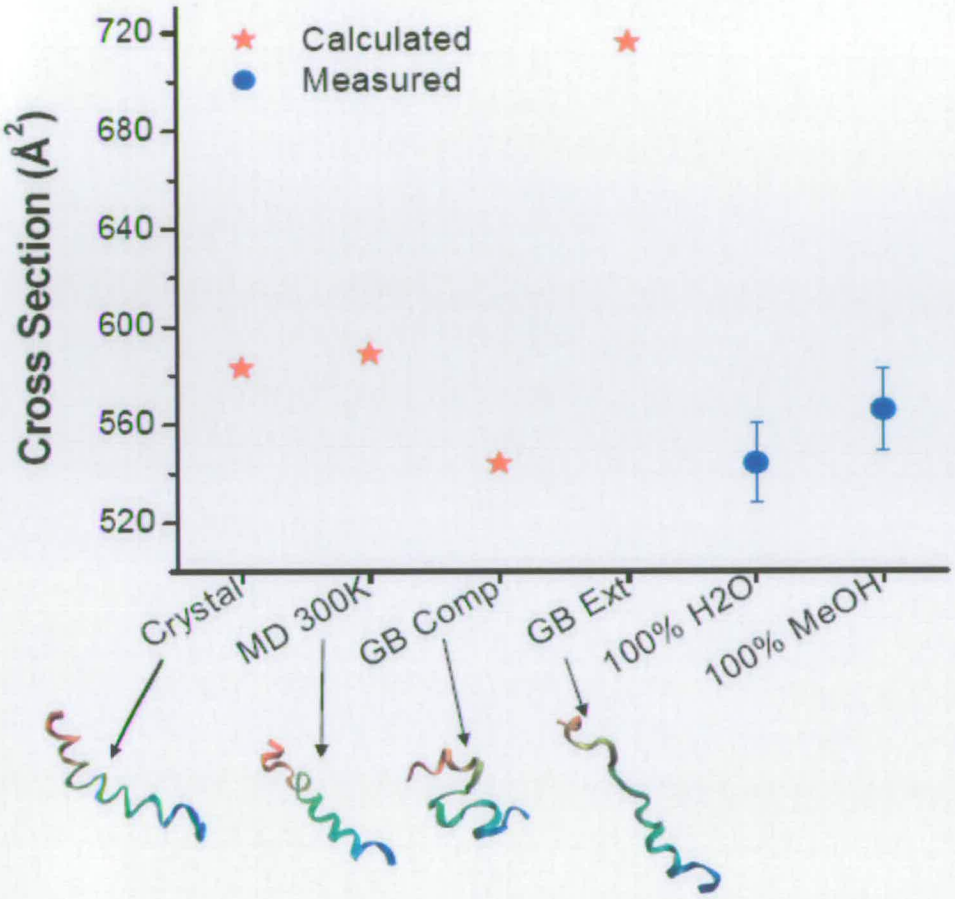

Figure 5-21 Experimental and theoretical cross sections of melittin $[M + 3H]^{3+}$

Figure 5-21 validates the experimental data obtained using the MoQToF by comparing the two extreme solvent conditions (with +/- 3% error bars) to data obtained from the crystal structure,[17] molecular dynamics (calculated in-house using the crystal structure minimised at 300K by Lippens and Kalapothakis[23]) and simulated annealing structures using Generalised Born solvent (GB) to represent water (Kalapothakis). The latter is represented by compact and extended structures. Although the compact structure with no α-helix evident is in good agreement with the experimental aqueous data, the extended structure is not sampled. This supports indications of hydrophobic collapse occurring during gas phase exchange (discussed

in Section 5.3). The value obtained from the methanol solution is in strong agreement with the crystal structure generated cross sections exhibiting α-helical structures.

5.5 Conclusions

Exchange in the ion trap is charge state dependent and is summarised below

	$[M+2H]^{2+}$	$[M+3H]^{3+}$
Overall Exchange	• ~50% max • [H] depletion always logarithmic	• Solvent memory during first isolation window • Maximum exchange over 90 s
Solvent	• Methanol better solvent at low temperatures	• Some structural retention from methanol
Capillary Temperature	• Difficult to obtain at low temperatures • Exchange rates not affected up to 200°C	• Influences 2° population from methanol in first 10 s at low temperatures
Isolation Steps	• Rapid exchange during first 2.5 s of each isolation step	• Rapid exchange during first 2.5 s of each isolation step
Peak Broadening	• Smoother at higher temperatures	• Most significant at low temperatures from methanol solutions

Table 5-5 Summary of gas phase exchange of melittin

Comparisons of gas phase show strong agreement with regards to helical retention.

CID data confirmed the presence of some structural retention in the N-terminal region, corroborated by analysis of the y13 fragment generated by nozzle-skimmer dissociation, collisional cross sections from ion mobility data and molecular dynamics.

5.6 References

[1] Kaltashov IA. and Feneslau C, *Proteins: Str. Func. Gen.*, 1997, **27**, 165-170
[2] Goeringer DE., McLuckey SA., *J Chem Phys*, 1996, **104**, 2214-2221
[3] Gronert S., *J Am Soc Mass Spectrom*, 1998, **324**, 945
[4] Evans SE., Lueck N., Marzluff EM., *Int J Mass Spectrom.*, 2003, **222**, 175-187

[5] Green MK and Lebrilla CB, *Int J Mass Spectrom*, 1998, **175**, 15-26
[6] Englander SW., Sosnik TR., Englander JJ., Mayne L., *Curr Op Struct Bio.*, 1996, **6**, 18-23
[7] Campbell, S. Rodgers, M. T. Marzluff, E. M. Beauchamp, J. L. *J. Am. Chem. Soc.* 1995 ,**117** ,12840 -12854
[8] Freitas MA., Hendrickson CL., Emmett MR., Marshall AG., *Int J Mass Spectrom*, 1999, **185-187**, 565-575
[9] Kurt J. Lesker, Vacuum Pump Manual
[10] March RE., Todd JFJ., *Quadrupole Ion Trap Mass Spectrometry*, 2nd Edition, Wiley Interscience
[11] Aplin RT., Robinson CV., Schofield CJ., Westwood NJ., *Journal of Chemical Society, Chemical Communications* , 1994, 2415-2417
[12] Benesch JLP., Robinson CV., *Curr. Op, Struct. Biol.*, 2006, **16**, 245-251
[13] Heck AJR, van den Heuvel RHH., *Mass Spectrom Rev*, 2004, **23**, 368-389
[14] Harrison AG., *Mass Spectrom Rev.*, 1997, **16**, 201-217
[15] Demmers JAA., Rijkers DTS., Haverkamp J., Killian KA. and Heck AJR., *J Am Chem Soc.*, 2002, **124**, 11191-11198
[16] Huang Y., Triscari JM., Tseng GC., Pasa-Tolic L., Lipton MS., Smith RD., Wysocki VH, *Anal Chem B.*, 2006, **A-K**
[17] Terwilliger C. and Eisenberg D., *J. Bio. Chem.*, 1982, **257**, 6016-6022
[18] Lam, Y.; Wassall, S.; Morton, C.; Smith, R.; Separovic, F. *Biophys. J.* **2001**, *81*, 2751-2761
[19] Vogel, H. *FEBS Letters* 1981, **134**, 37-42
[20] Inagaki, F.; Shimada, I.; Kawaguchi, K.; Hirano, M.; Teresawa, I.; Ikura, T.; Go, N. *Biochemistry* 1989, **28**, 5985-5991
[21] Okada, A.; Wakamatsu, K.; Miyazawa, T.; Higashijima, T. *Biochemistry* 1994, **33**, 9438-9446
[22] McCullough BJ *et al.* private communication
[23] Lippens J. and Kalapothakis J., private communication

6 Cyclophilin A – Hydrogen/Deuterium Exchange

6.1 Introduction

In this chapter, three MS based HDX methods for analysing protein conformers are applied to the CypA-CsA complex. Results are presented and strengths and weaknesses of each approach are discussed.

Chapters 4 and 5 discussed analysis of melittin, a small intact protein, using HDX-MS techniques. Similar methodologies can be applied to larger proteins. The approach adopted here aims to provide a global picture of conformational change, when coupled with data from fragmentation techniques such as enzymatic digestion[1] or dissociation techniques.[2,3,4] HDX-MS can provide details of conformational changes at the residue level[5] analogous to NMR.[6] This chapter describes work using HDX on apo CypA and when incubated with the ligand CsA. This is an example of the strength of MS as a technique which can reveal conformational changes when ligands bind to their target protein. These direct infusion approaches provides a basis from which to perform more detailed experiments or for use as a screen to probe the behaviour of a series of ligands.

The process of understanding the differences between CypA with and without CsA bound uses the following stratagem. Preliminary studies adopt a strategy of direct analysis comparing *d*-uptake by native CypA and CypA-CsA by monitoring the total mass shift. Whilst this provides a view of the role CsA plays on the stability of CypA in solution, another method such as PLIMSTEX[7] (the background to which is discussed in Chapter 1) is then employed to provide complementary evidence from HDX of solution phase binding. Finally, having established the ability to maintain a native-like structure of CypA and its binding partners in a solvent free environment, (Chapter 3), gas phase exchange studies are also utilised to compare H/D exchange of the apo- and holo- proteins.

To study dynamics of larger proteins, detection of conformers or intermediates is desirable. Kaltashov, Eyles and co-workers have performed extensive studies, measuring *d*-loss during re-folding of pseudo-wild type cellular retinoic acid binding protein I (CRABP I), a 15 kDa protein, by monitoring back exchange rates.[8] They also studied the unfolding dynamics of the β-sheets in CRABP I and established the presence of a bimodal distribution identifying two discrete exchange populations and hence defining two distinguishable conformations.[9] In the early to mid 1990s McLafferty and co-workers[10] began using H/D exchange to infer a relationship between protein conformation, charge states generated by ESI and known solution phase conformation(s). In a comparison between ion mobility mass spectrometry and gas phase HDX for the well characterised protein Ubiquitin, Freitas *et al.*[11] made an important finding. As the charge on the protein increases so too does the recorded collision cross section.[12] However Freitas noted that higher charge states exhibited less *d*-uptake. This is attributable to the requirement of the relay mechanism[13] - that a proton donor and acceptor are < 5Å from each other. As the protein unfolds giving a larger cross section, this critical distance is exceeded. This work showed clearly that care must be taken in interpreting gas-phase HDX data. The Freitas study and all the above examples involved the analysis of proteins under denaturing conditions. Here we employ native ESI-MS.

PLIMSTEX, a solution based method incorporating reverse phase chromatography pioneered by Gross and co-workers[7] enables an understanding of backbone dynamics by back exchanging the deuterated side chain groups but leaving the labile amide backbone deuterated whilst on the column. The protein is then eluted directly into the mass spectrometer. The experiments described here discuss two approaches where back exchange is achieved under native and non-native buffering conditions.

Whilst SUPREX is not utilised in these studies, Wang *et al*[14] used the technique effectively to compare purified CypA / CypA-CsA with endogenous CypA (over expressed in lung tumour tissue lysate) with CsA added. By titrating with denaturant (*d*-guanidinium chloride, GdmCl) they were able to calculate the folding free energies (ΔG) of CypA and subsequently the binding affinities (K_ds) of CsA in the

two environments. Their findings, summarised in Table 6-1, demonstrate the dissociation constant of purified protein is twice that of the unpurified.

CypA Sample		ΔG_f (kcal/mol)	SUPREX K_d (nM)
Purified	- CsA	11.3 ± 0.7	
	+ CsA	15.5 ± 0.7	77 ± 17
Unpurified	-CsA	9.4 ± 0.2	
	+ CsA	14.1 ± 0.8	32 ± 20

Table 6-1 Summary of comparison of K_ds of CsA with purified and unpurified CypA as calculated by Wang *et al*[14] using SUPREX

Stable intermediate conformers were not detected so an EX2 regime i.e. the refolding of the protein is faster than the H/D exchange rate of unprotected amide protons, was adopted. This is shown to be more effective in the presence of CsA.

Kipping and Shierhorn[15] monitored CsA exchange rather than CypA by MALDI-ToF. CsA has only 4 amide hydrogens all of which exchange rapidly in solution. They were able to prove the existence of an H-bond in the Abu pocket of the CypA binding site by its ability to significantly reduce back exchange to less than 11%.

Comprehensive H/D exchange studies performed on CypA by Shi *et al.*[6] utilised SEA HSQC (solvent exposed amide - heteronuclear single quantum coherence), which are 2D NMR experiments which correlate proton and heteronuclear resonances and identified four exchange populations. A summary of their residual exchange rates is listed in Table 6-2. 59 residues exchanged so fast they were not quantifiable by this method; 21 residues occupied the secondary population with an exchange rate (k_{ex}) > 1 x 10^{-2} min^{-1}; 29 fell into the 'moderate exchange rate' population with rates ranging 1 x 10^{-4} min^{-1} < k_{ex} < 1 x 10^{-2} min^{-1}. The final 'slow exchanging' population with k_{ex} < 1 x 10^{-4} min^{-1} involved the remaining 44 residues with labile hydrogens. This left twelve remaining residues unable to exchange, four

of which are prolines with no labile hydrogens. They also showed that 80% of the residues occupying the CsA binding pocket have k_{ex} values > 1 x 10^{-4} min^{-1}.

Perhaps the most interesting finding is that *all* the residues in the binding site are flexible and as such favour complex formation. Using these findings, one would expect to see the *d*-uptake of native CypA by MS to be faster than its CypA-CsA counterpart.

Having prior knowledge of the CypA-CsA binding site was useful, although it did not restrict other interpretations of the HDX data presented in this chapter. These mass spectrometry based studies were designed to analyse the rates of exchange on CypA and to ascertain any differences which may arise in the presence of a ligand, in this case CsA.

Exchange rate range / min^{-1}	Residue	Orientation
$k_{ex} < 1 \times 10^{-4}$	V6, F7, F8, D9, I10, A11, V12, V20, F22, E23, **F25***, **V29***, A33, E34, N35, F36, R37, A38, L39, S40, T41, **I57***, **Q63***, G64, I97, L98, S99, M100, F112, **F113***, I114, C115, F129, G130, K131, V132, V139, E140, A141, M142, I157, I158, D160, G162	* involved in α-helix like turn α2(V139-M142); β1(V6-V12); β2(V20-E23); β5(I97-M100); β6(F112-C115); β7(F129-V132) constitute hydrophobic core
$1 \times 10^{-4} < k_{ex} < 1 \times 10^{-2}$	E15, L17, G18, L24, A26, K31, T32, Y48, S51, F53, **R55***, **F60***, **M61***, C62, E86, L90, G96, **A101***, T116, A117, D123, **H126***, V127, V128, K133, I138, E143, F145, A159	18 residues incorporated 2° structure
$k_{ex} > 1 \times 10^{-2}$	**T5***, K28, G42, F46, G50, G65, I78, Y79, D85, N87, I89, H92, G94, T107, N108, G109, T119, **L122****, **G134***, R144, **C161***	incorporated in unstructured loop * involved in 2° structure
Residues disappearing in the first spectrum	D13, G14, R19, S21, D27, E43, K44, G45, G47, K49, C52, H54, I56, G59, D66, F67, T68, R69, N71, **G72***, **T73***, G74, G75, K76, S77, G80, K82, F83, E84, F88, K91, T93, **N102***, **A103***, G104, N106, S110, **Q111***, K118, E120, **W121***, G124, K125, G135, M136, N137, G146, S147, N149, G150, K151, T152, S153, K154, K155, I156, Q163, L164, E165	Unstructured loop * involved in binding site

Table 6-2 CypA amide H/D exchange rates of individual amino acids as calculated by Shi *et al.*[6] using NMR data

6.2 Solution Phase HDX Studies : Part 1 - Direct Infusion

As demonstrated in Chapter 3, it is possible to preserve the conformation of native CypA found in solution for gas phase analysis. Following on from this, 20 μM solutions of CypA and CypA-CsA (1:1) complex were incubated in 10 mM *d*-ammonium acetate (pD 7.2) or *d*-water. The mass shift was monitored over time by DI-ESI using a Q-ToF mass spectrometer (Micromass UK) and equated to *d*-uptake.

The aim was to obtain a direct comparison between apo- and holo- CypA exchange rates under both environments thereby allowing interpretation of the effect buffer has on CypA and its overall structural stability.

6.2.1 The Effect of Buffer on Protein Structure

Figure 6-1 depicts typical spectra of CypA in *d*-water, *d*- and non-*d*-ammonium acetate solutions after incubating for 3 minutes. Initial observations were particularly interesting with regard to potential conformer populations.

CypA in *d*-ammonium acetate demonstrated a mass increase when compared to protein in non-*d*-buffer. Considerable peak tailing and loss of resolution is evident. Salt adducts are routinely detected on native proteins and these become indistinguishable from adduct free protein once deuterated. Side chain and backbone labile hydrogens exchange at different rates depending on a) their location within the secondary and tertiary structure and b) their neighbouring amino acids i.e. the intrinsic exchange rate of the primary sequence (see Chapter 1, Section 1.5). Evidence describing the influences of these factors in proteins has been discussed by Englander and co-workers.[16]

When incubated in *d*-ammonium acetate, two peaks are detected (Figure 6-1 A). The overall mass increases were calculated using the mid-point of the peak maxima. After 3 minutes, increases detected were 166.7 Da for peak A and 276.9 Da for peak B. Peak A represents, on first assumptions, what is thought to be a less dynamic structure. The mass increase equates to 110 Da less than peak B and as such

demonstrates an apparent lack of solvent accessibility to regions of the protein. PPIase assays♠ (data not included), routinely conducted on each batch of protein did not detect the presence an active and / or inactive form. The open structure was therefore unlikely to be a result of permanent denaturation and as such the refolding rate is slow enough for exchange to occur (EX1 regime).

A midway 235.5 Da increase is calculated for CypA in *d*-water. On this basis the decreased buffering capacity of water prevents the complete unfolding and refolding of CypA. It maybe that the protein partially unfolds and refolding is slow enough to permit exchange.

♠ performed by members of the Walkinshaw group

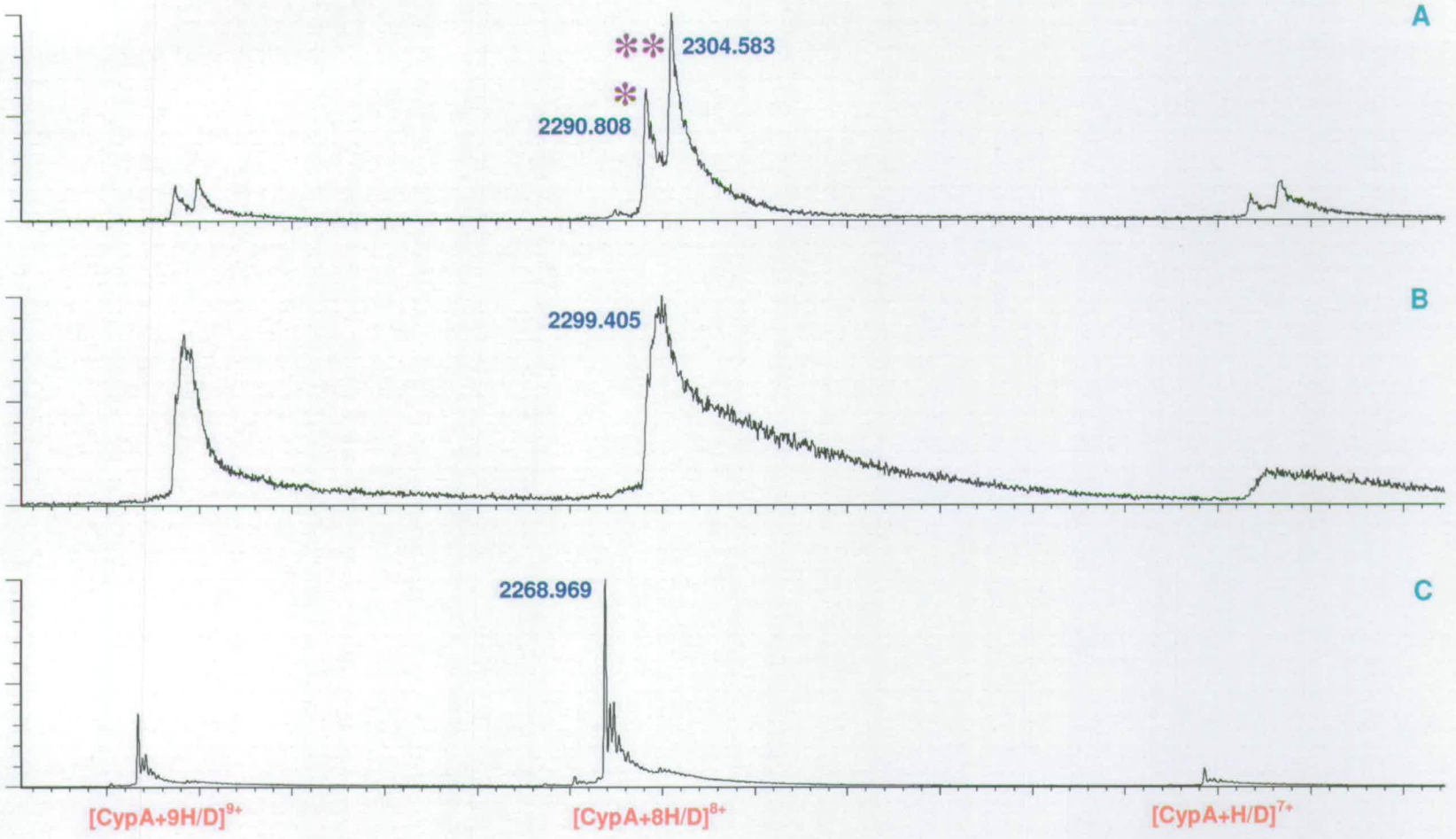

Figure 6-1 A comparison of CypA incubated in 10mM *d*-ammonium acetate (A), *d*-water (B) and deuterium free ammonium acetate (C) for 3 minutes (* Peak A; ** Peak B)

Binding CsA does not affect the peak distribution. Figure 6-2 shows the more solvent exposed peak (peak B) remains dominant. The act of exposing ligand to the protein enforces a conformational change. It is likely therefore, that with a K_d in the range 10-40 nM,[17] exchange can happen within the period of dissociation.

K_ds proved difficult to calculate using methods outlined in Chapter 3. The unbound CypA peak is extremely small and although manual analysis of raw data allowed the calculation of the values presented, the lack of baseline resolution on the two 'conformers' means use of intensity data would be best served with a peak fitting approach. This was not taken here.

The legitimacy of peak B being a conformational or isomeric artefact is contentious. The explanation above alluded to an apparent structural rearrangement on dilution with *d*-ammonium acetate resulting in one population totally unfolding followed by rapid refolding and, a second population which has only partially unfolded. Several explanations are discussed below:

1) *Two environmental factors*. a) pH change in the buffer. This is dismissed as the difference between *d*- and non *d*- buffer is 0.4 pH units. A sudden reduction in concentration however can cause a structural rearrangement as the protein readjusts to slightly different buffering conditions. b) Temperature differential. This can be dismissed as all water stocks and buffers are stored at 4°C prior to use.
2) *Presence of a limited amount of dimer in solution*. No dimer has ever been detected by mass spectrometry although it is possible that it would dissociate during desolvation. The interaction of two CypA molecules would possibly negate the forming of the complex and this clearly does not happen.
3) *The buffering capacity of d-ammonium acetate is faster than d-water*. This enables the buffer to distinguish between structural intermediates. These conformers are not stable for a long enough period for exchange to take place in *d*-water.

4) *Non-covalent adduct.* The mass difference between the conformers post exchange ranges 100 – 104 Da. There is evidence of salt and buffer adducts with peak broadening and tailing in both *d*-buffer and *d*-water. It therefore suggests the possibility of a contaminant in the *d*-ammonium acetate which binds to the CypA without disruption of the active binding site. In these experiments, the mass range was 500-3500 Da and as such potential contaminant peaks below 500 Da were not detected.
5) *Another form of CypA.* a) It is possible the protein has undergone a misfold during expression resulting in a more open or dynamic structure. A variation in induction temperature or times may result in a temporary disruption of the folding process. b) Expression is in *E. coli* and there may have been a mixture of vector populations within the culture for this batch. The latter is less plausible as all culture stocks were derived from the same transformation.

The anomaly appears to be batch specific and as such the most likely explanations are 4) and 5a). The SUPREX studies by Wang *et al.*[14] discussed in the introduction to this chapter also found evidence of two isomers in both their purified and tissue lysate CypA. They attributed this anomaly there to slight variations in the sequence resulting from minor sequence variations during expression. Analysis by MALDI-ToF failed to resolve them once deuterated however and so were regarded as inconsequential to the study. For these reasons it is valid to ignore peak B for the following analyses and focus solely on data from peak A.

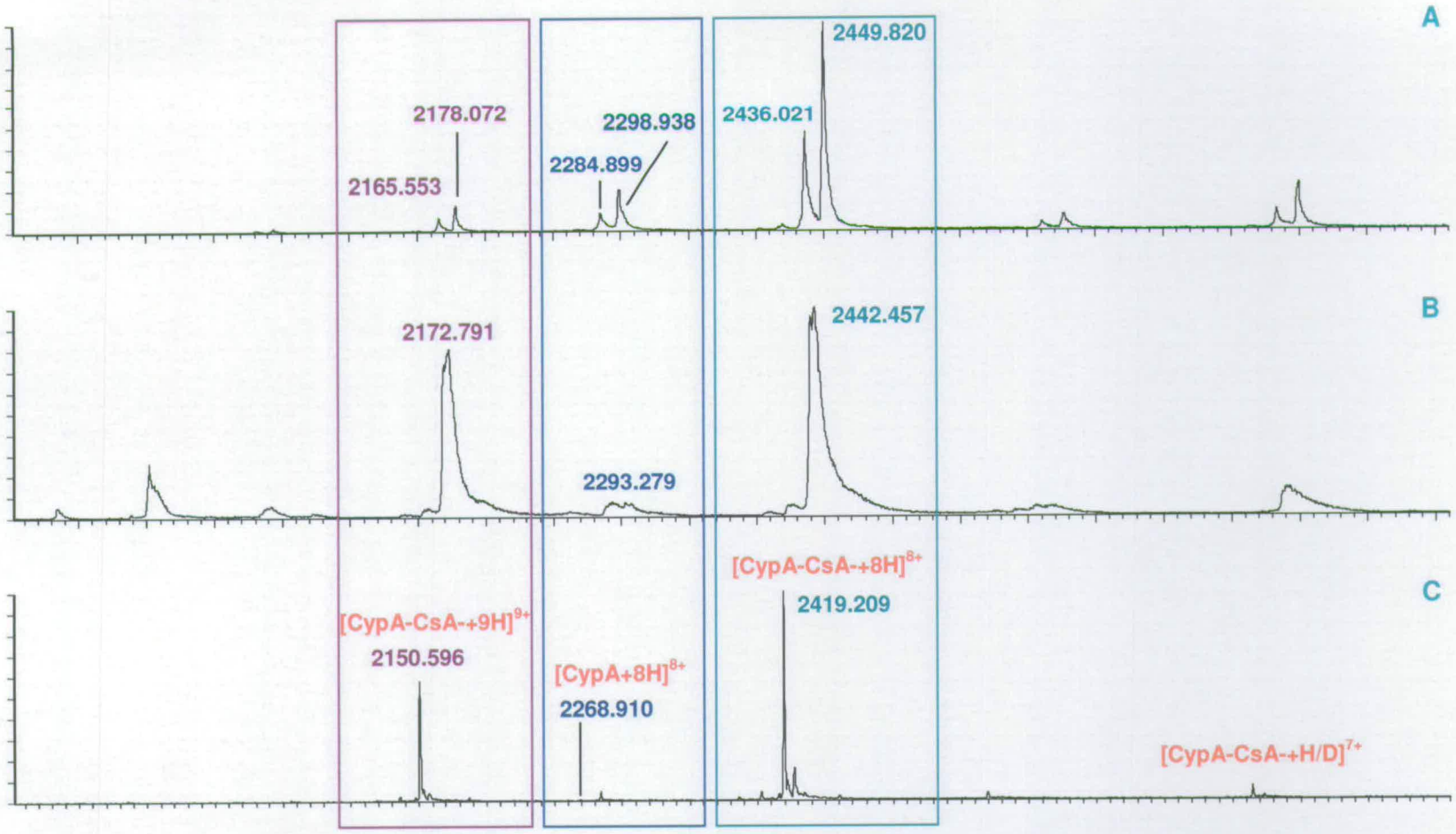

Figure 6-2 CypA-CsA (1:1) post 3 minute incubation in 10mM *d*-ammonium acetate (A), *d*-water (B) and deuterium free ammonium acetate (C)

6.2.1.1 Comparison of H/D Exchange Rates

Deuterium uptake was monitored over a period of days and is examined using deconvoluted data in all cases. Figure 6-3 shows the difference in deuterium uptake when the protein with and without the ligand is incubated in either water or buffer. Rates for peak A and *d*-water were calculated from 3 mins up to 23 mins (primary exchange rates) and exchange rates are listed in Table 6-3. Illustrated in Figure 6-4 are plots of the natural log of hydrogen depletion over 3 days for CypA only; unbound CypA after incubation with CsA; and the CypA-CsA complex. The exchange of CsA involved in the complex has been incorporated into the calculated mass shifts. Table 6-3 also summarises approximated mass increases between 0 and 23 mins and 23 mins and 3100 mins (3 days) to simplify the differences in overall *d*-incorporation within the population.

Protein Configuration	Solution	Approximated *d*-Uptake (Da)			k / mins^{-1}
		0-23 mins	23-3100 mins	TOTAL	1° Pop^{n}
CypA Only	Water	204	28	232	7.13×10^{-3}
	Peak A Buffered	165	15	180	4.66×10^{-3}
CypA-CsA Bound	Water	153	29	182	5.19×10^{-3}
	Peak A Buffered	156	21	177	8.66×10^{-3}
CypA-CsA Unbound	Water	147	30	177	4.38×10^{-3}
	Peak A Buffered	158	15	173	8.38×10^{-3}

Table 6-3 Approximated mass increases for CypA over two time ranges with the exchange rate, k calculated from the initial linear region

During first 23 minutes, ligand free CypA in water exchanges 32 labile hydrogens more than with buffer. This increases to a difference of 52 over the remaining time period. This supports the hypothesis that there is increased flexibility in water for approximately two thirds of the protein.

Conversely, where ligand is present the uptake appears marginally lower in water than buffer although, this is open to question as the difference lies within the experimental error. The exchange rates of bound and unbound CypA in water decrease by approximately 27% during the first time period but these remain constant in a buffered environment. Immediate exposure of complex to *d*-ammonium acetate appears to increase solvent accessibility relative to *d*-water. i.e. some rapid exchange occurs outwith the detectable time period with the first detectable value obtained after approximately 3 minutes.

This supports the findings of Shi *et al.*[6] who stated the rates of exchange for 59 labile hydrogens in the unstructured loop were so rapid they could not be calculated. The protein is sensitive to sudden changes in temperature, pH and concentration. Rapid dilution prior to analysis is likely to result in an unfolding and refolding which will affect the extent of the initial exchange in the unstructured loop.

The secondary population shows less stability overall in water in each protein configuration by averaging an increase of 30 Da, approximately 12 Da more than the buffered protein over the following 3 days. This latter observation is probably a result of the reduced buffering capacity of water having a detrimental effect.

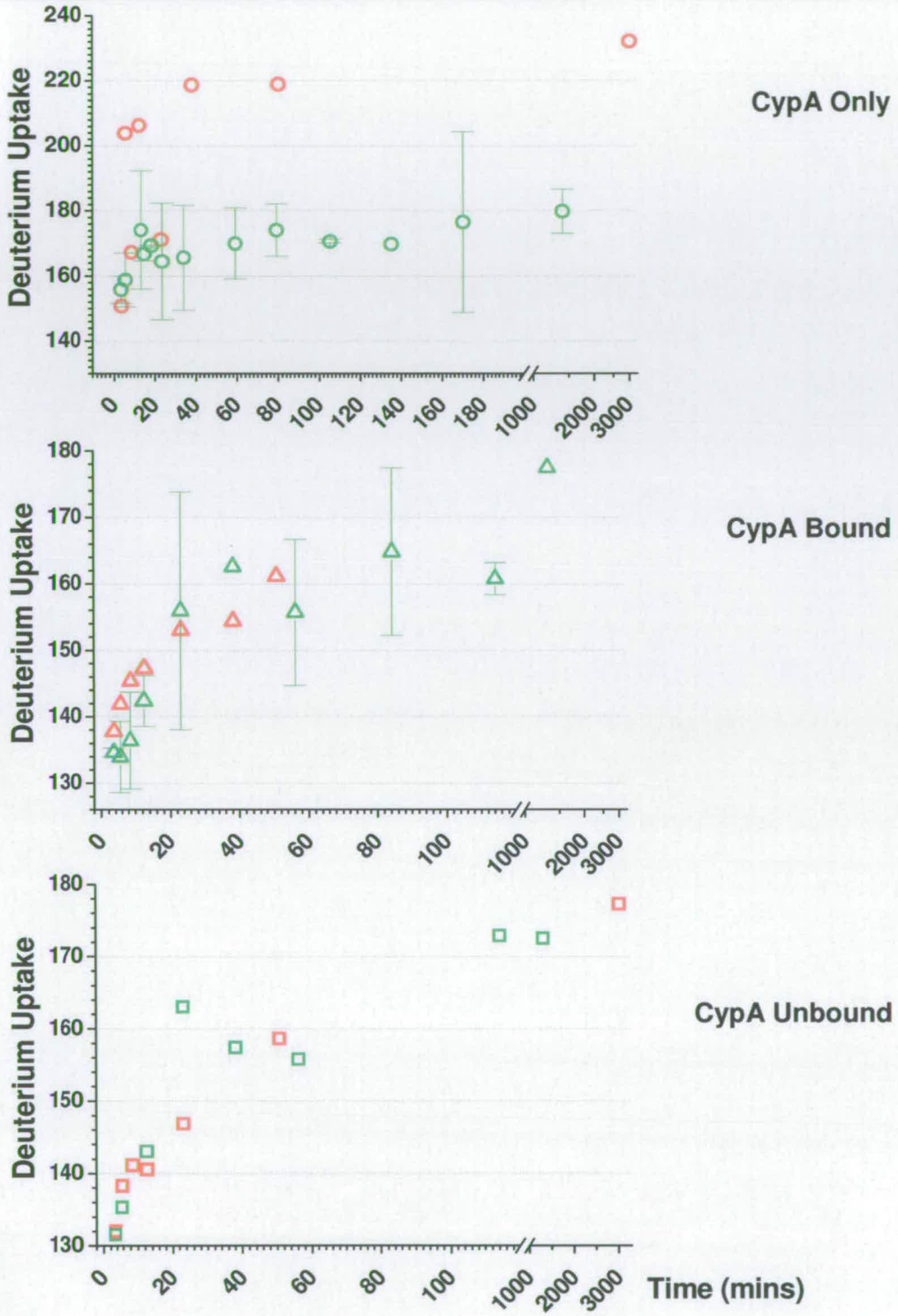

Figure 6-3 Deuterium uptake using deconvoluted data from solutions with *d*-water and 10mM *d*-ammonium acetate (— Water; — Peak A buffered)

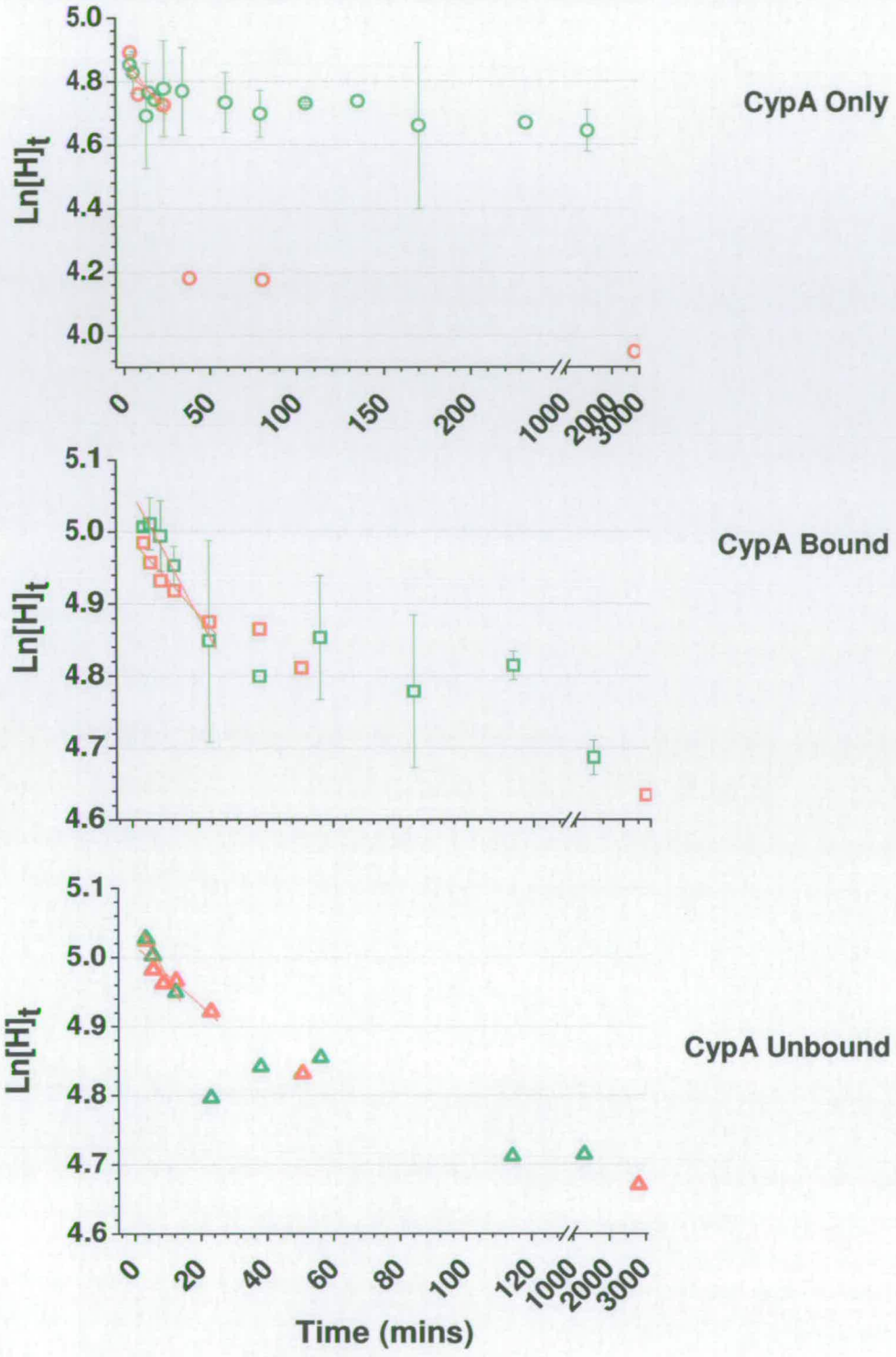

Figure 6-4 Exchange rates using deconvoluted data from solutions sprayed from *d*-water and 10mM *d*-ammonium acetate (— Water; — Peak A buffered)

Both *d*-water and *d*-buffer incubated complex exhibit similar extent of exchange levels of 153 and 156 deuteriums respectively. Equivalent exchange values are seen for unbound CypA in the presence of ligand. Either a) the unbound CypA is representative of protein released from complex by nozzle-skimmer dissociation or b) CypA exhibits solvent memory, indicating that the conformation of the observed unbound form is determined by a memory of having been complexed. The latter explanation supports the EX1 regime and spectra acquired represent a 'snap-shot' of the protein conformation in solution at any given time.

Despite the differences in rates and quantity of *d*-uptake, all protein species exhibit a logarithmic relationship with regards to deuterium incorporation up to 114 minutes (Figure 6-5).

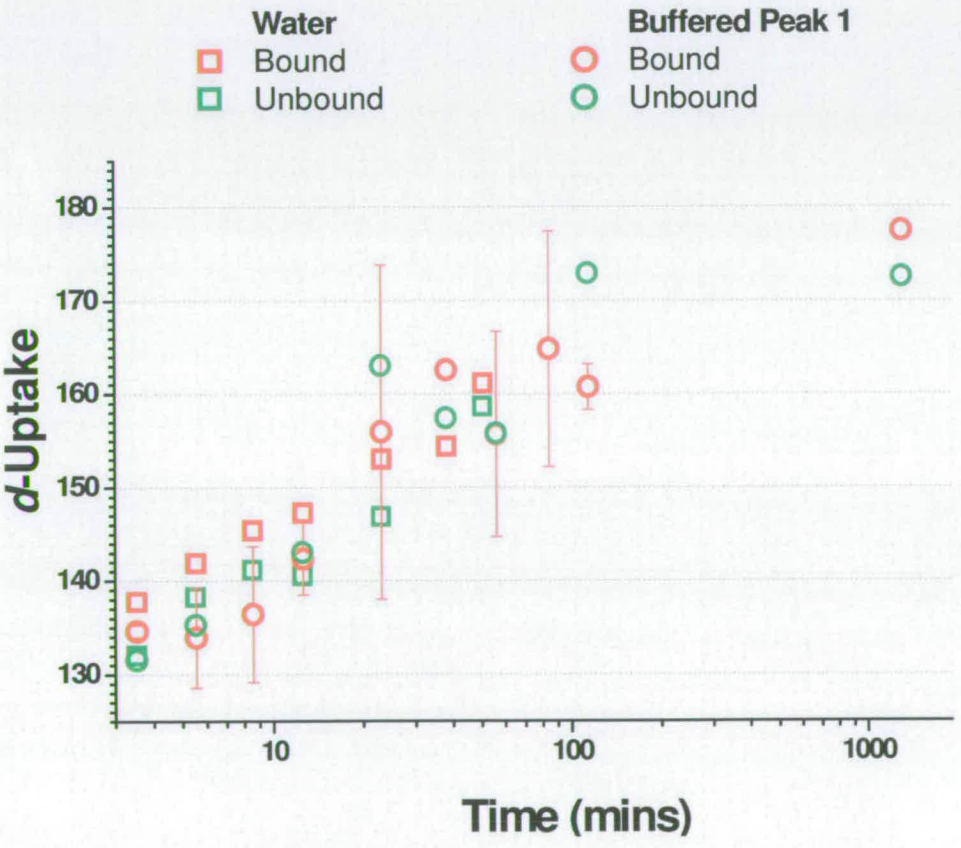

Figure 6-5 Deuterium uptake of CypA-CsA conformers exhibiting a logarithmic relationship of exchange up to 104 mins.

The broad experimental error negated the ability to use a comparison between bound and unbound CypA. To distinguish between deuteriums incorporated via CsA or CypA therefore, the following procedures could be utilised:

1) CID on the isolated complex - as performed on melittin in Chapter 4.
2) Peptic digests post H/D exchange. Smith *et al.*[1] developed a method in the early 1990s incorporating a peptic digest on exchanged complexes followed by rapid LC-MS analysis whereby *d*-uptake on each peptide could be calculated. Back exchange occurs however during the elution step and keeping the whole system below 4°C complicates the logistics of the procedure. Although MS interface software technology is improving all the time, assigning peptides which arise from digestion by the non-specific enzyme pepsin, is problematic, even with structural data, and this will be further complicated when the peptides are also deuterated or partially deuterated.

The data here demonstrates the potential of the method with regards to detecting global structural changes thus acting as an aid to understanding of the binding process of CsA. The presence of two peaks still raises issues with the integrity of the data and has thus prompted the use of reverse phase chromatography, i.e. the more sophisticated solution method, termed PLIMSTEX.

6.2.2 CsA Only

There are 5 labile hydrogens within CsA, four of which are in the amide backbone. The conformation of CsA in aqueous solution has never been studied due to its poor solubility. Studies have shown however the backbone conformation is totally rearranged on binding to CypA. The *cis* peptide bond between residues MeLeu-9 and MeLeu-10 in free CsA is converted to a *trans* peptide bond on binding CypA[18,19] (Figure 6-6). Its bound and unbound structures have been studied by Walkinshaw and co-workers[20] using crystal structures and by Wüthrich and co-workers[21] using NMR and these illustrate the change in hydrogen bonding leading to a change in configuration. Wenger and co-workers used synthetic analogues of CsA[22] and

molecular dynamics[23] to induce conformational changes in water prior to complexation with CypA to ascertain whether they were solvent or protein driven.

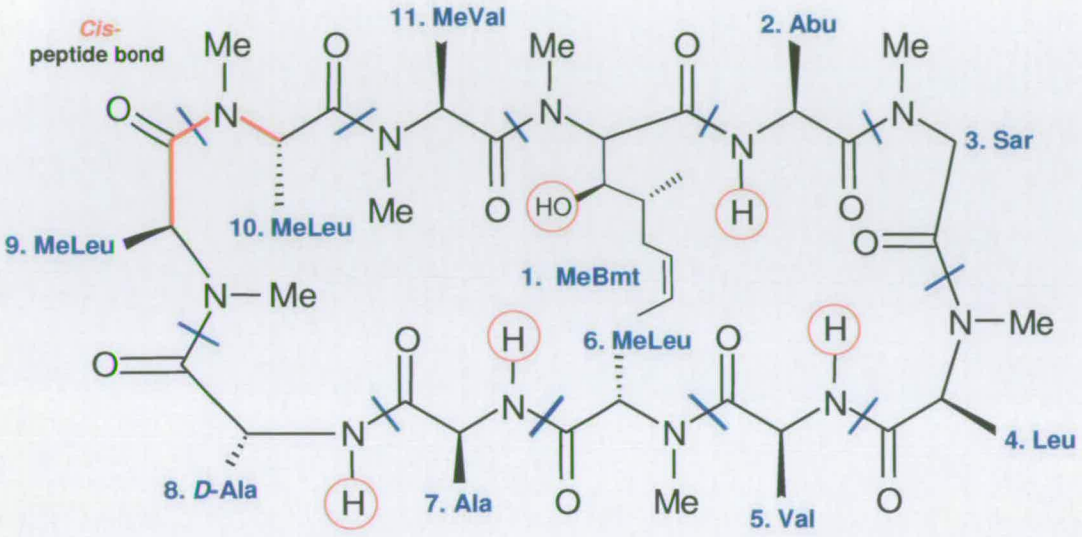

Figure 6-6 Simplified schematic of CsA with *cis* peptide bond and the labile hydrogens highlighted in red

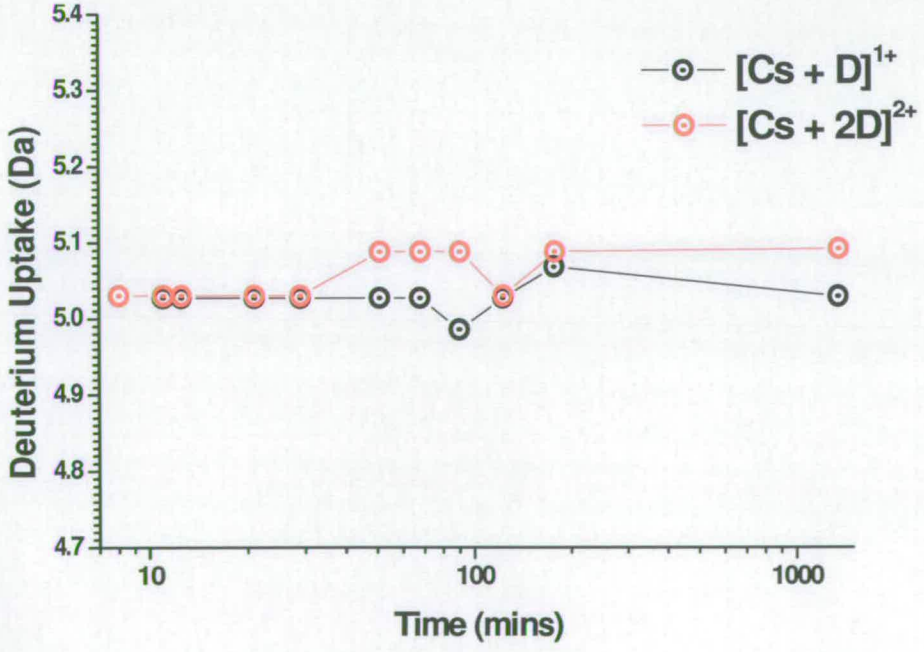

Figure 6-7 CsA H/D exchange over a 22.5 hour period

Deuterium uptake by CsA over 22.5 hours is plotted in Figure 6-7. Maximum exchange is achieved in less than 3 minutes. The calculated uptake of less than 0.15 mass units implies experimental error and the increase is regarded as insignificant. This result was identical to that found for unbound CsA incubated with CypA where ligand peaks were detected (data not shown).

Cyp-18-CsA MALDI-ToF-MS studies performed by Kipping and Shierhorn[15] calculated the amide backbone hydrogen exchange rate of uncomplexed CsA to be 30 min^{-1} at pD7.8 in ammonium carbonate. Once complexed with Cyp-18, the Abu-2 amide proton on CsA forms an intermolecular H-bond which exchanges at a much slower rate. This suppression of exchange resulting from the hydrogen could not be detected within the time frame of this experiment.

6.3 Solution Phase HDX Studies : Part 2 - PLIMSTEX

Section 6.2 demonstrates how HDX coupled with MS can provide global information on protein conformation in the presence of ligand and different buffering environments. PLIMSTEX (Chapter 1) can provide a simplified view with data reporting only on solvent accessibility of the amide hydrogens on the protein backbone. The protein is fully denatured and highly protonated by the time it reaches the mass spectrometer providing sharp well resolved peaks. This section discusses the optimisation of wash steps under native and denaturing conditions for the CypA-CsA system.

Direct infusion analysis of large proteins under native conditions however is not trivial. The approach described in Section 6.2 is subject to two major flaws:

1) A folded protein has fewer basic groups exposed and subject to protonation and this has a detrimental effect on ionisation efficiency. This problem is magnified when charging is produced by deuterium ions (D+) and therefore higher voltages and desolvation gas pressures may be required to initiate discharging of the droplet to form a Taylor cone. Salt ions (principally Na^+ and K^+), ubiquitous in most aqueous

solutions, often replace the protons on the analyte ion. This "charge-solvated" structure has a stabilising effect which can be further amplified by the presence of water to form salt-bridges.[24,25] This further complicates matters resulting in peak broadening and tailing rendering mass spectra difficult to interpret.

2) Labile hydrogens on amino acid side chains rapidly exchange from hydrogen to deuterium and vice versa. Unless specifically incorporated into secondary structure they can be extremely dynamic and will readily back-exchange. Resulting data often exhibits apparent variability in *d*-uptake increasing experimental error. This has been illustrated in the CypA direct infusion data presented in the previous section. However it does provide a useful starting point for identifying major conformational differences.

Coupling solution phase HDX to MS has great potential, and recently several methods have been developed which claim to be suitable for a wide range of proteins. Two of these have the similar attribute of providing protein for analysis in a denatured and highly charged state. SUPREX[26] as described in Chapter 1 and applied to CypA and CsA in Section 6.1 of this thesis is one such method. Early published SUPREX studies used MALDI-ToF, and this method tolerates the presence of some involatile salts however the use of a clean up LC step is preferable although this can induce non-specific back-exchange.

PLIMSTEX[27] (Chapter 1) is an alternative method, which has the benefit of eliminating involatile denaturants from the portion analysed by ESI. It also focuses on amide backbone exchange removing the problem regarding side-chain back-exchange. The potential benefits of this are realised in experiments on larger more complex proteins such as CypA.

6.3.1 'Native' and 'Non-native' Back-Exchange

In depth studies on CypA using PLIMSTEX are on-going and as such data presented here is limited to a discussion on the effect of on-column washing under native and denaturing conditions. A comparison of these two environments is discussed below.

The effect of side chain exchange is illustrated in Figure 6-8 after zero washing time and this represents the maximum exchange detectable using PLIMSTEX. The existence of conformers with side chains undergoing partial exchange during elution would be expected. It was expected these would be less distinct in adequately quenched and back exchanged examples. It is clear from this that the peak narrows and sharpens considerably after 2 mins 30 s of washing and as such the mass shift is considerably less than both 1 min and no washing. The development of the method and optimisation of washing times to ~90 seconds has been presented in Chapter 2.

Experiments involving native washing steps were performed using a 9.4T FT-ICR mass spectrometer (Bruker Daltonics). Peak widths of 3 *m/z* units for the 16+ charge state and approximately 40 Da for deconvoluted spectra were obtained. Experiments involving acid washing steps were performed using a low resolution LCQ ion trap (Thermo Corporation). Peak widths for the 16+ charge state and deconvoluted spectra were 7 *m/z* units and 115 Da respectively. The variability in peak widths obtained on different instruments suggests data cannot be compared. However, a study of peak shapes of CypA exchanged and washed under identical conditions were plotted with normalised intensities. The similarity in the shapes is strong and as such appears to comprise the same number of conformers (Figure 6-9).

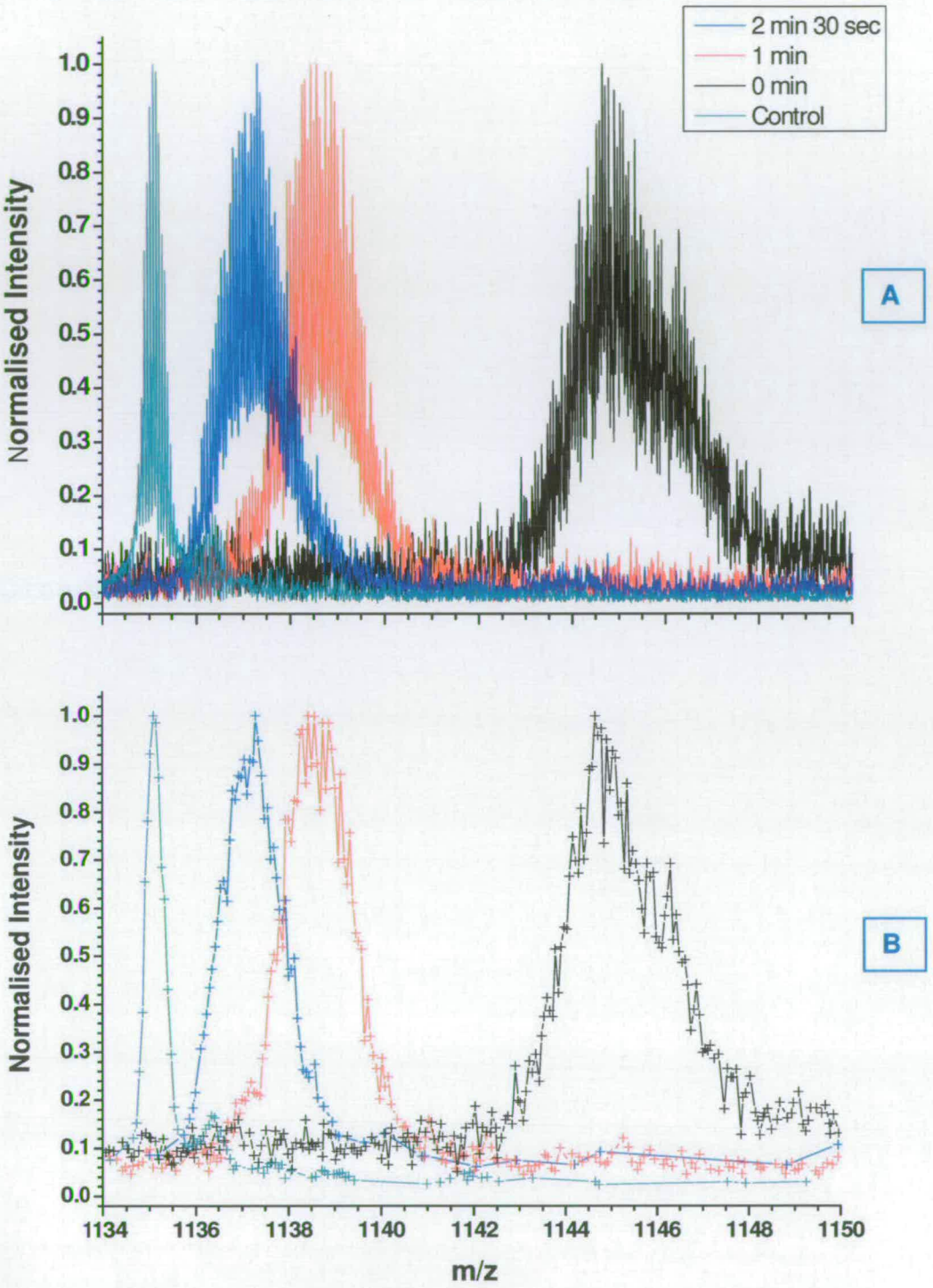

Figure 6-8 Isotopic distributions (A) of eluted peaks after various washing times are represented by distribution maxima (B) to outline peak shape.

A comparison of deconvoluted and individual charge state peak shapes is made. Figure 6-9 provides an example of $[CypA + 16H]^{16+}$ (16+) charge state peak compared to the deconvoluted peak derived from a charge state distribution comprising 10 *m/z* values. Peak shapes show strong similarities bearing a shoulder on the front end which confirm the assumption that uptake is independent of charge state under ideal PLIMSTEX conditions.

Experiments where back exchange is conducted under native conditions were attempted where the complexes were held on the column to protect both the binding domain, and the native fold from solvent exposure. Back exchange rates increase with pH but, keeping the protein in a 'less denatured' state could potentially provide more structural information. Exchange rates were reduced by a factor of 10 at 4°C.[28] Under native washing conditions approximately 40 amide hydrogens show resistance to back exchange between 1 and 3 minutes of washing. At low pH, this is increased to approximately 100 between 30 seconds and 2 minutes (see Chapter 2, Figure 2-11). Since the molecular ions obtained with a native wash (Figure 6-9A) shows a smaller mass increase to that obtained with a denaturing wash (Figure 6-9B), the protein appears to have undergone more back-exchange and therefore this variation to published PLIMSTEX conditions[29] is not successful. The quenching step (omitted in the experiments shown in Figure 6-9A) helps to prevent excessive back exchange and improve reproducibility (Chapter 2). The denaturing approach is proven by Gross and co-workers to be effective in studying complexes with regarding stoichiometry and binding affinities,[29] examples of which include insulin dimers; fatty acid carboxylates to intestinal fatty acid binding protein; porcine apo-calmodulin with Ca^{2+} and holo-calmodulin with melittin.

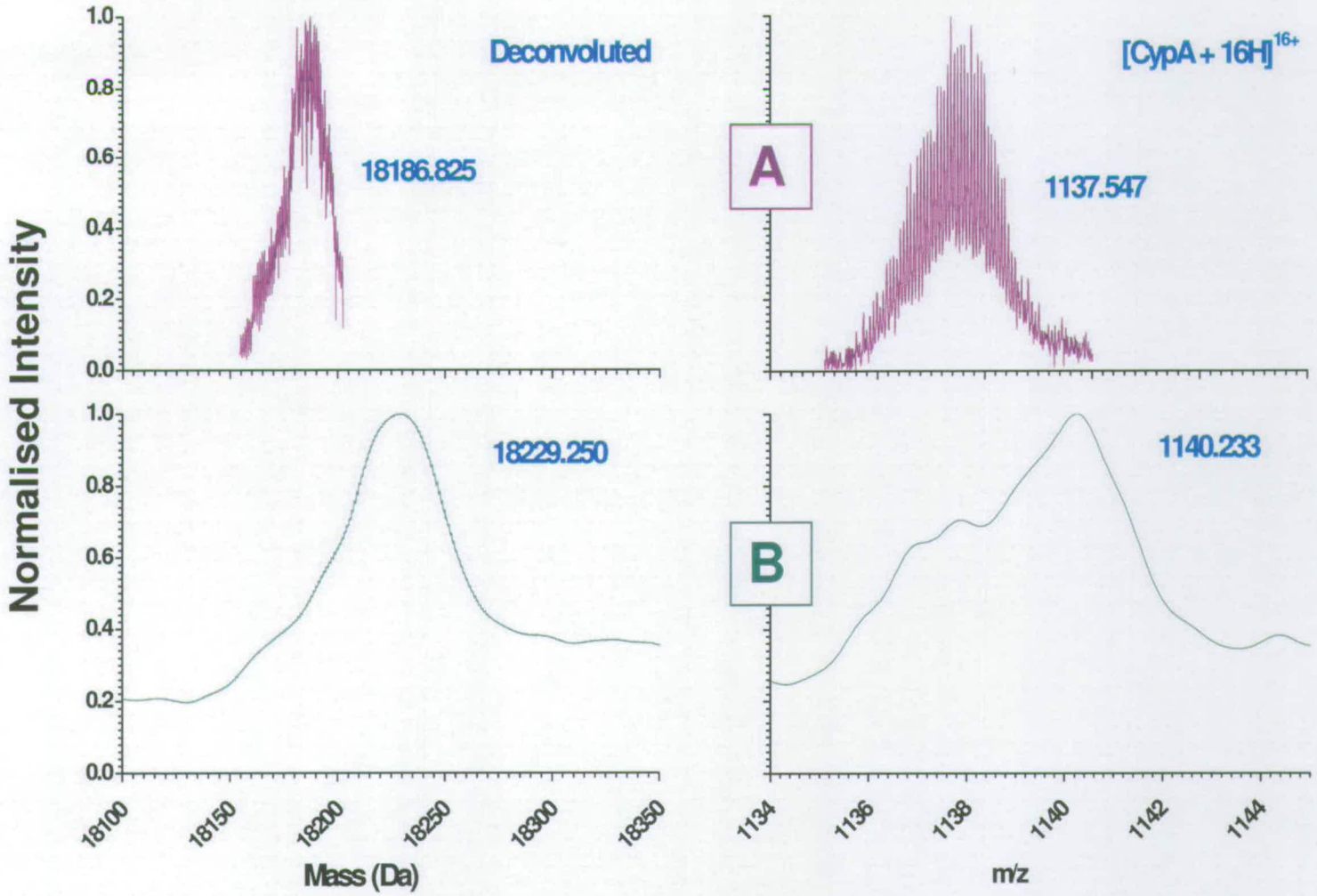

Figure 6-9 PLIMSTEX elution under (A) native FT-ICR-MS and (B) non-native LCQ ion trap back exchange conditions

6.3.2 *d*-Uptake and Peak Shapes of CypA and CypA-CsA

Direct infusion data has shown that there are no significant differences between overall deuterium incorporation into bound and unbound CypA when CsA is present in solution (Section 6.2). PLIMSTEX is employed here to corroborate this. Figure 6-10 illustrates the peaks shapes obtained for the 16+ charge state and deconvoluted spectra. The intensity has been normalised to enable a direct comparison although the relative abundance of CypA ions derived from a solution containing CsA was much lower. CsA has a high affinity for the column stationary phase and proved difficult to remove from the eluent. Consequently the following factors must be taken into consideration when drawing conclusions relating peak shape and width with regards to conformational diversity.

1) Free CsA may preferentially bind to the column inhibiting protein retention so much is lost to waste.
2) CsA preferentially ionises in comparison to CypA. This leads to an apparent reduction in protein intensity.
3) A lower intensity of protein results in fewer peaks which in turn leads to a narrower charge state distribution. Peak intensity also affects peak shape. The less intense peaks may be subject to a small amount of background interference and as such may not have such a defined shape.

The peak shapes of both the 16+ charge state and the deconvoluted spectra (Figure 6-10 A(i) and B(i) respectively and A(ii) and B(ii) respectively) are similar. However, the 16+ peaks for bound and unbound protein each have a shoulder on the leading edge which is not in the deconvoluted, and could be due to a low abundant conformer which does not exchange as much. This is counter intuitive as all the ions are exposed to identical washing and ionisation conditions and should therefore only differ in the number of protons they carry. However, because data considered at a charge state level suggests there are different conformers in solution it is possible that these, although denatured on the column, will give preference to a particular

charge state. These small differences are averaged out over the whole charge state distribution during deconvolution.

The bound and unbound peak widths are 3 Da for the 16+ peaks. There is a discrepancy between the deconvoluted data. Despite the overall deuterium incorporation being equivalent, the unbound protein spans 40 Da and the bound, 30 Da. It is assumed that this is proportional to the conformational differences between the two species, i.e. fewer conformers for the unbound form results in a narrower deconvoluted peak. This finding appears to contrast with that described earlier in this chapter for direct infusion experiments (Table 6-3) where no real difference is seen in the average amount of deuterium uptake between the bound and unbound forms. However this illustrates the benefit of isotopic resolution, since now the peak widths provide a useful insight to potential conformations.

XMass Interface Software for the FT-ICR-MS was used to calculate a theoretical isotopic distribution using the elemental formulæ of CypA and the CypA-CsA complex. The resulting spectra were calculated to have peak widths at half their height of approximately 0.5 Da. This value was used when employing Gaussian fitting to the $[CypA + 16H]^{16+}$ peaks. Figure 6-11 shows two 16+ charged peaks which have been fitted with 5 Gaussian peak distributions to compare the *d*-uptake across the whole isotopic distribution. A better fit is obtained for CypA only. Here the CypA peak shape is more defined and the signal is much more intense for the reasons explained above.

The two distributions situated at the extremities of the peak are small. Their integrity is suspect as these regions are variable and of low intensity. An estimate of 3 - 4 major species with different average exchange rates be estimated by eye taking into account the shoulders and curves present. These species could represent a larger number of transient conformers. A close fit was not achieved by fitting with 3 or 4 peaks so the number was increased to 5 implying these low abundant forms may play an important part in conformational diversity.

The overall *d*-uptake was calculated using the weighted means proportional to Gaussian peak intensity. Following incubation in buffer for approximately one hour and PLIMSTEX conditions described above, the average mass increase for CypA was 36.4 Da and for CypA-CsA 38.7 Da.

The maximum intensity of unbound CypA is spread across two Gaussian distributions creating a broad peak. The putative conformers spread across the peak exhibit a shoulder on the lower *m/z* region, tending towards a less solvent exposed structure. The bound CypA has a more defined central peak maximum with the most intense conformer playing a defining role in *d*-uptake. In the same vein, it also bares a shoulder on the right side of the peak. The resulting skew infers a more solvent exposed structure. It is also possible that side chains are still playing a role. Incomplete washing will lead to a mistaken belief that there are an apparent large number of conformers.

It is likely therefore from these data that the protein is subjected to further exchange during the ligand "off" period when the structure is less conformationally restrained. It is also important to reiterate that this data is revealing different exchange populations, which may be due to experimental conditions and / or reflect a number of distinct conformations in solution. Performing a CsA titration curve will establish a K_d value for the complex and will help to ascertain whether this increase is directly proportional to the ligand concentration. Direct infusion data implied binding the ligand resulted in slightly decreased solvent accessibility of the protein and this is corroborated here by the narrower peak shape.

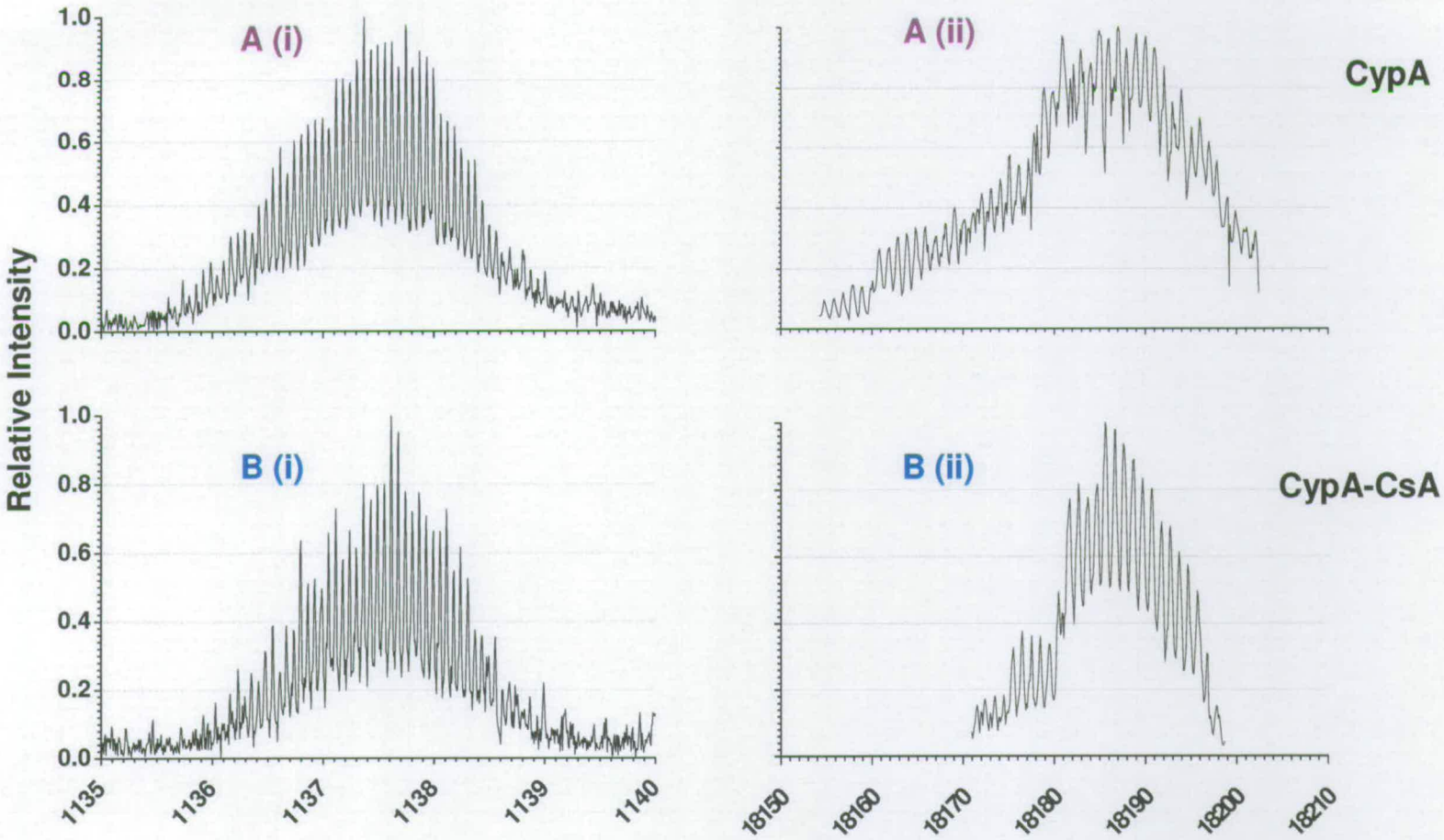

Figure 6-10 Comparison of peak shapes of CypA from solutions with (A) CypA only (i) $[CypA+16H]^{16+}$, (ii) deconvoluted and (B) CypA-CsA (i) $[CypA+16H]^{16+}$ and (ii) deconvoluted post native wash (1 min 30 s)

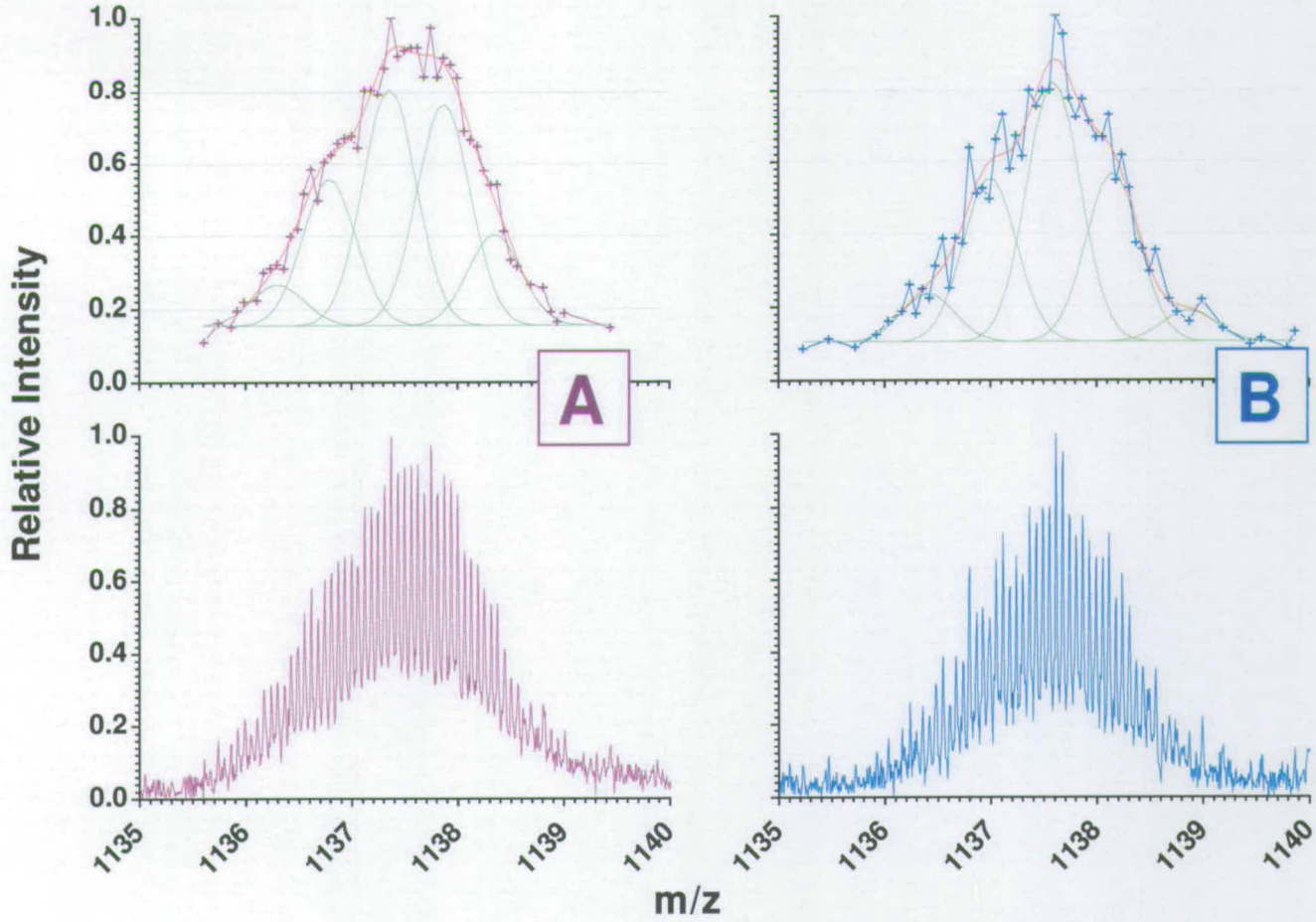

Figure 6-11 Comparison of Gaussian fitting of CypA from (A) protein only ($[CypA+16H]^{16+}$) and (B) protein-ligand solutions ($[CypA+CsA+16H]^{16+}$)

6.4 Gas Phase Exchange

The structure-activity relationship (SAR) of a protein is informed by its fold, which is dictated by the non-bonded interactions within the bio-structure. The strength and significance of each interaction to the fold is in turn affected by the solvent environment. Removal of solvent enables intrinsic and externally imposed interactions to be distinguished, a consequence of which helps to define the role the solvent itself plays on SAR.[30] These gas phase exchange studies are aimed at comparing *d*-uptake of CypA with CypA-CsA.

20 μM CypA and CypA-CsA in 10 mM ammonium acetate were analysed by nanoESI using the modified LCQ setup described in Chapter 2, and employed for melittin in the last chapter. The capillary temperature was maintained at 200°C, 125°C and 100°C and *d*-uptake compared accordingly.

Charge gain and loss was evident on analysis of CypA only solutions. Isolation of $[CypA+7H]^{7+}$ results in the detection of $[CypA+8H]^{8+}$ whereas conversely, isolation of the 8+ charge state results in detection of the 7+ charge state. Charge states 7+ and 8+ are always the most abundant ions when analysing CypA from 'native' buffering conditions. It is therefore assumed they are favoured in terms of stability. When the trap energy is increased (which occurs during isolation) charge stripping (electron loss) of $[CypA+7H]^{7+}$ or electron gain of $[CypA+8H]^{8+}$ results in an apparent 'switching' of charge. Two putative explanations for this are given below:

High energy electron stripping may occur during the ionisation process resulting in an increase in charge state.[31,32,33] Equation 6-1 illustrates what happens when analyte ion collides with a neutral (N) molecule such as He.

$$[CypA + 7H]^{7+\bullet} + N \longrightarrow [Cyp + 7H]^{8+} + N + e^-$$

Equation 6-1

Charge reduction in this context is attributed to electron capture where the reaction is slightly exothermic and therefore of lower energy than the stripping mechanism (Equation 6-2).[31] Breuker *et al.*[34] however demonstrated that excitation (in this instance caused by rf heating during isolation) of a multiply H-bonded ammonium group at a protonated lysine side chain, can result in an H• once the structure is cooled with the electron associating with the carbonyl group. With H-bonds being strengthened in a solvent free environment the resulting structure is thermally stable (Equation 6-3).

$$[Cyp + 8H]^{8+} + e^- \longrightarrow [Cyp + 8H]^{7+\bullet}$$

Equation 6-2

$$[Cyp + 8H]^{8+} \xrightarrow{H^\bullet} [Cyp + 8H]^{7+\bullet}$$

Equation 6-3

As previously discussed in Chapter 5, rf heating caused by the parent ion isolation process resulted in thermal unfolding of melittin. A similar effect was seen on isolation of CypA-CsA complex. Isolation of $[CypA+CsA+8H]^{8+}$ (8+ complex) resulted in detection of both the 8+ complex and $[CypA+7H]^{7+}$ (7+) protein. The relative intensities being at maximum 1:2; CypA-CsA : CypA only. Subsequent re-isolation steps failed to retain the CypA-CsA or CypA ions so all data analysed has been subjected to a maximum 10 second activation time.

6.4.1 Peak Shape with Time in the Gas Phase

Prolonging the presence of a solvent free environment may be detrimental to preserving the integrity of a solution stable structure. This is illustrated by Clemmer and co-workers[37,36] with experiments that trap ubiquitin for varying lengths of time prior to ion mobility analysis. A gas free environment with its dielectric of 1, can be

considered analogous to an apolar solvent, and may cause the exposure of hydrophobic amino acids. Since the interaction between CypA and CsA is strong and has an effect on the stability of the protein, and given that hydrophobic interactions are weakened and electrostatic forces strengthened in a solvent free environment, it can be anticipated that the stabilities of CypA only and CypA-CsA might be significantly different with respect to *d*-uptake. As a result the aim was to correlate *d*-uptake with peak shape.

Figure 6-12 depicts typical spectra for $[CypA+7H]^{7+}$ peaks (following isolation of $[CypA+8H]^{8+}$) acquired over an activation (trapping) time 10 - 100000 ms with a capillary temperature of 125°C. As trapping time is increased peak splitting becomes more evident so peak shape is defined by smoothing the distribution (red dotted line on 100000 ms spectrum). This is coupled with a decrease in ion intensity with time. All mass shifts are calculated using mid-points defined by full peak width of the distribution at half height.

The peaks broaden with increasing activation time and splitting becomes a factor after 5000 ms. Energy is lost from the ions causing them to fall outwith the instrument calibration, at which point they begin to collide with the buffer gas at different velocities causing them to alter their trajectories, stopping them from being ejected simultaneously. The resulting increase in size of the ion cloud leads to peak broadening. This hypothesis is supported when comparing with peak width of the control where non-*d*-methanol is in the trap. Non-*d*-CypA with a trapping time of 1000 ms bears a peak width marginally wider than its equivalent deuterated peak. Although this undoubtedly happens it does not explain the regularity of the splitting observed at the later times i.e. a series of peak approximately 3 Da apart. Therefore, peak shape is at least partially attributable to 'ion bunching' within the trap, rather than intermediates resulting from protein unfolding.

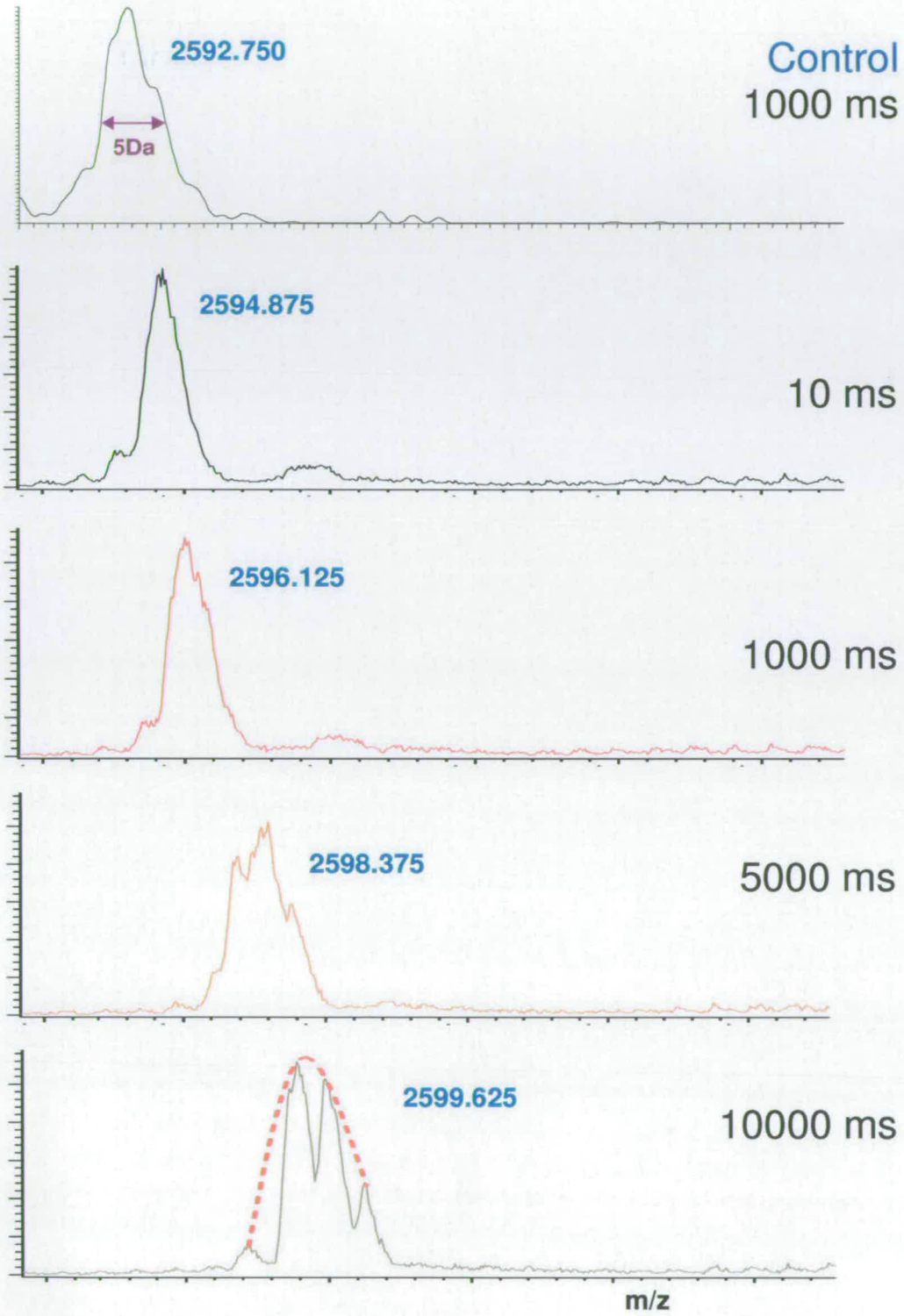

Figure 6-12 Changes in the $[CypA+7H]^{7+}$ peak shape with increasing activation time

Exposure of CypA to *d*-methanol in the ion trap at times greater than 10000 ms was desirable. Although as discussed above insights from peak shape are to be interpreted with caution, plotting *d*-uptake over a longer period was expected to elicit some information regarding analyte stability in the gas phase. To this end a software patch specifying an extended activation time command of 100 seconds was supplied by ThermoElectron. A graph of *d*-uptake with time (10 ms to 100 s) is plotted Figure 6-13 using CypA. The data here was obtained from the ion $[CypA+7H]^{7+}$ and has subsequently been 'deconvoluted' to give the mass increase for the neutral protein.

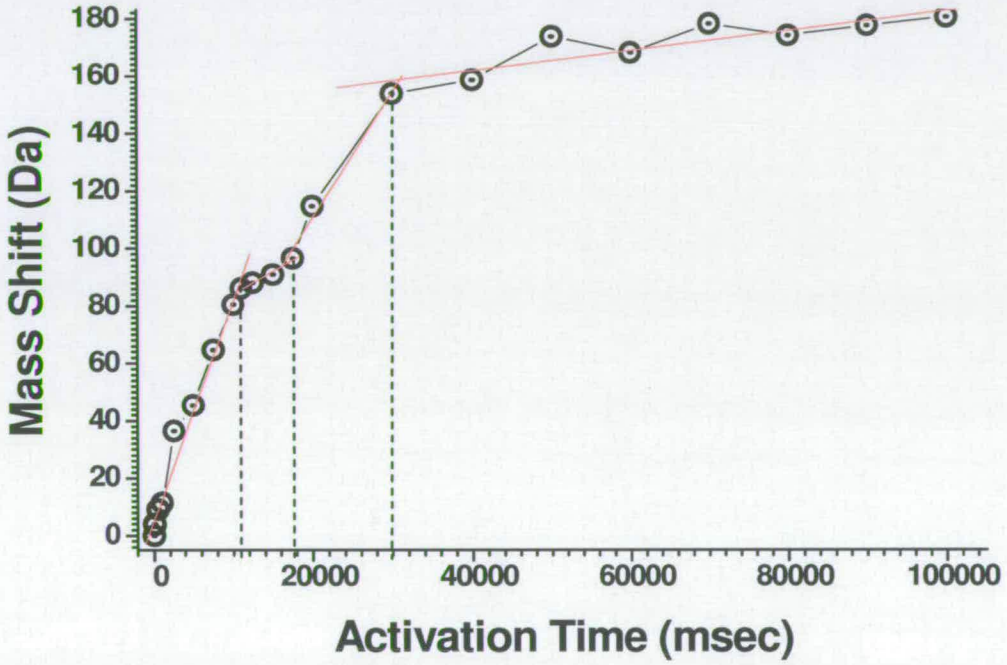

Figure 6-13 *d*-Uptake by CypA in the gas phase over 100000 ms activation time with capillary temperature, 100°C

The overall *d*-uptake over the first 11000 ms is linear and rapid after which, the uptake slows. A reduction in solvent exposure infers the presence of a stable intermediate with limited or no further unfolding over the following 6500 ms. The conformer is destabilised after 17500 ms and another stage of rapid exchange ensues, a result of what is interpreted as an unfolding event. After 30000 ms the exchange

starts to plateau. This event caused by a lack of exchangeable sites exposed to the bath gas, is not terminated as there continues to be a slight increase in *d*-uptake, reaching a maximum around 180 Da, a value equivalent to the maximum solution phase exchanges in *d*-ammonium acetate buffered CypA where CsA has been co-incubated, but less than that seen for CypA by itself. The most likely explanation being that the protein unfolds so far in the first 30 seconds and then undergoes hydrophilic collapse preventing further exchange. Any relay mechanism initiating exchange at this point will be considerably hindered or even arrested.

These conclusions are supported by studies on ubiquitin and cytochrome C by Clemmer and co-workers who compared conformers of equivalent charge states by ion mobility mass spectrometry (IMMS) (the gas phase equivalent of gel electrophoresis) and ions trapped for some number of seconds.[35,36] IMMS on its own determined that collisional cross sections of each protein at different charge states were related to the degree of unfolding. In these studies ions were trapped for specified amounts of time either with a double drift cell experiment[35] or with a Paul trap drift cell apparatus,[36,37] and the ensuing conformers separated by ion mobility. A folded structure may unfold but will ultimately migrate into a gas stable conformation. As the trapping time was increased, multiple unfolded intermediates were detected until a point came when they collapsed into a compact structure.[37] Both approaches were in agreement however that an analysis temperature of 300K did not exert any influence on the unfolding process. It was also ascertained that structures in both the mobility cell and trap do not reach equilibrium i.e. once unfolded in vacuum, the process does not reverse.

6.4.2 The effect of capillary temperature on exchange

Capillary temperature plays a critical role with respect to desolvation and ionisation. Temperatures as low as 60°C, whilst efficient enough for small proteins such as melittin do not provide efficient desolvation for CypA. Temperatures of approximately 100°C – 125°C improve the detection of both CypA and CypA-CsA.. An initial study monitoring the intensity of the complex peak as the capillary temperature dropped was performed (data not shown). The temperature had to be low

enough to retain complex integrity but high enough to maintain a steady beam of ions. It is also feasible that given optimal ionisation conditions, the binding interface is enhanced in a solvent free environment. Electrostatic interactions with the aromatic residues His-126 and Trp-121 are expected to strengthen in a solvent free environment.

Figure 6-14 shows the natural log of hydrogen depletion of CypA at 125°C and 200°C at the two dominant 'native' charge states +7 and +8. Results for gas phase experiments on melittin determined that capillary temperature did not play a significant role on deuterium exchange, the inference here is that melittin exhibited some denaturation during desolvation at temperatures as low as 60°C. CypA, being a larger more intricate protein required higher capillary temperatures during the ionisation process. 200°C resulted in greater *d*-uptake than the lower temperature of 125°C (Figure 6-14 and Table 6-4). This was attributed to partial unfolding on desolvation of CypA. The trap temperature is assumed to be kept close to ambient temperature[38] and so coupled with collisional cooling of ions entering the trap, the increase in exchange is unlikely to be caused by increased kinetics.

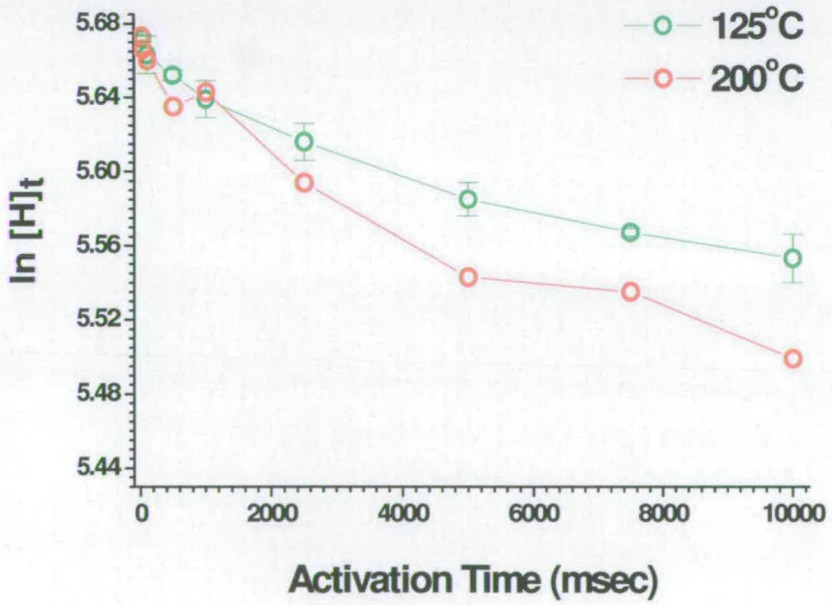

Figure 6-14 Hydrogen depletion of gas phase exchange on CypA $[Cyp+7H]^{7+}$ with capillary temperatures 125°C and 200°C

		d-Uptake (Da)	
	Capillary Temperature	**$[CypA+7H]^{7+}$**	**$[CypA+8H]^{8+}$**
CypA Only	**200ºC**	46.29 ± 16.6	55.54 ± 9.1
	125ºC	32.90 ± 3.4	42.74 ± 6.5
CypA Unbound	**125ºC**	25.18 ± 2.0	
CypA-CsA	**125ºC**		30.66 ± 2.9

Table 6-4 Mass shifts after 10 s activation time between the 7+ and 8+ charge states of CypA only, CypA Unbound (released from Complex) and CypA-CsA

Maximum exchange after 10 s activation times for ligand free solutions are listed in Table 6-4. The increase in uptake for CypA at capillary temperature 200°C is ~13 deuteriums greater than 125°C for both charge states. The overall uptake however is charge state dependent, $[Cyp+8H]^{8+}$ exchanging 9 to 10 deuteriums more than $[Cyp+7H]^{7+}$. This follows the same trend as melittin where the higher charge states exchange at a greater rate and extent, this being a result of the presence of an extra proton able to initiate exchange and a somewhat more unfolded structure. *d*-uptake is reduced when the protein is involved in the complex, inferring increased stability of the structure. Fewer labile hydrogens are exposed because either a) the presence of CsA is directly blocking them or b) a less mobile protein prevents the relay mechanism from probing the structure. This is discussed further in Section 6.4.3.

This result can be compared with a study performed by Freitas *et al.*[11] Here the native like charge states of ubiquitin (5+ to 8+) also exhibit an increase of deuteration as the charge state is increased – for the same reasons given above with CypA – more solvent accessibility and more exchange initiating protons. However at higher charge states this trend is reversed. The 13+ charge state of ubiquitin exhibits a lower exchange rate and total *d*-uptake than 12+. The conclusion drawn in this study was that increased charging results in unfolding of the ubiquitin and a reduced availability of donor – acceptor sites positioning themselves within 5Å of each other. However, in this work with far more native electrospray conditions for the protein,

both $[M+7H]^{7+}$ and $[M+8H]^{8+}$ are thought to be compact near native structures (evidenced by their retention of ligands, Chapter 3) and therefore the effect seen by Freitas at high charge states would not be expected.

Marzluff performed several HDX experiments in a Paul trap involving smaller proteins including melittin and insulin which have been discussed in the previous chapters.[39] In quadrupole ion traps, the global monitoring of *d*-uptake is limited by the short trapping times. As has been demonstrated in these studies, this causes structural rearrangement as a result of rf heating. As a consequence more extensive gas phase exchange protein folding studies by Kaltashov[8] and Freitas[11] have been performed using FT-ICR-mass spectrometers as they essentially have unlimited ion trapping times. Future studies might consider this with the CypA-CsA system.

6.4.3 The Affect of Releasing CypA from CypA-CsA on *d*-Uptake

d-Uptake by CypA in the solution phase is reduced when CsA is present. This result is reiterated in the following gas phase exchange experiments and supports the work of Shi *et al.*[6] described in section 6.2.2 which confirms the presence of CsA forming an H-bond with CypA where exchange is considerably slowed.

Rates of hydrogen depletion are plotted in Figure 6-15. Isolation of the complex results in partial dissociation which releases CypA with charge state 7+. It is plausible that in the absence of external factors (solvent buffer ions *etc.*) this species may retain a memory of its complexed state. Maximum uptakes of deuterium listed in Section 6.4.2, Figure 6-4 state *d*-uptake of unbound product CypA 7+ is nearly 8 deuteriums less than for ligand free CypA 7+. This implies the structure either a) collapses in on itself in the solvent free environment when the CsA is released or, b) the complex structure is more constrained when bound to the ligand and this conformation is retained on release of the CsA i.e. the protein exhibits solvent memory. This effect is more pronounced with $[Cyp+Cs+8H]^{8+}$ where complex is retained during isolation and exchanges ~12 fewer deuteriums than ligand free CypA

8+. This suggests that binding CsA provides a more stable or less conformationally dynamic structure.

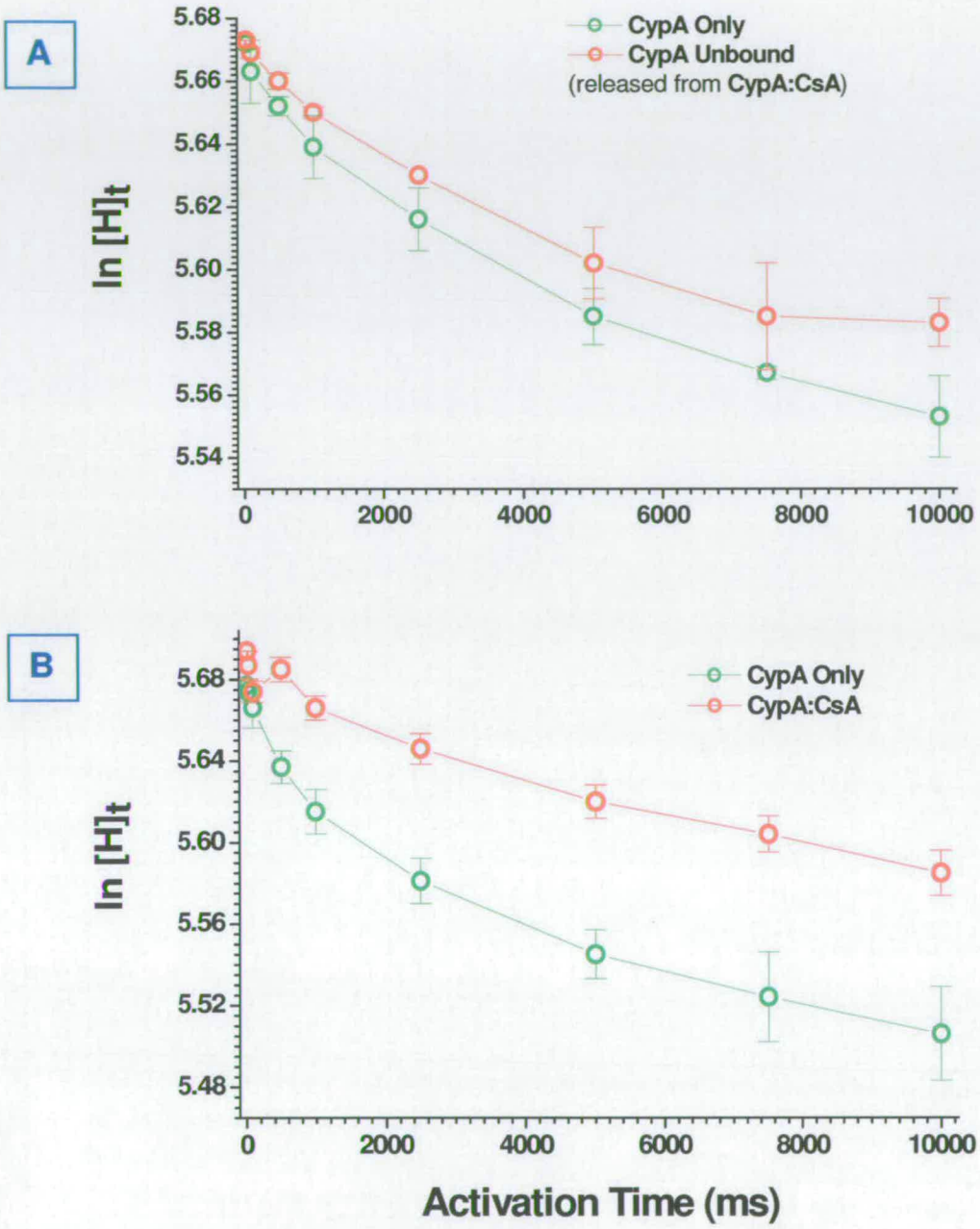

Figure 6-15 Hydrogen depletion on (A) $[Cyp+7H]^{7+}$ comparing CypA only, CypA released from CypA-CsA and (B) $[Cyp+8H]^{8+}$ comparing CypA only and the complex with a capillary temperature of 125°C

Retaining ions in the trap for prolonged periods of time results in a gradual increase in mass. This may be accompanied by unfolding of the structure leading to a more solvent exposed protein. Preliminary data here indicates the presence of one stable intermediate formed around 15000 ms. After the formation of this intermediate *d*-uptake slows dramatically for 6000 ms.

The maximum *d*-uptake achieved by CypA in the gas phase after 100 seconds was ~180 deuteriums. This is in agreement with the results obtained with *d*-ammonium acetate buffered CypA in solution and with CypA co-incubated with CsA.

6.5 Conclusions

This Chapter has compared the use of HDX methods both in solution and in the gas phase on the protein CypA. A number of findings have been presented:

1. Direct infusion

   Ammonium acetate has a stabilising affect on CypA and CypA-CsA when compared to water, as revealed by less H/D exchange. The presence of CsA also exerts a stabilising influence, exchange is also reduced when ligand is present.

2. PLIMSTEX

   Washing the protein using native buffer does not protect the binding domain from excess back exchange. CsA caused problems with data interpretation by being preferentially ionised compared to the protein thus quenching its signal.

3. FT-ICR

   A comparison of isotope fitting to peak shapes with LCQ obtained data on CypA and CypA-CsA using PLIMSTEX suggests a slight increase in *d*-uptake when CsA is present. Peaks shapes were shown to be reproducible between mass spectral systems supporting this data. This infers the ligand has a destabilising rather than stabilising effect on the protein.

4. Gas Phase HDX

Gas phase studies of CypA are charge state dependent even though both $[Cyp+7H]^{7+}$ and $[Cyp+8H]^{8+}$ represent a narrow native like charge state distribution, both retaining the CsA ligand. Exchange can be directly compared to that observed in DI-ESI HDX experiments. Exchange of CypA is much greater than that of the complex. Protein generated as a result of dissociation caused by rf heating during isolation exhibited some solvent memory as shown by exchange being lower than protein from a ligand free solution.

.

PLIMSTEX has so far proven unsuitable for studying CypA and its complex with CsA. Some success was achieved with DI-ESI despite the possible contamination. Findings using DI-ESI agree with gas phase studies which are shown to be reproducible and representative of the solution phase.

6.6 References

[1] Smith DL., Deng Y-Z. and Zhang Z-Q., *Journal Of Mass Spectrometry*, 1997, **32**, 135-146
[2] Jennings KR., *Int. J. Mass Spectrom.*, 2000, **200**, 479-493
[3] Zhai H., Han X., Breujer K. and McLafferty FW., *Anal. Chem.*, 2005, **77**, 5777-5784
[4] Zubarev RA., Kelleher NL. and McLafferty FW., *J. Am. Chem. Soc.*, 1998, **120**, 3265-3266
[5] Truhlar SME., Croy CH., Torpey, Koeppe JR. and Komives EA., *J Am Soc Mass Spectrom.*, 2006, **17**, 1490-1497
[6] Shi Y-H., Lin D-H., Huang J-Y. and Shen X., *Chin. J. Chem.*, 2006, **24**, 973-979
[7] Zhu MM., Rempel DL., Du Z. and Gross M., *J. Am. Chem. Soc.*, 2003, **125**, 5252-5253
[8] Kaltashov IA. and Eyles SJ., *J. Mass Spectrom.*, 2002, **37**, 557-565
[9] Eyles SJ., Dresch T., Gierasch LM. and Kaltashov IA., *J. Mass Spectrom.*, 1999, **34**, 1289-1295
[10] Suckau D., Shi Y., Beu SC., Senko MW., Quinn JP., Wampler FM. and McLafferty FW., *Proc. Natl. Acad. Sci.* 1993, **90**, 790-793
[11] Freitas MA., Hendrickson CL., Emmett MR. and Marshall AG., *Int. J. Mass Spectrom.*, 1999, **185-187**, 565-575
[12] Badman ER., Hoaglund-Hyzer CS. and Clemmer DE., *J Am Soc Mass Spectrom.*, 2002, **13**, 719-723
[13] Campbell S., Rodgers MT., Marzluff EM. and Beauchamp JL., *J Am Chem Soc.*, 1995, **117**, 12840-12854
[14] Wang MZ., Shetty JT., Howard BA., Campa MJ., Patz EF. and Fitzgerald MC., *Anal. Chem.*, 2004, **76**, 4343-4348
[15] Kipping M. and Shierhorn A., *J. Mass Spectrom.*, 2003, **38**, 271-276
[16] Bai Y., Milne JS., Mayne LC. and Englander SW., *Prot Struct Funct Gen* 1993, **17**, 75–86
[17] Wear MA. and Walkinshaw MD., *Anal. Biochem.* 2006, **359**, 285-287
[18] Altshuh D., Vix O., Rees B. and Thierry J-C., *Science*, 1992, **26**, 91-93
[19] Kofron JL., Kuzmic P., Kishmore V., Gemmecker G., Fesik SW. and Rich DH., *J. Am. Chem. Soc.*, 1992, **114**, 2670-2675
[20] Pflugl G. and Walkinshaw M., *Nature*, 1993, **361**, 91

[21] Weber C., Wider G., von Freyberg B., Traber R., Braun W., Widmer H. and Wüthrich K., *Biochemistry*, 1991, **30**, 6563-6574
[22] Wenger RM., France J., Bovermann G., Walliser L., Widmer A. and Widmer H., *FEBS Letts*, 1994, **340**, 255-259
[23] Lautz J., Kessler H., van Gunsteren, WF., Weber HP. and Wenger RM., *Biopolymes*, 1989, **29**, 1669-1687
[24] Lemhoff AS., Bush MF. and Williams ER., *J. Am. Chem., Soc.*, 2003, **125**, 13576-13584
[25] Bush MF., Forbes MW., Jocknusch RA., Oomens J., Polfer NC., Saykally RJ. and Williams ER., *J. Phys. Chem. A*, 2007, **111**, 7753-7760
[26] Powell, K.D. and Fitzgerald, M.C., *J. Comb. Chem.*, 2004, **6**, 262-269
[27] Zhu MM., Rempel DL., Du Z. and Gross M., *J. Am. Chem. Soc.*, 2003, **125**, 5252-5253
[28] http://www.HXMS.com HDX website written and maintained by Engen JR.
[29] Zhu MM., Chitta R. and Gross ML., *Int. J. Mass Spectrom.*, 2005, **240**, 213-220
[30] Kaltasov IA. and Eyles SJ., *Mass Spectrometry in Biophysics*, Wiley, 2005, Chapter 10
[31] He M. and McLuckey SA., *J. Mass Spectrom.*, 2004, **39**, 1231-1259
[32] Nielsen ML., Budnik BA., Haselmann KF. and Zubarev RA., *Int. J. Mass Spectrom.*, 2003, **226**, 181-187
[33] Danell AS. and Glish GL., *J. Mass Spectrom.*, 2001, **212**, 219-227
[34] Breuker K., Oh H-B., Lin C., Carpenter BK. and McLafferty FW., *Proc. Natl. Acad. Sci.*, 2004, **101**, 14011-14016
[35] Koeniger SL., Merenbloom SI. and Clemmer DE., *J Phys Chem B*, 2006, **110**, 7017-7021
[36] Badman ER., Myung S. and Clemmer DE., *J Am Soc Mass Specrom*, 2004, **16**, 1493-1497
[37] Myung S., Badman ER., Lee Y-J. and Clemmer DE., *J Phys Chem B*, 2002, **106**, 9976-9982
[38] Gronert S., *J Am Soc Mass Spectrom.*, 1998, **9**, 845-848
[39] Evans SE., Lueck N. and Marzluff EM., *Int. J. Mass Spectrom.*, 2003, **222**, 175-187

Appendices A-E

Appendix A – Exchangeable Hydrogens

Residue	Exchangeable H's	Residue	Exchangeable H's
Pro	0	Cys	2
Gly	1	Asp	2
Ala	1	Glu	2
Val	1	His	2
Leu	1	Tyr	2
Ile	1	Trp	2
Met	1	Asn	3
Phe	1	Lys	3
Ser	2	Gln	3
Thr	2	Arg	5

Table showing maximum number of exchangeable hydrogen atoms on each neutral residue

Appendix B – Melittin Structural Publications

Publication	Technique	M/T*	Structure
Anderegg RJ., Wagner DS., Stevenson CL. and Borchardt RT., J. Am. Soc. Mass Spectrom. 1994, 5, 425-433	HDX-MS	M	3 proton populations. CID shows α-helix not on first 4 amide bonds. N-terminal helix, less stable than C-terminal
Dempsey CE, Biochemistry, 1988, 27, 6893-6901	NMR	M	pH dependent HDX in methanol; N-terminus more stable than C-terminus
Evans SE., Lueck N., Marzluff EM., Int J Mass Spectrom.,2003., 222, 175-187	Gas Phase HDX-MS	M	Monomer
Gerig JT., Biophys. J. 2004, 86, 3166-3175	NOE and fluorinated R-OH	M	Helical at each end
Iwadate M., Asakura T., Williamson MP., Eur J Biochem., 1998, 257, 479-487	Temperature dependent NOE	M	Monomer structures very similar to a dimer of dimers by crystallography
Kaltashov IA., Feneslau C., Prot. Struct. Funct. Gen., 1997, 27, 165-170	MIKE	M	α-helical stability enhanced in gas phase
Lam Y.-H., Wassell S.R., Morton C. J., Smith R. and Separovic F., Biophys J., 2001, 81, 2752-2761	Solid State NMR in lipid membranes	M	α-helix at N terminus irrespective of environment. Completion of helix in lipid and lipid-like environment
Zhu MM., Chitta R., Gross ML., Int J Mass Spectrom., 2005., 240., 213-220	PLIMSTEX	M	CaM:Melittin complex stoichiometry, 1:1
Bachar M. and Becker OM., Biophys. J., 2000, 78, 1359-1375	Molecular Dynamics	ML	Monomer orientates itself on lipid bilayer with highly protonated N-terminus. C terminus anchors to surface of membrane
Naito A., Nagao T., Norisada K., Mizuno T., Tuzi S. and Saito H., Biophys. J., 2000, 78, 2405-2417	NMR with magnetically orientated lipid bound melittin	ML	Perpendicular helix monomer through lipid bilayer

Hirota N., Mizuno K. and Goto Y., J. Mol. Biol, 1998, 275, 365-378	CD, modelling	T	R-OH different effectiveness (TFE and HFIP less effective), formation of micelle-like structures – tetramer in more water soluble alkanols
Pandit A., Larson OFA., van Stokkum IHM., van Grondelle R., Kraayenhof R., van Amerongen H., J Phys Chem B., 2003, 107, 3086-3090	Ultra-fast polarised fluorescence	T	Helix forms first, then associates into tetramer. Buffers: dist. Water; 10mM Hepes/10mM NaCl; 100mM Hepes/2M NaCl;
Terwilliger TC. and Eisenberg D, J. Biol. Chem., 1982, 257, 6010-6015	X-ray crystallography	T	Tetramer in high salt
Wang F. and Polavarapu PL., Biopolymers (Biospectroscopy), 2003, 70, 614-619	Vibrational CD and IR	T	Conformational change: Low pH ; KCl; TFE = mixed structure. pH 11; 0.06-0.6M KCl; 25% TFE = α-helix
Pawlak M., Meseth U., Dhanapal B., Muter M. and Vogel H., Protein Science, 1994, 3, 1788-1805	Fluorescence, CD,	Ti	Template assembled melittin tetramer. α-helix induced by R-OH; aggregation in 100mM NaCl and increasing [protein]
Takei J., Remenyi A., Clarke AR. and Dempsey CE., Biochemistry, 1998, 37, 5699-5708	NMR, CD, Fluorescence	Ti	Self associating synthetic dimers. Monomer at pH 1.7; 3.0; 7.0 at 18μM in phosphate buffer, divalent anions present

* M = monomer detected; ML = Monomer within lipid bilayer; T = tetramer; Ti = Tetramer induced using synthetic linkages

NB. Naturally occurring dimer has never been detected.

Appendix C – Q-ToF Ultima Parameters

Parameter	Setting*	Parameter	Setting
Capillary (kV)	~1.6	Transport	5.0 (-5.8)
Cone (V)	50 (59)	Aperture 2	40 (-4.2)
Extraction Cone	1.2	Acceleration V	200 (-198)
RF Lens	1.0	Focus	8 (-9)
Source	65 (65)	Tube Lens	55 (-55)
LM/HM Resolution	10	Offset 1	-0.6 (-52.8)
Collision (V)	5.0 (7.0)	Offset 2	0.0 (-53.4)
Ion Energy	2.0	Pusher	980 (919)
Steering	0.1 (-7.95)	TOF (kV)	9.1 (-9.18)
Entrance	53 (-50.6)	Reflectron	34.87 (2.08)
Prefilter	5.0 (-0.6)		
Multiplier	670		
MCP	2316 (2312)		

*Values in brackets denoted typical read back values

Appendix D - Competitive Binding

The synthetic ligands used here aggregate to form clusters (discussed in Chapter 3, Section 3.2.2.2). If it is assumed that these compete for the CypA binding pocket then it is comparable with that of competitive binding by a second ligand. The preferential binding of one ligand over another depends on their relative affinities, relative concentrations and whether, in the case of different ligands, they bind at the same site i.e. direct competition (Equation 1).

$$[P] = \frac{[P \cdot L_1]K_d^{L1}}{[L_1]} = \frac{[P \cdot L_2]K_d^{L2}}{[L_2]} \Longrightarrow \frac{[P \cdot L_1]}{[P \cdot L_2]} = \frac{K_d^{L1}}{K_d^{L2}} \frac{[L_2]}{[L_1]}$$

Equation 1

It follows that if the ligands are present in equal concentrations but with significantly different K_d values, the ligand with the lowest K_d will be bound to the greater extent. But, if they bind at different sites, are in excess of the protein and have maximum occupancy, then the difference in affinity becomes immaterial.

To artificially raise the binding affinity of the weaker ligand, simply increasing the concentration will have the desired effect. Therefore, binding affinities should always be calculated with respect to relative concentration.

Calculating dissociation constants using mass spectrometry relies on relating peak intensities to concentration (Equations 2). The amount of unbound ligand is derived by subtracting bound ligand from the initial concentration incubated. This method assumes there is no preferential ionisation and no significant association / dissociation of non-covalent complexes during desolvation.

$\mathbf{P_{TOT}}$ = unbound and bound **Protein** intensities
P = unbound **Protein** peak intensity
PL = bound **Protein:Ligand** peak intensities (competitive use PL_1, PL_2 etc)

[P] = $P / P_{TOT} \times [P_{init}]$
[PL] = $PL / P_{TOT} \times [P_{init}]$

Non Competitive:

[L] = $[L_{init}] - [PL]$
$\mathbf{K_d} = [P][L] / [PL]$
$\mathbf{K_d} = [P] ([L_{init}] - [PL]) / [PL]$

Competitive: if $[P] = [L_1] = [L_2]$

$\mathbf{[L1_{unbound}]} = [P] + [PL_2]$
$\mathbf{K_{d1}} = [P] ([P] + [PL_2]) / [PL_1]$
$\mathbf{K_{d2}} = [P] ([P] + [PL_1]) / [PL_2]$

Equations 2

Appendix E – K_ds for all CypA-Ligand Complexes

ZMD MANUAL

LIGAND		CONC^N (μM)	K_d (μM)		n
			Transformed	σ	
KB17/4	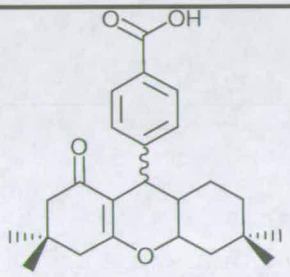	100	117.24		1
KB17/7	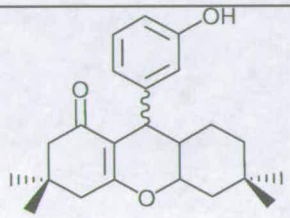	100	354.81	14.53	2
KB22/5	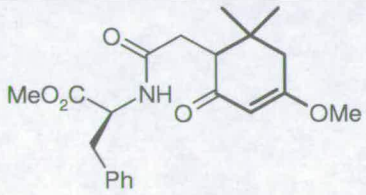	100	51.42	21.57	2
KB22.6	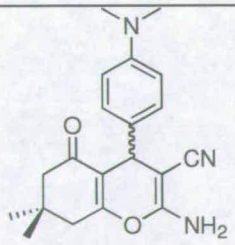	100	368.61		1
KB22/8	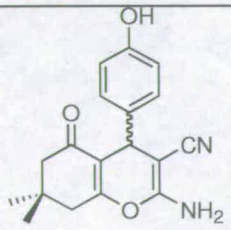	100	186.51	190.81	2

Appendix E – K_ds for all CypA-Ligand Complexes

ZMD MANUAL

LIGAND		CONC^N (μM)	K_d (μM)		n
			Transformed	σ	
KB17/4	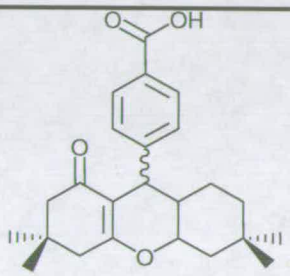	100	117.24		1
KB17/7	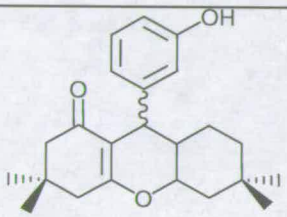	100	354.81	14.53	2
KB22/5	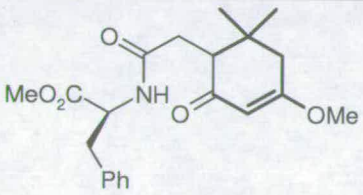	100	51.42	21.57	2
KB22.6	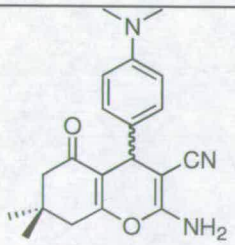	100	368.61		1
KB22/8	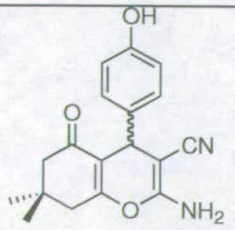	100	186.51	190.81	2

KB69/12	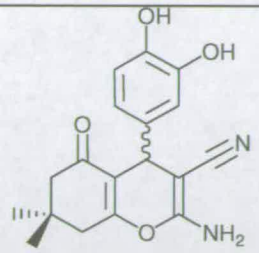	100	33.247	10.96	3
KB69/15	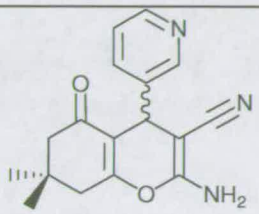	100	691.05		1
KB69/19	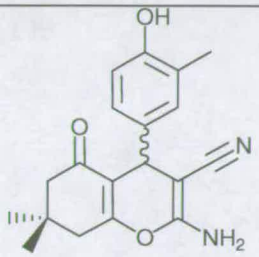	100	239.44		1
KB69/3	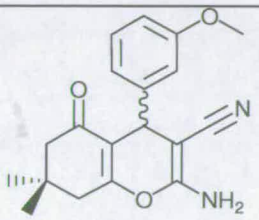	100	67.81		1
KB69/5	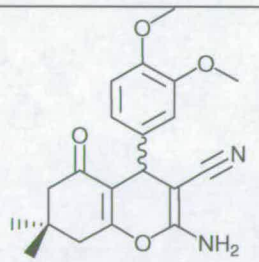	100	176.61	50.00	2
KB69/8	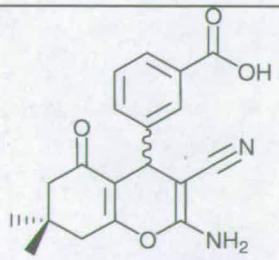	100	24.00		1
KM184	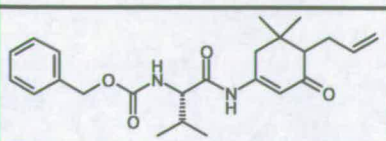	20 40 100 200	68.67 290.53 442.52 394.15	22.57 379.01 274.40	5 1 6 4

KM19	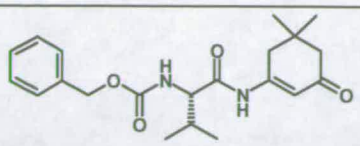	20 40 100 150 200	32.90 79.31 150.03 170.90 581.01	12.91 21.62 84.03 127.40	2 4 5 4 1
KM198	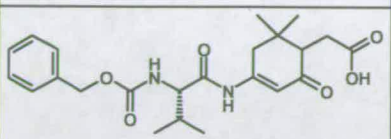	100	137.13		1
KM249/02	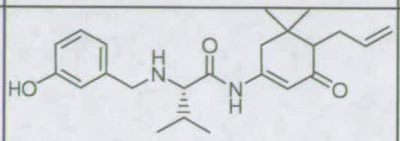	100	690.42	211.02	6
KM257	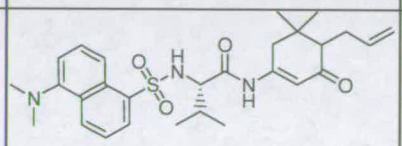	100	552.92	103.48	3
KM5	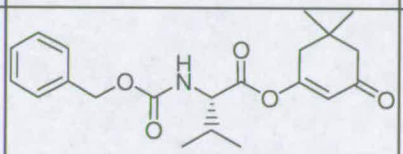	100	260.31		1
CD250/03	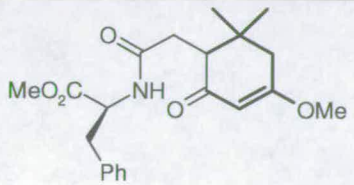	40	64.18		1
CD259/02	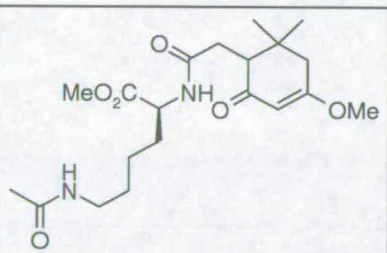	100	376.87		1
CD261/02	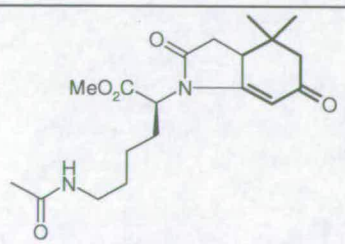	20 100	22.93 85.12		1 1

CD272/02	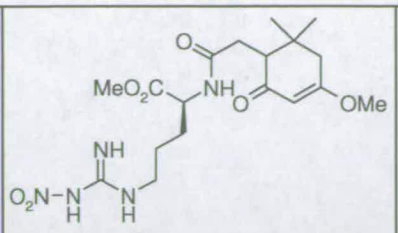	20 100	48.85 61.55		1 1
CD274/02	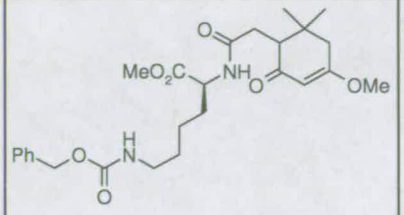	100	247.65		1
CD278/02	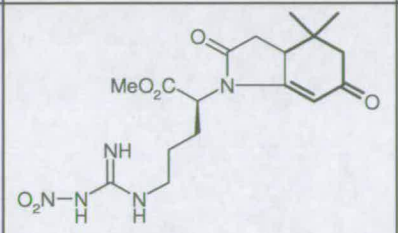	20 100	115.64 33.10	158.37 6.92	2 4
CD290/02	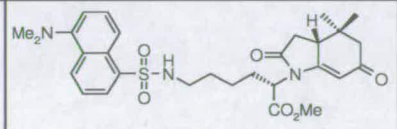	20 100	218.88 227.05	139.92	1 2
CD354/02	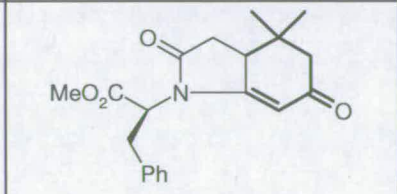	100	1012.37		1
CD357/03	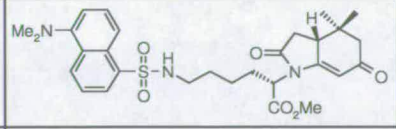	100	316.11	15.66	3
CD358/02	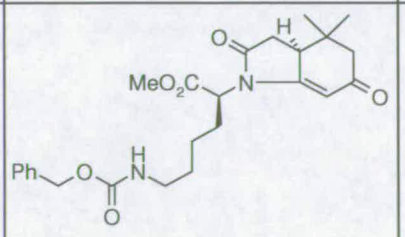	100	344.27		1

CD359/02	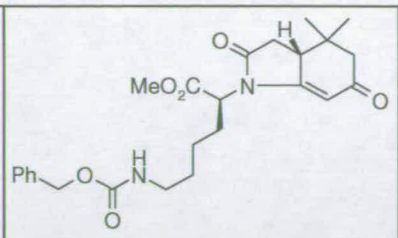	100	333.81	161.69	4
CD361/02	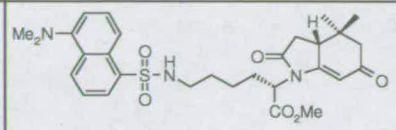	100	289.87	64.61	6

LIGAND		CONC^N (µM)	K_d (µM)		n
			Transformed	σ	
KB17/4	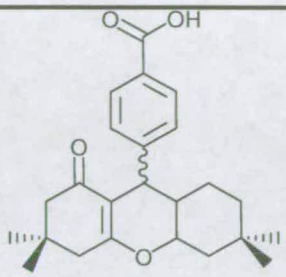	100	180.62	190.48	2
KB17/7	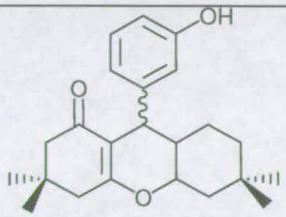	100	103.06	71.95	2
KB22/5	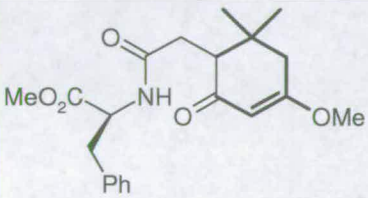	100	31.18		1
KB22/6	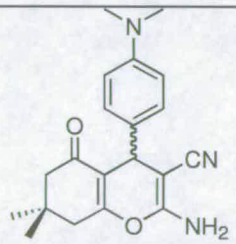	100	65.17		1
KB22/7	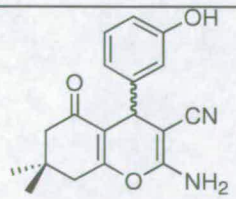	100	122.29		1
KB22/8	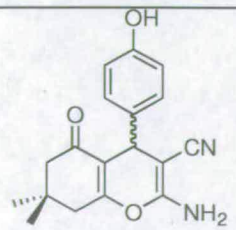	100	27.98		1

KM183	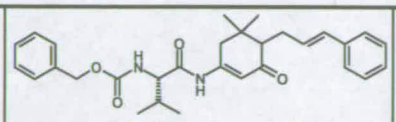	100	187.37		1
KM192A2	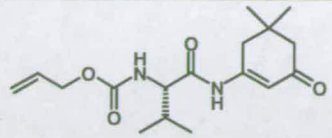	100	112.44		1
KM192B1	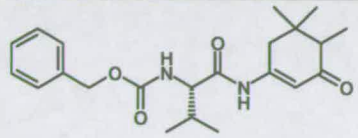	100	341.74		1
KM192B4	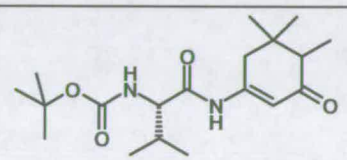	100	158.74		1
KM192C1	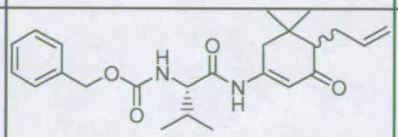	100	181.63		1
KM192C4	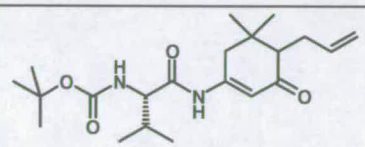	100	520.26		1
KM192F1	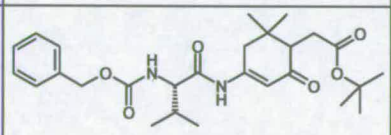	100	209.39	49.03	2
KM192F2	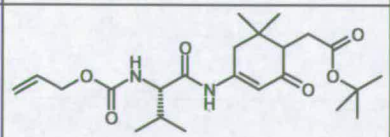	100	196.59		1
KM192F4	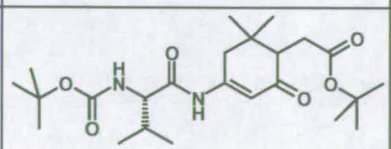	100	545.87		1
KM198	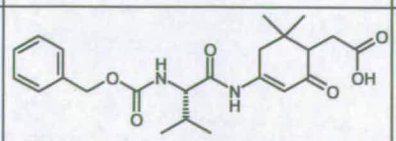	100	55.02		1

KM199A	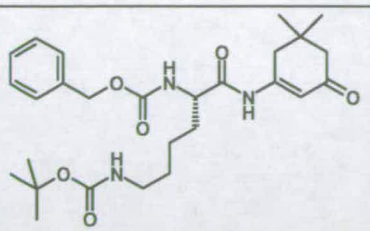	100	67.86	10.99	2
KM207	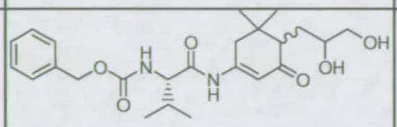	100	243.90		1
KM48	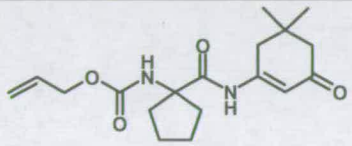	100	403.88		1
KM54	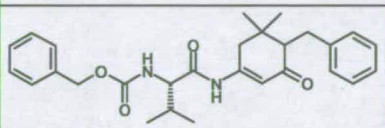	100	389.69		1
CD250/03	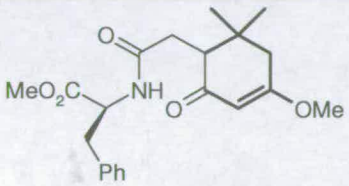	100	91.93		1
CD255/06	No structure available	100	181.16		1
CD272/02	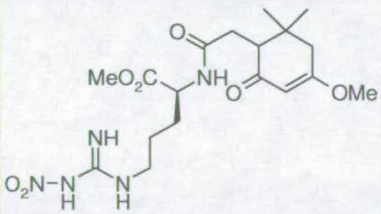	100	62.76		1
CD274/02	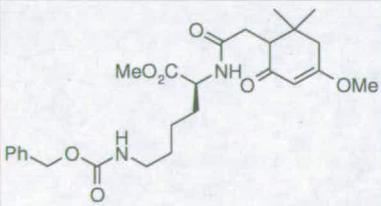	100	234.14	104.09	2
CD278/02	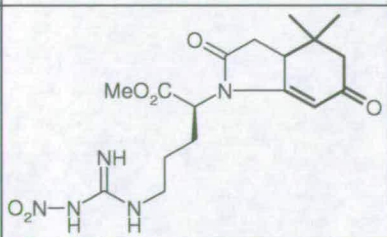	100	94.92	90.25	2

CD290/02	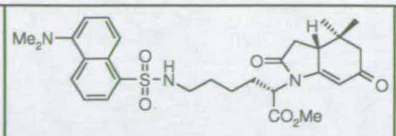	100	126.20		1

NANOMATE

LIGAND		CONC^N (μM)	Kd (μM) Transformed	σ	n
CD365/01	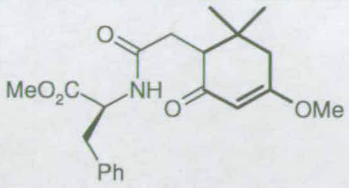	40 100	- -		1 1
KB69/12	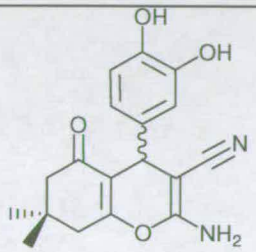	40 100	96.09 41.41		1 1
KB22/5	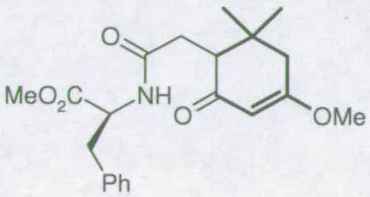	40 100	97.66 63.00		1 1
CD278/02	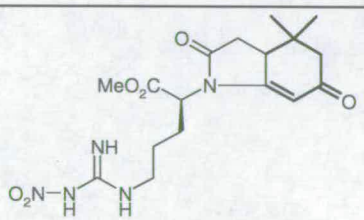	40 100	104.05 31.95		1 1
KB17/4	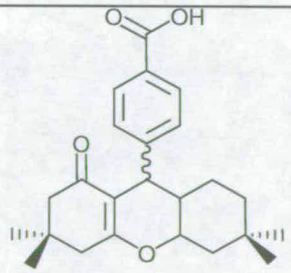	40 100	112.54 72.68		1 1
CD359/02	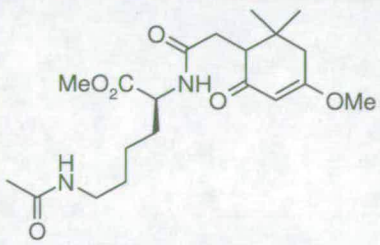	40 100	142.843 120.603		1 1

CD357/03	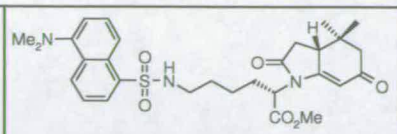	40 100	152.69 133.19		1 1
CD361/02	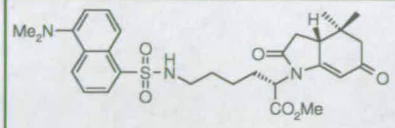	40 100	153.56 113.19		1 1
CD358/02	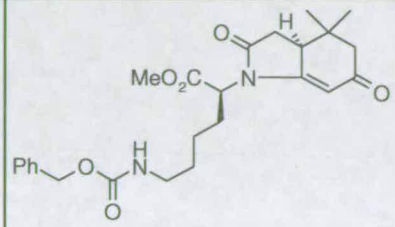	40 100	166.85 159.42		1 1
KM198	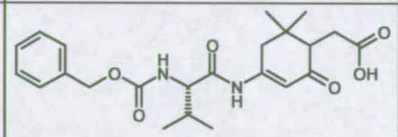	40 100	168.38 113.50		1 1
KB69/3	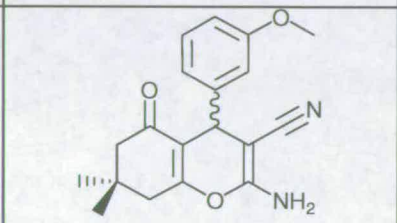	40 100	171.50 227.10		1 1
KB17/7	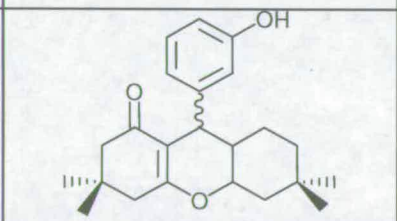	40 100	196.88 157.08		1 1
KB22/6	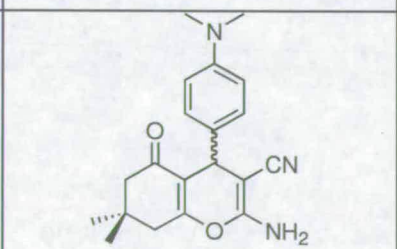	40 100	209.44 202.83		1 1
KM257	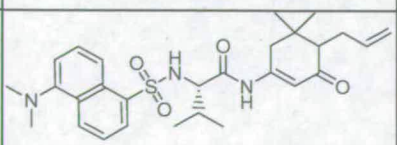	40 100	221.92 253.43		1 1

KB22/8	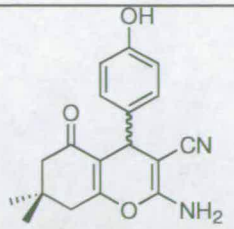	40 100	232.53 158.99		1 1
KM184	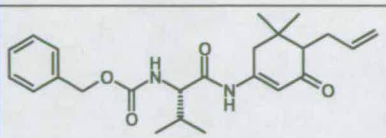	40 100	254.68 218.11	24.75 14.05	6 2
KM249/02	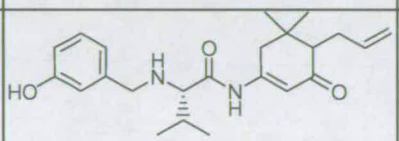	40 100	285.85 313.86		1 1
KM19	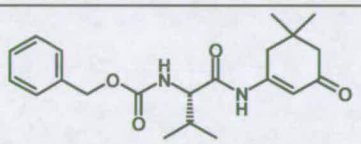	40 100	301.58 390.50		1 1
KB69/15	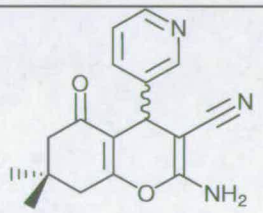	40 100	605.38 362.80		1 1
KM183	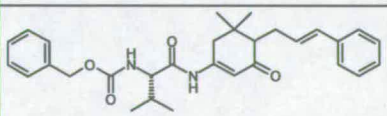	40 100	876.50 1720.69		1 1
KM5	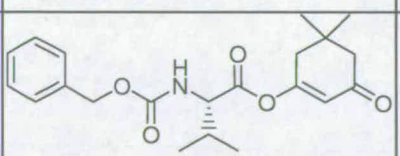	40 100	1053.62 271.97		1 1
KM249/04	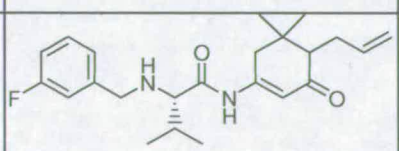	40 100	1442.81 841.97		1 1
CD354/02	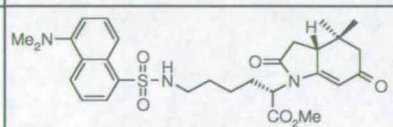	40 100	2228.29 1868.34		1 1